



ICCEEE 2017

**1st International Conference of
Chemical, Energy and Environmental Engineering**

19-21 March, 2017

Hilton Alexandria Green Plaza, Isis ballroom
Smouha, Alexandria, Egypt

STUDY ON PRODUCTION OF LIQUID FUELS FROM PLASTIC WASTES

A.I. kilany^a, M. Hussain^b, A.A.Amer, Yhia.S^c.

^aMiddle East Oil Refinery, Amreya Free Zone, El King Marriott, Alexandria , Egypt

^bAlexandria University, Faculty of Engineering, Lotfy El-Sied st. Alexandria

^cAlexandria University, Faculty of Engineering, Lotfy El-Sied st. Alexandria

E-mail address: eng.kilane@gmail.com, akelani@eprom-midor.com.eg, phone +201228374463

Abstract

Pyrolysis of waste P.P, LDPE and mixture of P.P and LDPE was conducted in laboratory scale, semi-batch stainless steel reactor in a temperature range from 490 to 550°C using bentonite or alumina as a catalyst. Pyrolysis products, such as pyrolysis oil, non-condensable gases and char were analyzed to assess the influence of pyrolysis temperature, presence of catalyst and feed composition on the process. It was found that thermal pyrolysis produced higher liquid yield as the temperature increased to 540°C in case of P.P and at 510°C in case of LDPE or the mixture. Pyrolysis of waste P.P. produced higher liquid fuel value in both thermal and catalytic pyrolysis. The Catalytic pyrolysis produced more liquid yield more than thermal pyrolysis. The oil produced from the catalytic pyrolysis was fully analyzed and the results show that it can directly be used as engine fuel after fractionation or as feedstock to petroleum refineries. FTIR analysis showed that oil obtained from the catalytic pyrolysis of P.P., LDPE and the mixture contains aliphatic hydrocarbons which are similar to petroleum fuels like diesel, gasoline and kerosene.

Key Words: waste plastic, Pyrolysis process, Pyrolysis oil, aliphatic hydrocarbons

1 Introduction

The growth of the plastics consumption has been occurring rapidly in the last six decades due to their ability to be simply formed and, their light weight. These excellent properties enabled plastics to replace wood and metals in many applications. However, huge increase in plastic wastes from industrial and municipal products worldwide rose to 280 million tons in 2012 [1]. Egypt produces annually about 16.2 million tons of municipal solid waste, plastic amount to nearly 6% of it. only about 30% of this waste was recycled, 33% are land filled, 5% reused, and 32% is burnt [2]. The main components of the household plastic waste streams include the following types of plastics: polyethylene, low-density polyethylene (LDPE), high-density polyethylene (HDPE), polypropylene (PP), polyvinyl chloride (PVC), polystyrene (PS) and polyethylene-terephthalate (PET). Egypt also is the largest oil and natural gas consumer in Africa, accounting for about 20% of petroleum and other liquids consumption and 40% of dry natural gas consumption in Africa in 2013. Egypt's total primary energy consumption was 1.7 million barrels per day (bpd) of oil equivalent in 2014 according to the British petroleum statistical review of world energy. And the present rate of economic growth is

unsustainable without consumption reduction of fossil energy like crude oil, natural gas or coal. At the same time huge amount of waste plastic which is exported with low price or land filled which causes harmful effects to the environment can be used as a substituent source of energy [3]. There was difficulty of land filling or incineration of plastic wastes due to the unavailability of suitable places for technically adequate landfills or incinerators. In addition, depending on the waste nature, combustion may produce pollutants like light hydrocarbons, nitrous and sulfur oxides, dusts, dioxins and other toxins which have a highly negative impact on the environment . Recycling of plastic is the ideal solution to reduce the amount of waste that hardly can be disposed of and reduce its carbon footprint. There are many different methods of waste plastic recycling techniques such as mechanical, biological, thermal and chemical recycle. Thermal treatment or pyrolysis has been extensively studied in the past decades for generating an alternative environmental and economical option for waste processing. This option has a number of advantages over conventional methods, i.e. incineration or land filling as it produces liquid hydrocarbon, gases and carbonaceous char that can be used as a fuel pyrolysis takes place in the absence of air and the recovery of products is always achieved. Overall, pyrolysis process is considered as a beneficial option in waste treatment largely due to the products generated and the energy recovery when compared to other methods. In this study, the pyrolysis process is implemented on three types of waste plastic feed stock: polypropylene, low density polyethylene. The process was carried out in a semi batch stainless steel reactor. TGA analysis was carried out to determine the effective temperature for pyrolysis. The effect of pyrolysis temperature, catalyst type, catalyst to feed ratio, and reaction time on the produced liquid fuel yield were studied. Finally, full laboratory analysis was done for liquid fuel produced to assess its suitability as fossil fuel substitute.

2 Experimental Technique

Fig.1 shows the apparatus used in the work ,Sample of 50 gm of waste plastic (polypropylene, LDPE) was weighed and cut into 4 x 4 pieces and then charged into an unstirred 311 cm³ well-sealed stainless steel reactor. The outlet of the reactor is connected to a two-stage condenser to separate the condensable gases. In case of catalytic pyrolysis, different catalyst to plastic ratios (1:2, 1:3, 1:4 and 1:5) were added to the reactor and the reactor was tightly sealed and placed inside the furnace (Vulcan 3-550). . Air was removed from the reactor using vacuum pump. Heating was carried out at different pyrolysis temperatures from 490 °C to 550 °C at a rate of 25°C min⁻¹. The condensable gases products were condensed, collected and weighed. After the completion of the pyrolysis process, the solid residue left inside the reactor was also weighed. The weight of the non-condensable gases was calculated as the difference between the initial waste weight and the total weight of the liquid and solid product from the following equation.

$$\text{Gases, wt, (gm)} = (\text{total waste plastic}) \text{ wt, (gm)} - (\text{liquid} + \text{solid residue}) \text{ wt, (gm)}$$

The percentage of liquid fuel yield was calculated in both thermal and catalytic pyrolysis at different pyrolysis temperature, different catalyst type and different ratios of plastic to catalyst if present, by previous equation.

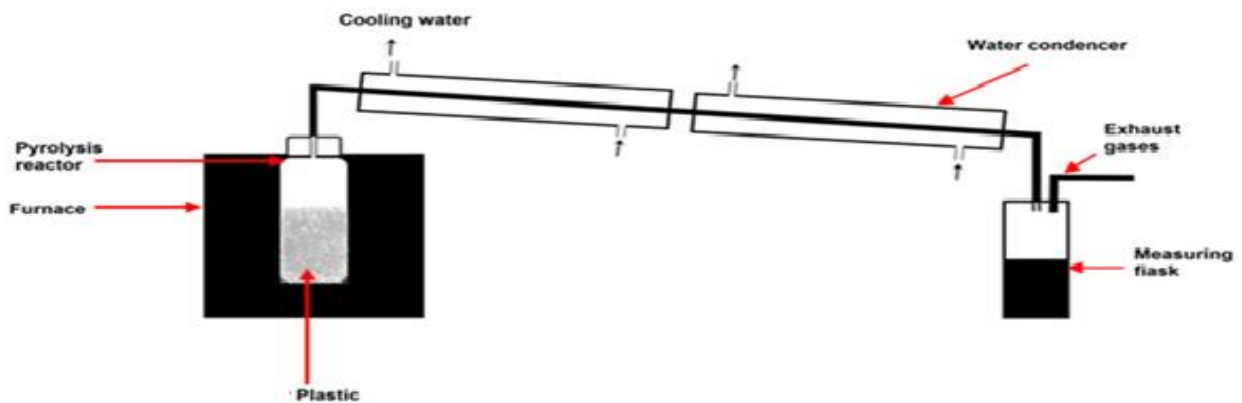


Figure (1): experimental set up apparatus

3 Results and discussion

3.1. TGA for waste plastic samples (Polypropylene and LDPE)

Thermo gravimetric analysis was conducted on the samples to determine the temperature of thermal degradation (Fig.2 and 3), referred to as the critical temperature, and which will be used as the effective pyrolysis temperature. TGA results show that the 50% weight loss for PP and LDPE was 330 and 382°C, while the degradation completed at 430 and 509°C respectively. From these results, it is expected that the mixture of different composition will demonstrate a variety of temperatures depending on its initial composition.

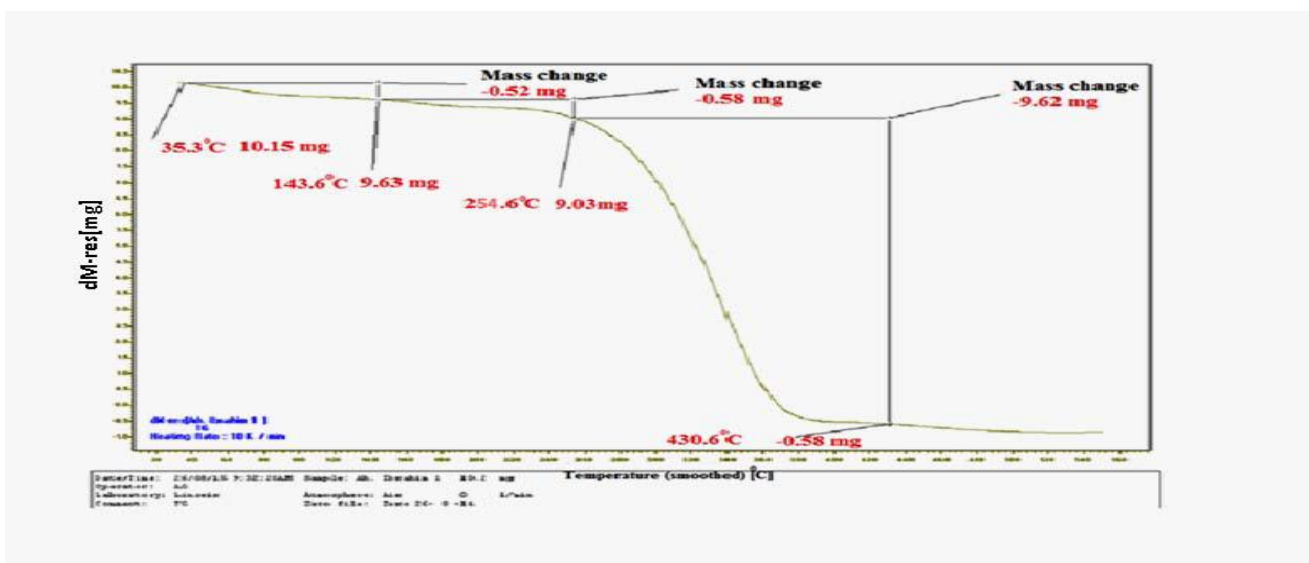


Figure (2): TGA for waste polypropylene sample

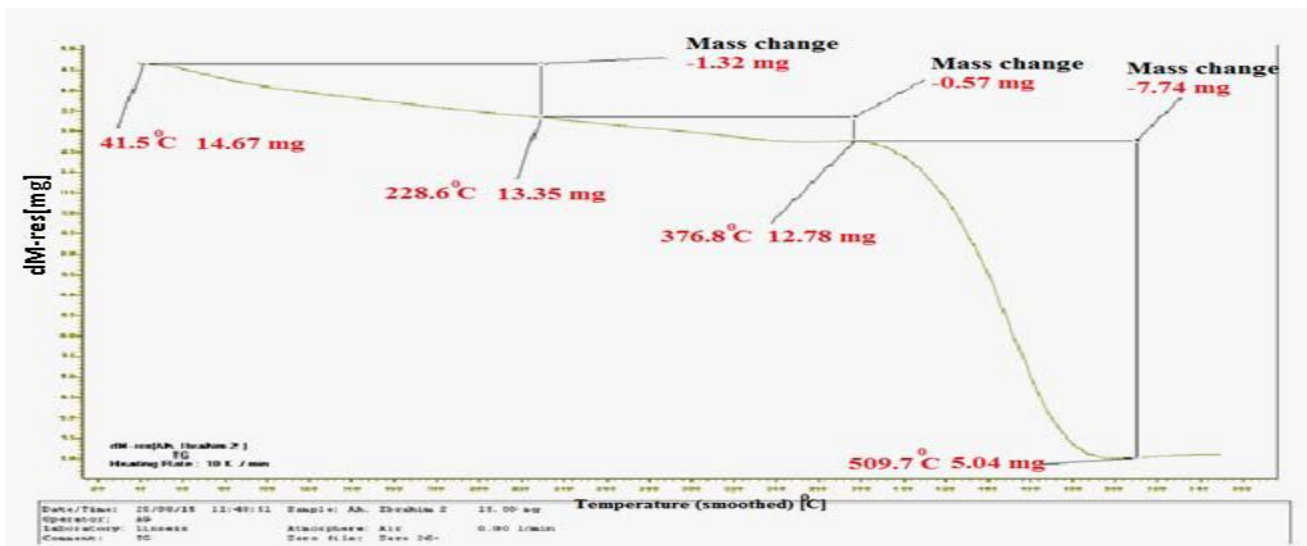


Figure (3): TGA for waste Low density polyethylene (LDPE) sample

3.2. Effect of pyrolysis temperature on product yield

Three different fractions, namely condensable liquid products, non condensable gases and solid residue, were obtained during pyrolysis. Figure (4) and (5) show the yield distribution of the different fractions and the effect of increasing the pyrolysis temperature from 490 to 540°C.

3.3. Polypropylene pyrolysis:

Fig.4 shows that by increasing pyrolysis temperature from 490°C to 540°C liquid yield increased from 82 % wt to 87.8 % wt then slightly decreased to 84 % wt when the pyrolysis temperature was increased to 550°C. However, when the pyrolysis temperature was increased from 490°C to 540°C gas fraction slightly decreased from 13.6% wt to 10.8 %wt. Similarly, solid residue yield also decreased from 4.4 % wt to 1.4% wt. Although, when temperature was increased to 550 °C gas fraction increased again from 10.8 %wt to 13.6 %wt and solid residue yield also increased from 1.4 %wt to 2.4 %wt.

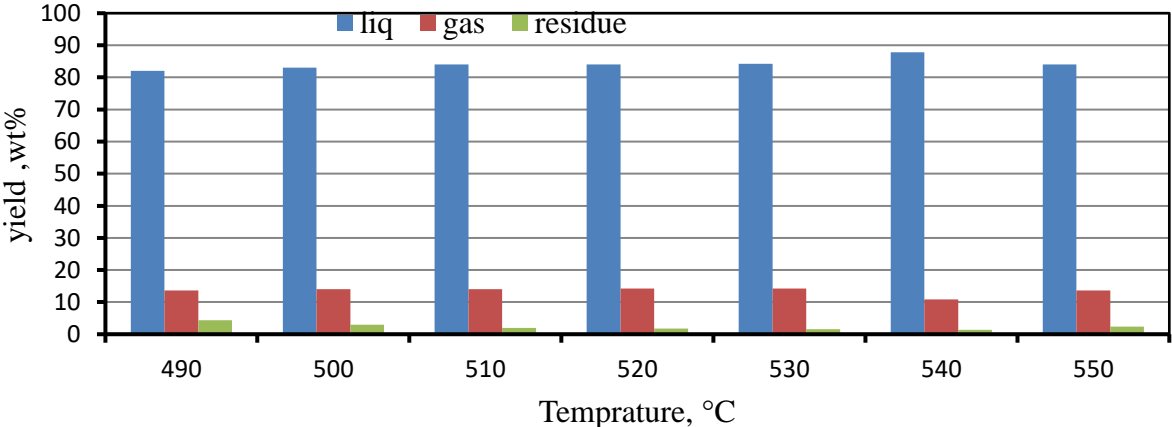


Figure (4): Effect of pyrolysis temperature on yield during polypropylene thermal pyrolysis

3.3.1. LDPE pyrolysis

Fig.5 shows that by increasing pyrolysis temperature from 490 to 510°C, the liquid yield increased from 35.4% wt to 39% wt then slightly decreased to 36.8 wt% when the reaction temperature was increased to 550 °C. On the other hand, when the pyrolysis temperature was increased from 490 °C to 510 °C gas fraction slightly decreased from 10% wt to 8.4 %wt. Similarly, solid residue yield also decreased from 54.6 % wt to 52.6% wt. Although, when temperature was increased to 550 °C gas fraction increased from 8.4 %wt to 9.6 %wt and solid residue yield also slightly increased from 52.6 %wt to 53.6%wt

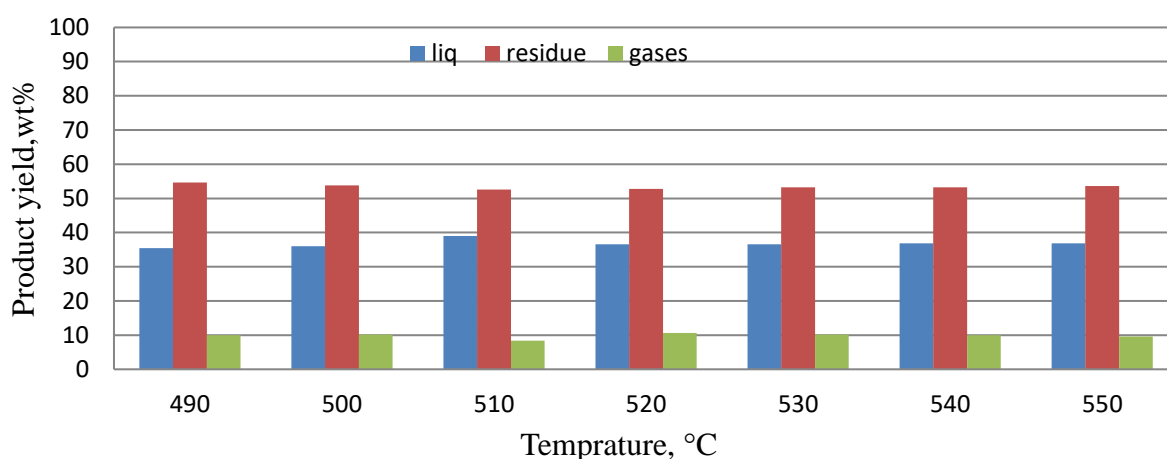


Figure (5): Effect of pyrolysis temperature on product yield from LDPE Thermal pyrolysis

For the above figures (4), and (5) it can be concluded that by increasing pyrolysis temperature liquid yield was increased but it's noted that gas fractions increased at high temperatures due to increase in the reaction time which allow secondary cracking of pyrolysis oil to non condensable gases. The results also suggest that the decreased residue mainly converted to pyrolysis oil during P.P pyrolysis up to 540°C and this is agree with Yuan Xue et al [4].

3.4. Effect of catalyst

3.4.1. Poly propylene pyrolysis

The effect of using catalyst such as bentonite and alumina during pyrolysis of polypropylene was studied for catalyst to P.P ratio of 1:3 and at different temperature values of (490,500,510,520,530,540,550) °C. Fig.6 shows that oil yield increased in catalytic pyrolysis compared with thermal pyrolysis at all temperature values also shows that using alumina as a catalyst produce highest weight percentage of oil yield than using of bentonite at different pyrolysis temperature. This is might be due to that catalyst can enhance cracking of long chain hydrocarbons into lighter and shorter chain hydrocarbon and this is agree with A. Lopez et al [5].

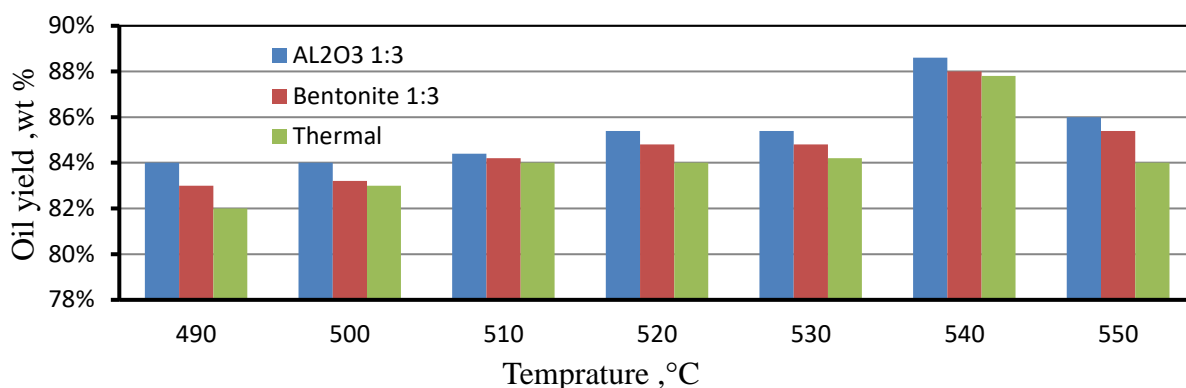


Figure (6): Effect of presence of catalyst (alumina or bentonite) on oil yield at different temperature of polypropylene pyrolysis at catalyst to P.P ratio of 1:3

3.4.2. LDPE pyrolysis

The effect of using catalyst such as bentonite and alumina during pyrolysis of LDPE at catalyst to LDPE ratio of 1:5 and different temperature values of (490,500,510,520,530,540,550) °C was studied. Fig.7 shows that oil yield increased in catalytic pyrolysis compared with thermal pyrolysis at all temperature values and also show that using bentonite performed slightly better in terms of producing of liquid yield over using alumina as a catalyst.

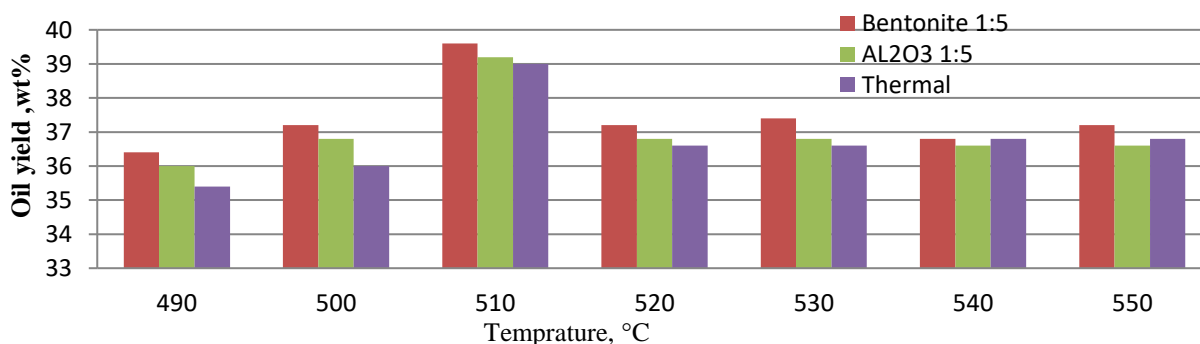


Figure (7): Effect of catalyst (Alumina or bentonite) on oil yield at different temperature of LDPE pyrolysis at catalyst to LDPE ratio of 1:5

3.5. Effect of catalyst ratio

3.5.1. Effect of catalyst to waste polypropylene ratio

The effect of catalyst to waste P.P ratio was studied using different ratios of (1:2, 1:3, 1:4, and 1:5) at constant temperature of 540 °C. Figure (4.5) and table (A.3) shows that as the catalyst to waste P.P ratio increase the yield of oil also increase up to 88.6wt% at 1:3 alumina catalyst to waste P.P ratio then decreased again. The same behavior occurred in case of using bentonite as a catalyst in which oil yield also increase to 88 wt% at 1:3 bentonite catalyst to waste P.P ratio then decreased again. It can also be noticed that alumina performed slightly better in terms of producing of liquid yield over using bentonite as a catalyst in all catalyst to P.P ratios. In conclusion, the presence of catalyst can enhance cracking reaction but increasing the amount of catalyst to P.P ratio more than 1:3 can decrease liquid

fractions and increase gaseous fractions in which long chain hydrocarbon liquid converted to short chain hydrocarbon gases and this is agree with mochamad syamsiro et al [6].

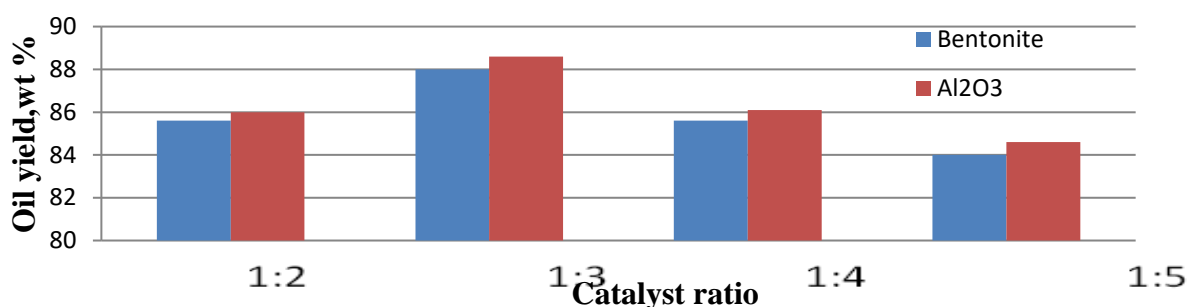


Figure (8): Effect of catalyst (AL₂O₃ and bentonite) to waste polypropylene ratio on oil yield at constant temperature of 540 °C.

3.5.2. 4.2. LDPE pyrolysis

The effect of catalyst to waste LDPE ratio was studied using different ratios of (1:2, 1:3, 1:4, and 1:5, 1:6) at constant temperature of 510 °C. Fig.9 shows that as the catalyst to waste LDPE ratio increase the yield of oil also increase to 39.6wt% at 1:5 bentonite catalyst to waste LDPE ratio then decreased again. The same behavior occurred in case of using alumina as a catalyst in which oil yield also increase to 39.2 wt% at 1:5 alumina catalyst to waste LDPE ratio then decreased again. It can also be noticed that bentonite performed slightly better in terms of producing of liquid yield over using AL₂O₃ as a catalyst in all catalyst to LDPE ratios. the presence of catalyst can enhance cracking reaction and this is agree with mochamad syamsiro et al [6].

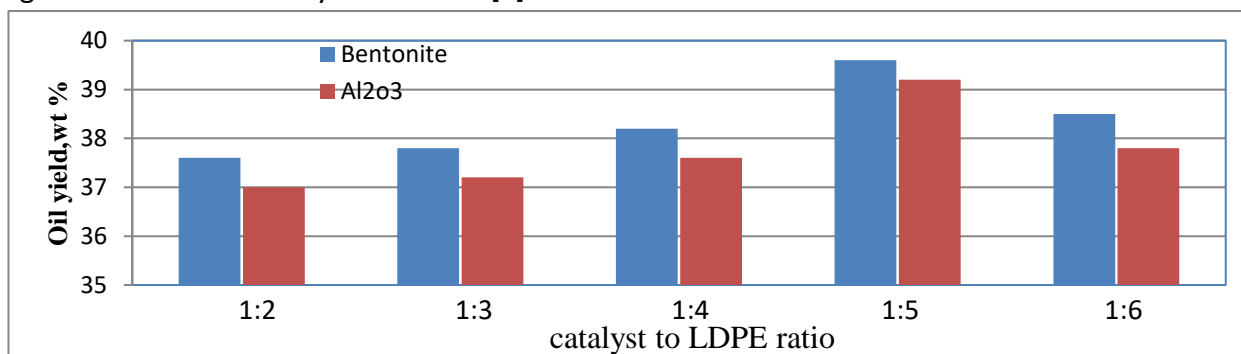


Figure (9): Effect of catalyst (Alumina and bentonite) to waste LDPE ratio on oil yield at constant temperature of 510 °C.

3.6. Properties of oil produced from waste plastic pyrolysis

Oil sample produced from catalytic pyrolysis of polypropylene using AL₂O₃ as a catalyst at catalyst ratio of 1:3 and pyrolysis temperature of 540 °C and pyrolysis oil from LDPE using bentonite as a catalyst at catalyst to LDPE ratio of 1:5 and pyrolysis temperature of 510 °C was fully analyzed to know its properties. Table (2) shows fraction distillation results of the oil and it is observed that, the boiling point range of the oil is between 85 and 361°C, which infer the presence of mixture of different oil components such as gasoline, kerosene and diesel in the oil. 30% of oil recovery occurs in the range from 180°C to 184°C, which similar to the boiling point range of gasoline. While the 70% is in the same

range of kerosene and diesel. Table (3) shows physical and chemical properties of oil produced by tested oil sample using prescribed IS of ASTM methods [8]. All the other fuel properties of the oil obtained is almost similar and comparable to petroleum fractions moreover, it has high calorific from 46.5 to 49.2 MJ/kg value and low sulfur content of 3 ppm and also low nitrogen content. From this result, it can be concluded that the oil produced in the catalytic pyrolysis can be used as a substitute of petro fuels in engine.

Table (2): fractions Distillation of oil produced from waste plastic pyrolysis

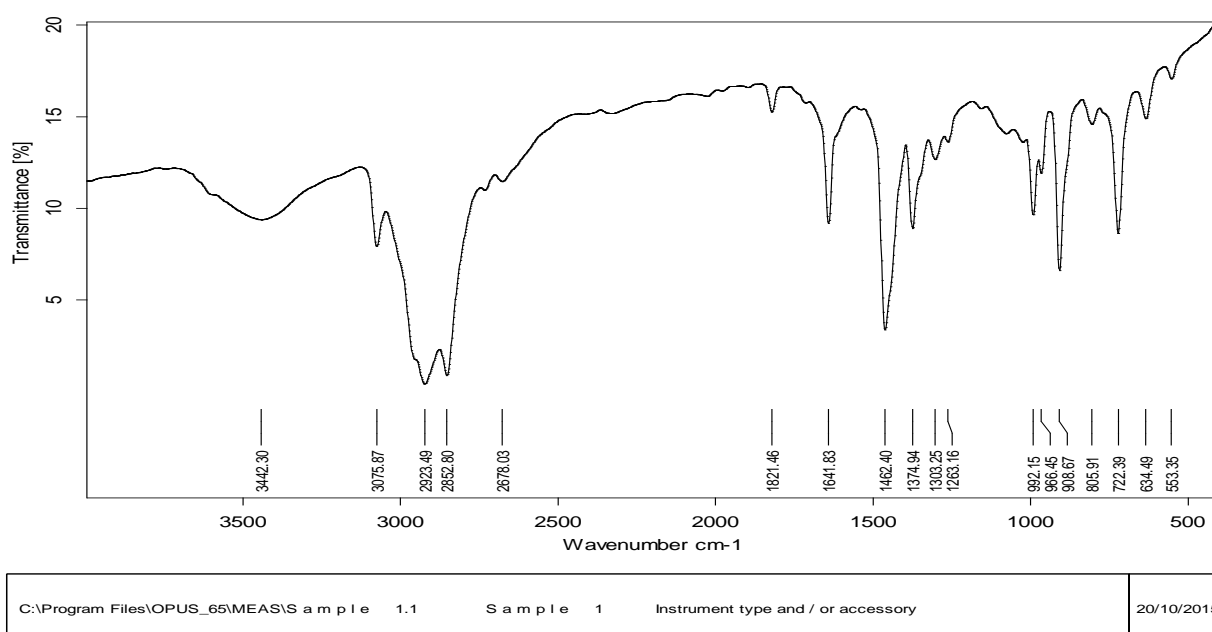
Distillation%	IBP	5	10	30	40	50	60	70	80	90
P.P oil Temp, °C	90	125	150	184	242	290	320	334	345	361
LDPE oil Temp, °C	85	120	145	180	240	285	320	330	347	360

Table (3): chemical and physical properties of oil produced from P.P,LDPE and mixture of waste plastic

Properties	P.P fuel oil property results	LDPE fuel oil property results	Test method
Gross cal value MJ/kg	46.5	49.2	ASTM D 4868
cetane index	80.2	85	ASTM D 4737-A
Density Kg/m ³	788	798	ASTM D 4052
Kinematic viscosity@40 °C	2	2.2	ASTM D 445
pour point, °C	24	30	ASTM D 97
color	Pale yellow	pale yellow	ASTM1500
Total sulphur PPM	3	3.2	ASTM 4294
Boiling point range	90-361	85-360	ASTM D 86

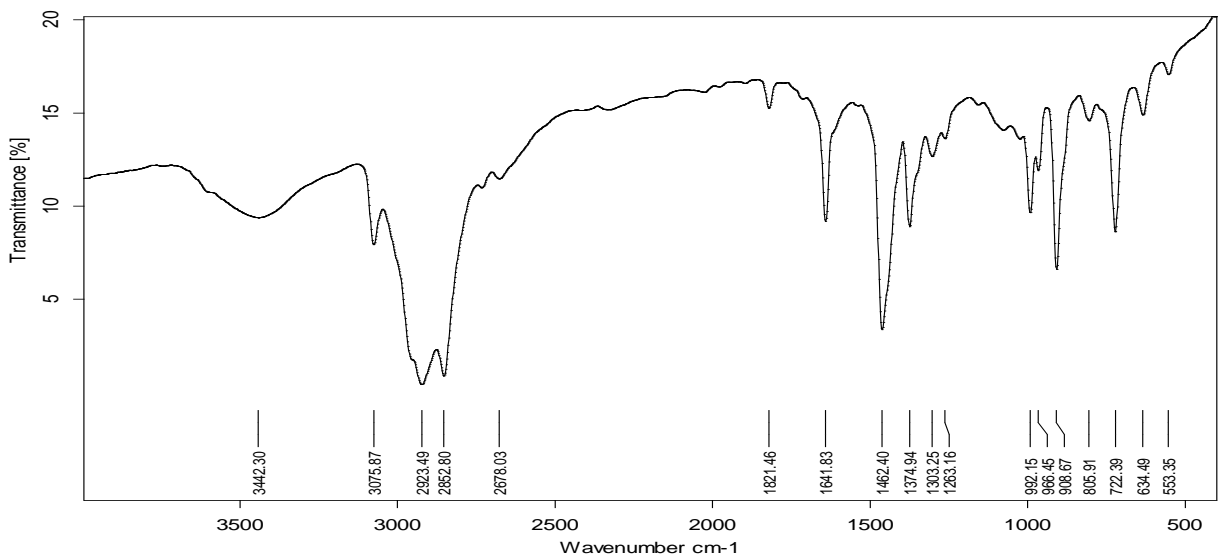
3.7. FTIR of oil produced from polypropylene and LDPE

The FTIR of the oil produced from P.P catalytic pyrolysis at 540 °C and alumina catalyst to P.P ratio of 1:3, and for the oil produced from LDPE catalytic pyrolysis at 510 °C and bentonite catalyst to LDPE ratio of 1:5 was done in a Burker-tensor Fourier transformed infrared spectrophotometer in the range of 500-3500 cm⁻¹ to know the functional group composition. Figure (10) and (11) shows the following types of functional groups of (alkanes, alkenes and oxygenated hydrocarbon) which are similar to light fractions of petroleum products



Page 1/1

Figure (10): FTIR of oil produced from pyrolysis of P.P using alumina as a catalyst in 1:3 ratios



C:\Program Files\OPUS_65\MEAS\S a m p l e 1.1 S a m p l e 1 Instrument type and / or accessory 20/10/2015

Figure (11) FTIR of oil obtained from pyrolysis of LDPE using bentonite as a catalyst in 1:5 ratio at 510 °C.

3.8. Comparison between commercial diesel and liquid fuel produced from waste plastic pyrolysis

The commercial diesel has some properties such as cetane index, density, viscosity, cloud point; sulphur content and distillation range are all important properties to diesel fuel. The quality of the liquid fuels from pyrolysis of plastics will vary with pyrolysis operation conditions .Table (4) shows comparison between properties of diesel petroleum fraction and oil produced from pyrolysis of P.P and LDPE. It can be noticed that both fuels has equivalent values of chemical and physical properties. Moreover, high calorific value and low sulphur content of pyrolysis oil.

Table (4): Comparison between chemical and physical properties of oil produced from P.P, and LDPE catalytic pyrolysis and commercial light diesel

TESTS	Oil produced from P.P Pyrolysis	Oil produced from LDPE Pyrolysis	Light Diesel	Test Methods
Gross cal value, MJ/kg	46.51	49.21	45	ASTM D 4868

cetane index	80.2	85	80	ASTM D 4737-A
Density ,Kg/m ³	788	798	849	ASTM D 4052
Kinematic viscosity@40 °C	2	2.2	2.9	ASTM D 5771
pour point, °C	24	30	12	ASTM D 97
color	Pale yellow	Pale Yellow	yellow	ASTM1500
Total sulphur, PPM	3	3.2	500	ASTM 4294
Boiling point range,°C	90-361	85-360	175-360	ASTM D 86

4 Conclusions

Thermo gravimetric analysis of waste P.P and LDPE indicated that their degradation temperature occurred at 430°C and 509° respectively which indicate the range of pyrolysis temperature.

The highest weight percentage yield of liquid fuel oil produced from thermal pyrolysis obtained at 540 °C in case of using polypropylene and at 510°C in case of using LDPE as a feed stock for pyrolysis reactor.

Pyrolysis of polypropylene as a feed stock produce higher Liquid fraction compared with pyrolysis of LDPE.

Catalytic pyrolysis using bntonite or alumina as a catalyst has higher Liquid fraction compared with thermal pyrolysis

Using alumina as a catalyst during catalytic pyrolysis for P.P produce higher Liquid fraction than using bentonite while the opposite occurred in case of LDPE catalytic pyrolysis in which bentonite produce higher percentage of Liquid fraction than using alumina.

The highest weight percentage yield of liquid fuel oil produced from catalytic pyrolysis of P.P and LDPE obtained at catalyst ratio of 1:3 and 1:5 respectively.

Fraction distillation for produced liquid fuel indicate that the boiling point range of the produced oil in the same range of petroleum fractions which infers the presence of mixture of different oil components such as gasoline, kerosene and diesel in the oil.

properties of the oil sample was obtained at the optimum pyrolysis process conditions and this results showed that oil sample produced from pyrolysis of P.P and LDPE has high calorific more than 46.5 MJ/kg value and low sulfur content of 3 ppm and other good properties such as pour point, density, cetane index ,viscosity and color.

FTIR was done for produced liquid fuel sample from pyrolysis of P.P and LDPE at optimum pyrolysis process conditions for each type of waste plastic to know the function group of oil produced and the results shows that main the components of produced oil is aliphatic hydrocarbon such as (alkanes ,alkenes) and oxygenated hydrocarbon which is similar to light fractions of petroleum products like gasoline, kerosene and gas oil .

References

1. [Http://www.petroleum.gov.eg/ar/MediaCenter/LocalNews/Pages/mop_05072014_!.aspx](http://www.petroleum.gov.eg/ar/MediaCenter/LocalNews/Pages/mop_05072014_!.aspx),access ed(7/2/2016)
2. Costa veils, "Global Recycling Markets of Waste Plastic," University of Leeds, Vienna, Sept. 2014.
3. Magdy, G., Nagwa, M., and Ibrahim, M., " National Study for Plastic Recycle Sector In Egypt," Plastic Technology Center, Alexandria, Egypt, Jan 2008.
4. B.P., Statistical Review of World Energy, the British Petroleum Company, June 1996. ,<https://www.eia.gov/beta/international/analysis.cfm?iso=EGY>,accessed(1/2/2016)
5. Yuan Xue ,Shuai Zhou and Robert C., "Fast Pyrolysis of Biomass and Waste Plastic in a Fluidized Bed Reactor," Fuel Journal, v156, pp.40-45, 2015.
6. Mochamad Syamsiroa, HarwinSaptoadi, Tinton Norsujianto, PutriNoviasria,Shuo Cheng, Zainal Alimuddinc and Kunio Yoshikawa, "Fuel Oil Production from Municipal Plastic Wastes in Sequential Pyrolysis and Catalytic Reforming Reactors," Renewable Energy and Energy Conservation,Indonesia,v47,pp.180-188,2014.
7. Filipe Paradela, Filomena Pinto and Ana M. Ramos, "Study of the Slow Batch Pyrolysis of Mixtures of Plastics, Tires and Forestry Biomass Wastes," Journal of Analytical and Applied Pyrolysis, v85, pp.392-398, 2008.
8. ASTM international directory of testing laboratories, west Conshohocken, USA, v 5, 2003
9. Sheng C., and Azevedo, JLT., "Estimating the Higher Heating Value of Biomass Fuels from Basic Analysis Data," Biomass and Bioenergy,pp.499-507, 2005.
10. Demirbas, A., "Effects of Moisture and Hydrogen Content on the Heating Value of Fuel," Energy Sources, Part A: Recovery, Utilization, and Environmental Effects, pp.649-655, 2007.

Abbreviations and Acronyms

P.P	Poly propylene
LDPE	low density poly ethylene
M.S.W	Municipal solid waste

TGA Thermo gravimetric analysis
SPI Society of plastic industry

Acknowledgements

Thanks first and last to ALLAH as we are owed to HIM for his great care, support and guidance in every step in our life. I could finish this thesis only by HIS guidance and will. I wish to express my deep appreciation and gratitude to **Prof. Dr. Mohamed Hussein Abdel Majeed** for his valuable comments, guidance, patience and encouragement throughout my study. I would also like to sincerely thank my supervisor **Prof. Dr. Gihan Farouk Malash**, for her keen supervision, assistance and continuous guidance to perform this work. My sincere thanks are also directed to **Dr. Amer Abdel Razek Shoier** for his dedication, brilliant suggestions and guidance this research work.

Finally, I wish to express my deepest gratitude to my parent and my wife for their unlimited support and encouragements. Thank you for your understanding, and encouragement, for always being my side through all those difficult times and for the happiness we will share in the future.

APPENDIX

Table (A.1): Effect of pyrolysis temperature on product distribution during polypropylene thermal pyrolysis

Temperature, °C	Liquid yield, wt%	Gas yield, wt%	Residue yield, wt%
490	82%	13.6%	4.4%
500	83%	14%	3%
510	84%	14%	2%
520	84%	14.2%	1.8%
530	84.2%	14.2%	1.6%

540	87.8%	10.8%	1.4%
550	84%	13.6%	2.4%

Table (A.2): Effect of presence of catalyst (alumina or bentonite) on oil yield at different temperature of polypropylene pyrolysis at catalyst to P.P ratio of 1:3

Temperature, °C	Liquid yield ,wt % using Al ₂ O ₃	Liquid yield, wt % using Bentonite	Liquid yield, wt % Thermal pyrolysis
490	84%	83%	82%
500	84%	83.2%	83%
510	84.4%	84.2%	84%
520	85.4%	84.8%	84%
530	85.4%	84.8%	84.2%
540	88.6%	88%	87.8%
550	86.0%	85.4%	84%

Table (A.3) : Effect of catalyst (Al₂O₃ and bentonite) to waste polypropylene ratio on oil yield at constant temperature of 540 °C

Catalyst Ratio	Liquid yield ,wt % using Bentonite	Liquid yield, wt % using Al ₂ O ₃
1:2	85.6%	86%
1:3	88%	88.6%

1:4	85.6%	86.1%
1:5	84%	84.6%

Table (A.4): Effect of pyrolysis temperature on product yield from LDPE Thermal pyrolysis

Temperature, °C	Liquid yield, wt%	Gas yield, wt%	Residue yield, wt%
490	35.4%	10.0%	54.6%
500	36%	10.2%	53.8%
510	39%	8.4%	52.6%
520	36.6%	10.6%	52.8%
530	36.6%	10.2%	53.2%
540	36.8%	10%	53.2%
550	36.8%	9.6%	53.6%

Table (A.5): Effect of catalyst (Alumina or bentonite) on oil yield at different temperature of LDPE pyrolysis at catalyst to LDPE ratio of 1:5

Temperature, °C	Liquid yield ,wt % using Al ₂ O ₃	Liquid yield ,wt % using Bentonite	Liquid yield, wt % Thermal pyrolysis
490	36 %	36.4%	35.4%

500	36.8%	37.2%	36.0%
510	39.2%	39.6%	39%
520	36.8%	37.2%	36.6%
530	36.8%	37.4%	36.6%
540	36.6%	36.8%	36.8%
550	36.6%	37.2%	36.8%

Table (A.6): Effect of catalyst (Al_2O_3 and bentonite) to waste LDPE ratio on oil yield at constant temperature of 510 °C

Catalyst Ratio	Liquid yield, wt % using Bentonite	Liquid yield, wt % using Al_2O_3
1:2	37.6%	37.0%
1:3	37.8%	37.2%
1:4	38.2%	37.6%
1:5	39.6%	39.2%
1:6	38.5%	37.8%

Table (A.7): Effect of pyrolysis temperature on product distribution of mixed waste plastic of (P.P and LDPE) in 1:1 ratio

Temperature, °C	Liquid yield, wt%	Gas yield, wt%	Residue yield, wt%
490	55.3%	21%	23.7%
500	57.5%	19.5%	23%
510	60%	17.7%	22.2%
520	58%	19.2%	22.7%
530	57.5%	19%	23.5%
540	57.5%	19.2%	23.2%
550	57%	20.2%	22.7%

Table (A.8) : Effect of catalyst (Alumina or bentonite) on oil yield at different temperature of waste plastic mixture pyrolysis at catalyst to mixture ratio of 1:4

Temperature, °C	Liquid yield, wt % using Al ₂ O ₃	Liquid yield ,wt % using Bentonite	Liquid yield, wt % Thermal pyrolysis
490	56.2%	55.7%	55.2%
500	58.0%	57.5%	57.5%

510	61.0%	60.7%	60.0%
520	58.7%	58.2%	58.0%
530	57.7%	57.7%	57.5%
540	59.0%	58.0%	57.5%
550	58.0%	57.5%	57.0%

Table (A.9): Effect of catalyst (Al_2O_3 and bentonite) to waste plastic mixture of (P.P and LDPE) ratio on oil yield at constant temperature of 510 °C

Catalyst Ratio	Liquid yield, wt % using Bentonite	Liquid yield, wt % using Al_2O_3
1:2	55.0%	55.7%
1:3	55.7%	56.2%
1:4	60.6%	61.0%
1:5	56.5%	57.5%

Enhancement of Hydrogen Engine cavitation with Mixed Fuel: A Review and case study (Part A)

Mohamed R. Gomaa^{1,2} Yasser M. Ashoosh^{*,1}

1,* Mechanical Department, Benha Faculty of Engineering, Benha University, Benha, Egypt

2Mechanical Department, Faculty of Engineering, Mu'tah University, Al karak, Jordan

*Tel: +201110520614, Email: y3shoosh@gmail.com

High lights

- 1- Hydrogen Engine and main problems
- 2- Nano material usage for engine cavitation solutions
- 3- Duke Engines with Hydrogen Fuels

Abstract

Making the better ways for the hydrogen production cheap, safely for the environment and easy with different application of combustion engine application by hydrogen fuel production by a combined method from photovoltaic, electrolysis, thermal depravity and displacement of NG (natural gas) and coal.

Actually, nobody can gainsay that the hydrogen combustion engines are the more important issue. **ICHE** (Internal combustion hydrogen engine) presents much of the promise as cell of hydrogen production and other extraction methods; it can reduce dependences on oil fuel and reduced emissions as CO₂ carbon dioxide. The cavitation methods treatment that was resulted in ICHE cylinders was studied theoretically. This study included modification on hydrogen engines that appear a new technics more safe and successful. Advisors will be using a neo technics in the mixing fossil fuel and deduce it by comparison with hydrogen-fuel, as well as new and characteristic in a research addition to added water vapor as element of this mixture. The different methods to get the hydrogen process of mixing more secure are studied.

Keywords

Hydrogen production, Hydrogen Engine, Duel fuel, Engine Cavitation, Duke Engines.

1.1 INTRODUCTION

Specific fuel energy of hydrogen is high, high flame speed, the flammability with wide range, and cleans burning characteristics which suggest a possibility of high combustion performance in ICE (internal combustion engines).

At the first of 1990s, FSEC hydrogen was conducted research by using in at ICE. [HYTEST](#) was the name of this work that resulted from the development of a mixed fuel. Today, DOE (Department of energy) and vehicles manufacturers work on ICEs hydrogen-powered continually [1]. By using of hydrogen as a power carrier, two motivators are resulted; (1) to provide energy from fuel without emissions (carbonless) society and (2) to manage renewable sources of energy. The first, of motivations requires a briefly discussion and the second, it's self-evident.

The hydrocarbon-fuels reformation was the more common and the way of cost effective to produce hydrogen-fuel today, specifically NG. [Greenwood et al. \[2\]](#) reported the viability and cost of NG reformation with sequestration of carbon dioxide as a way of cost effective to reduce yearly levels of CO₂ emission. He debates that the minimal CO₂ sequestration was obtained if economy of hydrogen was introduced then the cost additional of NG reformation and posterior [3].

Air pollution is serious problems in the world that are obtained from combustion of fossil-fuel. So, the enquiring for a fuel friendly with environmental as hydrogen fuel as a power carrier. Some researcher was working on the ways to reduce engines emissions.

The increasingly use of [CIE](#) (compression ignition engine) in vehicles cause's in the quality of air to a level.

The deposit formation inside of the cylinder combustion engine could affect the emissions of exhaust from vehicles. One probable method to solve this matter was to use additives mixed with the fuel [4].

The combustion properties of Hydrogen's unique may improve performance, thermal efficiency (break thermal efficiency) and CO₂ emission levels in ICHE and also useful for saving. The diffusion coefficient of hydrogen, 0.61cm²/s, was higher than gasoline diffusion coefficient, 0.16cm²/s, for that reason, it improves the homogeneousness of combustible mixture. This work-done on the alternator used a two-stroke scavenging system, dynamic modeling, electromagnetic, combustion, and researches of fuel. The Sandia and Magnequench design a small-scale was be finished, and tested. The scavenging work

system ingredient of learning how to model KIVA-3V, and designing, testing the scavenging experiments. It was conducted the modeling by Ron Moses of Los Alamos NL (National Laboratories). The alternator modeling was being performed.

Outside of modeling and research, an industrial co-operation has made with international Caterpillar and Magnequench, a major of rare permanent magnet materials of earth supplier. Although the current environmental and energy policies has forced researchers to be interested in non-polluting and clean alternative fuels for transport sectors, the major energy sources demand was supplied by, conventional fuel, fossil fuels.

That was made a Convention on Climate Change, through the period between 1990-2004, CO₂ emission Maximized by 27%, and the energy consuming in transport pats was increased by 37% [5, 6].

1.1.1 OBJECTIVES

For the accomplishment of this module, the specialized will understand:

1. The hydrogen properties combustive that relate to its use as a fuel combustive.
2. The air to hydrogen fuel mixtures, air/fuel, ratio and compares it with other fuels.
3. The kinds of pre-ignition problems were being facing in an ICHE and a solution.
4. The different types of ignition systems that will use with ICHE.
5. The issues of crankcase ventilation that belonging to use in ICHE.
6. The performance, thermal efficiency, emissions, output power and hydrogen mixed with different hydrocarbon fuel in ICHE.

1.2 Hydrogen Engines

The vehicles which using ICHE made some difficult to clear up how to refacing them. Therefore, this sector does not service as a manual repaired, but only an outline description of the hydrogen-fuel

engine, operation and its main components, its benefits, drawbacks and how can be redesigned and modified to minimize the drawbacks. Generally, getting an ICE to run by hydrogen fuel was not difficult. Getting an ICE to run good, however, was more a challenge. The points now to differentiate between just run of a hydrogen-fuel engine and one that runs well. The [Nakagawa et al. \[7\]](#) was the advances reported trying to elaborate a hydrogen-fuel engine. The engine operates on the principal of vacuum, in which the pressure condition of atmosphere drives aback of piston against a vacuum pressure to power produce. Although the ICE was run satisfactorily, for the practical vacuum never become for engines. For Sixty years earliest, and during his operation and work on combustion engines between the 1860s-1870s, the [N. A. Otto](#) (the deviser of the, gasoline cycle, Otto cycle) mentioned that used a gas fuel, which content of over 50% of a hydrogen. Also, the Otto experimented previously with gasoline and found the work it dangerous, he returns to use gaseous fuels.

The best energy/weight ratio of hydrogen-fuel engine, therefor it's used on a wide area in the program of space.

Liquid hydrogen was the fuel that choice for engines of rockets, and was utilized in the stages of the vehicles launch on space missions such as Apollo moon mission, Skylab, the mission of Viking to Mars and the mission of Voyager to Saturn. In these years, the researcher concerns on environment and air cleaner, along with precision air regulation pollution and the will to minimize the fossil fuels dependency which maximize and rekindled the hydrogen fuel as a special vehicular fuel [\[8\]](#).

1.2.1 Combustive and Exothermal Hydrogen Properties.

The Hydrogen properties that make it a combustible gas-fuel are (1) flammability with wide range (2) low required ignition energy (3) small quenching interval (4) the temperature of auto ignition is high (5) high speed of flame at theoretical ratios (6) high diffusivity (7) the density very low.

1.2.1.1 Flammability with Wide Range

By comparison of hydrogen-fuel with other fuel the hydrogen has flammability with a widish range. The use of hydrogen-fuel in an ICE results a good combusted with a wide range of fuel to air mixture.

1.2.1.2 Low Required Ignition Energy

The amount of ignition energy required for hydrogen-fuel is less than that required for gasoline. This makes a hydrogen-fuel engine ignite with lean mixtures. The wide flammability range of a hydrogen-fuel means that almost any mixture can ignite by a hot-spot. Unfortunately, hot-spots and hot gases can act as ignition sources, especially for low required ignition energy. This can create flash-back problems and premature ignition.

1.2.1.3 Small Quenching Interval

Gasoline has a larger quenching interval than hydrogen. Consequently, the flame of hydrogen is closer to the wall of the cylinder before extinguishing than other types of fuels. The smaller quenching interval can increase the trend for backfire.

1.2.1.4 Auto Ignition Temperature

Hydrogen has a relatively high auto-ignition temperature. In fact, it's important to know the auto-ignition temperature to limit the CR (compression ratio) of the engine, since the temperature is related to CR during the compression process. The relation between CR and temperature rise is obtained by: $T_2 = T_1 (V_1/V_2)^{(\gamma-1)}$

where V_1/V_2 is the compression ratio, T_1 and T_2 are the absolute initial and final temperatures, and γ is the ratio of specific heats. The final temperature is limited by CR.

1.2.1.5 High Flame Speed

Hydrogen flame speed is higher than gasoline fuels. This means a hydrogen engine can closely approach the ideal thermodynamical cycle engine. Leaner mixtures decrease flame velocity significantly.

1.2.1.6 High Diffusivity

The diffusivity of hydrogen-fuel and disperse ability in the air is very high with comparable to gasoline. The advantageous and characteristics of hydrogen-fuel due to two reasons. Firstly, it's easy to make fuel-air mixture with uniform. Secondly, the hydrogen rapidly disperses if leak develops is obtained. Thus, unsafe terms can be cut-down or avoided.

1.2.1.7 Low Density

The density of hydrogen is very low. These results affected in two way problems when hydrogen used in an ICE. Firstly, its necessary needed to a very hug volume to larder sufficiency hydrogen to allow a vehicle engine an adequate range. Secondly, the hydrogen-air mixture energy density is low; hence the output power was reduced.

1.2.2 Air to Hydrogen Fuel Ratio

The stoichiometric mixture of hydrogen-fuel and oxygen is shown by: $(2\text{H}_2 + \text{O}_2) \rightarrow 2\text{H}_2\text{O}$. The mole of complete combustion products of H_2 and O_2 equal two and one moles, respectively.

Because the air was used as the oxidizer instead of oxygen, the nitrogen needs to beaded in the reactants and included in the products calculations; for simplicity, the contents of dry air was taken for combustion by mole analysis $(\text{O}_2 + 3.762 \text{N}_2) = 4.762$ air by moles.

The A/F volume based (air volume / fuel volume) equal to $[4.762/2] = 2.4:1$ and the combustion chamber percent invader by hydrogen for a theoretical mixture: $\% \text{H}_2 = [\text{volume of } \text{H}_2 / (\text{air volume} + \text{H}_2 \text{ volume})] = [2 / (4.762 + 2)] = 29.6\%$. The theoretical A/F ratio to insure complete combustion based on mass (the mass of air to mass of fuel) equal to $[137.3\text{g} / 4\text{g}] = 34.33:1$ by mass and this value is greater for gasoline (A/F ratio (14.7:1)) required.

Since hydrogen fuel is a gaseous at ambient parameters it expanded more in the cylinder of combustion than a liquefied fuel.

Fig. 1 illustrated the different volumetric combustion cylinder for hydrogen and gasoline fuelled engine. At theoretical conditions, hydrogen displaces around 30% from the cylinder of combustion, compared to around 1:2% for gasoline cylinder. The comparison of combustion cylinder volumes content and energy held for hydrogen and gasoline fuelled engines indicated in Fig. 1 [9].

Combustion cylinder volumetric content and energy held comparison for hydrogen and gasoline fuelled engines dependence, the used method to measure, meter, a hydrogen-fuel to the engine, the compared power output of a hydrogen-fuel to a gasoline-fuel engines at intake manifold can be found from 85% to 120% for high injection pressure.

The air-fuel-ratio can be expressed by another form equivalence ratio, phi (Φ). Phi is introduced as the $(A/F)_{the.}/(A/F)_{act.}$. For a theoretical mixture, the $(A/F)_{act.}$ is equivalent to the $(A/F)_{the.}$ and thus the results of phi equals unity. For lean air to fuel ratios, phi results will be less than unity [10].

Fig. 1 Combustion cylinder volumetric content and energy held comparison for hydrogen and gasoline fueled engines [7, 9].

1.2.3 Problems of Pre-Ignition and Solutions

The main essential problem that opposed in the operational development of hydrogen-fuel engines is premature-ignition. Premature-ignition was a higher problem in hydrogen-fuel engines than gasoline-fuel engines, because lower ignition-energy of hydrogen's fuel, flammability wider extent and shorter quenching distance. Premature-ignition obtained by an engine inefficient and rough engine running. Premature-ignition effects on developing backfire conditions if the premature-ignition occurs behind the IV, intake valve, and the flame travels will return to induction system [11].

Some results of different research reported that the pre-ignition obtained from different positions of hot-spot inside the cylinder of combustion chamber, these positions as exhaust valve, spark plug and carbon deposits. Also, some research reported that the backfire occur when overlap happens between the opening of the valves of intake and exhaust [12].

Fig. 2 Injector construction with constant volume.

1.3 Delivery Fuel Systems

There are different systems of the fuel delivery as central injection, port injection and direct injection. The central injection or a carburetor, the injection is at the inlet of the manifold of air intake.

In the case of port injection, the injection occurred at port entrance. In port injection, the air is injected independently at the starting the intake-stroke to ease the hot remaining gases and cool any hot-spots.

Direct injection was higher sophisticated technologically and includes shaping mixture of fuel-air inside the combustion-cylinder after the closed of air inlet valve [13].

The inlet pressure supplied for injection port directed to be higher than for central systems or carbureted, but less than for direct injection systems. The CVI (constant volume injection) system, illustrated in Fig. 2, uses a mechanical shaft-cam operated device to time setting of the hydrogen injection to each combustion cylinder.

The EFI (electronic fuel injection) system measure, meters, the hydrogen to each combustion cylinder. These systems use solenoid valves (individual EFI) for each combustion cylinder and plumbed to a center of the intake manifold are a common fuel rail located down.

Whereas, the difference between the CVI and EFI systems that the first one and second one uses a constant and variable injection timing, respectively. Also, the first and second uses variable fuel and constant fuel rail pressure, respectively [14].

The direct injection systems are economic and require a rail pressure higher fuel than the other methods [13].

Water injecting into the stream of hydrogen before to mixing with air has produced better performance results instead of injecting it into the hydrogen-air mixture. The problem of this method is that water can mixed with the lubrication oil, so vehicle must be ensure good seals to ensure mixing of water with oil not occurs and do not leak [7].

1.5 Design of Engine

The most important controlling are knock and pre-ignition to re-design the engine for using hydrogen fuel, specifically the cooling system and the combustion cylinder.

Since, the unburned hydrocarbon is not obtained in hydrogen engines, the bore-to-stroke ratio can be used large and two spark plugs in this engine. The water cooling or passive cooling systems must be provided to give uniform cooling flow to all engine locations that needs cooling. Additional measures to decrease the probability of resignation are using of two small exhaust valves as opposed to a single large one, also the development of an scavenging effective system, that is, displacing fresh air from the combustion cylinder with exhaust gas [15].

1.5.1 Crankcase Ventilation

The crankcase ventilations more important in hydrogen engine than for gasoline engines. The gasoline engines unburned fuel can sweep by the piston, piston rings, and enter the crankcase. Since hydrogen has a less ignition energy limit than gasoline, any unburned hydrogen entering the crankcase has a larger chance of igniting. So, hydrogen should be protected from accumulating in the ventilation. The noise or engine fire is obtained from Ignition within the crankcase. Also, the sudden pressure rise is occurs when ignites of hydrogen within the crankcase. So, the relief pressure valve must be put on the cover valve to relieve the increased pressure. The exhaust of hydrogen fuel is H₂O (water vapor). The water mixing into the ventilation crankcase oil reduces its lubrication ability, resulting in a bigger degree of engine wear [15, 16].

1.6 Performance and effected parameters analysis

1.6.1 Thermal Efficiency

The theoretical performance and ideal thermodynamic efficiency of an Otto cycle engine is based on the CR, compression ratio, and the specific heat ratio of the fuel is expressed by the equation [7]:

$$\eta_{th} = 1 - \frac{1}{\left(\frac{V_1}{V_2}\right)^{\gamma-1}}$$

where V_1/V_2 is the compression ratio, γ is the specific heat ratio, and η_{th} is the thermal theoretical efficiency.

The molecular structure of fuel related to specific-heat ratio and the less molecular structure, the γ (specific-heat ratio) will higher. Hydrogen ($\gamma = 1.4$) has simpler molecular and higher specific-heat ratio than the conventional gasoline ($\gamma = 1.1$) [4, 17].

Fig. 3 Hydrogen engine emissions [7]

1.6.2 Combustion and Hydrogen Engine Emissions

The hydrogen fuel combustion with air, oxygen and nitrogen, produces H_2O , water, and also produce NO_x (nitrogen oxides). The nitrogen oxide is prepared due to the generated high temperatures within the combustion cylinder during combustion. The high temperature generated inside cylinder causes combination of some nitrogen with oxygen in the air [7].

The nitrogen oxides amount formed depends mainly on, the A/F ratio, the compression ratio of engine, the speed of the engine, the timing ignition and whether condition.

In addition to nitrogen oxides, the carbon monoxide, or/and carbon dioxide can be appear through the exhaust gas, due to oil seeped burning in the combustion cylinder.

1.6.3 Engine Emissions

The engine operating strategy used a rich or lean A/F ratio, the engine of hydrogen fuel can zero emissions produce (as low as a few ppm) to high NO_x and significant carbon monoxide emissions.

Figure 3 illustrates a relation typically NO_x related to ϕ for the engine uses a hydrogen fuel. A similar graph for gasoline including some other (CO, NO_x and HC) emissions is presented in Fig. 4. The trend curve of NO_x for a gasoline and hydrogen engines are similar and gain as ϕ increased. However, as shown in Fig. 4 the reduction of NO_x in a gasoline engine accompanier with increased of hydrocarbons and carbon monoxide [3].

Fig. 4 Emissions for a gasoline engine [4]

1.6.3 Output Power Produced

The maximum theoretical power output from a hydrogen fuel engine depends on the A/F ratio and systems of the fuel injection used method.

As reported, the content of this mixture energy is less than of energy mixture of the gasoline fuel. Since, the methods of carbureted and port injection mix the fuel-air prior to the combustion chamber, these systems finite the theoretical maximum power to approximately 85% of gasoline engines [3].

While, for direct systems injection, the maximum theoretical output was approximately 15% larger than for gasoline fuel engine.

Unfortunately, this also decreases the output power to approximately half of that a similar sized gasoline fuel engine. To make-up the loss of power, the hydrogen fuel engines are usually bigger than the gasoline fuel engines, and/or are equipped with turbo-chargers or super-chargers [7].

1.7 Hydrogen Gas Mixtures

The hydrogen can be used as additives of a hydrocarbon fuel advantageously in ICE. Hydrogen was mixed with HPNG (high pressure natural gas) as additive purpose since both of gases can storage in the same depot.

Current vehicles of this type tend to work using a single fuel or else but not both at the same time.

A one available commercially gas mixture contains 20% H₂ and 80% NG known as Hythane [7]. This ratio of gas mixture, no modifications is needed or required to a NG engine, and the results studies shown that the emissions of this mixture are reduced by more than 20%. The engine modifications are required if the mixture increases more than 20%, but in this mixture the emissions will reduced.

Lean operation of ICE means economy and oxides of nitrogen emissions.

Regarding output power, hydrogen combining the mixture's density of energy at leans by gaining the hydrogen-to-carbon ratio, thereby, the torque will improves at wide-open choke conditions. However, the vehicle ranges reduced by difficulties of associated with saving enough hydrogen amounts [17].

1.8 Coating of Combustion Chambers Cylinders by Graphite

The microscopic, weaving microscopic structures and angles and distances of deflection of graphite atoms are illustrated in Figs. 5, 6 and 7.

The aims of this study on increase protection and cavitation by the use of internal graphite coating cylinder combustion chambers are:

- 1- Increased protection using Nano-material graphene Come to prevent the cavitation formation (cavities) internal protrusions to-cylinder fuel burn and protect the engine cylinder of cracks resulting from hydrogen explosion also during combustion.
- 2- To prevent thermal infusion present in all General Motors, which leads to the loss of a large amount of power generated.

The most important characteristics that serve the project are as follows;

- 1- A graphene bears high at high temperatures.
- 2- Graphene largely retains the heat.
- 3- The durability of graphene shocks 20 times the cross stresses and vibrations, and this will serve our research a lot.

The idea and action steps

- 1- A is extracted graphene from graphite material extraction in one the ways mentioned earlier
- 2- The selection of the sample microscopically well to made sure there are free from unwanted impurities
- 3- Provide completely closed and there is no source of air transmission or fans or other environment (rooms treadmill completely).
- 4- Mixed graphite form 8 alloy steel average used in the manufacture of carbon combustion chambers.
- 5- The process of heat process on the alloy composition and then conduct operations and operating appropriate for the specified design.

1.8.2 Summarized Results

The results can be summarized as follows:

- 1- Will be addressing the problems of cavitation cylinders burning fuel of 60% almost looked for durability is high for the metal to scratches or breakage vibrations or sudden shocks.
- 2- Will be providing a very good cooling a percentage of 40% and it is so good.
- 3- Metal currently average calories as the cost is almost US \$ 1 gram and thus can be easily traded.
- 4- Finally resist corrosion problem that may occur as the result of leaving the engine pH for a period without running which using material silicon alternative to the walls of the cylinder.

Fig. 5 The microscopic structure of the material graphite alloy

Fig. 6 Weaving microscopic structure of graphite

Fig.7 Angles and distances of deflection of graphite atoms

The study concentrated on using of hydrogen with high efficiency and performance of newly and innovative in design engine which claims to motor cocks (duke engine).

Our study relies here on the using a new engine newly inventor engine of the so-called Duke engine. This engine was characterized by a different number of features homogeneity engine pH suitable better than the multiple aspects with the same design standard engines in V and we use diesel or gasoline engines, are currently trying to find workshops shared between OUT ([Oakland technical University](#)) of the State of new Zealand, to convert these previous ideas into the new engine generation. The inside and outside construction of the duke engine are shown in [Figs. 8](#) and [9](#) respectively.

Features rooster engine (Duke Engine) has the characteristics as following:

- 1- Fix a problem cavities and cracks resulting from the process of explosion of hydrogen during combustion tests on the engine [Auckland](#) in New Zealand, the development center has shown resistance to the engine, sudden internal explosions of fuel combustion and this is too important when our use of fuel is a hydrogen was a third solution for us in this our research to cure the cracks problem and internal cavities of the IC chambers walls [18], where the internal explosions not only just the cavities occurrence, but also claim to a process of self-ignition of the car is damaged, the engine that can overcome the conventional engine in this district, because the piece part to low temperature extremes in conventional engines and engine offset in turkeys was not to use on the hot exhaust valves in combustion systems
- 2- Circular design engine and therefore provides 30% approximately of the under-utilized space in the design and also lighter than other traditional species and this will be reflected on the rate of fuel consumption.
- 3- Engine internally ignition System composite of three instead of six candles in a six-cylinder engines also consists of five burners instead of six, so it gives us the same generated power in the six-cylinder engines.
- 4- Also characterized as dealing well with high CR ratio engines and this is very suitable for hydrogen.
- 5- Resistant to vibration is very large and also the noise (negligible 1st-order or 2nd-order vibration) which supports the idea of his making on the circular motion of the pistons and not reciprocating.
- 6- Fewer complexes in design than conventional engines.

Fig.8 The engine installation from the inside

Fig.9 The engine installation from the outside

1.9 Experimental Work

Practical experience of running a hydrogen-fuel engine and accounts (RIG development) must be introduced. The small (Fiat X1) engine that is used in experimental, shown in [Fig. 10](#), actually the

engine connected with a load generator, used to electricity generation as a load, and the engine properties and characteristics are used in experiments;

Make: Fiat X1-9 (X1-9-1500)

Displacement: 956cc

Bore* Stroke: 73*61mm

Number of Cylinder: Four

Compression Ratio: 7.1:1

Rated Output: 70 HP at 6000rpm

Ignition System: TCI

Ignition timing: BTDC 15

Spark plug: two anodes (MICO-super-WBBC)

Starting system: DC motor

Air cleaner: Wet type

Lubrication: System Forced splash

Fuel: Gasoline (petrol start)

Fuel tank capacity: 10 liters Gasoline

Fig.10 Diagram and engine system components

Assistive measuring devices:

1. Cylinder hydrogen pressure of 150 bars.
2. Pressure Meter
3. Dual-pressure regulator
4. Root Lemaitre
5. Injector natural gas (CNG Injector)
6. The tank of fuel
7. DISC prevent reverse flame (flame trap)

The primary function of the flame trap is to avoid propagation of backfire during engine operation into the gaseous fuel cylinder. As illustrated in Fig. 11, the flame trap was connected to supply line between the hydrogen fuel injector and the hydrogen gas cylinder.

8. Valve to stopping reverse pressure (Safety valve)

Safety valve is used to avoid any case of excess pressure inside the flame trap, while, Non-return valve it avoids back flow of water contained in the flame trap with reverse relative pressure.

The Exhaust Emission Analysis: The various gases from the exhaust were analyzed by AVL Digges analyzer. The volumetric fuel consumption was measured using a glass burette. The time taken by the engine to consume a fixed volume was measured using a stopwatch. The volume divided by the time taken for fuel consumption gives the volumetric flow rate. Also, the hydrogen was metered by a hydrogen rotameter. The tachometer with photo reflective sensor was used for measurement of RPM. The temperature measurements by thermocouples of Chromel-Alumel K-type, were connected to a 6 channel digital panel meter to measure temperatures of exhaust gas

Fig.11 cylinder blocker flames reverse inhibitor pressure, (flame trap)

1.9.1 Experimental Action Steps:

First it will be some minor work adjustments on the user's motor that is where you will be provided with petting room burning one for hydrogen-fuel and other fuel-initiator, which we can use gasoline or natural gas.

Second, will use the valve to estopping reverse pressure, and also to prevent reverse flame as shown in Fig. 11, the spectrum of safety.

Third, the using a hydrogen cylinder pressure of 150 bars and installing dual-pressure regulator, Fig. 10.

Fourth, was the welding of aluminum rod and attach it to a sensitive reading speed (rev / min).

Fifth, are using the scoreboard account of the process of operating control and replicate more than once proved the validity of the results.

1.9.2 Experimental Results and Discussion

Fig.12 Curve shows the break thermal-efficiency from the average effective pressure of pure gasoline Hydrogen 100%.

Fig.13 Curved heat generated from the exhaust if you use gasoline-kerosene and 100% hydrogen.

Fig.14 Curved nitrogen oxides generated from the burning of both (gasoline and kerosene) and 100% hydrogen

Fig.15 Curved exhaust temperature when using the (gasoline and kerosene) and 100% hydrogen

Fig.16 Curved non-hydrocarbons burned completely when using the (gasoline and kerosene) and 100% hydrogen

The main final results that are obtained from Figs. [12-16](#) are summarized as:

- 1) To obtain a hydrogen gas at rates of new mixing it helps in the treatment of many problems unresolved problem of internal cavitation is this research is new of its kind in the treatment of this problem in new ways and innovative.
- 2) The emissions reduction of nitrogen and the first gas and carbon-dioxide by higher than 80% and treatment of heat emission.
- 3) Increase capacity and break thermal efficiency generated of the engine by between 75% of the 85%.
- 4) Treat a problem early ignition engines to hydrogen and thus better cleaning and regular speed to burn and burn up to 100 % of the total combustion of fuel used.
- 5) Treating a complement to the main problem of cavities and cracks in the walls of the cylinder combustion using a graphene nanoparticles rooms and that gives us 80% of the resistance to explosions occurring in the cylinder combustion of the mixture where it's 20 times the hardness of steel.
- 6) The new design using cock's engine (Duke engine) will provide us with 30% of under-utilized space in conventional engines and design unique and different helps us to reduce vibrations and noise by a large margin and also high-flow performance and holds a significant percentage compression of fuel of hydrogen, which increases the output efficiency of each these factors together his candidacy to make the engine better for us to use this fuel.

1.10 Conclusion

Hydrogen ICE vehicles presented a major promise: the opportunity to improve security of energy and reduce emissions as carbon-dioxide by stuck the vehicle of the light duty sector off of gasoline. And much like hydrogen FCVs (Federation credential verification service), there are significant hurdles to overtake and the adoption of hydrogen ICE vehicles, involving both technological improvements so it is competitive with gasoline-based anagrams as well as implementing a hydrogen fueling infrastructure [18]. Looking beyond those similarities, distinctions quickly arise because of the nature the hydrogen ICE technology that differentiates it from fuel-cell and gasoline vehicles. The most critical differences

are the produced power by the engine, the fuel economy, the tank of fuel size, and the state of development of the technology. Complicating any comparison is the vast uncertainty inherent in future vehicle technologies, hydrogen ICE included. If the fuel-cell technology is developed to its potential, the fuel economy advantage it has over the hydrogen ICE technology appears to present a compelling case for FCVs in the long-term. This is particularly true because the higher fuel economy allows to a smaller fuel tank size for the same range, and fuel tank size is almost certain so that a key limitation for hydrogen vehicles. However, the issue of power may prove so that a thorn in the flank, side, of FCVs, particularly for vehicles that need the capacity to perform at high loads, since adding more fuel-cell stacks can add significantly to cost of the vehicle. Buses and trucks clearly fall into this category, and light duty vehicles such as light trucks and sport-utility vehicles may also fall into it, depending on the final cost of fuel-cells.

Symbols

Nomenclature		
A	air volume	m ³
F	fuel volume	m ³
T	Absolute temperature	K
V	Volume	m ³
Greek symbol		
Φ	Equivalence ratio = $(A/F)_{the.}/(A/F)_{act.}$	--
γ	Specific heat ratio	--
η_{th}	the thermal theoretical efficiency	--
Abbreviation		
CIE	Compression ignition engine	
CR	Compression ratio	
CVI	Constant volume injection	
DOE	Department of energy	
EFI	electronic fuel injection	
FCVS	Federation credential verification service	
HPNG	High pressure natural gas	
ICE	Internal combustion engine	
ICHE	Internal combustion of hydrogen engine	
NL	National Laboratories	

Subscripts/superscripts		
act.	Actual condition	
the.	Theoretical condition	
1	Initial condition process	
2	Final condition process	

Acknowledgment

I extend my thanks and appreciation to all who helped us in the preparation of this research and to the Benha faculty of Engineering, Benha University to provide the starting in this project.

References

- [1] B.L. Salvi, K.A. Subramanian. Experimental investigation on effects of compression ratio and exhaust gas recirculation on backfire, performance and emission characteristics in a hydrogen fuelled spark ignition engine. International Journal of Hydrogen Energy, 41, Issue 13, 2016, PP. 5842–5855
- [2] J.B. Greenwood, P.A. Erickson, J. Hwang, E.A. Jordan. Experimental results of hydrogen enrichment of ethanol in an ultra-lean internal combustion engine. Int J. Hydrogen Energy 2014; 39:12980-90.
- [3] Changwei J, Shuofeng W. Effect of hydrogen addition on combustion and emission performance of a spark ignition gasoline engine at lean conditions. Int J Hydrogen Energy 2009; 34:7823-7834.
- [4] Sopena C, Dieguez PM, Sainz D, Urroz JC, Guelbenzu E, Gandia LM. Conversion of a commercial spark ignition engine to run on hydrogen: performance comparison using hydrogen and gasoline. Int J Hydrogen Energy 2009; 35:1420-1429.
- [5] Kenneth Gillingham. Hydrogen internal combustion engine vehicles: a prudent intermediate step or a step in the wrong direction. Stanford University, Department of Management Science & Engineering. Global Climate and Energy Project, Precourt Institute for Energy Efficiency, 2007.
- [6] European Environment Agency. Climate for a transport change. Term 2007: indicators tracking transport and environment in the European Union. Published 3 Mar 2008. ISSN 1725-9177.

[7] Kenji Nakagawa, Kimitaka Yamane, Tetsuya Ohira. Potential of Large Output Power, High Thermal Efficiency, Near-zero NOx Emission, Supercharged, Lean-burn, Hydrogen-fuelled, Direct Injection Engines. *Energy Procedia* 29 (2012) 455 – 462.

[8] Yu Chen, Robert Raine. The effects of hydrogen supplementation on idle performance and emissions of an SI engine original. *Fuel*, 176, 2016, PP. 190–199.

[9] Fontana, G., Galloni, E., Jannelli, E., and Minutillo, M., "Performance and Fuel Consumption Estimation of a Hydrogen Enriched Gasoline Engine at Part-Load Operation," SAE Technical Paper 2002-01-2196, 2002, doi:10.4271/2002-01-2196.

[10] Whiete CM, Streeper RR, Lutz AE. The hydrogen-fueled internal combustion engine: a technical review. *Int J Hydrogen Energy* 2006; 31:1292-1305.

[11] Gianluigi Lo Basso, Livio de Santoli, Angelo Albo, Benedetto Nastasi. H2NG (hydrogen-natural gas mixtures) effects on energy performances of a condensing micro-CHP (combined heat and power) for residential applications: An expeditious assessment of water condensation and experimental analysis. *Energy*, 84, 2015, PP. 397–418.

[12] Kline SJ, McClintock FA. Describing uncertainties in single sample experiments. *Mechanical Engineering*. 1953; 75: 3-8.

[13] Heywood JB. *Internal combustion engine fundamental*. New York: McGraw-Hill, Inc.; 1988.

[14] Kahraman E, Ozcanlı SC, Ozerdem B. An experimental study on performance and emission characteristics of a hydrogen fuelled spark ignition engine. *Int J. Hydrogen Energy* 2007; 32: 2066-2072.

[15] Mohamed M. EL-Kassaby, Yehia A. Eldrainy, Mohamed E. Khidr, Kareem I. Khidr. Effect of hydroxy (HHO) gas addition on gasoline engine performance and emissions. *Alexandria Engineering Journal*, Volume 55, Issue 1, March 2016, Pages 243–251

[16] Haiming Wu, Xiumin Yu, , Yaodong Du, Xiangbin Ji, Renxu Niu, Yao Sun, Jiaqi Gu. Study on cold start characteristics of dual fuel SI engine with hydrogen direct-injection. *Applied Thermal Engineering*, 100, 2016, PP. 829–839

[17] College of the Desert, Palm Desert, CA, USA. Hydrogen Fuel Cell Engines and Related Technologies: Revision 0, December 2001

[18] K.V. Shivaprasad, S. Raviteja, P. Chitragar, G.N. Kumar. Experimental investigation of the effect of hydrogen addition on combustion performance and emissions characteristics of a spark ignition high speed gasoline engine. *Procedia Technol.*, 14 (2014), pp. 141–148

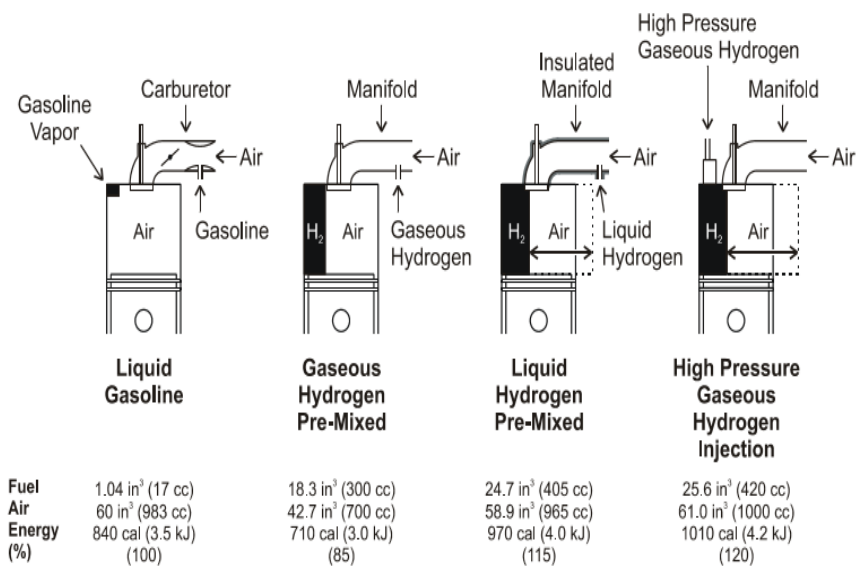


Fig. 1 Combustion cylinder volumetric and energy comparison for hydrogen and gasoline fueled engines.

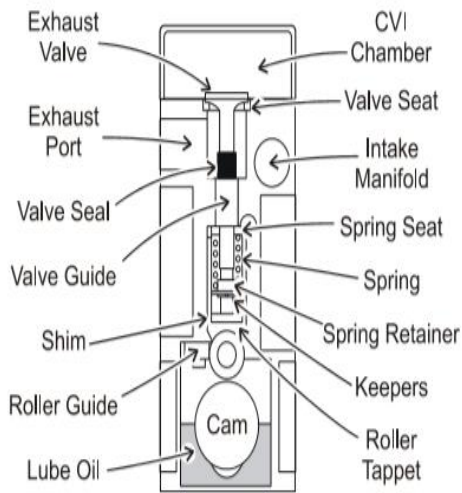


Fig. 2 Injector construction with a constant volume.

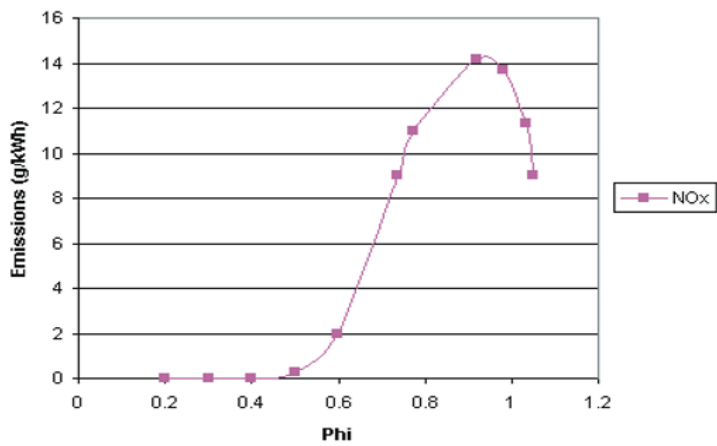


Fig. 3 Hydrogen engine emissions.

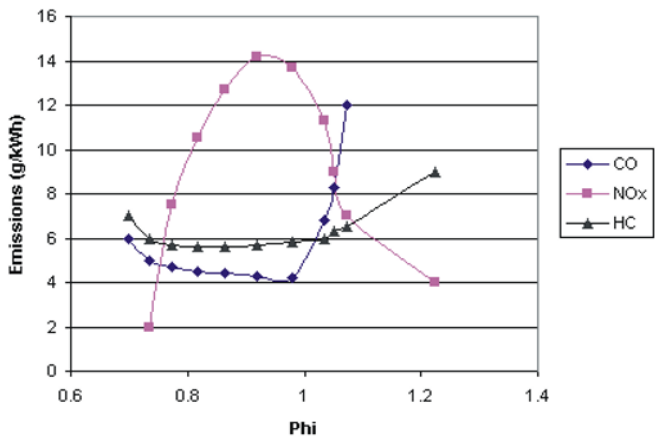


Fig. 4 Emissions for a gasoline engine.

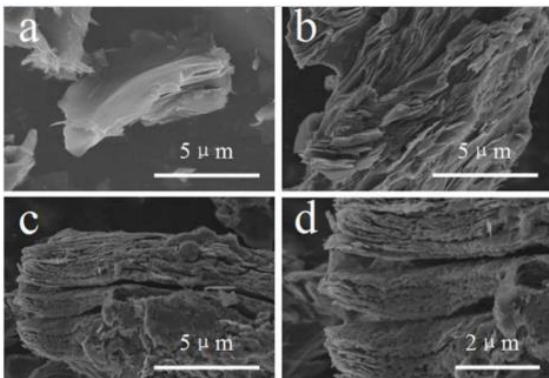


Fig. 5 The microscopic structure of the material graphite alloy

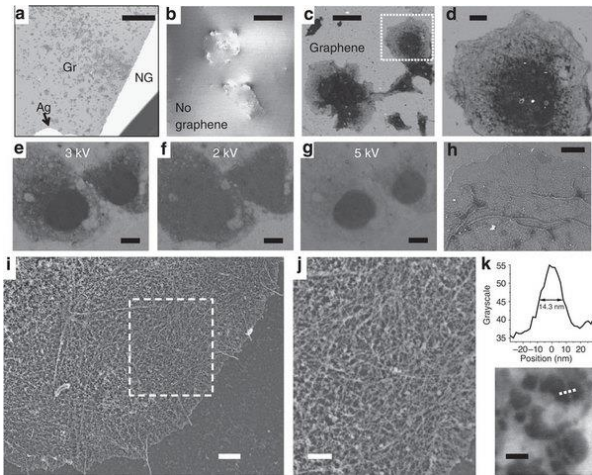


Fig. 6 Weaving microscopic structure of graphite

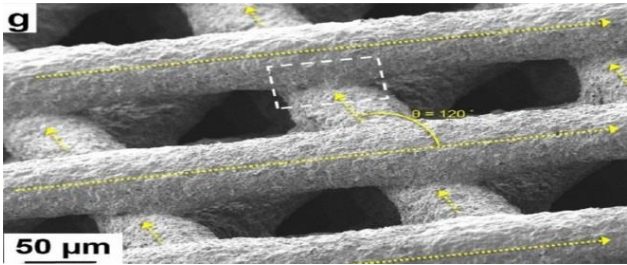


Fig. 7 Angles and distances of deflection of graphite atoms

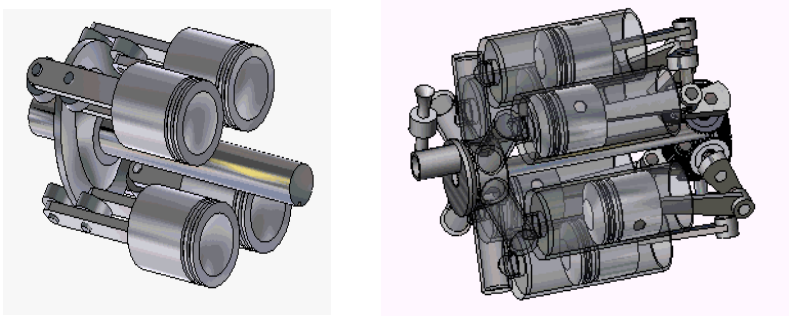


Fig. 8 The engine installation from the inside



Fig. 9 The engine installation from the outside

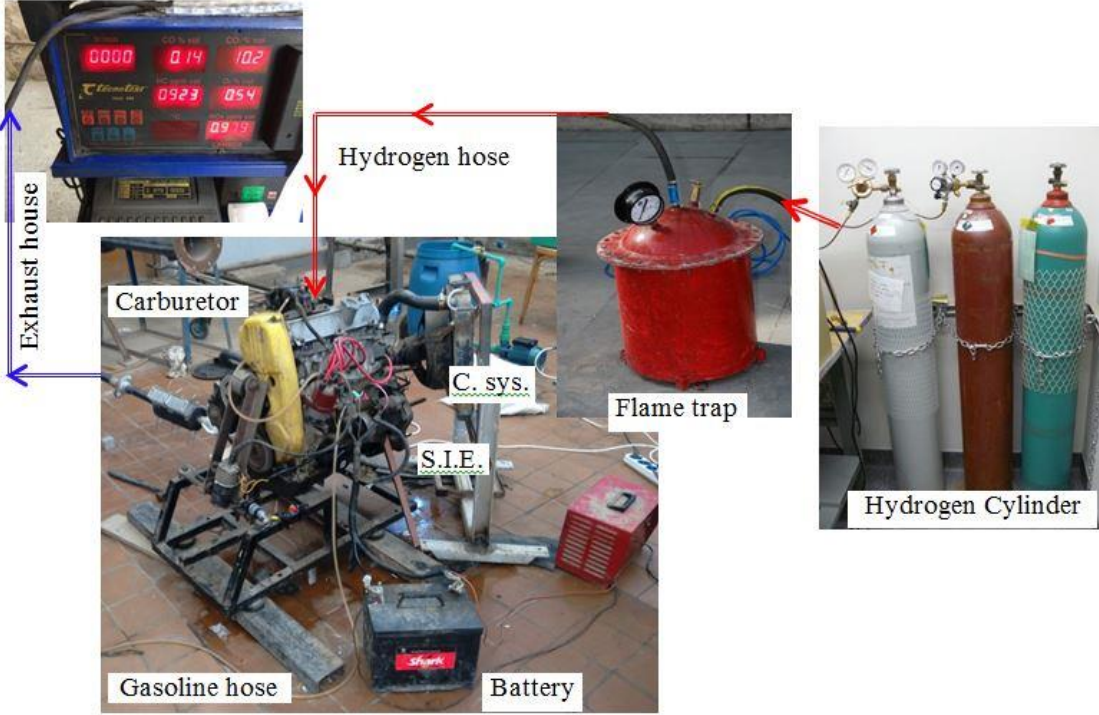


Fig.10 Diagram and engine system components

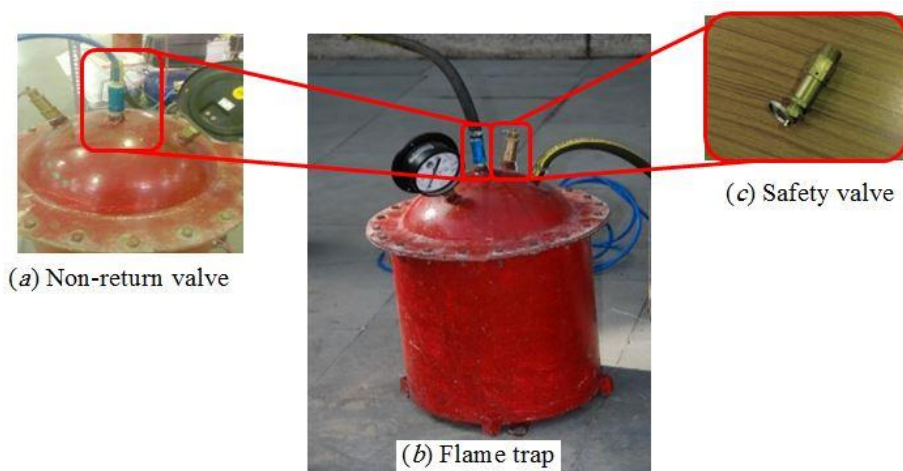


Fig.11 cylinder blocker flames reverse inhibitor pressure, (flame trap)

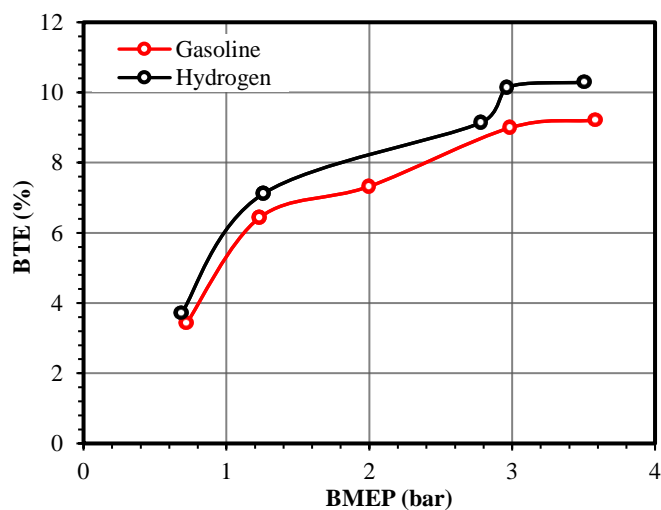


Fig.12 Curve shows the break thermal efficiency from the average effective pressure of pure gasoline Hydrogen 100%.

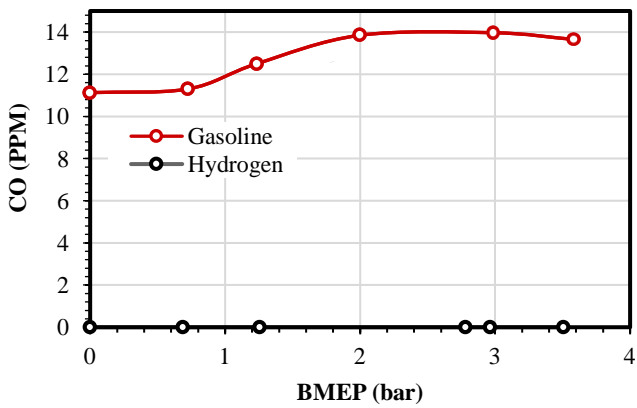


Fig.13 Curved heat generated from the exhaust if you use gasoline-kerosene and 100% hydrogen.

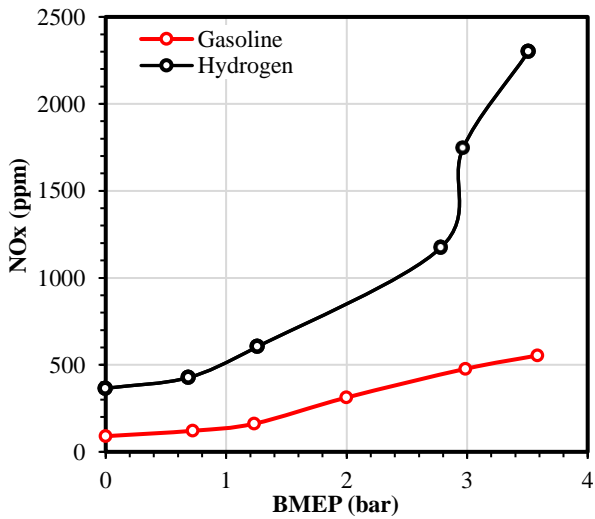


Fig.14 Curved nitrogen oxides generated from the burning of both (gasoline and kerosene) and 100% hydrogen.

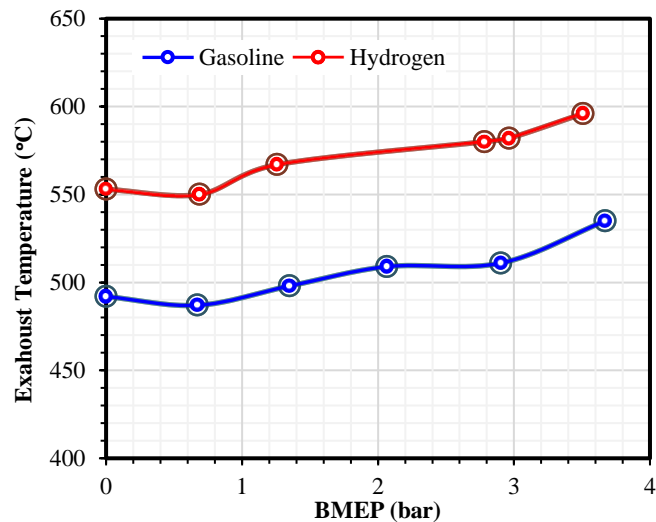


Fig.15 Curved exhaust temperature when using the (gasoline and kerosene) and 100% hydrogen

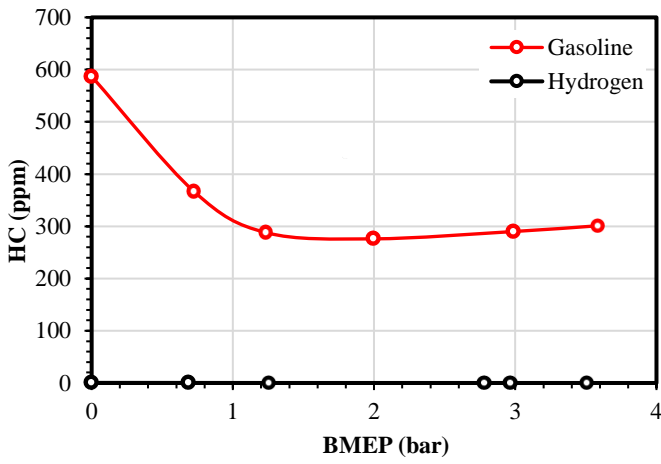


Fig.16 Curved non-hydrocarbons burned completely when using the (gasoline and kerosene) and 100% hydrogen

The degradation of methylene blue in water solution through photocatalysis using TiO₂ in a helical fluorinated ethylene propylene tubing reactor

A.H. Maghawry^{i*}, S.A. Nosierⁱⁱ and M. Husseinⁱⁱⁱ

^{i,ii,iii} Chemical Engineering Department, Faculty of Engineering, Alexandria University, Alexandria, Egypt

*Email: ahmaghawri@gmail.com

Abstract:

A photocatalytic reactor, using Titanium dioxide (TiO₂) as a catalyst and fluorinated ethylene propylene tubing (FEP) as a transmitter for the UV radiation (wave length: 254 nm), was developed and used to degrade methylene blue (MB) in water solution through an advanced oxidation process (AOP).

The mode of operation was UV radiation transmitted through FEP, along with TiO₂ (Nano particle, Anatase) as a catalyst mixed with the flowing solution. The reactor was used mainly to try a modern technique of photocatalysis, in which the solution flowed inside narrow tubes exposed continuously to UV radiation. In addition to evaluating the efficiency of using the FEP tubing in transmitting UV radiation, comparing it to earlier researches that used quartz glass.

Through the experimentation process, the effect of the flow rate, initial concentration of the solution, pH value, TiO₂ dose, the effect of UV radiation without using a catalyst and the performance of the TiO₂ in the removal of the dye without using UV radiation, were all studied.

The study showed that the FEP tubing is a very competitive material when compared to quartz glass, which is very difficult to use in such applications. In addition, it showed that the efficiency of the process can be greatly affected by the manipulation of the flowrate, initial concentration and pH of the solution, where 3 pH value, 10 ppm initial concentration of MB and 125 ml/min flow rate produced the best results. It also showed clearly that the UV radiation efficiency is almost doubled using Anatase TiO₂ as a catalyst when compared to not using a catalyst.

Keywords: Photocatalysis, AOP, methylene blue, Anatase TiO₂, fluorinated ethylene propylene

1 Introduction

Wastewater is currently considered a major issue facing the public health and challenging the sustainability of our surrounding environment ^[1]. Discharged wastewater, especially those from factories and laboratories, imposes a serious challenge and hinders our efforts to protect the surrounding environment ^[2]. Industrial and domestic effluents disturb the balance of the nature through a wide range of pollutants such as those with high chemical oxygen demand, different pH than that of the environment they are released into, or even those containing toxic compounds that will eventually harm both marine and human life ^[3]. Therefore, it is a major concern nowadays to limit water pollution and control its impact on the environment ^[4].

Various industries use organic compounds as one of the main chemicals in its synthesis of special chemical products such as, synthetic resins, pharmaceutical products, dyes, etc. ^[5].

Textile industry discharges wastewater effluent that includes a large variety of chemical additions and dyes, extending the challenge to contain chemical composition along with the liquid waste ^[6]. Dyes represents a great and increasing danger on the environment, as 1-20% of the global dyes production

is lost and released as effluents through the process. The release of these wastes can also lead to the formation of dangerous byproducts through chemical reactions such as oxidation or hydrolysis[7] . What also should be noted is that dyes may have toxic effects and may affect light penetration in the water where it was discharged [2] .

Some methods, such as charcoal activated adsorption, have been successfully proven effective low cost methods, except for the fact that they are considered incomplete, as solid wastes are produced as a consequence, and this represents an additional source of pollution to the environment [8] .

During the last period, a new technology, relying on the oxidation of some hazardous organic compounds through advanced oxidation processes (AOP), gained a strong interest as it is viewed to have a very promising future [9,10,11].

Advanced oxidation processes (AOPs) were proved to be effective alternative methods in the treatment of wastewaters that contains dyes and other wastes [3] . Heterogeneous photocatalytic oxidation of a large variety of organic wastes using semi-conductors, such as TiO₂, has been particularly investigated in further details during the last period [12] .

Using Titanium Dioxide as a photocatalyst, in TiO₂/ UV system, has been given a great attention; because of its high efficiency; being non-toxic, inexpensive, highly reactive and photo-chemically inert. These characteristics allowed it to be a main player when it comes to oxidizing wastewater containing phenolic compounds or dyes [3, 13].

One of the main purposes of this study is to show if FEP tubing can be used instead of quartz glass. This is in addition to measuring the effect of the flow rate, initial concentration of the MB, dose of TiO₂ and pH value of the solution on the efficiency of the process.

2 Material and methods

The apparatus used, showed in figure 1, consisted of a 2-liters beaker filled with MB solution (molecular formula C₁₆H₁₈ClN₃.XH₂O where X ranges from 2, 3 and molecular weight =319.86) with Titanium dioxide (Nano particle, Anatase) continuously mixed with the solution using a magnetic stirrer. The solution was then moved using an adjustable flow dosing pump of a maximum capacity of 1.5 L/hr. The solution was then moved through the FEP tubing of 4 mm inner diameter and 6 mm outer diameter with a total length of 15-ft. The FEP was wrapped around a 60-cm long UV lamp with a wavelength of 254 nm, the lamp and the tubing were fit into a Plexi-glass compartment covered with a reflective layer. The solution then flowed back to the tank with a small spacing between the end of the tubing and the solution surface to cause the bubbling that ensures the required oxygen supply for the reaction.

Samples were extracted using 2-ml syringe and separated from the TiO₂ using table top Centrifuge. The final sample was measured using a visible light Spectrophotometer.

All the chemicals used were of laboratory reagent grade and used without additional purification.

Through all experiments the exposed volume of solution to the UV in the tubing was around 38 ml all the time, as the 15-ft. plastic tubing was wrapped spirally around the lamp in order to utilize all UV radiation output.

Flow rate was controlled using a built-in facility in the pump itself. The output flow rate of the pump was measured and calibrated before starting the runs as the pump controls the flowrate as a percent of the maximum output, which varies with the pressure applied. The dosing pump recirculates the mixture between the reactor and the tank (beaker).

Before starting any experiment the lamp was left to stabilize for 15 minutes and 1 L solution of MB – including the suspended TiO₂- was kept in the beaker to be mixed for 10 minutes using the magnetic stirrer.

MB solution was prepared by dissolving a certain amount of methylene blue into distilled water to achieve the required initial concentration.

The solution was left to room temperature without applying controls on it and the pH was adjusted using diluted sulfuric acid solution or diluted sodium hydroxide solution.

Every 5 minutes a sample of 2 ml were extracted using a syringe, the sample is then placed in the centrifuge for 25 minutes on 3000 rpm speed, to separate the suspended TiO₂ catalyst.

The analysis was carried out by measuring the absorbance with spectrophotometer at 662 nm. This wavelength was the maximum absorption wavelength of the MB that was measured earlier.

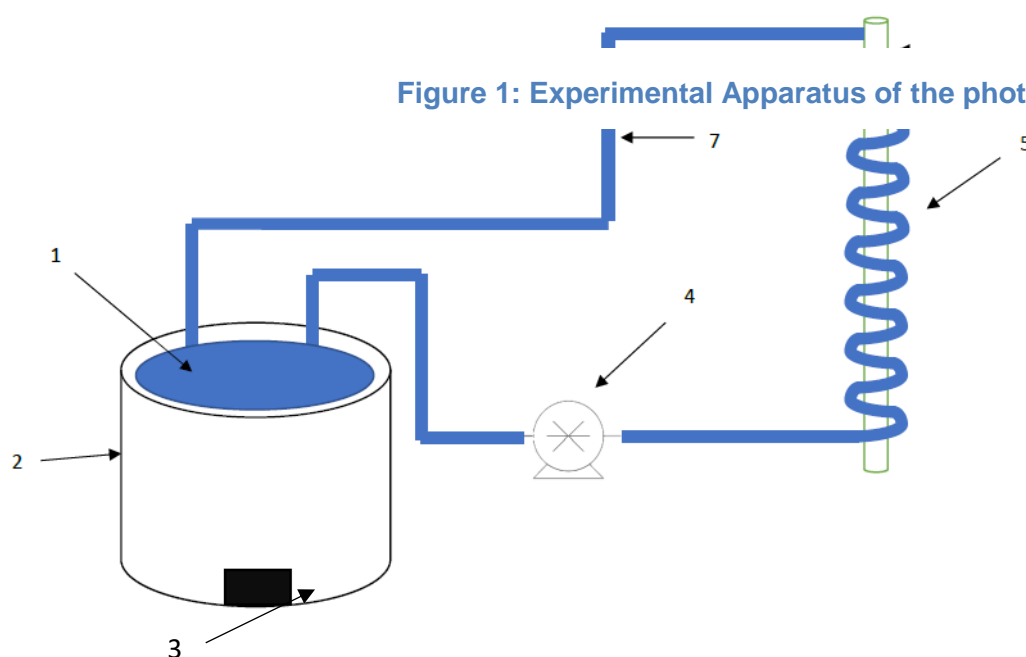


Figure 1: Experimental Apparatus of the photocatalytic reactor

3 Theory/calculation

AOP processes are based on the production of hydroxyl radicals (HO•) which are the main agents responsible for the oxidation of a large number of aqueous organic contaminants [14, 15].

Photocatalysis using TiO₂ is most studied and activated by ultraviolet (UV) light (wavelength < 400nm) due to its band gap energy of 3.2eV [16] . The process starts with the excitation of the TiO₂ by the UV of wavelength of $\lambda \leq 400$ nm, forming electron- hole pairs (e⁻cb, h⁺vb). The hole generates a hydroxyl radical, which in turns degrade the organic pollutants in the water, while Oxygen that is supplied from air is reduced by the free excited electron, preventing the recombination of the electron and the hole as showed in Figure 2 and equations 1-5 [17] .

1. absorption of efficient photons

$$\text{TiO}_2 + h\nu \rightarrow e^-_{cb} + h^+_{vb};$$
2. oxygen adsorption leading to O₂⁻ free radicals

$$(\text{O}_2)_{ads} + e^-_{cb} \rightarrow \text{O}_2^{\cdot-};$$
3. formation of OH• radical by photo-holes

$$(\text{H}_2\text{O} \leftrightarrow \text{H}^+ + \text{OH}^-)_{ads} + h^+_{vb} \rightarrow \text{H}^+ + \text{OH}^{\cdot};$$
4. oxidation of organic (R) by OH• radical or holes

$$\text{R} + \text{OH}^{\cdot} \rightarrow \text{R}^{\cdot} + \text{H}_2\text{O};$$

$$\text{R} + h^+ \rightarrow \text{R}^{\cdot+} \rightarrow \text{degradation products}$$

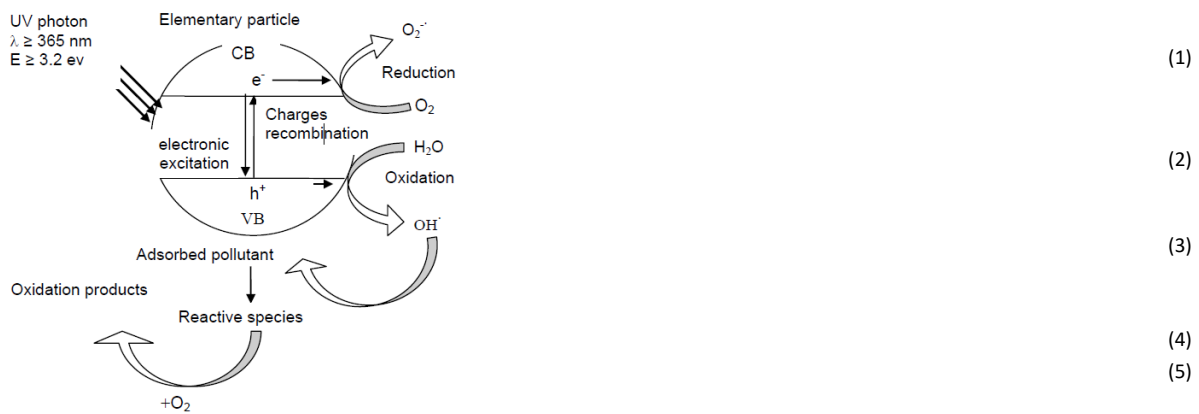


Figure 2:

Mechanism diagram of photocatalytic degradation

4 Results and discussion

Various parameters were studied in order to have a better understanding of the extent of their effect on the degradation of the methylene blue. The effect of pH, flowrate inside the tubing, initial concentration of the methylene blue and the dose of TiO_2 , were all studied by measuring methylene blue's concentration changes over time

The percent removal was calculated for each experiment at all points through equation 6:

$$\% \text{Removal} = \frac{C_t - C_0}{C_0} * 100 \quad (6)$$

Where C_t is the concentration at certain time (mg/L) and C_0 is the initial concentration (mg/L).

4.1 Effect of the initial concentration

Applying same process with the same conditions using 4 different initial concentrations of methylene blue solution produced very close results, in Figure 3 using 5 ppm allowed around 90% removal while 10, 15 and 20 ppm allowed around 80%, showing how the rate of reaction was only improving on the low concentrations. Figure 4 confirms the first finding as the same process was applied using a different TiO_2 dose and pH value. However, the results were not strongly changed for the 5 and 10 ppm initial concentrations of the methylene blue solutions.

For further analysis, Figure 14 (Kinetics: first order reaction model) illustrated that the rate of reaction reached its peak at 10 ppm, therefore, 10 ppm can be considered the optimum initial concentration in these trials.

This can be explained through the following; first, when the dye concentration increases, the generation of hydroxyl radicals on the catalyst's surface decreases. This is caused by dye ions covering active sites. Second, the increase in the dye concentration hinders photons from reaching the

photocatalyst surface in a process called “UV screening effect”, leading to a slower production of hydroxyl radicals which are required to oxidize dye molecules decreasing the photocatalytic activity [3,4,8,18]

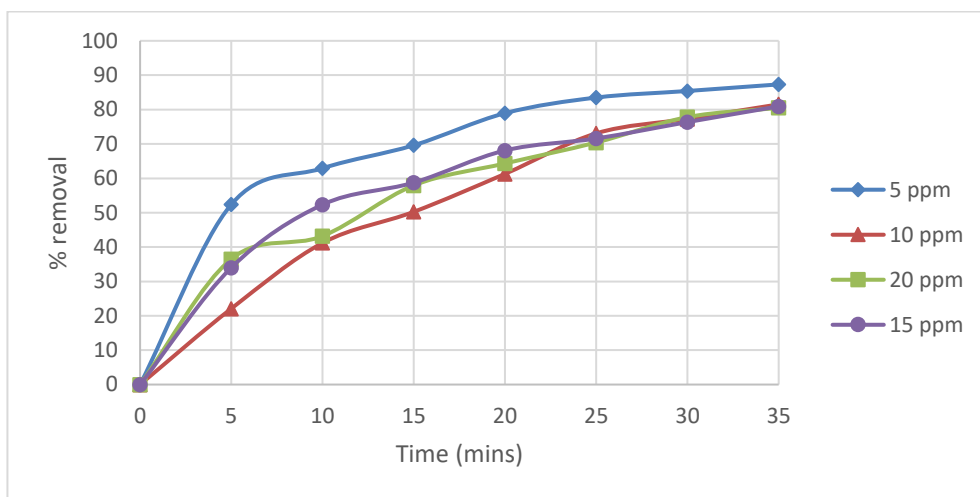


Figure 3: Effect of time on the percentage color removal of MB at different initial concentrations (Flow rate= 87.5 ml/min, TiO₂ dose= 1 g/L, initial pH= 3)

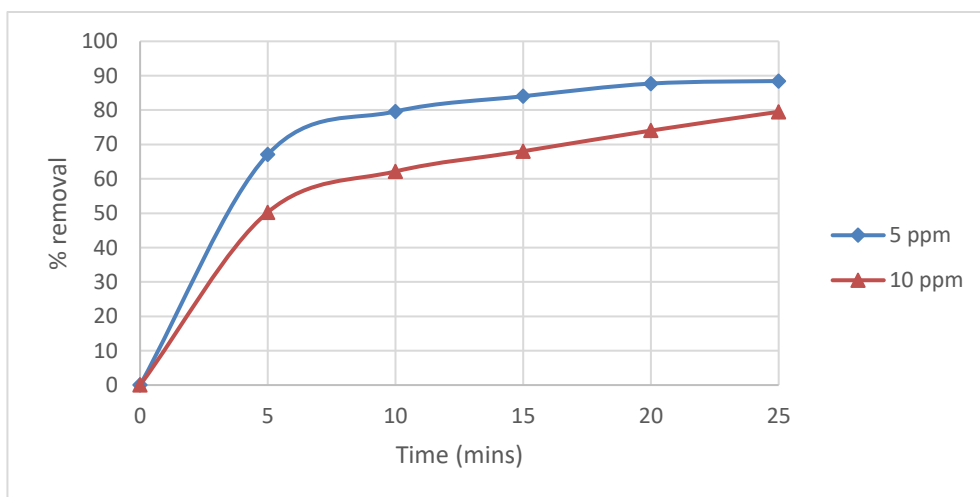


Figure 4: Effect of time on the percentage color removal of MB at different initial concentrations (Flow rate= 125 ml/min, TiO₂ dose= 1 g/L, initial pH= 7)

4.2 Effect of the TiO₂ dose

In order to study the influence of the amount of TiO₂ applied per liter of solution as a catalyst, the same process with the same conditions was applied using 4 different TiO₂ doses.

The experiments produced almost identical results, especially as showed in Figure 5. In Figure 6, the higher initial concentration used caused a little variance in the performance of the different doses. While the effect is minute, it is obvious that the smaller the quantity of TiO₂ used per volume of solution is, the less methylene blue it can remove.

These results are in-line with previous work done [17] .

This finding can be explained first by the increase in the total active surface area when we increased the dosage of the catalyst that increased the hydroxyl and superoxide radicals formation.

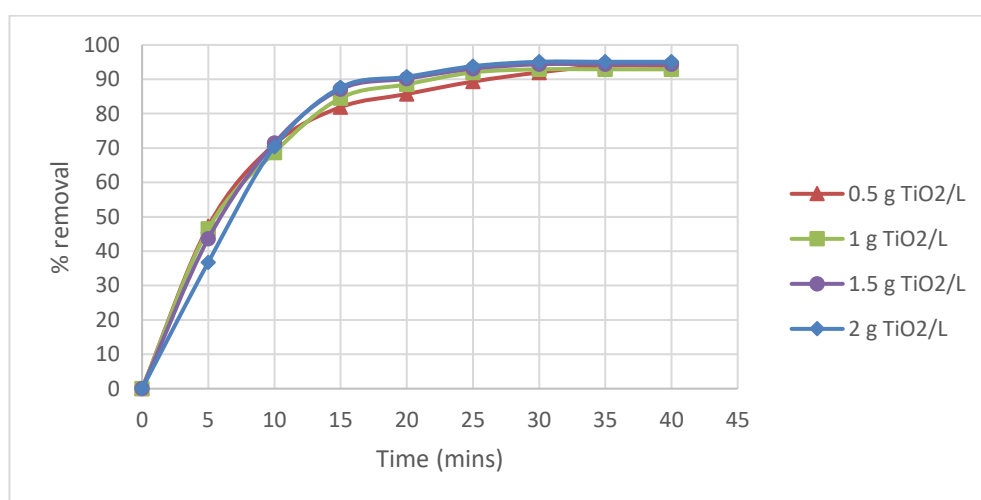


Figure 5: Effect of time on the percentage color removal of MB at different TiO₂ doses

(Flow rate= 125 ml/min, initial MB concentration=10 ppm, initial pH= 3)

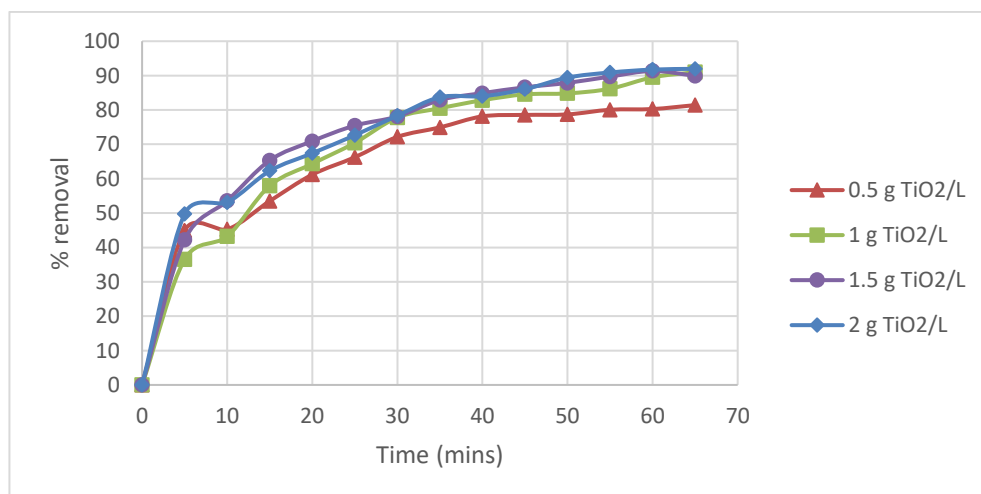


Figure 6: Effect of time on the percentage color removal of MB at different TiO₂ doses

(Flow rate= 87.5 ml/min, initial MB concentration=20 ppm, initial pH= 3)

4.3 Effect of pH

In order to study how the pH of the solution affects the degradation efficiency, the same process with the same conditions was applied using 4 different pH values. 3 for acidic, 7 for neutral, 9 and 11 for alkaline conditions.

The experiments showed that using a neutral solution produces very weak results in terms of % removal of methylene blue from the solution if compared with either the acidic or the basic solution.

Acidic solution kept showing higher rates of removal on different conditions, and especially at higher initial concentrations of solutions the basic solution failed to sustain a high percent removal similar to that of the acidic.

This can be explained by the surface charge of catalyst. Zero charge (pHpzc) (the point of zero net charge on the surface of the catalyst) is approximately at pH value of 6.25 in the case of TiO_2 [4], making the catalyst surface positively charged below Zero charge pH (acidic medium) and negatively charged above it (basic and neutral mediums) and this is due to the amphoteric behavior of TiO_2 . In an acidic medium, the MB is positively charged and the TiO_2 is negatively charged, this will cause an attraction force between the particles, allowing more MB particles to get adsorbed on the TiO_2 particles [19], and this can explain the high removal in the case of the acidic pH value. On the other hand, above the point of Zero charge the opposite happens, electrostatic interactions happen between negatively charged TiO^- and the MB cations, increasing its adsorption on its surface and therefore; increasing the rate of the degradation [3], this can justify the improvement that happened as the pH moved away from the Zero charge.

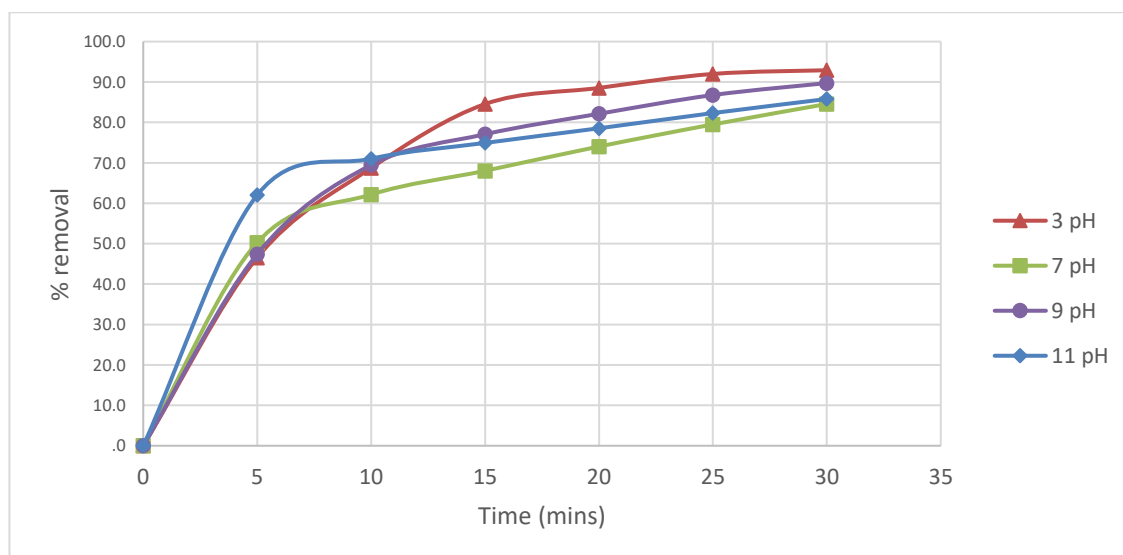


Figure 7: Effect of time on the percentage color removal of MB at different initial pH values

(Flow rate= 125 ml/min, initial MB concentration=10 ppm, TiO_2 dose= 1 g/L)

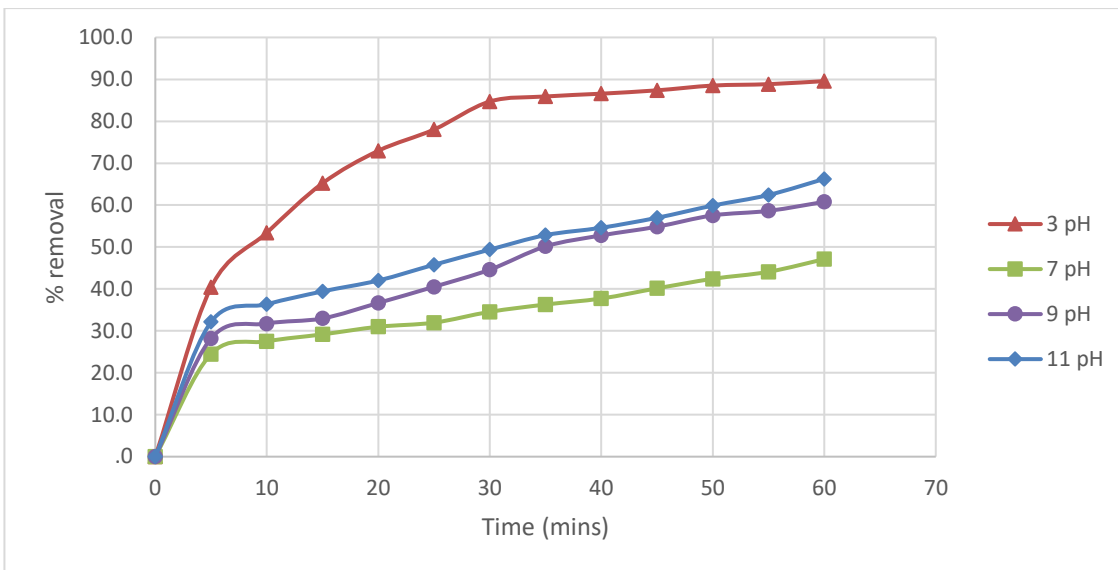


Figure 8: : Effect of time on the percentage colour removal of MB at different initial pH values
 (Flow rate= 125 ml/min, initial MB concentration=20 ppm, TiO₂ dose= 1 g/L)

4.4 Effect of the flow rate

In order to study the effect of the flow rate of the solution on the degradation efficiency, the same process with the same conditions was applied using 4 different flow rates.

The effect of the flow rate is obvious, especially at the very low rates (12.5 ml/min) the performance of the process drops significantly in both terms of the highest % removal reached and the time required to reach this percent. As the flow rate increases the efficiency of the process improves strongly.

This can be explained by the smaller resistance to mass transfer of MB molecules on the diffusion layer of the TiO₂ particles.

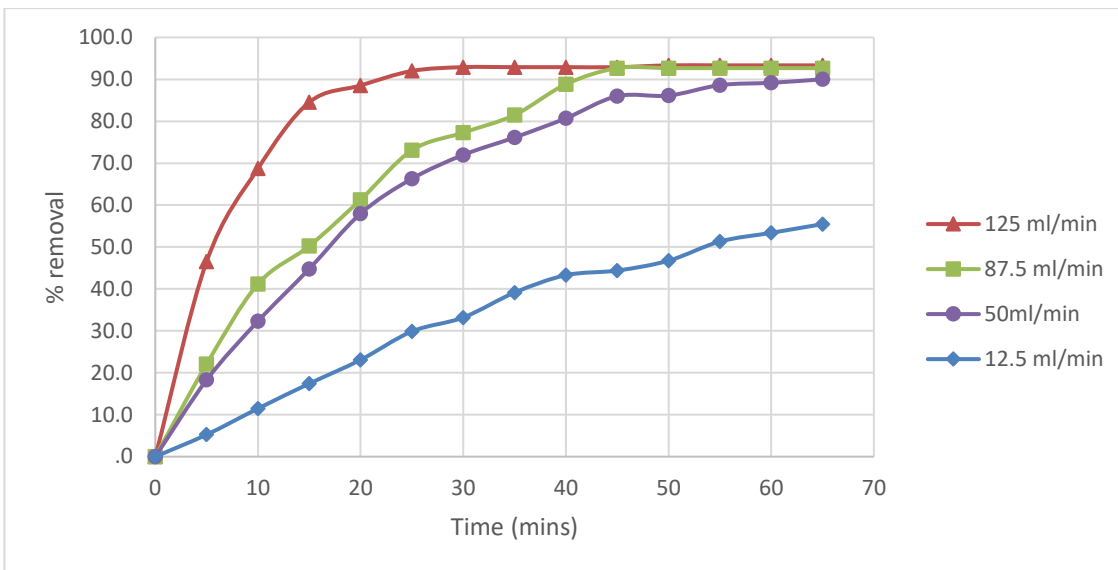


Figure 9: Effect of time on the percentage color removal of MB at different flow rates (initial pH = 3, initial MB concentration=10 ppm, TiO₂ dose= 1 g/L)

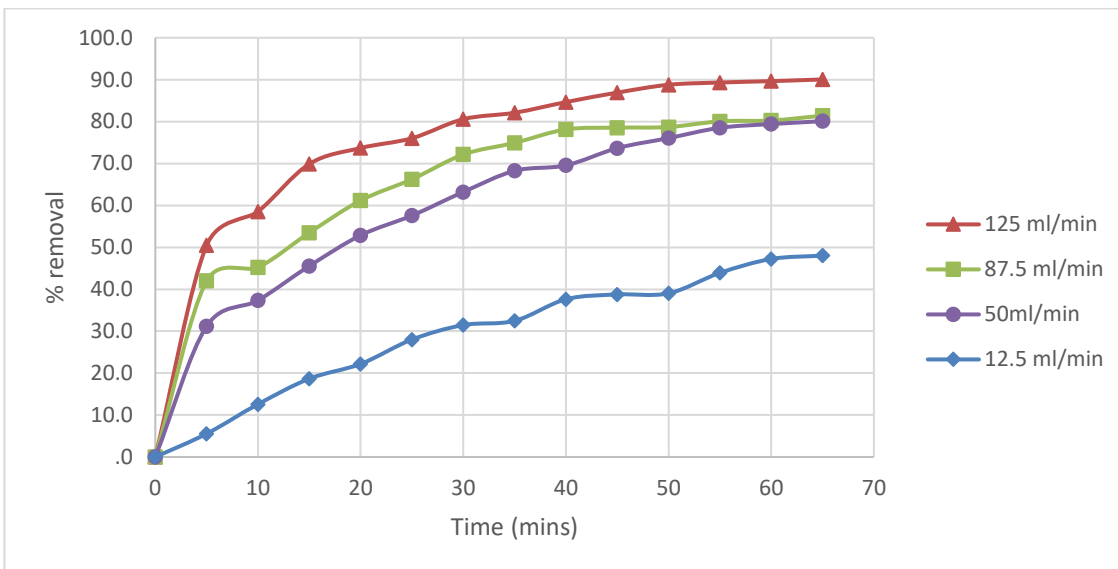


Figure 10: Effect of time on the percentage colour removal of MB at different flow rates (initial pH = 3, initial MB concentration=20 ppm, TiO₂ dose= 0.5 g/L)

4.5 Experimenting with no catalyst

At this phase, the experiment is done without using a catalyst, keeping only the effect of the UV radiations on the degradation of methylene blue.

Comparing Figure 5 with Figure 11, the drop of percent removal appears to be quite significant, as the removal, without using a catalyst, didn't exceed 40% after 35 minutes. On the other hand, the percent

removal was far better using the catalyst TiO_2 being higher than 90% removal after the same period of time.

This can be explained by the reduced production of hydroxyl radicals when we omitted using the catalyst, as the catalyst generated holes were used to form hydroxyl radicals.

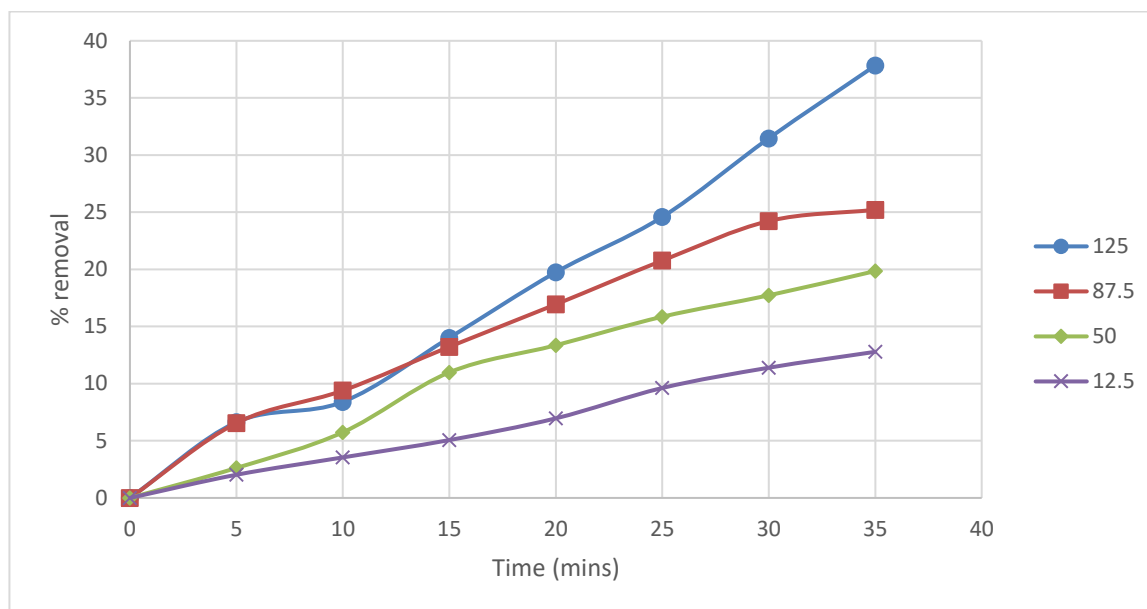


Figure 11: Effect of time on the percentage color removal of MB at different flow rates (initial pH = 3, initial MB concentration=10 ppm, no catalyst)

4.6 Experimenting without UV radiation using TiO_2 catalyst

For the same conditions of the previous experiment, TiO_2 was used again while omitting the UV radiations, keeping only the effect of the TiO_2 on the degradation of methylene blue.

Through this experiment, it was obvious that the TiO_2 , when used alone, doesn't have almost any effect.

Comparing Figure 12 with both Figure 5 and Figure 11, it is obvious how UV radiation is definitely the crucial part for the degradation process to happen.

This can be explained by the fact that without the UV radiation the production of the hydroxyl radicals, which are the main agents responsible for the oxidation of the dye molecules, will not happen in the first place. On the other hand, the minute removal that happened (less than 8% were removed after 35 minutes in the best conditions) can be explained by the adsorption that happened on the surface of the TiO_2 itself.

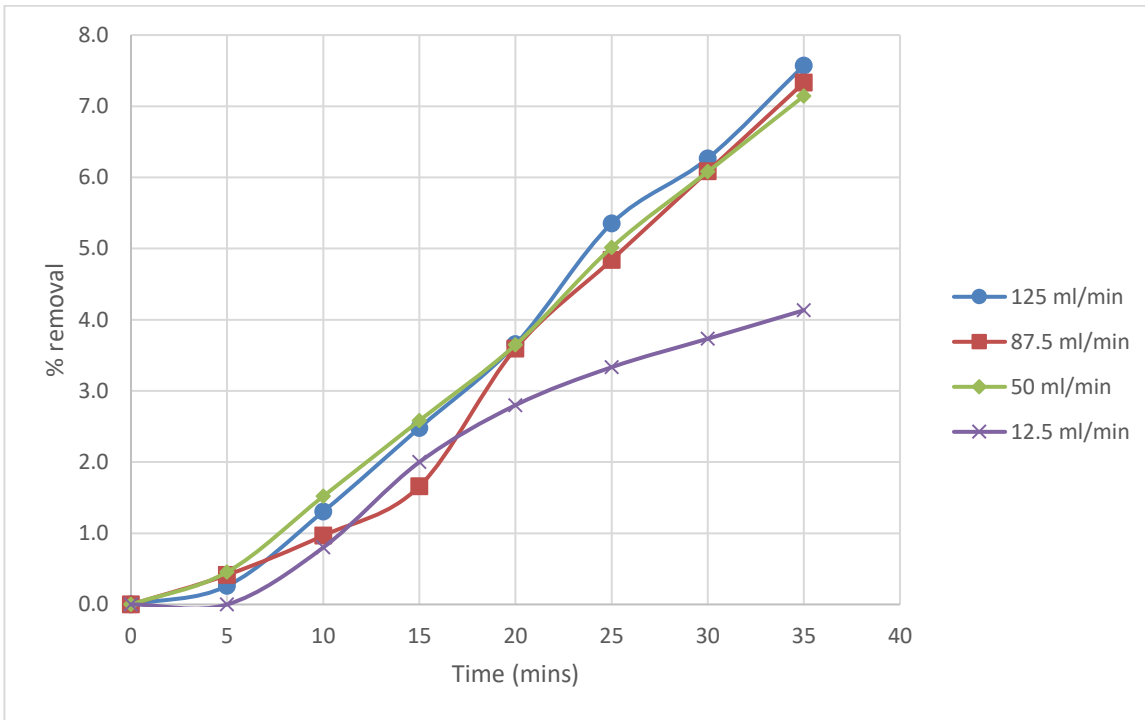


Figure 12: Effect of time on the percentage color removal of MB without UV radiation at different flow rates
(initial pH = 3, initial MB concentration=10 ppm, TiO₂=1 g/L)

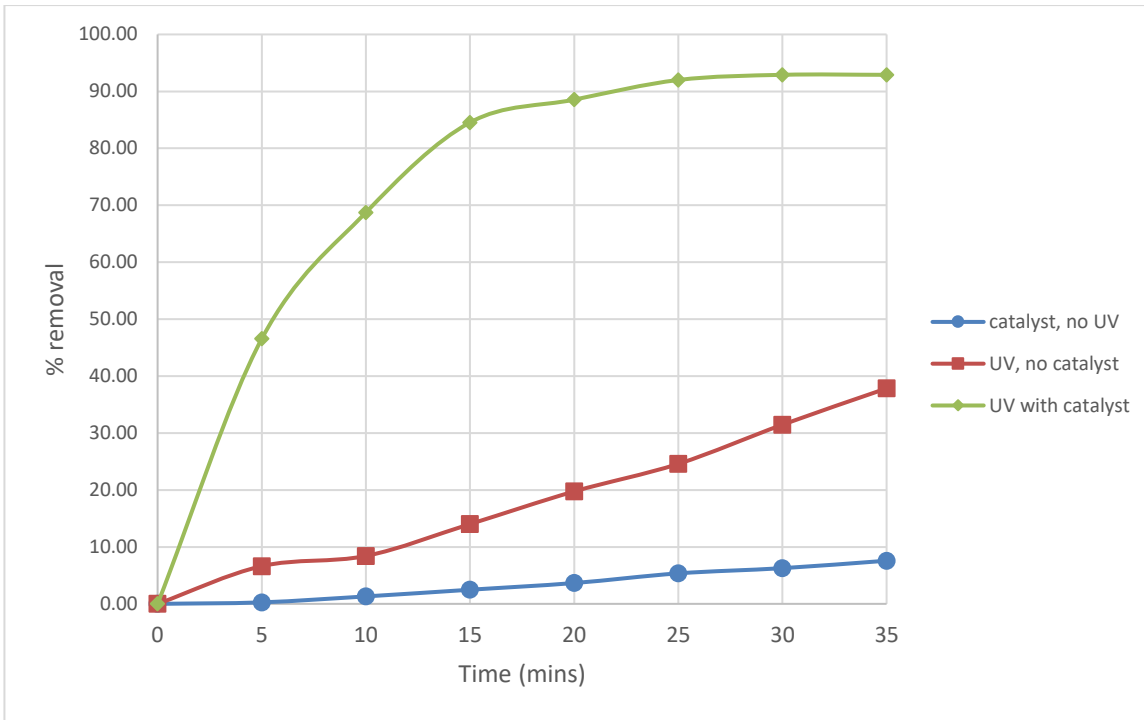


Figure 13: Effect of time on the percentage color removal of MB comparing the effect of using UV and catalyst at 125 ml/ min

(initial pH = 3, initial MB concentration=10 ppm, TiO₂=1 g/L)

4.7 Kinetics of the degradation

Kinetics modeling of the degradation of MB was done using 2 models, first; Lagergren pseudo-first order model, and second; Ho's pseudo-second-order model.

Lagergren pseudo-first order model:

$$q = q_e(1 - e^{-k_1 t}) \quad (7)$$

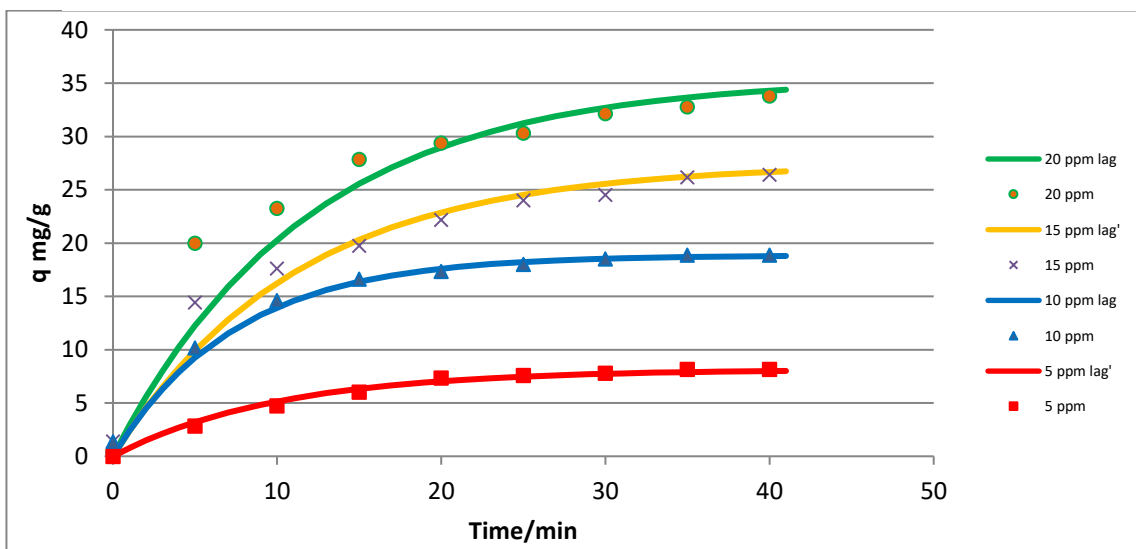
Ho's pseudo-second-order model:

$$q = \frac{q_e^2 k_2 t}{1 + q_e k_2 t} \quad (8)$$

Where q_e is the amount of MB removed per g TiO₂ at equilibrium (mg/g), q is the amount of MB removed per g TiO₂ at time t (mg/g), k_1 is the rate constant of pseudo-first-order adsorption (1/min) and k_2 is the rate constant of pseudo-second-order adsorption (g/mg min).

In the below figures 14 and 15 the actual data was plotted against both models. Lagergren pseudo-first order model is better fitting the actual data. This is confirmed in earlier results where the photocatalytic degradation of dyes was found to be better fitting first order reaction model [8, 17].

Figure 14: Fitting data to Lagergen pseudo-first order model
 (initial pH = 3, flow rate=125 ml/min, TiO₂=0.5 g/L)



k1 (5 ppm)	k1 (10 ppm)	k1 (15 ppm)	k1 (20 ppm)
0.10	0.135	0.09	0.085

Table 1, values of Constants (1/min)

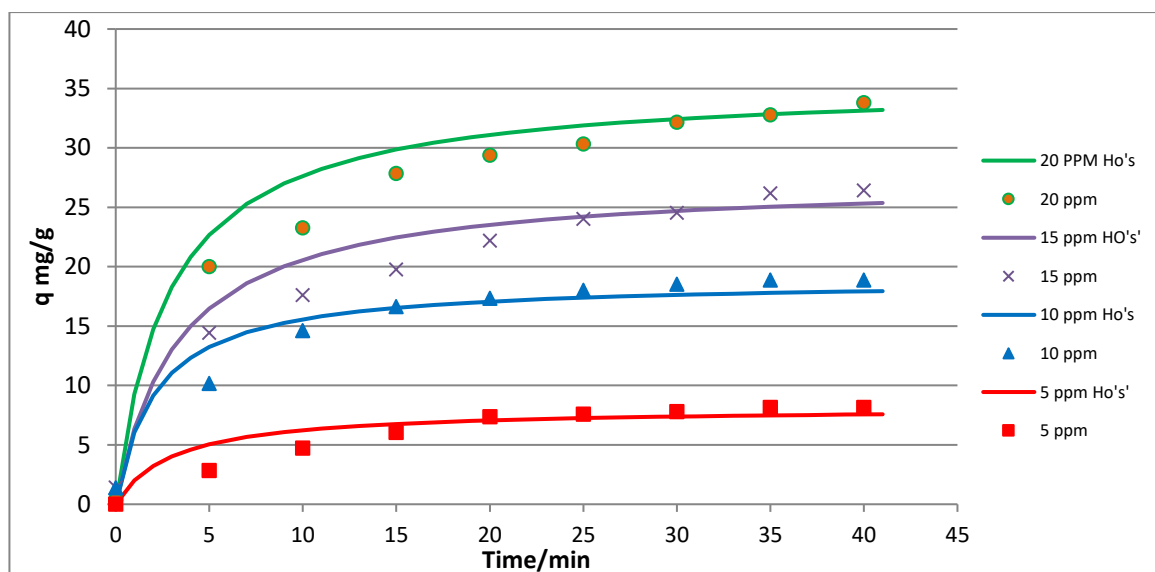


Figure 15: fitting data to HO's pseudo-second order model

(initial pH = 3, flow rate=125 ml/min, TiO₂=0.5 g/L)

k2 (5 ppm)	k2 (10 ppm)	k2 (15 ppm)	k2 (20 ppm)
0.04	0.025	0.011	0.01

Table 2: values of Constants (g TiO₂/mg MB. min)

5 Conclusion

The performance of this photocatalysis reactor that used FEP tubing, proved to be a very promising technology to degrade dyes like methylene blue and many other wastes in effluents. It also proved to be competitive if compared to earlier researches^[17] that used quartz glass tubing.

According to the results of this work, the removal of methylene blue by photocatalytic technique using TiO₂ as a catalyst through the used reactor, the following findings were obtained:

- As flow rate increases, the performance of the reactor improves significantly
- Acidic solutions (3 pH) appeared much better in terms of improving % removal
- 10 ppm can be considered the optimum initial concentration of the MB, comparing it to 5,15 and 20 ppm, while increasing the initial concentration caused a decrease in the rate of removal
- Increasing the dose of TiO₂ didn't cause a huge improvement in the rate of removal. Therefore, it had a minute effect on the overall performance of the process
- The reaction was found to depend completely on the UV radiation availability, and to be affected to a great extent by the usage of catalyst (TiO₂)
- The reaction can be considered to be fitting pseudo first order model

6 References

- [1] M.C. Venceslau, S. Tom and J.J. Simon, Characterization of textile wastewaters- a review. *Environmental Technology*, 15, 917-929, 1994.
- [2] U.G. Akpan and B.H. Hameed, Parameters Affecting the Photocatalytic Degradation of Dyes Using TiO₂-Based Photocatalysts: A Review. *Journal of Hazardous Materials*, V170, N2–3, pp.520–529, 2009.
- [3] K.C. Bubacz, methylene blue and Phenol Photocatalytic Degradation on Nanoparticles of Anatase TiO₂. *Polish Journal Of Environmental Studies*, V19, N4, pp.685–691, 2010.
- [4] K. Mondal and A. Sharma, Photocatalytic Oxidation of Pollutant Dyes in Wastewater by TiO₂ and ZnO Nano-Materials – A Mini-review. *Chemical Engineering journal*, pp.36-72, 2012.
- [5] H. Rashed, OVERVIEW ON CHEMICAL OXIDATION TECHNOLOGY. Ninth International Water Technology Conference, pp. 115-132, Sharm El-Sheikh, Egypt, 2005.
- [6] A. Al-Kdasi, A. Idris, K. Saed and C.T. Guan, Treatment Of Textile Wastewater By Advanced Oxidation Processes – A Review. *Global Nest: the Int. J.*, Vol 6, No 3, p.222–230, 2004.
- [7] I.K. Konstantinou, T.A. Albanis, TiO₂-assisted photocatalytic degradation of azodyes in aqueous solution: kinetic and mechanistic investigations—A review. *Appl. Catal. B: Environ.* 49, 1–14, 2004.
- [8] S.B. Gajbhiye, Photocatalytic degradation study of methylene blue solutions and its application to dye industry effluent. *International Journal of Modern Engineering Research*, V2, N3, pp.1204–1208, 2012.
- [9] K. Tennakone, C.T.K. Tilakaratne and I.R.M Kottegoda, Photomineralization of carbofuran by TiO₂-supported catalyst. *Water Research*, 31, 1909-1912, 1997.
- [10] N. Azbar T. Yonar and K. Kestioglu, Comparison of various advanced oxidation processes and chemical treatment methods for COD and color removal from a polyester and acetate fiber dyeing effluent, *Chemosphere*, 55, 35-43, 2004.
- [11] A. Mokrini, D. Ousse and S. Esplugas. Oxidation of aromatic compounds with UV radiation/ozone/hydrogen peroxide. *Water Sci. Technol.*, 35, 95-102, 1997.
- [12] D.F. Ollis, Contaminant degradation in water: heterogeneous photocatalysis degrades halogenated hydrocarbon contaminants. *Environmental Science and Technology*, 19, 480-484, 1985.
- [13] R.W. Matthews, Purification of water with near-U.V. illuminated suspensions of Titanium Dioxide, *Water Research*, 24, 653-660, 1990.
- [14] O. Legrini, E. Oliveros and A.M. Braun, Photochemical processes for water treatment. *Chem. Rev.*, 93, 671-698, 1993.
- [15] C.P. Huang, C. Dong and Z. Tang, Advanced chemical oxidation: its present role and potential future in hazardous waste treatment. *Waste Management*, 13, 361-377, 1993.
- [16] H. Tang, H. Berger, P.E. Schmid and F. Lévy, Optical properties of anatase (TiO₂). *Solid state Commun.*, 92, 267-271, 1994.
- [17] N. Laoufi, The degradation of phenol in water solution by TiO₂ photocatalysis in a helical reactor. *Global NEST*, Vol 10, No 3, 404-418, 2008.

- [18] K.M. Joshi and V.S. Shrivastava, Removal of methylene blue Dye Aqueous Solution Using Photocatalysis. International Journal of Nano Dimension, V2, N4, pp.241–252, 2012.
- [19] R. Al-Anbari, A.H. Al-Obaidy, E. Abd, Comparative study on decolorization efficiency of blue azo dye-235 using TiO_2 , V_2O_5 and ZnO as photocatalysis. Journal of Engineering and sustainable development, Vol 20, No 06, 2520-0917, 2016.

Removal of Methylene Blue from Aqueous Solution Using New Activated Carbons Developed from Ficus Nitida: Adsorption Equilibrium and Kinetics

Amal Elkassas^{1,*}; Riham Hazzaa²; Ibrahim Gar Al-Alm Rashed³; Mohamed Hussien Abd-El-Magied⁴

¹Chemical Engineering Department, Higher Institute of Engineering and Technology, New Damietta, Egypt.

²Petrochemicals Engineering Department, Pharos University, Alexandria, Egypt.

³Faculty of Engineering, Mansoura University, Mansoura, Egypt.

⁴Chemical Engineering Department, Alexandria University, Alexandria, Egypt.

*E-mail: amalelkassas88@gmail.com.

Abstract

In the present study activated carbon was prepared from Ficus nitida as a low cost adsorbent to remove methylene blue (MB) from aqueous solutions. The physical and chemical characteristics of raw Ficus nitida and activated carbon with high efficiency (activation temperature 900°C, activation time 0.5h) were examined using different techniques such as Scanning Electron Microscopic (SEM) and Fourier Transform Infrared Spectrometer (FTIR). The effects of initial dye concentrations, contact time, pH, adsorbent dosage and temperature on methylene blue dye removal were investigated. Langmuir, Freundlich and Temkin adsorption isotherms were examined to monitor the adsorption behavior. Langmuir isotherm best suited the adsorption data compared to other models. The pseudo-first-order model, pseudo-second-order model, Elovich model and intraparticle diffusion models were applied to the adsorption Kinetic data. Thermodynamics parameters of adsorption process were also determined in this study. The results revealed that activated carbon prepared from Ficus nitida can be used as an adsorbent to remove methylene blue (MB) from polluted wastewater.

Keywords: Ficus nitida; Activated Carbon; Adsorption Isotherms; Adsorption Kinetics; Adsorption Thermodynamics; Methylene Blue

1. Introduction

Nowadays, water pollution is a serious issue because it affects our lives and is expected to get worse over coming decades [1]. Some of organic and inorganic water pollutants are dangerous because of their highly toxic and carcinogenic nature. Therefore, water treatment, recycling of polluted and wastewater are the best approaches to get safe water for our routine activities [2].

Among the best methods were used in water treatment are reverse osmosis, ion exchange, electrodialysis, electrolysis and adsorption. Adsorption is a fast, inexpensive and widely applicable technique [3].

Commercially activated carbon is a remarkable highly adsorbent material with a large number of applications in the remediation of contaminated groundwater and industrial wastes such as colored effluents. However, activated carbon is an expensive adsorbent due to its high costs of manufacturing and regeneration. For the purpose, authors tried to explore the application of activated carbon as adsorbent from inexpensive natural source for removing unwanted hazardous compounds from contaminated water [4]. Agricultural byproducts and waste materials used for the production of activated carbons include, Apricot stones [5] , Olive stone [6] , Pomegranate peel [7] , Sugarcane bagasse [8], Tomato [9] , Watermelon [10] , Ficus carica bast [11] , Coconut shell [12] , Corn cob [13] , Desiccated coconut residue [14] and Banana peel [15].

The aim of this study is the preparation of activated carbon from *Ficus nitida* and study the adsorption of methylene blue (MB) onto *Ficus nitida* activated carbon from aqueous solution. The influence of various experimental factors such as contact time, initial dye concentration, adsorbent dosage, temperature and pH of dye solution were investigated. The equilibrium data were analyzed using Langmuir, Freundlich and Temkin isotherm models depending on temperature to determine the best isotherm to correlate experimental data. The kinetic models pseudo-first-order, pseudo-second-order, intraparticle diffusion and Elovich were studied and thermodynamics parameters of adsorption process were also determined in this study.

2. Materials and Methods

2.1. Adsorbate

Methylene blue (MB) purchased from National Company, Egypt was chosen as the adsorbate in this study. The stock solution was prepared by dissolving 1 g of dye in one litre distilled water. The chemical formula of methylene blue dye is $C_{16}H_{18}ClN_3S$ and its molecular weight is 319.85. The pH of initial dye solution can be adjusted by the addition of drop wise of 0.1 N HCl or 0.1 N NaOH and measured using a pH meter. All chemicals used were of analytical reagent grade.

2.2. Raw material

In Egypt, there are many kinds of tree species planted as street trees, windbreaks and shelterbelts and there are large quantities of wood branches and leaves resulted annually from the pruning process that can be used in various purposes such as *Ficus* species and ornamental trees. *Ficus nitida* is a popular ornamental tree grown widely regions in Egypt [16].

2.3. Preparation of activated carbon

Ficus nitida used in the present study for production of activated carbon was collected from Faculty of Agriculture Damietta University, Egypt. It was washed thoroughly with distilled water to remove any surface dirt and adhering impurities. The washed Ficus nitida dried in air for few days and then was dried in oven at 70°C for 3 h until a constant weight was reached, cut into small pieces, crushed, and sieved by standard sieves (Retch AS 200 – Germany) to obtain different particle size (600-850µm). The dried Ficus nitida was subjected to thermal activation by carbonization in a muffle furnace. The sample was placed in a well-sealed stainless steel tube in the muffle furnace, where it was physically activated and carbonized in the absence of air at different carbonization temperatures (400–900°C) and at times (0.5–3 h). The most efficient carbonization temperature was achieved at 900°C and activation time 0.5 h. Scanning Electron Microscope (SEM) analysis was performed to study the morphology of FNAC (model SEM JEOL JSM 6360 LA Japan) and Chemical characterization of surface functional groups was detected by Fourier Transform Infrared Spectrometer (FT/IR-4100 JASCO).

2.4. Adsorption studies

Batch adsorption studies were conducted in a set of 250 ml Erlenmeyer flasks containing 1 g adsorbent dose of particle size (850-600µm) and 100 ml dye solutions with various initial concentrations. The flasks were agitated in an isothermal water-bath shaker at 150 rpm and 25±2°C. The samples were taken at different time intervals until the equilibrium was reached. The experimental data were analyzed for equilibrium and kinetic studies. The effects of initial concentration of MB (10, 30, 50, 70 and 100 ppm), contact time (3 h), pH of the solution (2–9) and the temperature (25, 35, 45 and 55°C) on the adsorptive removal of MB were investigated. The samples withdrawn were centrifuged for 10 min. The dye concentration before and after adsorption were determined using spectrophotometer (UNICO 1200/1201) at wavelength 664 nm. MB uptake at time t, q_t (mg.g⁻¹), and at equilibrium, q_e (mg.g⁻¹), was calculated by the following equation:

$$q_t = \frac{(C_i - C_t)V}{M} \quad (1)$$

$$q_e = \frac{(C_i - C_e)V}{M} \quad (2)$$

Where c_i , c_e and c_t (mg.L⁻¹) are the initial, equilibrium concentrations, and concentration at time (t) of dye, respectively, V (L) is the volume of the solution, and M (g) is the mass of adsorbent used. The percentage removal of MB was calculated as follows:

$$\% \text{Removal} = \left(\frac{C_i - C_t}{C_i} \right) * 100 \quad (3)$$

3. Results and Discussion

3.1. Scanning Electron Microscopy (SEM)

Scanning electron microscopy (SEM) is a primary tool for characterizing the surface morphology and fundamental physical properties of the adsorbent. (Figure 1) shows SEM micrograph of dried raw Ficus nitida, activated carbon prepared from Ficus nitida and activated carbon after adsorption. The carbonization of Ficus nitida created pores and holes. The surfaces of the thermally carbonized carbons are full of cavities indicating the possibility for the dye to be adsorbed.

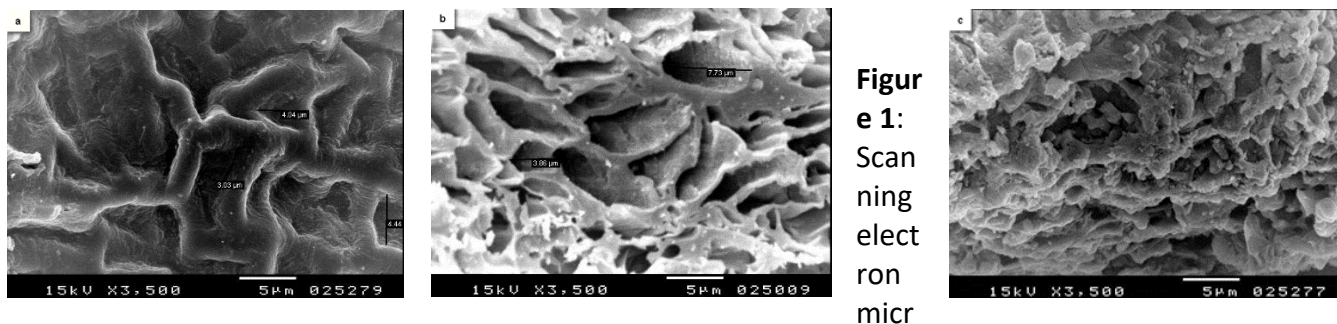


Figure 1:
Scanning electron microscopy (SEM) micrographs of (a) Raw Ficus nitida, (b) Activated carbon prepared from Ficus nitida and (c) Activated carbon after adsorption.

Micrographs (SEM) of (a) Raw Ficus nitida, (b) Activated carbon prepared from Ficus nitida and (c) Activated carbon after adsorption.

3.2. Fourier Transform Infrared Spectrometer (FT-IR)

FTIR spectra of Ficus nitida and activated carbon prepared from Ficus nitida were obtained to identify their functional groups. The spectrum was recorded from 4000 to 400 cm^{-1} . FTIR spectra as shown in (Figure 2). The Ficus nitida exhibited hydroxyl functional group, including hydrogen bonding at stretching frequency 3318 cm^{-1} . The intense bands at 2917 and 2852 cm^{-1} were assigned to the asymmetric C-H aliphatic stretching. Presence of strong stretching frequency band at 1731 cm^{-1} attributable to C=O of ester group, an absorption peak at 1608 cm^{-1} due to C=C, in addition to frequency bands at 1448 and 1317 cm^{-1} due to CH₂ bending. Peaks in wave numbers 1240 and 1072 cm^{-1} showed the presence of C-O bond. FTIR of the activated carbon showed the absence of the stretching frequency at 3318 cm^{-1} due to OH group, which confirm that OH group was dehydrated through preparation of activated carbon. Also, FTIR devoid of the intense bands at 2917 and 2852 cm^{-1} due to the asymmetric C-H aliphatic stretching in addition to disappearance of the two bending bands at 1448 and 1317 and presence of CH₂ bending band at 1419 cm^{-1} , which indicate that the activation removed a significant amount of hydrogen. The stretching absorption band at 1731 cm^{-1} observed for the raw materials is associated with the carbonyl C=O. This band was absent in the prepared activated carbon, and instead low intensity band at 1698 cm^{-1} indicating that the thermal activation broke many bonds in aliphatic and aromatic species and eliminate many volatile and light substrates.

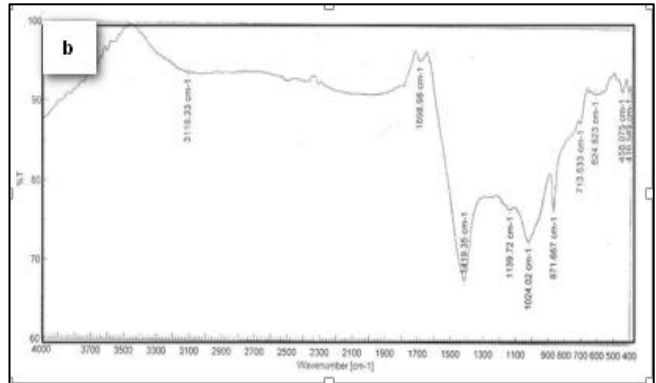
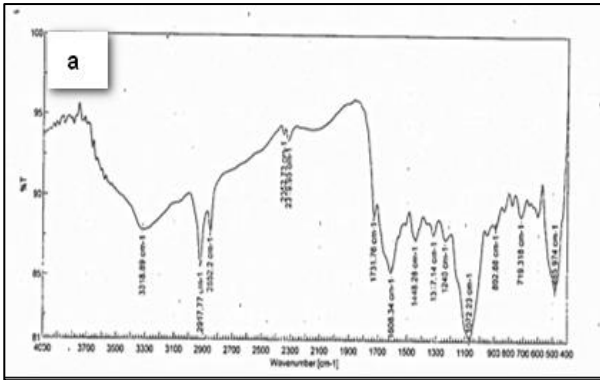


Figure 2: FTIR spectra of (a) *Ficus nitida* and (b) Activated carbon from the *Ficus nitida*

3.3. Batch adsorption experiments

3.3.1 The yield of *Ficus nitida* activated carbon

The effect of activation temperature and time on yield is shown in (Figure 3). As the activation temperature increases from 400 to 900°C, the yield decreases from 50% to 31%. The yield decreases with increasing activation temperature. This can be attributed to the loss of volatile materials when the temperature increases [17]. The increase of time doesn't show any significant decreases in the yield.

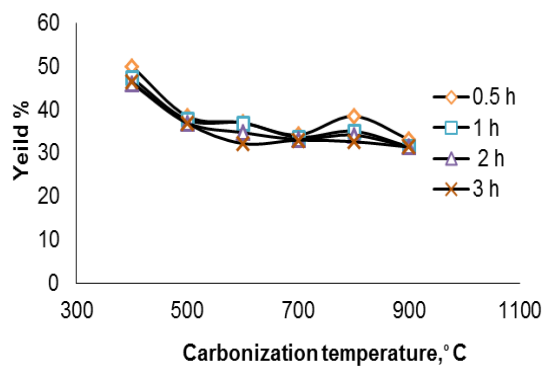


Figure 3: Effect of carbonization temperature on the yield of activated carbon at different activation time.

3.3.2 Effect of initial concentration of dye and contact time on adsorption

Effect of contact time and initial dye concentration (10, 30, 50, 70 and 100 ppm) on the amount of MB adsorbed by FNAC were studied and shown in (Figure 4). (Figure 4) shows that the amount of MB adsorbed by FNAC at different initial dye concentration. The amount of MB adsorbed by FNAC increased with increase in contact time and reached equilibrium at 3h. The amount of MB adsorbed by FNAC at equilibrium increased from 0.939 to 6.936 mg/g for an increase in initial dye concentration from 10 to 100 ppm. The previous observations show that the amount of MB adsorbed increased with increase in initial concentration of the MB dye. When the initial concentration increased, the mass transfer driving force becomes larger, hence resulting in higher adsorption of MB [18].

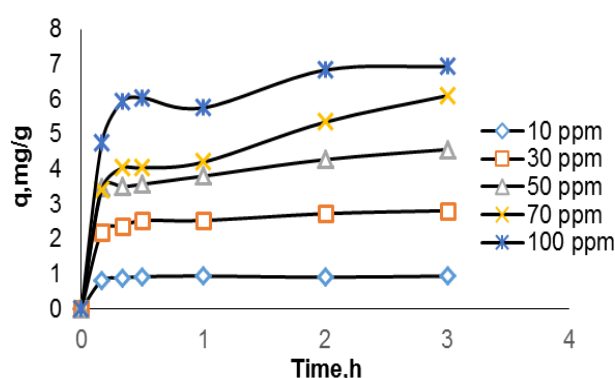


Figure 4: Effect of contact time on adsorption of MB at various initial concentrations (Temperature = $25 \pm 2^\circ\text{C}$, FNAC dose = 1gL^{-1} , agitation speed = 150 rpm).

3.3.3 Effect of solution pH on adsorption

The pH of dye solution plays an important role in the whole adsorption process and particularly on the adsorption capacity [19]. The effect of pH on the adsorption of MB onto both adsorbents within the pH range from (2–9) was investigated at 50 ppm initial concentration of MB as shown in (Figure 5).

The results indicate that the maximum removal percent was 91 % for FNAC at optimum pH 6. By increasing pH, the positively charged surface decrease, consequently, the rate of adsorption increase until it reaches to maximum at pH 6. The experiment showed that above pH 6, the rate of adsorption decrease might be to acquiring the active surface negatively charge.

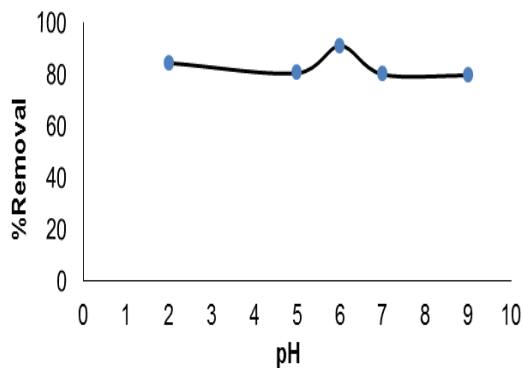


Figure 5: Effect of solution pH on MB adsorbed by FNAC

3.3.4 Effect of Adsorbent dose

The effect of dose onto the adsorption of MB by FNAC was investigated from (0.4, 0.6, 0.8, 1 and 1.2 g) with initial MB concentration of 50 mg/L. (Figure 6 (a)) shows that the percent removal of MB onto FNAC increases from 54 % to 92% with the increase in adsorbent dose ranged from 0.4- 1.2g after which there is no significant removal with further increase in the adsorbent dose. (Figure 6 (b)) shows that the amount of dye adsorbed decreases from 6.834 to 3.842 mg/g with the increase in adsorbent dose ranged from (0.4 - 1.2 g). This may be due to the availability of more adsorbent sites as well as greater availability of specific surfaces of the adsorbents. However, no significant changes in removal efficiency were observed beyond 1 g. So, gram is considered the optimal dose for FNAC loading [11].

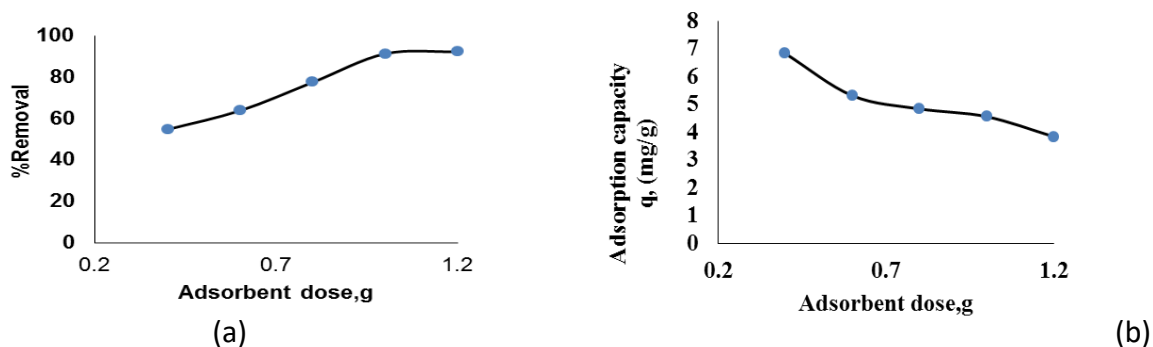
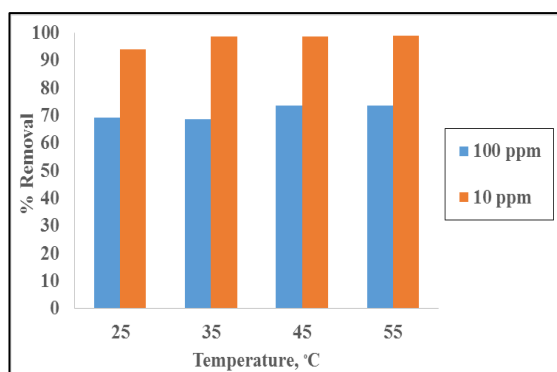


Figure 6: Effect of adsorbent dose on methylene blue dye adsorption by FNAC.

3.3.5 Effect of temperature

The effect of solution adsorption process was adsorption temperature at adsorbent dose 1gm and MB 10 ppm and 100 ppm of increasing the temperature from 25-55°C, increase the percentage removal from 69.35% to 73.6 % respectively for initial concentration of MB 100 ppm. However for initial concentration of MB 10 ppm the percentage removal increased from 94 % to 99 % for the increase of temperature from 25-55°C respectively. Increasing temperature may decrease the viscosity of the solution and increase the rate of diffusion of the dye to the external boundary layer and the internal pores of the activated carbon. Similar results were also reported [20].



on adsorption

temperature on the studied by varying the 25, 35, 45 and 55°C, initial dye concentration of MB. (Figure 7) shows that

Figure 7: Effect of temperature on MB adsorption

3.4 Adsorption Isotherms

The adsorption isotherm indicates how the adsorption molecules are distributed between the liquid phase and the solid phase when the adsorption process reaches an equilibrium state. The analysis of the isotherm data by fitting them to different isotherm models is an important step to find a suitable model that can be used for design purposes [21]. Adsorption isotherm study was carried out on three isotherm models: Langmuir, Freundlich and Temkin isotherm models. The applicability of the isotherm equation to describe the adsorption process was judged by the correlation coefficients (R^2) values. (Figure 8) shows that the adsorption isotherms fitting for adsorption of methylene blue onto Ficus nitida activated carbon and the adsorption capacity and other parameters were evaluated using the isotherm models, as shown in (Table 1). However Langmuir model is the best model describing adsorption of MB onto FNAC. The results of this study revealed that best isotherm models fitted for MB adsorption were determined in the order: Langmuir > Temkin > Freundlich. (Table 2) lists a comparison of adsorption capacities of methylene blue dye onto different adsorbents.

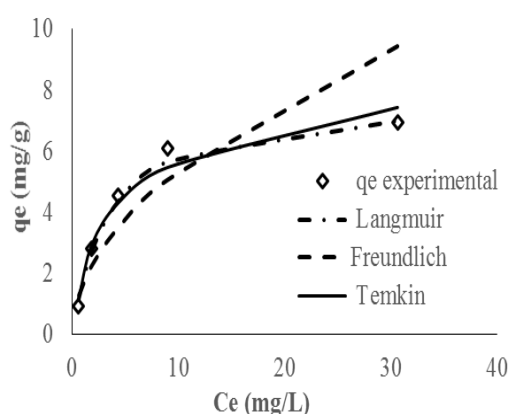


Figure 8: Adsorption isotherms fitting for adsorption of methylene blue onto Ficus nitida activated carbon.

Table 2 The adsorption capacity for methylene blue by various adsorbents			ion
Adsorbent	Maximum monolayer (Q_m) mg/g	References	
Corncob based activated carbon	0.84	[22]	
Almond shell-activated carbon	1.33	[23]	
Apricot stones-activated carbon	4.11	[23]	
Coir pith carbon	5.87	[24]	
Sugarcane bagasse activated carbon	6.73	[8]	
Ficus nitida activated carbon	7.77	Present study	

Hazelnut shell-activated carbon	8.82	[23]
Activated date pits	12.9	[25]
Olive stone activated carbon	16.12	[6]
Rice husk activated carbon	28.5	[26]

The adsorption kinetics of methylene blue onto FNAC were studied with respect to different initial concentration. For evaluating the adsorption kinetics, the pseudo first order, the pseudo second order, Elovich model and intraparticle diffusion model were used to fit the experimental data by using linear regression analysis method. The parameters of this models are summarized in (Table 3). The higher correlation coefficient (R^2) values indicate the fitness of the model pseudo second order is the best model for removal of MB onto FNAC.

3.5.1 Pseudo-first-order model

The pseudo first order rate expression is given as [27]:

$$\log (q_e - q_t) = \log(q_e) - k_1 t / 2.303 \quad (4)$$

Where q_e and q_t (mg.g^{-1}) are the amounts of adsorbate adsorbed at equilibrium and at any time respectively and k_1 (h^{-1}) is the rate constant. The plot of $\log (q_e - q_t)$ versus (t) is not shown. The values of k_1 and correlation coefficient (R^2) were listed in (Table 3). The experimental $q_{e,\text{exp}}$ values did not agree with the calculated $q_{e,\text{cal}}$ values obtained from the linear plots. This reveals that the adsorption of MB onto the FNAC does not follow pseudo first order kinetic model.

3.5.2 Pseudo-second-order model

The linearized form of the pseudo second order model as given is:

$$t/q_t = 1/K_2q_e^2 + t/q_e \quad (5)$$

Where K_2 is the rate constant of adsorption ($\text{g.mg}^{-1} \cdot \text{h}^{-1}$). The values of q_e and K_2 are determined from the slope and intercept of the plot of (t/q_t) against (t) as shown in (Figure 9) and listed in (Table 3). The correlation coefficient for the second-order kinetic model was greater than 0.995 for adsorption of MB onto FNAC. In addition, the values of The calculated $q_{e,\text{cal}}$ show good agreement with the experimental data.

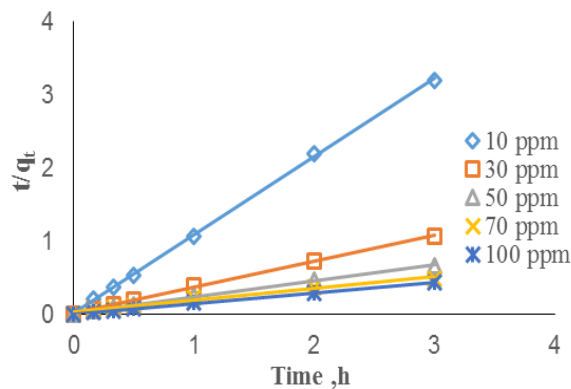


Figure 9: Pseudo- second -order kinetic models for the adsorption of MB onto FNAC

3.5.3 Elovich model

The Elovich model equation is generally expressed as:

$$q_t = 1/\beta \ln (\alpha\beta) + 1/\beta \ln (t) \quad (6)$$

Where α is the initial adsorption rate (mg /g. h), β is the desorption constant (g/mg) during any one experiments. The plot of (q_t) versus $\ln (t)$ is not shown. The Elovich model parameters α , β and Correlation coefficient (R^2) were listed in (Table 3). The correlation coefficient (R^2) is less than that of pseudo second order model.

3.5.4 Intraparticle diffusion model

The adsorption mechanism of adsorbate onto adsorbent follows three steps: film diffusion, pore diffusion and intraparticle transport. The slowest of three steps controls the overall rate of the process. The intraparticle diffusion model can be expressed as:

$$q_t = K_{id} t^{1/2} + C \quad (7)$$

Where K_{id} is the intra-particle diffusion rate constant (mg (g h)⁻¹), and C is a constant indicates the thickness of the boundary layer (mg.g⁻¹).The intraparticle diffusion plots of the experimental results, (q_t) versus ($t^{1/2}$) for different adsorbent are shown in (Figure 10). The values of K_{id} , C and correlation coefficient (R^2) are listed in (Table 3). The values of C obtained from intraparticle diffusion model indicate that thickness of the boundary layer increased by increasing the initial MB concentration and that intraparticle diffusion may not be the controlling factor in the adsorption process. The results revealed that more than one process affected the adsorption and the adsorption process contain both the surface adsorption and intraparticle diffusion .These observations had been reported by others [28].

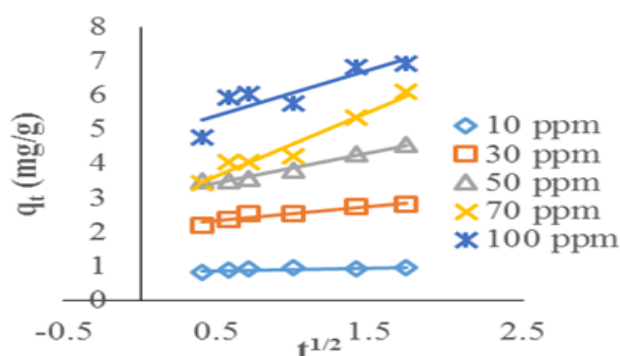


Figure 10: Intraparticle diffusion model for adsorption of MB onto FNAC

Finally, it can be concluded that the pseudo-second-order kinetic model provided a good correlation for the adsorption of MB onto FNAC. This suggested that the overall rate of the adsorption process was controlled by chemisorption [29]. The results were in agreement with the previous works on adsorption of MB onto activated carbons prepared from bamboo [30] and oil palm fiber [31].

Table 3 Kinetic model parameters for the adsorption of various initial concentrations of MB onto FNAC					
	10 ppm	30 ppm	50 ppm	70 ppm	100 ppm
q_{exp}	0.939	2.813	4.561	6.101	6.936
Kinetics model					
Pseudo-first-order					
q_{cal}	0.125	0.459	0.986	1.942	1.203
K₁	0.292	0.118	0.183	0.264	0.392
R²	0.033	0.023	0.1815	0.368	0.202
Pseudo second-order					
q_{cal}	0.936	2.83	4.589	6.158	7.04
K₂	74.522	6.434	2.261	0.829	1.803
R²	0.9995	0.9988	0.9954	0.9788	0.9961
Elovich					
β	27.472	4.98	2.573	1.173	1.525
α	2.7*10 ⁹	79538.49	10836.874	231.933	8847.229
R²	0.6269	0.9573	0.8857	0.8849	0.8159
Intraparticle diffusion					
C	0.835	2.12	3.012	2.678	4.715
K_{id}	0.067	0.419	0.874	1.896	1.362
R²	0.7647	0.9097	0.9754	0.9543	0.7665

3.6 Adsorption thermodynamics

Thermodynamic parameters evaluated for MB adsorption onto FNAC are the Gibbs free energy change (ΔG), enthalpy change (ΔH) and entropy change (ΔS). These parameters were calculated using the following equation [11].

$$\Delta G = -2.303 RT \log K_D \quad (8)$$

The K_D value was calculated using the following equation:

$$K_D = \frac{q_e}{C_e} \quad (9)$$

Also,

$$\Delta G = \Delta H - T\Delta S \quad (10)$$

$$\ln K_D = \frac{\Delta S}{R} - \frac{\Delta H}{RT} \quad (11)$$

Where R ($8.314 \text{ J mol}^{-1} \text{ K}^{-1}$) is the universal gas constant, T (K) is the absolute solution temperature. The values of ΔH and ΔS were calculated from the slope and intercept of plot between ($\ln K_D$) versus ($1/T$) for initial MB concentration of 30 ppm (Figure 11). The calculated values of ΔH , ΔS and ΔG are listed in (Table 4). The positive value of ΔH indicates that the adsorption of MB onto FNAC is an endothermic reaction. The positive value of entropy change ΔS shows the increased randomness at the solid/liquid interface of FNAC for MB dye. The negative value of ΔG indicated the feasibility of the process and the spontaneous nature of the adsorption with a high preference of MB onto the prepared activated carbon.

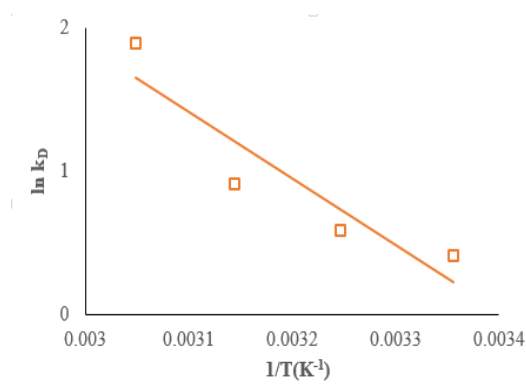


Figure 11: Plot of $\ln K_D$ versus $1/T$ for 30 ppm initial MB concentration.

Table 4 Thermodynamic parameters for the adsorption of MB onto FNAC.

ΔH (J/mol)	38438.95
ΔS (J/mol K)	130.89
ΔG (J/mol)	
298 K	-567.94
308 K	-1876.90
318 K	-3185.86
328 K	-4494.81

4. Conclusions

Activated carbon has been prepared from *Ficus nitida* for removal of methylene blue dye from aqueous solutions. The maximum removal of methylene blue was attained at pH 6. Equilibrium data were fitted to Langmuir, Freundlich and Temkin isotherms and the equilibrium data were best described by the Langmuir isotherm model ($R^2 = 0.9967$) with maximum monolayer adsorption capacity of 7.77 mg/g. The adsorption process is governed by the pseudo-second order reaction, at various initial dye concentrations. Thermodynamic studies indicated that the adsorption process is endothermic. The results indicated that *Ficus nitida* activated carbon could be used as a low-cost adsorbent for the removal of methylene blue from wastewater.

References

- [1] A.R. Alley, Water quality control handbook, McGraw-Hill Education, Europe, London, 125-141, 2000.
- [2] F. Woodard, Industrial waste treatment handbook, Butterworth-Heinemann, Boston, 376-451, 2001.
- [3] A. Imran, V.K. Gupta, Advances in water treatment by adsorption technology, Nat. Protoc 1.6. (2006) 2661-2667.
- [4] M. A. Mohammed, A. Shitu, A. Ibrahim, Removal of methylene blue using low cost adsorbent: a review, Res. J. chem. Sci., 4(1) (2014) 91-102.
- [5] C. Djilani, R. Zaghdoudi, F. Djazi, B. Bouchekima, A. Lallam, A. Modarressi, M. Rogalski, Adsorption of dyes on activated carbon prepared from apricot stones and commercial activated carbon, J Taiwan Inst Chem Eng, 53 (2015) 112-121.
- [6] R. Hazzaa, M. Hussein, Adsorption of cationic dye from aqueous solution onto activated carbon prepared from olive stones, Environ. Technol. Innov., 4 (2015) 36-51.
- [7] N. K. Amin, Removal of direct blue-106 dye from aqueous solution using new activated carbons developed from pomegranate peel: Adsorption equilibrium and kinetics, J. Hazard. Mater, 165(1) (2009) 52-62.
- [8] R. Hazzaa, M. Hussein, Cationic dye removal by sugarcane bagasse activated carbon from aqueous solution, Global Nest J, 17 (2015).

- [9] H. Saygılı, F. Güzel, Effective removal of tetracycline from aqueous solution using activated carbon prepared from tomato (*Lycopersicon esculentum* Mill.), industrial processing waste, *Ecotoxicol. Environ. Saf.*, 131 (2016) 22-29.
- [10] R. Lakshmiathy, N. C. Sarada, N. Jayaprakash, Agricultural wastes as low cost adsorbents for sequestration of heavy metal ions and synthetic dyes from aqueous solution: A mini review, In National conference on Nanomaterials for Environmental, 8(5) (2015) 25-31.
- [11] D. Pathania, S. Sharma, P. Singh, Removal of methylene blue by adsorption onto activated carbon developed from *Ficus carica* bast, *Arabian J. Chem.*, (2013).
- [12] U. Isah, G. Abdulraheem, S. Bala, S. Muhammad, M. Abdullahi, Kinetics, equilibrium and thermodynamics studies of CI Reactive Blue 19 dye adsorption on coconut shell based activated carbon, *Int. Biodeterior. Biodegradation*, 102 (2015) 265-273.
- [13] G. O. El-Sayed, M. M. Yehia, A. A. Asaad, Assessment of activated carbon prepared from corncob by chemical activation with phosphoric acid, *Water. Resour. Ind.*, 7 (2014) 66-75.
- [14] M. A. Yahya, C. Z. C. Ngah, M. A. Hashim, Z. Al-Qodah, Preparation of Activated Carbon from Desiccated Coconut Residue by Chemical Activation with NaOH, *J. Mater. Sci. Res.*, 5(1) (2016) 24.
- [15] R. Hazzaa, M. Hussien, Adsorption of cationic basic dye from aqueous solution onto activated carbon derived from banana peel, *Proceedings of the 14th International Conference on Environmental Science and Technology Rhodes, Greece*, (2015).
- [16] H. I. Aly, A. B. El-Sayed, Y. M. Gohar, M. Z. Salem, The Value-Added Uses of *Ficus Retusa* and *Dalbergia Sissoo* Grown in Egypt: GC/MS Analysis of Extracts, *J. Forest Prod. Ind.*, 2(3) (2013) 34-41.
- [17] M. O. Marin, C. F. Gonzalez, A. Garcia, V. G. Serrano, Preparation of activated carbon from cherry stones by physical activation in air. Influence of the chemical carbonization with H₂, *J. Anal. Appl. Pyrolysis*, 94 (2012) 131-137.
- [18] R. Baccar, P. Blanquez, J. Bouzid, M. Feki, M. Sarra, Equilibrium, thermodynamic and kinetic studies on adsorption of commercial dye by activated carbon derived from olive-waste cakes, *Chem. Eng. J.*, 165 (2010) 457-464.
- [19] M. Ghaedi, A. Golestani Nasab, S. Khodadoust, M. Rajabi, S. Azizian, Application of activated carbon as adsorbents for efficient removal of methylene blue: Kinetics and equilibrium study, *J. Ind. Eng. Chem.*, 20(4) (2014) 2317-2325.
- [20] A. Gürses, A. Hassani, M. Kirans, Ö. Acisli, S. Karaca, Removal of methylene blue from aqueous solution using by untreated lignite as potential low-cost adsorbent: Kinetic, thermodynamic and equilibrium approach, *J. water process Eng.*, 2 (2014) 10-21.
- [21] I. A. W. Tan, A. L. Ahmad, B. H. Hameed, Adsorption of basic dye on high-surface-area activated carbon prepared from coconut husk: Equilibrium, kinetic and thermodynamic studies, *J. Hazard. Mater.*, 154(1) (2008) 337-346.
- [22] R.L. Tseng, S.K. Tseng, F.C. Wu, Preparation of high surface area carbons from corncob using KOH combined with CO₂ gasification for the adsorption of dyes and phenols from water, *Colloids Surf. A*, 279 (2006) 69–78.

- [23] A. Aygun, S. Yenisoy-Karakas, I. Duman, Production of granular activated carbon from fruit stones and nutshells and evaluation of their physical, chemical and adsorption properties, *Micropor. Mesopor. Mat.* 66 (2003) 189–195.
- [24] D. Kavitha and C. Namasivayam, Experimental and kinetic studies on methylene blue adsorption by coir pith carbon, *Bioresour. Technol.*, 98 (2007) 14–21.
- [25] F. Banat, S. Al-Asheh, L. Al-Makhadmeh, Evaluation of the use of raw and activated date pits as potential adsorbents for dye containing waters, *Process Bio chem.* 39 (2003) 193–202.
- [26] P. M. K. Reddy, K. Krushnamurthy, S. K. Mahammadunnisa, A. Dayamani, C. Subrahmanyam, Preparation of activated carbons from bio-waste: effect of surface functional groups on methylene blue adsorption, *Int. J. Environ. Sci. TE.*, 12 (2015) 1363-1372.
- [27] S. Lagergren, *Handlingar*, 24 (1898) 1-39.
- [28] L. Yu, Y. Luo, The adsorption mechanism of anionic and cationic dyes by Jerusalem artichoke stalk-based mesoporous activated carbon, *J. Environ. Chem. Eng.*, 2 (2014) 220-229.
- [29] B.H. Hameed, A.L. Ahmad, K.N.A. Latiff, Adsorption of basic dye methylene blue onto activated carbon prepared from rattan sawdust, *Dyes Pigm.* 75 (2007) 143-149.
- [30] B.H. Hameed, A.T.M. Din, A.L. Ahmad, Adsorption of methylene blue onto bamboo-based activated carbon: kinetics and equilibrium studies, *J. Hazard. Mater.* 141 (2007) 819-825.
- [31] I.A.W. Tan, B.H. Hameed, A.L. Ahmad, Equilibrium and kinetic studies on basic dye adsorption by oil palm fiber activated carbon, *Chem. Eng. J.*, 127 (2007) 111-119.

Removal of sulfate ion from lean brine in chlor-alkali industry using anion exchange resin

S. R. Bassiouney^{1,*}, S. A. Nosier², M. Hussein³

^{1, 2, 3} Department of chemical engineering, faculty of engineering, Alexandria University, Alexandria, Egypt

Abstract

Sulfate anions represents the most popular impurity in depleted brine cycle which accumulate on membranes during electrolysis decreasing current efficiency, also sodium sulfate deposits cause an interruption of the normally smooth cathode surface layer and thus reduce the OH⁻ ion rejection capacity. This work focused on removal of sulfate ions using Purolite® A830, a polystyrenic Macro porous weak base anion exchange resin that was regenerated by hydrochloric acid. Experiments were carried out in a stirred tank reactor and the variables studied were initial concentration of sulfate ions which ranged from 3000-9000 ppm, impeller rotational speed which ranged from 100 to 500 rpm, resin dosage ranged from 550: 1100 g per 1 liter of solution and PH value which ranged from 1 to 3. The results show that the maximum removal of sulfate ion was 55% at speed of rotation 200 rpm, resin dosage 1100g and PH=1. Equilibrium adsorption isotherms Freundlich and Langmuir have been studied and it is shown that the results matched with Langmuir model; also adsorption kinetics proved that the results can be described by Pseudo second order model.

Keywords: sulfate; chlor-alkali; anion exchange resin; lean brine

1. Introduction

The chlor-alkali industry is one of the biggest electrochemical operations, which produces Cl₂ and NaOH through the electrolysis of NaCl solutions. The most popular anionic impurity in brine is sulfate, which precipitate in membrane near cathode side and leads to reduce current efficiency. In membrane cells, there are about 7 g/l Na₂SO₄ in the depleted brine and there are a lot of methods to hold the sulfate concentration beyond this level. This problem happened as it is the recycle of the brine around a continuous system, any sulfate in the raw salt or in depleted brine will eventually exceed the maximum limited amount of sulfate, this means that chlor-alkali plants have to purge a portion from the brine, but this method has two major disadvantages which are the cost of the lost

salt and any environmental problems which caused by the disposal of brine, Nevertheless most of plants use this method to decrease concentration of sulfate in circulated brine. [1]

Sulfate emissions can be controlled also by Nano filtration which uses membrane in spiral wound modules placed in cylindrical housings. Another method of removing sulfate is to precipitate by either barium or calcium ion and both are used commercially, while barium is a powerful agent for sulfate removal it is rather toxic, its compound must be handled carefully, expensive and subsequent removal of excess barium from the brine is relatively difficult. [1]

Adsorption using an ion exchange resin is one of the most popular methods for the removal of ions from water over the past few decades [2-6]. Processes for ion removal using an ion exchange resin have been developed by different authors [7-9]. Many studies on the adsorption of ions on ion exchange resins such as Duotite IRN77 [10], NKA-9[3] and Amberlyst A21 [11] have been reported. Chabani et al [12] investigated equilibrium and kinetic parameters for the removal of nitrates from aqueous solutions by adsorption onto an ionized adsorbent, Amberlite IRA 400. Their studies showed this resin is an effective adsorbent for the removal of nitrates from aqueous solutions with 96% removal efficiency. Haghsheno et al [13], studied kinetics and fixed bed operation of removal

*Corresponding author: email address: shericola_90@hotmail.com

of sulfate anions from an industrial waste water by an anion exchange resin Lewatit K6362. The results showed that the maximum removal of sulfate anions takes place in the resin dosage of 100mg/100ml. Fil et al [14], illustrated the adsorption of Ni(II) onto Dowex HCR-S, experiments were done to evaluate effect of resin dose, speed of stirring, PH, initial Ni (II) concentration on removal of Ni (II). Moreover, it is found that the results of adsorption isotherms can be predicted by Sips equation, and Pseudo Second order kinetic model.

The objective of this study is to remove sulfate ions from the lean brine in chlor-alkali industry instead of wasting large amounts of brine which can enter the cycle of the brine again, and this is done by using ion exchange resin in a batch stirred tank reactor, in addition the parameters that influences the ion exchange such as the initial sulfate concentration, PH of solution, rotational speed of impeller and resin dosage. Also this work aimed to evaluate kinetics and adsorption isotherms for the adsorption of sulfate on Purolite A830.

2. Materials and methods:

2.1. Apparatus and ion exchange resin

Experiments were carried out in 4.5 liters plexi glass vessel with 25 cm height and 18 cm diameter. Four baffles were fixed on the wall of the vessel with dimensions 25 cm height and its thickness is 1.5 cm each baffle was set a part by 90 ° angle from the other [15] as shown in fig.(1). The agitator consists of stainless steel shaft fitted with four blades 45 °, the stirrer was coated with epoxy resin. The shaft was driven by a 0.5 hp motor which was fixed firmly against a steel frame to prevent vibrations, the rotation speed was controlled by inverter [7]. The weak anion exchange resin Purolite A830, was used in this study, its physical properties and chemical characteristics as reported by the suppliers was shown in table (1).

Before using the resin, it should be treated by washing with distilled water until the effluent water is clear, immerse the resin in 2-4% ammonia solution for 4 hours then wash with clean tap water to show neuter washing water, after that soak the resin again in 4-5 % HCl solution for 3 hrs. and wash

with tap water to show neuter washing water, acid and alkali solution can be repeated for 2 or 3 times to have sufficient results [16].

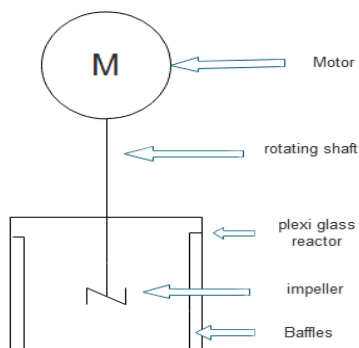


Fig.1. Schematic diagram of the batch experimental setup.

2.2. Preparation of the solution and procedures :

A solution of NaCl of 190 g/l including 3000 ppm sulfate was prepared by dissolving 4.4375 g of sodium sulfate and 190 g NaCl in 500 ml distilled water then complete the volume into 1 liter, different concentration of sulfate was prepared by the same method by changing weight of sodium sulfate. The solution is filtered through qualitative filter paper and adjusted to the desired PH using drops of 5% HCl solution. A sample of 10 ml was withdrawn from the solution for analysis. The lean brine was added to a known weight of resin and agitated for a predetermined period at known speed. A sample was withdrawn every 2 minutes then analyzed by precipitation as barium sulfate and dissolution of precipitate in excess of EDTA using Eirochrome black T as indicator [17]. The saturated resin undergo regeneration by washing with excess distilled water so the resin can return back to its free base ionic form, then soak it in a solution of 5% HCl of volume double the volume of the resin for 1 hr., fast rinse of the resin should be done by HCl for 15 min., then wash with tap water only 2 times.

The variables studied were initial concentration of sulfate (3000, 5000, 7000, and 9000) ppm, PH of the solution (1, 2, and 3), impeller rotational speed (100,200,300,400 and 500) rpm and resin dosage (550, 825, and 1100) g/l.

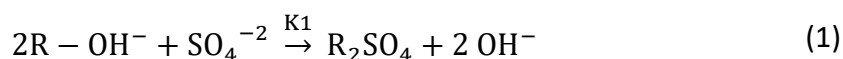
Table 1
Characteristics of Purolite A830 anion exchange resin

characteristics	values
Polymer structure	Macroporous polyacrylic crosslinked with divinylbenzene
appearance	Spherical beads
Functional group	Complex amine
Ionic form	Free base
Total capacity	2.7 eq/L (60.1 Kgr/ft ³)(FB form)

SBC	0-5 %
Moisture retention	50-56 % (FB form)
Particle size range	300-1200 μm
Uniformity coefficient (max.)	1.7
Reversible swelling. FB Cl (max.)	20 %
Specific gravity	1.1
Temperature limit	35 $^{\circ}$ C (FB form)

3. Theory :

Ion exchange removes undesired ions from brine by transferring them to ion exchange resin, which takes them while returning back an equivalent number of desirable species kept on ion exchange resin. Sulfate ion can be removed from brine through anion exchange resin. This can be expressed as follows:



Where R is the ion exchange radical, K_1 and K_2 are the forward and backward reaction rate constants respectively [13].

Adsorption isotherm demonstrates the relationship between the amounts of adsorbate on adsorbent and the concentration of dissolved adsorbate in the liquid phase at equilibrium. Equations which are usually used to describe isotherm are those developed by Freundlich [18] and Langmuir [19].

The Langmuir isotherm equation can be written in the following linear form:

$$\frac{C_e}{q_e} = \frac{1}{(Q_m K_L)} + \frac{C_e}{Q_m} \quad (2)$$

Where, C_e (mg/l) is the concentration of sulfate at equilibrium, q_e (mg/g) the adsorption capacity, k_l (l/mg) the Langmuir adsorption constant, Q_m (mg/g) is the maximum sulfate uptake.

The adsorption capacity after reaching equilibrium q_e (mg/g) was calculated using this formula:

$$q_e = \frac{(C_o - C_e)V}{W} \quad (3)$$

Where, C_o and C_e (mg/g) are the concentrations of sulfate initially and at equilibrium respectively, V is the volume of the solution and W (g) is the mass of adsorbent.

While Freundlich isotherm is expressed as:

$$q_e = K_f C_e^{\frac{1}{n}} \quad (4)$$

Where K_F (l/g) is the Freundlich constant that relates to sorption capacity, n is the Freundlich exponent that relates to sorption intensity. To obtain the constants K_F and n , the linear form of the equation (4) can be used to plot a graph between $\text{Log } q_e$ versus $\text{Log } C_e$.

$$\log q_e = \log K_F + \frac{1}{n} \log C_e \quad (5)$$

In most cases values of n lie between 1 and 10 indicating favorable adsorption [13].

Beside adsorption isotherms, the determination of kinetics regarding sulfate removal is considered another important study.

Pseudo first order model [20] can be expressed by equation:

$$\frac{dq}{dt} = k_1(q_e - q) \quad (6)$$

Where q_e (mg/g) is amount of sulfate adsorbed on ion exchange resin at equilibrium, q (mg/g) is amount of sulfate adsorbed at certain time t , k_1 is the Pseudo first order's rate constant. By integration of equation (6) at $q = 0$ and $t = 0$, equation (7) can be obtained.

$$\ln(q_e - q_t) = \ln q_e - k_1 t \quad (7)$$

The constants k_1 and q_e can be determined by plotting $\ln(q_e - q_t)$ versus t .

Another model can be used which is Pseudo second order model [20]:

$$\frac{dq}{dt} = K_2 (q_e - q)^2 \quad (8)$$

Where K_2 is the rate constant of Pseudo second order at equilibrium, by integrating equation (8), the following equation can be obtained:

$$\frac{t}{q_t} = \frac{1}{K_2 q_e^2} + \frac{t}{q_e} \quad (9)$$

k_2 and q_e values can be calculated by plotting t/q_t versus t .

4. Results and discussion

4.1. Effect of solution PH on sulfate uptake:

Fig. 2 depicts the effect of initial solution PH on the removal of sulfate by Purolite A830. In order to find out the optimum PH for maximum removal efficiency, experiments were carried out at 3120 ppm sulfate solution, about 550 g resin were added to 1 liter of lean brine solution, PH ranged from 1-3 and the results were shown in fig. 2. It is obvious that the removal efficiency increases by decreasing the value of PH, removal efficiency reaches zero % at PH higher than 4, due to anions competition to be exchanged on the surface of the prepared ion exchange resins of which OH^- predominates. Maximum adsorption at acidic PH indicates that the low PH leads to an increase in H^+

ions on the surface of the resin which results in significantly strong electrostatic attraction between positively charged anionic resin surface and sulfate ions [21].

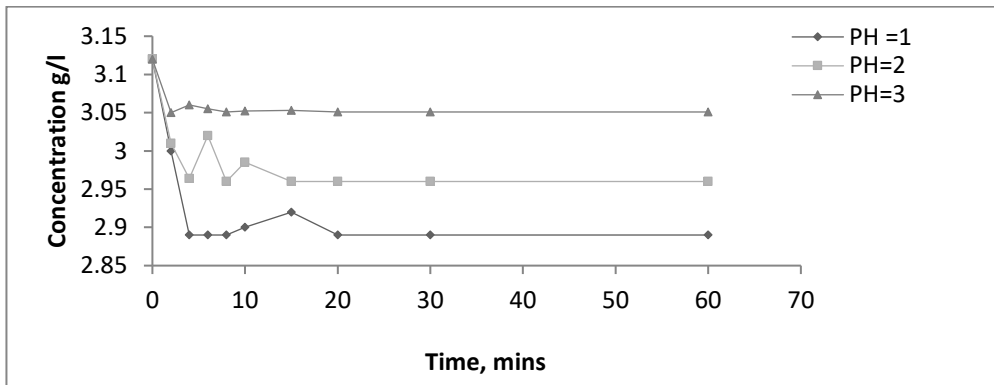


Fig. 2 Effect of solution PH on sulfate up take (initial concentration of sulfate= 3120 ppm; resin dosage = 550g/l; without stirring)

4.2. Effect of initial sulfate concentration and time:

Fig.3 shows that adsorption process depends on time. The sulfate removal increased with time and attained equilibrium at nearly 8 min. for all initial sulfate concentrations. It is also shown that the adsorption at various initial concentrations was fast in the initial stages and gradually decreased with the progress of the adsorption. From the figure It is clear that the amount of adsorbed sulfate increased by increasing initial concentration of sulfate. At low concentration the ratio of available surface to the initial concentration is larger, so the removal percentage becomes independent of initial sulfate concentration. Moreover, in the case of higher SO_4^{2-} concentrations this ratio is low; the removal then depends on initial concentrations [22]. The curves shows that at initial concentration 3000 ppm, percentage removal was 39%, while at 9000 ppm SO_4^{2-} percentage removal reached 55%.

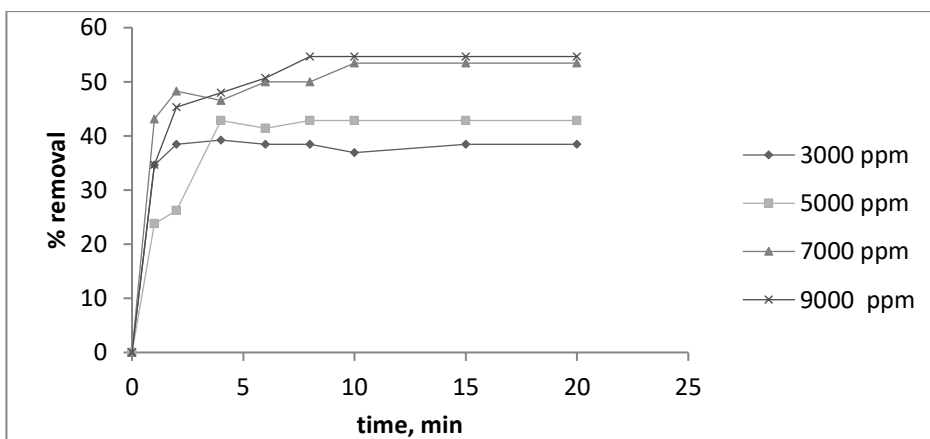


Fig. 3 Effect of initial sulfate concentration on percentage removal at different initial concentrations 3000,5000,7000,9000 ppm (PH of solution=1; resin dosage 1100g/l; rotational speed=200 rpm)

4.3. Effect of stirring:

Experiments were conducted to investigate the effect of stirring on sulfate removal for initial concentration 3000, 5000 ppm, with PH=1, resin dosage= 1100 g/l at different speed of rotation 100,200,300,400,500 rpm. As shown in Fig. 4, by increasing rotational speed the percentage removal of sulfate increases till 200 rpm, then decreases and increases again. This indicates that at higher speed more than 200 rpm, the mass transfer becomes negligible [22].

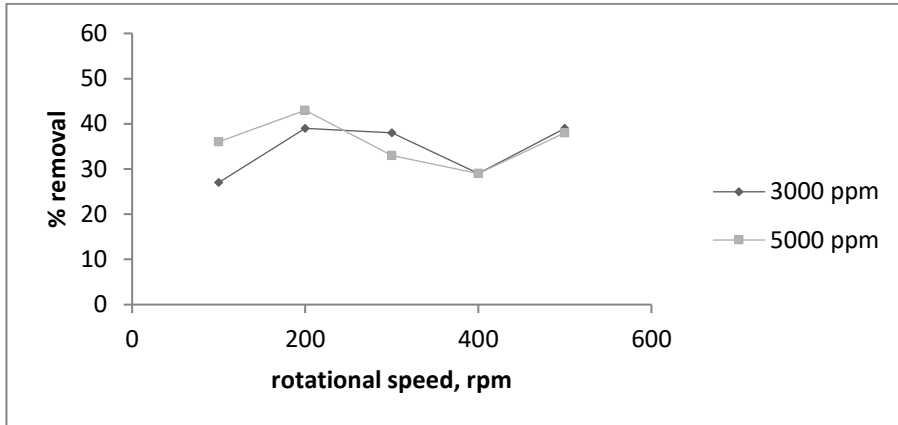


Fig. 4 Effect of stirring on percentage removal (PH of solution=1; initial concentration of sulfate=3000, 5000; resin dosage=1100 g/l)

4.4. Effect of resin dosage:

Fig.5 illustrates the effect of resin dosage on concentration of sulfate. It was found that at constant PH=1, rpm=200 at initial concentration of sulfate 9000 ppm, the removal efficiency increases by increasing resin weight, this is due to increasing the number of available sites by increasing adsorbent dose [8]. Also the figure showed that maximum removal was achieved at resin dose 1100 g/l.

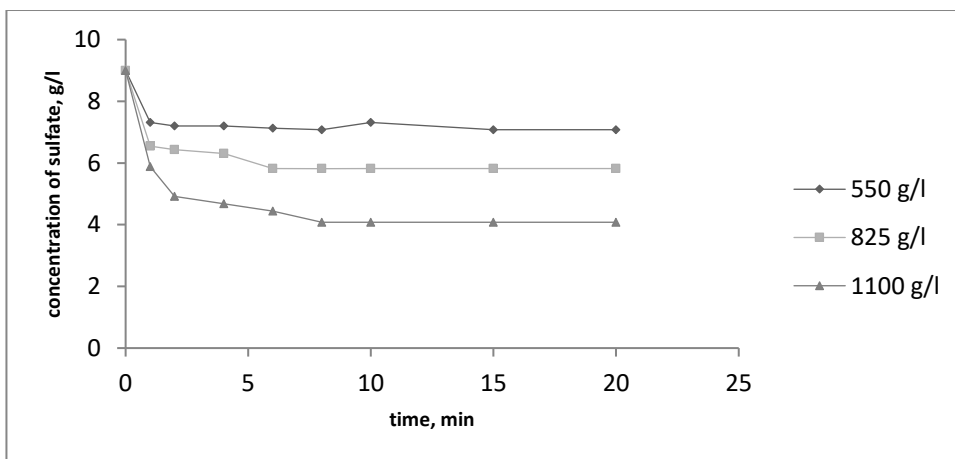


Fig. 5 Effect of resin dosage on sulfate uptake (PH of solution=1; rotational speed=200 rpm)

4.5. Adsorption isotherms :

The equilibrium data obtained in this study fitted to Freundlich adsorption isotherm, this is shown in Fig. 6, and the constants K_f and n for sulfate ions and ion exchange resins are listed in table 2. furthermore in this study, the equilibrium data were fitted to Langmuir adsorption isotherm and the results are shown in Fig. 7, The good coefficient's values of Langmuir isotherms is explaining strictly localized monolayer sorption phenomenon. Langmuir sorption isotherm hints towards surface homogeneity of the sorbent. Comparing results of two models, it is shown that the Langmuir isotherms can predict this system better than Freundlich isotherms.

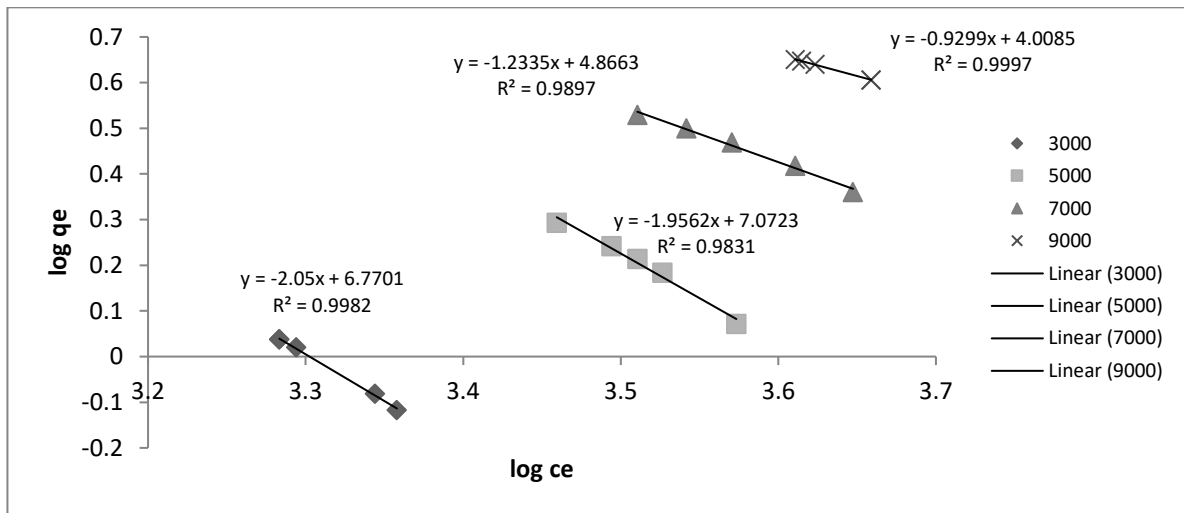


Fig. 6 Freundlich isotherm for the adsorption of sulfate using ion exchange resin

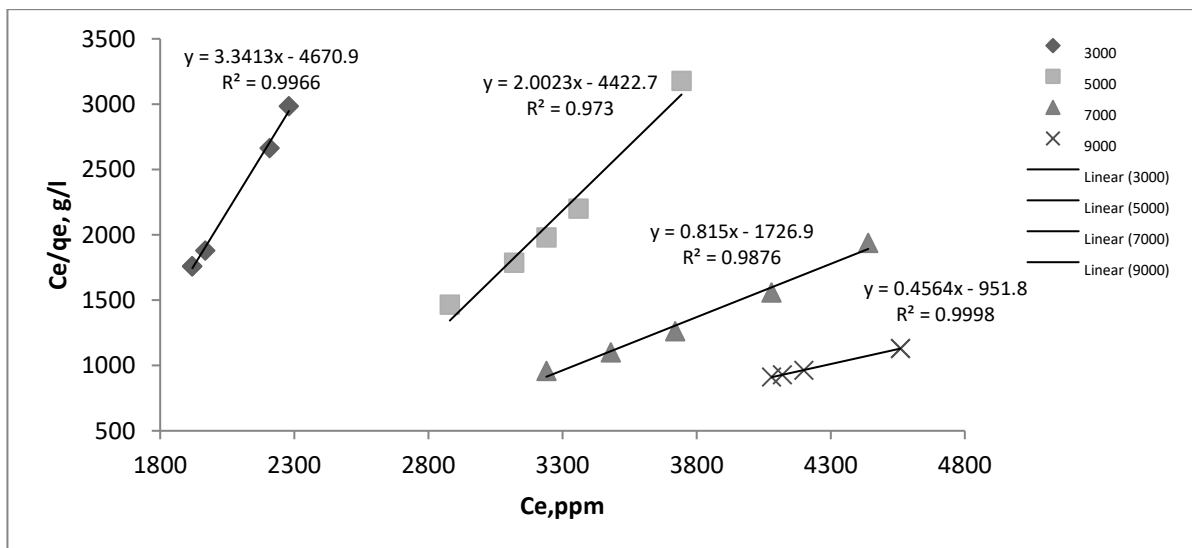


Fig. 7 Langmuir isotherm for the adsorption of sulfate using ion exchange resin

Table 2

Isotherms constants for SO_4^{2-} sorption in ion exchange resin Purolite A830:

concentration	Freundlich value	Langmuir value
---------------	------------------	----------------

3000	K_f	$5.88 \cdot 10^6$	K_L	$-7.16 \cdot 10^{-4}$
	$1/n_f$	-2.05	Q_m	0.299
	R^2	0.9982	R^2	0.9966
5000	K_f	$1.18 \cdot 10^7$	K_L	$-4.53 \cdot 10^{-4}$
	$1/n_f$	-1.956	Q_m	0.499
	R^2	0.9831	R^2	0.973
7000	K_f	$7.35 \cdot 10^4$	K_L	$-4.72 \cdot 10^{-4}$
	$1/n_f$	-1.2335	Q_m	1.226
	R^2	0.9897	R^2	0.9876
9000	K_f	$1.02 \cdot 10^4$	K_L	$-4.79 \cdot 10^{-4}$
	$1/n_f$	-0.929	Q_m	2.191
	R^2	0.9997	R^2	0.9998

4.6. kinetics studies :

In this study experiments were carried out at initial concentration of sulfate 9000 ppm at PH=1 and rotational speed 100 rpm, from fig. 8, 9 and table 3, it is shown that the values of q calculated from Pseudo second order kinetic model were much closer to q_{exp} than the values of q calculated from Pseudo first order model, moreover it is obvious that R^2 values are closer to unity in Pseudo second order. From these results, it is proved that sulfate removal by Purolite A830 can be described by Pseudo second order kinetic model.

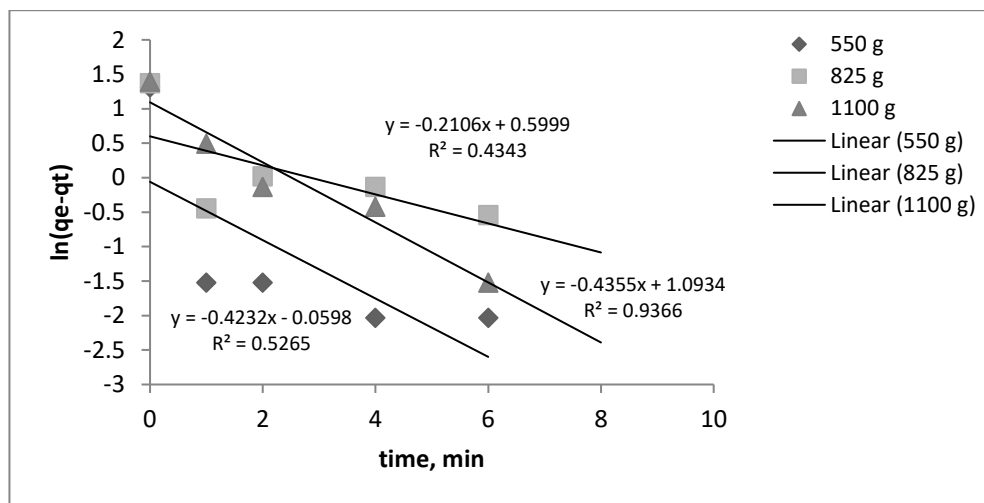


Fig. (8) Pseudo first order model of sulfate adsorption on ion exchange resin ($C_o = 9000$ ppm, PH = 1, rotating speed = 100 rpm)

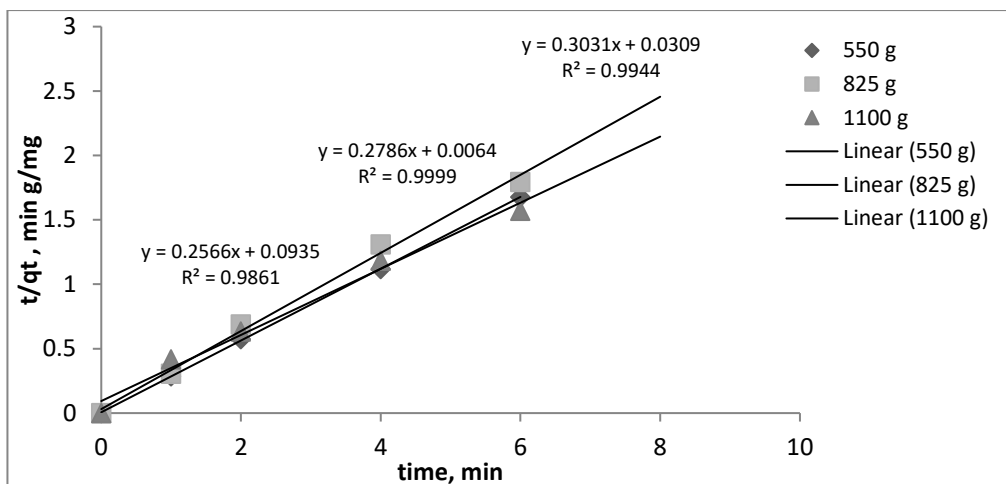


Fig. (9) Pseudo second order model of sulfate adsorption on ion exchange resin ($C_0 = 9000$ ppm, PH = 1, rotating speed = 100 rpm)

Table 3

Kinetics parameters for the adsorption of sulfate on Purolite A830.

Dose (g)	q_{exp}	Pseudo 1 st order			Pseudo 2 nd order		
		K_1	q_e	R^2	K_2	q_e	R^2
550	3.7	0.4232	0.94	0.526	12.13	3.589	0.9999
825	3.92	0.2106	1.82	0.434	2.97	3.299	0.9944
1100	4.03	0.4355	2.98	0.936	0.704	3.897	0.9861

5. Conclusions

In this study, Purolite A830 resin was used to remove sulfate from lean brine in chlor-alkali industry. The following conclusions were obtained:

1. When PH increases, percentage removal of sulfate ion decrease, so it is preferred to control all experiments at acidic medium of PH<3.
2. This resin is used effectively at high sulfate concentration >7000 ppm.
3. Max percentage removal of sulfate ion reached was 55%, to increase % removal more than 55% the resin dosage should be more than 1100 g/l.
4. It is preferred to take all experiments at rotational speed 200 rpm.
5. The obtained results revealed that these data fit Langmuir isotherm more than the Freundlich isotherm.
6. The adsorption process on resin particles was fast and equilibrium reached nearly at 8 minutes, this system can be predicted by Pseudo second order kinetic model.

Acknowledgements

The authors would like to thank Purolite Company and Misr chemical industries company for their support.

References

- [1] T. F. O'Brien, T. V. Bommaraju, F. Hine, Hand book of chlor-alkali technology; Vol. 1 fundamentals, Volume II : brine treatment, Springer US, 1580.
- [2] S. Rengaraj, Y. Kim, C.K. Joo, K. Choi, J. Yi, Batch adsorptive removal of copper ions in aqueous solutions by ion exchange resins: 1200H and IRN97H, Korean J. Chem. Eng. 21 (2004) 187.
- [3] Y. Omer, A. Yalcin, G. Fuat, Removal of copper, nickel, cobalt and manganese from aqueous solution by kaolinite, Water Res. 37 (2003) 948.
- [4] D. Muraviev, V. Gorshkov, A. Warshawsky, Ion Exchange, Decker, New York, 2000.
- [5] G.M. Tillman, Water Treatment Troubleshoot and Problem Solving, Lewis Publishers, New York, 1996.
- [6] J.P. Rawat, A. Ahmad, A. Agrawal, Equilibrium studies for the sorption of Cu^{2+} on lanthanum di ethanol amine—a chelating material, Colloid Surf. 46 (1990) 239.
- [7] A.H. Elshazly, A.H. Konsowa, removal of nickel ions from waste water using a cation exchange resin in a batch stirred tank reactor, desalination 158 (2003) 189-193.
- [8] S.Rengaraj, K. Yeon, S. Moon, Removal of chromium from water and waste water by ion exchange resins, journal of hazardous materials B87 (2001) 273-287.
- [9] J. Lehto, R. Harjula, H. Leino-nen, A. Paajanen, T. Larila, K. Mononen, L. Saarinen, Advanced separation of harmful metals from industrial waste effluents by ion exchange, J. Radioanal. Nuclear Chem. 208 (2) (1996) 435.
- [10] S. Rengaraj, S.H. Moon, Kinetics of adsorption of Co(II) removal from water and wastewater by ion exchange resins, Water Res. 36 (2002) 1783.
- [11] D. Guirmaraes, V.A. Leao, Batch and fixed bed assessment of sulfate removal by the weak base ion exchange resin Amberlyst A21, Journal of hazardous materials 280 (2014) 209-215.
- [12] M. Chabani, A. Amrane, A. Bensmaili, Kinetic modeling of the adsorption of nitrates by ion exchange resin, Chem. Eng. J. 125 (2006) 111–117.
- [13] R. Haghsheno, A. Mohebbi, H. Hashemipour, A. Sarrafi, Study of kinetic and fixed bed operation of removal of sulfate anions from an industrial waste water by anion exchange resin, Journal of hazardous materials 166 (2009) 961-966.
- [14] B.A. Fil, R. Boncukcuoglu, A.E. Yilmaz, S. Bayar, Adsorption of Ni(II) on ion exchange resin: kinetics, equilibrium and thermodynamic studies, Korean J. Chem. Eng., 29 (9), (2012), 1232-1238.
- [15] W. L. McCabe, J. C. Smith, P. Harriott, "Unit operation of chemical engineering", 5th edition, McGraw-Hill, Inc., New York, 1993.
- [16] www.hzresin.com/en/productinfo/detail_28_51_105.aspx.
- [17] G. H. Jeffery, J. Bassett, J. Mendham, R. C. Denney, "Vogel's text book Of Quantitative Chemical Analysis", 5th edition, John Wiley and sons Inc., 605 third Avenue, New York, 1989.
- [18] H.M.F. Freundlich, Uber die adsorption in Losungen, Z. Phys. Chem. (Leipzig) 57A (1906) 385-470.
- [19] I. Langmuir, "The constitution and fundamentals properties of solids and liquids", J. Am. Chem. Soc. 38(11) (1916) 2221-2295.
- [20] A.A. Hekmatzadeh, A. Karimi-Jashni, N. Talebbeydokhti, B. Klove, Adsorption kinetics of nitrate ions on ion exchange resin, Desalination 326, (2013), 125-134.

- [21] M. Fathy, Th. AbdelMoghny, A.E. Awadallah, A. A. Elbellihi, Study the adsorption of sulfates by high cross-linked polystyrene divinylbenzene anion exchange resin, *Appl Water Sci*, 2014.
- [22] S. Koumaiti, K. Raihi, F. Ounaies, B. B. Thayer, "Kinetic modeling of liquid phase adsorption of sulfate onto raw date palm seeds", *Journal of Environmental science and engineering*, 5, (2011) 1570-1580.

Intensification of the rate of production of Copper Powder from dilute Copper solutions by
Cementation on Vertical Vibrating Zinc Cylinder Fitted with Turbulence Promoters

M.E.F.Abdellatif *, D.A.El-Gayar and T.M.Zewail

Chemical Engineering Department, Faculty of Engineering, Alexandria University, Egypt.

Abstract

The combined effect of vibratory motion and turbulence promoters (TP) on the rate of Copper cementation on Zinc cylinder was investigated. The rate of Copper cementation was studied under different conditions of initial Copper ions concentration, the frequency and amplitude of oscillation and the geometrical parameters of TP such as their height and spacing. In addition, the influence of the presence of surface active agents (SAA) such as polyethylene glycol with molecular weight 400 (PEG 400) and cetyl trimethyl ammonium bromide (CTAB) on the rate of cementation was examined. The cementation rate was expressed in terms of the mass transfer coefficient. The results revealed that the mass transfer coefficient increases with increasing intensity of vibration whereas it decreases with increasing height and spacing of TP. The mass transfer coefficient increases with increase of initial Cu^{+2} concentration up to a certain limit and then declines with further increase in initial Cu^{+2} concentration. In general, the presence of SAA inhibited the rate of cementation by an amount ranging from 18.69 to 67.86 % depending on concentration of SAA, intensity of vibration and type of SAA. Correlation of the present mass transfer data using dimensionless analysis led to the following overall correlation:

$$\text{Sh} = 0.0001 \text{Re}^{1.19} \text{Sc}^{0.33} (d_e/d)^{0.45} (d_e/s)^{0.91}$$

For the conditions: $14993 < \text{Re} < 176406$, $1374 < \text{Sc} < 1593$, $8.3 < d_e/d < 25$ and $3.1 < d_e/s < 6.3$. This correlation is useful in the design and operation of such reciprocating Zinc cylinder used to conduct diffusion controlled cementation reaction.

Keywords: Cementation; Heavy metals recovery; Copper recovery; Wastewater treatment; Mass transfer; Vibratory motion; Surface active substances; turbulence promoters; Electrowinning of Zinc; Copper powder; Vibration.

***Corresponding author**

Mai Ezzat Farghaly Abdellatif

Email: mai.ezzat5@yahoo.com.

1. Introduction

In view of its simplicity where no expensive chemicals or sophisticated equipment are used, cementation is widely used to remove heavy metals from dilute solutions by precipitation on a less noble metal. The present work addresses the removal of Cu^{+2} by cementation on Zn which is used in practice in the following processes:

- i. Purification of ZnSO₄ leach liquor produced by leaching Zinc ores from Cu⁺² impurity prior to electro winning of Zinc in an electrolytic cell to obtain pure Zinc
- ii. Removal of Cu⁺² from industrial waste solutions discharged from industries such as metal finishing industry (electroplating, electroless plating, acid pickling of copper and copper alloys, electro polishing of copper and copper alloys), printed circuit industry and mining industry.

In this case cementation on Zinc not only rid the waste solution of the toxic Cu⁺² ions but also produces a valuable product, namely Copper powder which has important practical applications. Copper powder is used in the manufacture of metallic composites by the powder metallurgy techniques [1], also Copper powder is used as a catalyst in organic synthesis [2].

Cementation of Copper on less noble metals such as Zinc, Iron and Aluminum is known to be diffusion controlled [3][4][5], as such a means for enhancing the rate of cementation should be provided to the reactor, previous studies have used mechanical stirring [6][7], forced convection vibration [8][9], gas sparging [10], ultrasonic vibration [11] to intensify the rate of cementation.

The aim of the present work is to study the combined effect of mechanical vibration and turbulence promoters on the rate of Copper cementation on Zn. To this end a vertical oscillating Zinc cylinder fitted with circular plastic fins (ribs) was used as a reaction surface. Vibratory agitation is known to consumes lower energy than rotary agitation using impellers for a given degree of mixing [12].

Since waste solutions discharged by the electroplating industry frequently contain surface active agent along with Cu⁺², the present work also aims at investigating the effect of surface active agents on the rate of cementation.

2. Experimental Technique

2.1. Apparatus

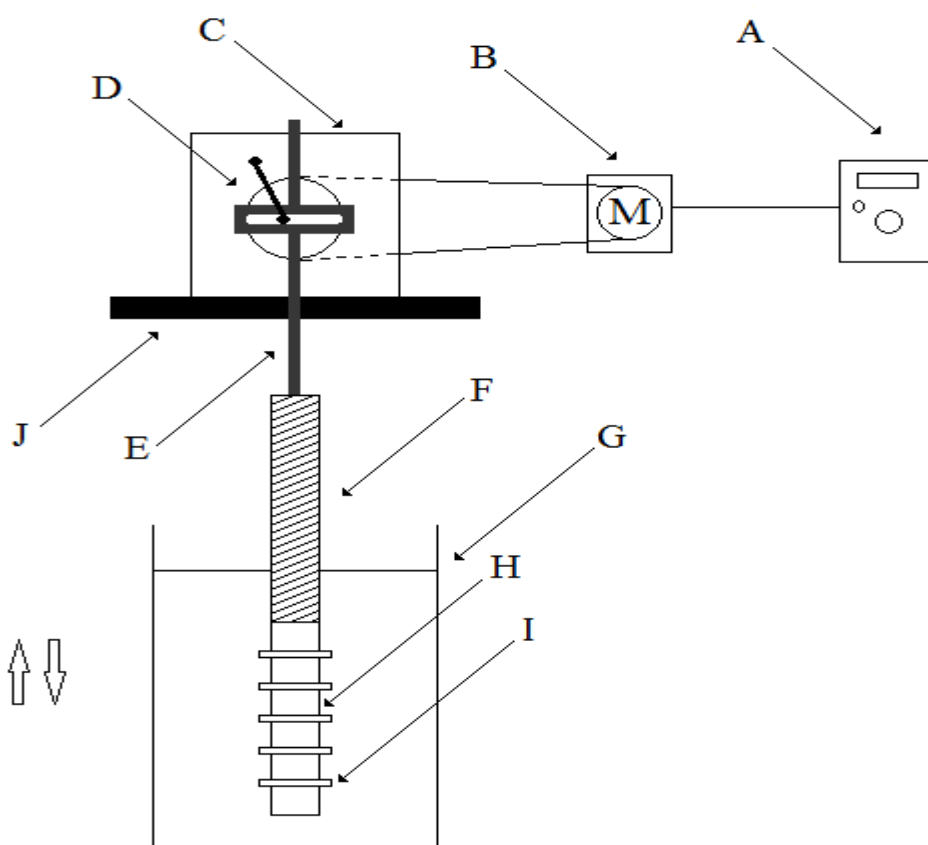
Fig (1-a) shows the experimental setup used in the present study. It consisted of the mechanical vibrator and the reactor. The reactor is composed of a plexiglass cylinder (G) of diameter 15 cm and height of 25 cm. A Zinc cylinder (H) of diameter 2.5 cm and height of 12 cm was placed in the center of the reactor at height of 3 cm from the bottom of the reactor. The Zinc cylinder was fitted with plexiglass ribs (I) of different diameters (heights) ranged from (0.5 to 1.5) cm and the spacing between them ranged from (2 to 4) cm as shown in Fig (1-b). The reciprocating Zinc cylinder was connected to the mechanical vibrator (C) by a plastic shaft (F) of diameter 2.5 cm and height of 26 cm. The plastic shaft was connected to the vibrator through crank shaft (E). Vibratory motion was induced to Zinc cylinder by means of mechanical vibrator. The mechanical vibrator consisted of a disc (D) rotated by means of an electrical motor (B) and was fixed on a stationary holder (J). The rotating motion of the disc was transferred into a reciprocating motion by means of a crank shaft connected to the disc at a distance from its center. The frequency of vibration was changed by inverter (A) to display rpm connected to the electrical motor. The amplitude was adjusted by adjusting the distance between the rotating disc center and the point of its connection with the crank shaft.

2.2. Procedures

The rate of cementation of Copper on Zinc was determined by measuring the change in concentration of Copper ions with time. Before each run, 3 L of fresh Copper sulfate solution were placed in the vessel; in the meantime, the solution was subjected to vibrational motion at the required vibration intensity. Before each run, Zinc cylinder was pickled in 10% HCl to remove any oxide layer, washed with distilled water and dried. Experiments were conducted for 40 minutes. Each 5 minutes a sample of 5 ml was withdrawn at different vibration intensities. Experiments were carried out at temperature 25 ± 2 °C. The samples were analyzed by Iodometry method [13]. The solution viscosity and solution density used in data correlation were measured by an Ostwald viscometer and density bottle respectively [14]. Diffusivity of CuSO_4 solution was obtained from the literature [15]. Table (1) shows a summary of the investigated parameters and their ranges. pH was fixed at 5.4 ± 0.1 during all the runs.

Table (1) a summary of all investigated parameters and their ranges

Studied parameter	Range
-------------------	-------



Initial Copper concentration, ppm	500- 3177
Frequency, rpm	200- 600
Amplitude, cm	0.5- 2
Rib height, cm	0.5- 1.5
Distance between ribs, cm	2- 4
Concentration of PEG 400, ppm	100- 300
Concentration of CTAB, ppm	100- 300

Fig (1-a) Experimental Setup

(A, inverter; B, electrical motor; C, mechanical vibrator; D, rotating disc; E, crank shaft; F, plastic shaft; G, plexiglass cylinder; H, Zinc holder.)
 cylinder; I, plexiglass ribs; J, stationary holder.)

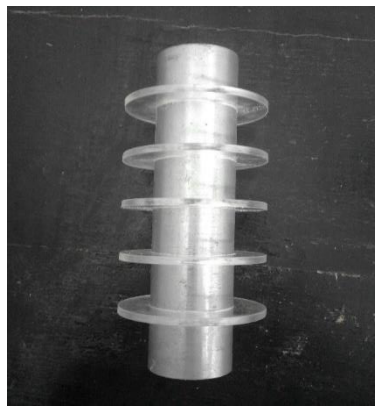


Fig (1-b) Zinc cylinder fitted with rib height of 1 cm and at spacing of 2 cm

3. Results and Discussion

The batch reactor design equation was used for calculating the mass transfer coefficient (K) [9].

$$V_s \ln C_0/C = KAt \quad (1)$$

Where V_s is the solution volume; C_0 and C are initial concentration of Copper ions and the concentration at any time t respectively; A is the active area of the oscillating Zinc cylinder; t is the time of reaction. The above equation is the integrated form of the material balance on active species equation of the batch reactor, namely

$$-V_s dC / dt = KAC \quad (2)$$

Fig (2) shows a typical plot of $\ln (C_0/C)$ versus time at different vibration intensity. The present data fit the first order kinetic model to a great extent. This trend is in consistence with previous studies [16].

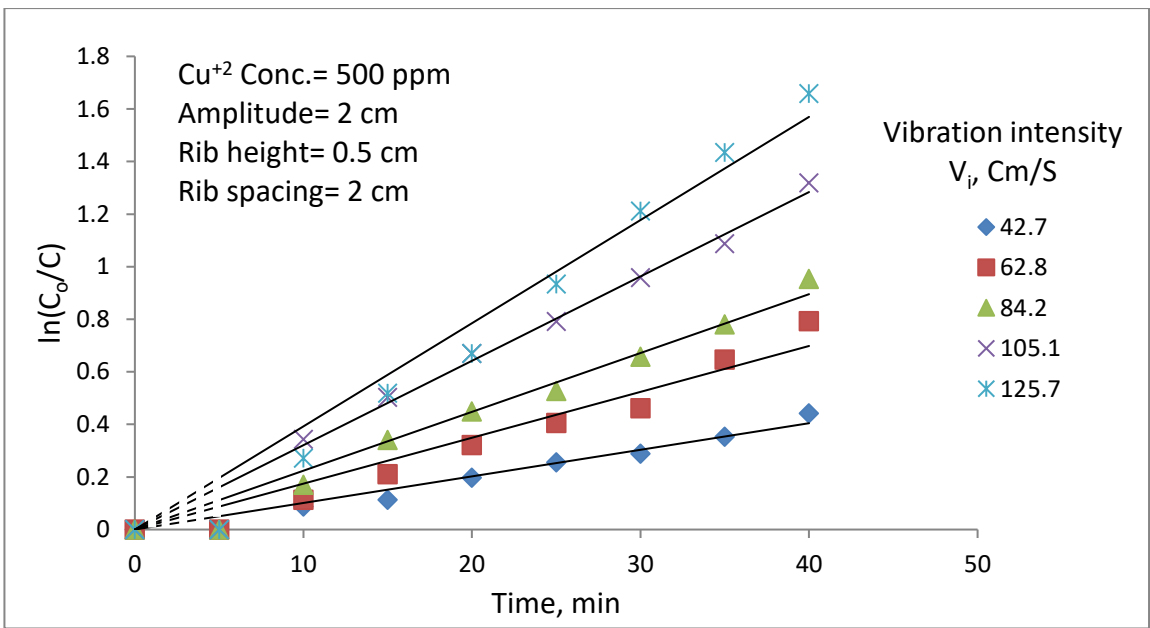


Fig (2) $\ln(C_0/C)$ vs. time at different vibrating intensities

3.1. Effect of initial Copper ions concentration

Fig (3) shows the effect of the intensity of vibration on the mass transfer coefficient at different initial Copper ions concentrations. It is well observed that the mass transfer coefficient increases with increasing initial Cu^{+2} ions concentration up to 1000 ppm, however the mass transfer coefficient declines with further increase of initial Cu^{+2} ions beyond 1000 ppm. The increase in the mass transfer coefficient may be attributed to the fact that a thin porous layer of deposited Copper ions formed on Zinc surface which increase surface roughness leading to increase in the rate of mass transfer. This porous layer allows Copper ions to diffuse through it to react with Zinc [17][18]. However the subsequent decrease in the mass transfer coefficient is attributed to the following causes: (i) during cementation, a denser solid porous layer of metallic Copper is formed on the surface of Zinc cylinder which inhibits the rate of cementation by virtue of increasing the resistance to Cu^{+2} diffusion towards the Zn surface, (ii) as the concentration of Cu^{+2} ions in solution increases interionic attraction forces between ions increase with a consequent decrease in the diffusivity of Copper ions [5][19][20], (iii) when increasing initial Copper ions concentration, the viscosity of solution increases [21], with a consequent decrease of Cu^{+2} ions diffusivity according to Stock's- Einstein equation ($D\mu/T$) [22].

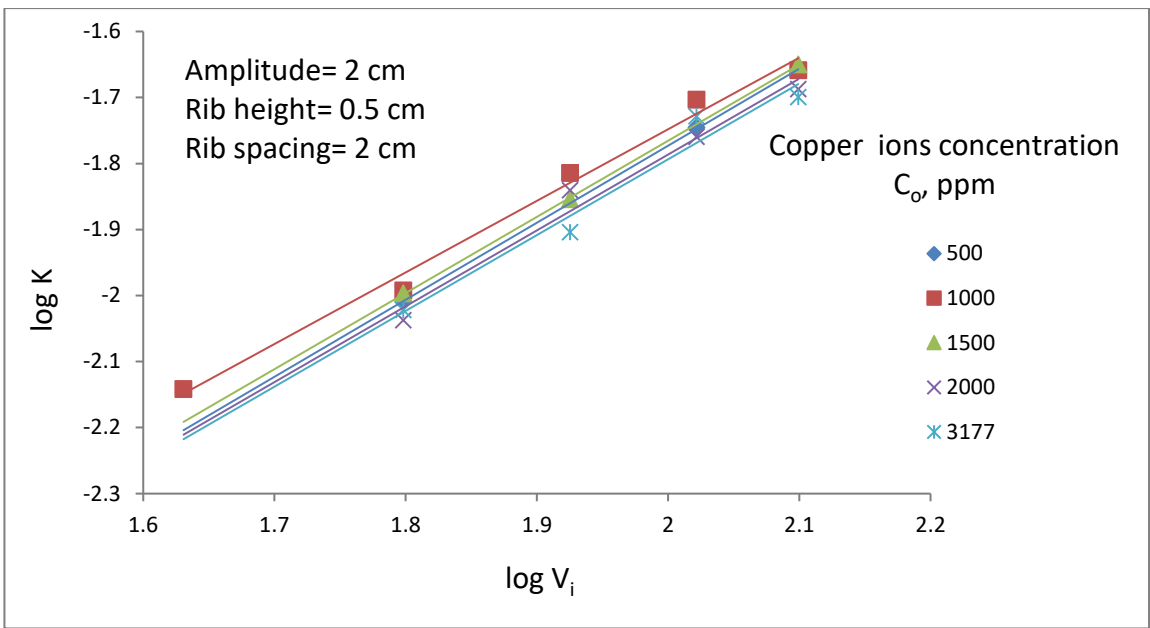


Fig (3) log K vs. log V_i at different Copper ions concentrations

3.2. Effect of frequency and amplitude (vibration intensity)

Fig (4) shows the effect of frequency (rpm) on the mass transfer coefficient at different amplitudes (a). The mass transfer coefficient increases by increasing both amplitude and frequency (vibration intensity) V_i (V_i = a (2πf)). The increase in the mass transfer coefficient with increasing frequency and amplitude of oscillation may be ascribed to the fact that cylinder oscillation gives rise to oscillatory flow in the form of large recirculating eddies along the height of the cylinder [23]. This oscillatory flow reduces the thickness of the hydrodynamic boundary layer and the diffusion layer at the cylinder surface and enhances the rate of mass transfer consequently (K=D/δ) [9][8].

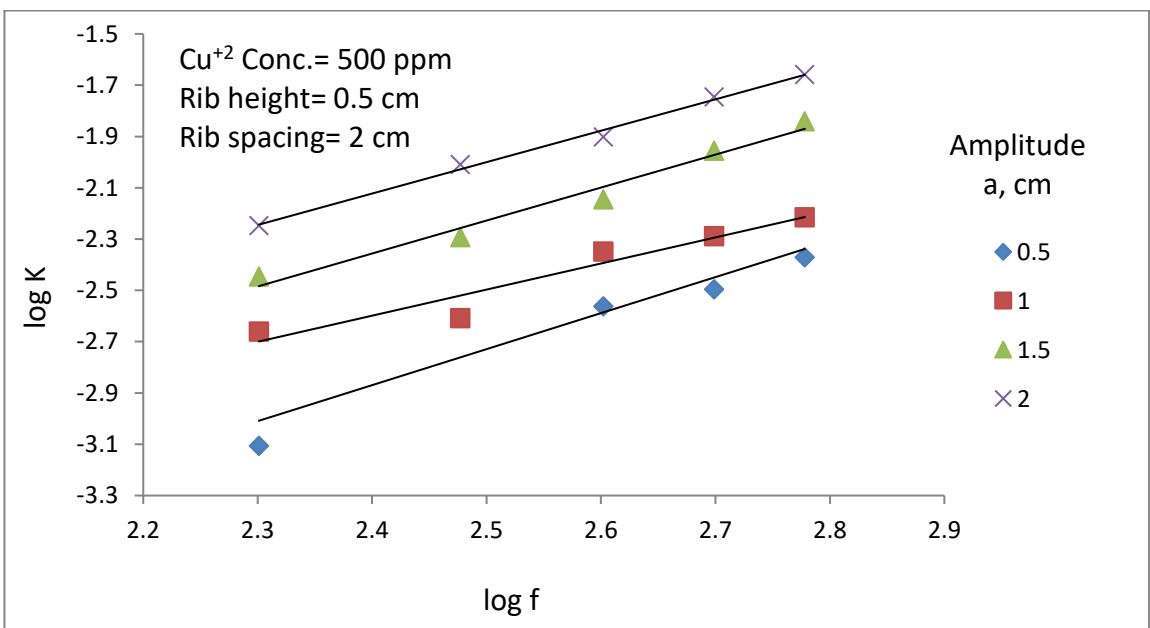


Fig (4) Effect of frequency of vibration on the mass transfer coefficient of copper cementation at different amplitude

3.3. Effect of turbulence promoters

Fig (5) shows log K versus log V_i in presence and absence of ribs. The data show that higher mass transfer coefficient is obtained in case of oscillating Zinc cylinder with ribs than in case of oscillating Zinc cylinder without ribs at the same vibration intensity. This trend may be ascribed to that the presence of ribs lead to flow separation at its surface with a consequent eddy formation. These eddies decrease the hydrodynamic and diffusion boundary layer and enhance the rate of mass transfer. In addition, the presence of ribs inhibits the formation of a continuous boundary layer at the Zinc surface with a consequent increase of its thickness along the Zinc cylinder height in contrast to the case of Zinc cylinder without ribs, where a continuous boundary layer is formed along the height of Zinc cylinder. Table (2) shows the enhancement ratio ($K_{\text{with ribs}}/K_{\text{without ribs}}$) at different vibration intensity. The enhancement ratio varies from 1.09 to 1.38 depending on the vibration intensity at rib height= 0.5 cm and rib spacing= 2 cm.

Table (2) the enhancement ratio at different vibration intensity

V_i, cm/s	42.73	62.83	84.2	105.13	125.66
Enhancement ratio	1.09	1.09	1.1	1.13	1.38

The modest increase in the rate of cementation in the presence of TP indicates that cylinder vibration plays a dominant role in enhancing the rate of diffusion controlled cementation. Despite the modest role of turbulence promoters, it would be of interest to optimize their dimensions. Figs (9,10) show the effect of TP separation and TP height on the rate of cementation.

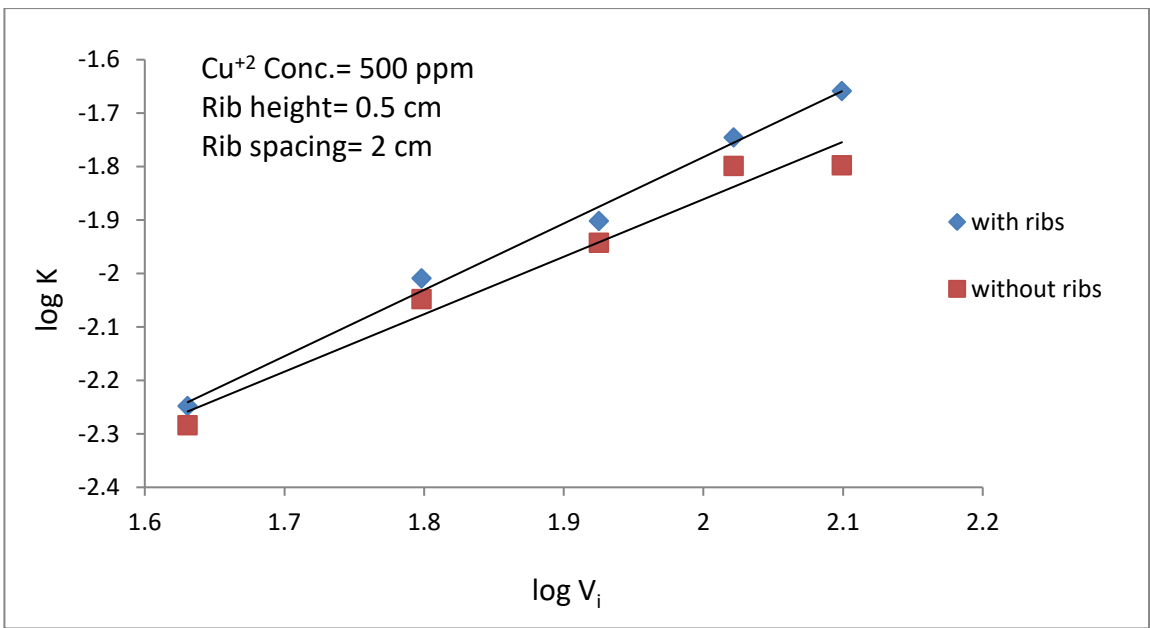


Fig (5) log K vs. log V_i for Zinc cylinder with ribs and without ribs

The rate of mass transfer at a stationary vertical surface is controlled mainly by natural convection, where the difference in density between the Copper sulfate solution near the Zinc surface and that in the bulk induces natural convection [24]. To check the accuracy of the experimental setup, the free convective mass transfer for stationary smooth non-vibrating Zinc cylinder was measured. Figs (6,7) show the effect of vibration compared to non-vibrating smooth Zinc cylinder, and the effect of vibration and turbulence promoters compared to non-vibrating smooth Zinc cylinder. Fig (8) show the relation between the intensification factor (K_v/K_o) and ($K_{v,r}/K_o$) Vs. Re_v where K_v is the mass transfer coefficient obtained by vibration without ribs, K_o is the mass transfer coefficient obtained for stationary smooth Zn cylinder and $K_{v,r}$ is the mass transfer coefficient obtained by vibrating the ribbed Zn cylinder. Table (3) show the enhancement ratio for vibrating smooth Zn cylinder (K_v/K_o) and for vibrating the ribbed Zn cylinder ($K_{v,r}/K_o$).

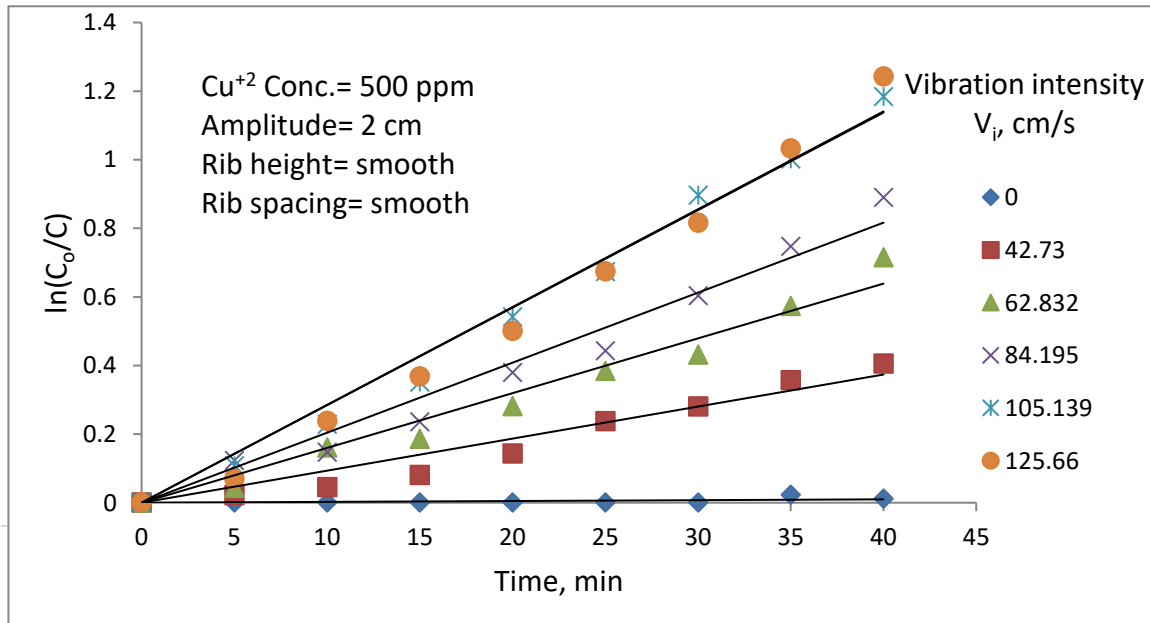


Fig (6) ln (C_o/C) vs. time at different vibrating intensities with natural convection for smooth Zinc cylinder

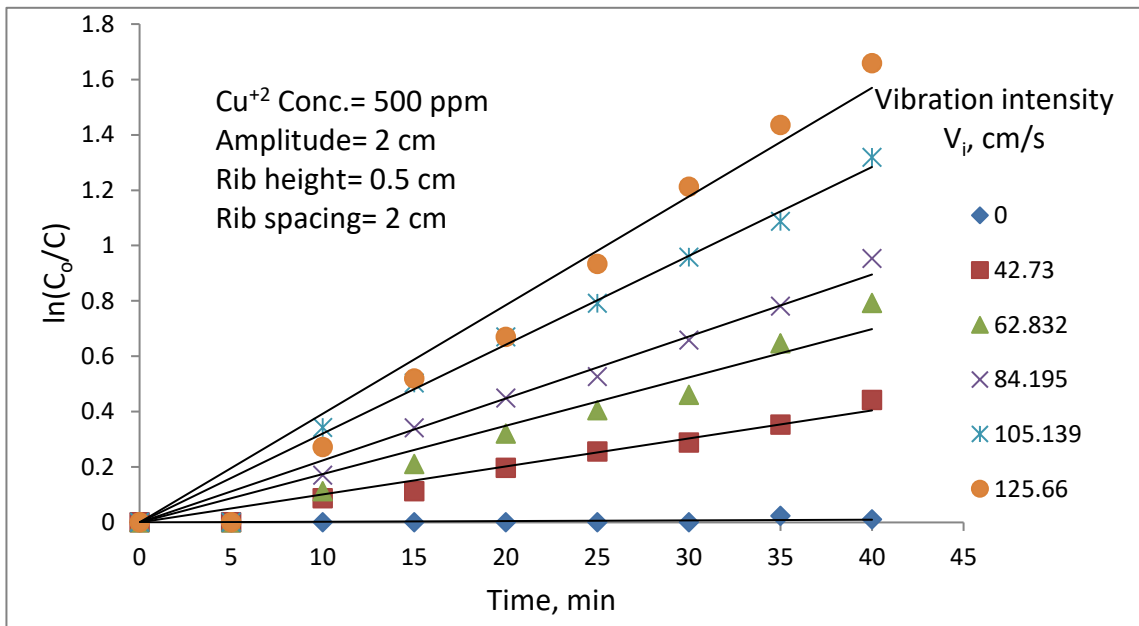


Fig (7) $\ln(C_o/C)$ vs. time at different vibrating intensities with natural convection for ribbed Zinc cylinder

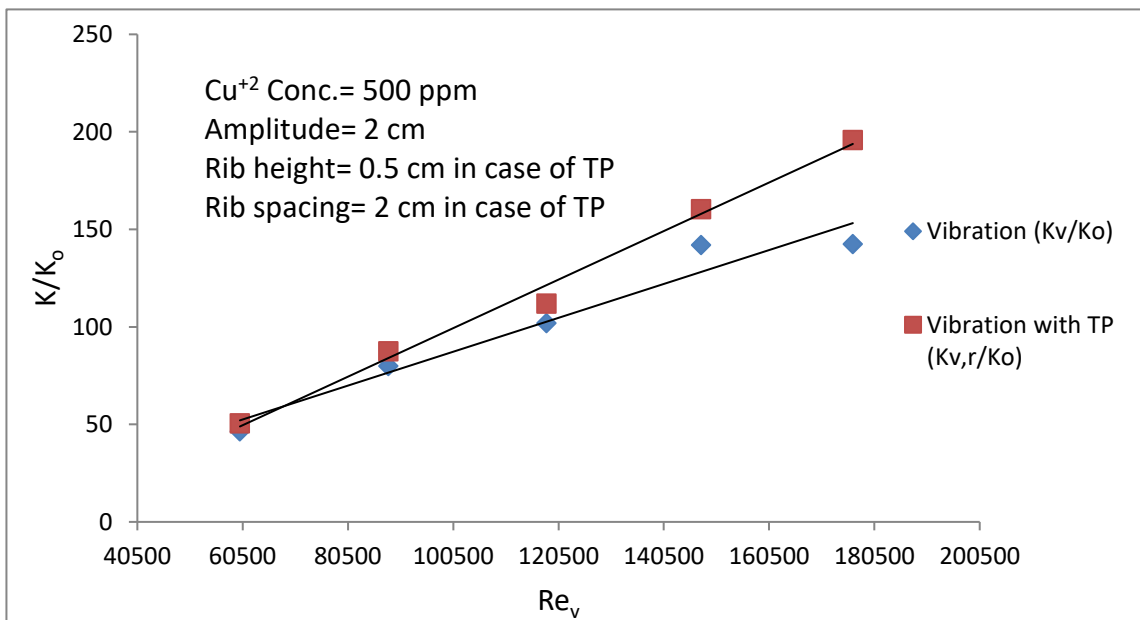


Fig (8) The intensification factor (the enhancement ratio) for vibrating smooth Zinc cylinder and for vibrating ribbed Zinc cylinder

Table (3). the enhancement ratio for vibration and turbulence promoters at different Reynold's number

Re_v	K_v/K_o	$K_{v,r}/K_o$
59985.89	46.47175	50.46931
88205.79	79.95139	87.44683
118195.9	101.938	111.9319
147585.2	141.9137	160.4025
176406	142.4134	195.8809

3.3.1. Effect of ribs spacing

Fig (9) shows the effect of spacing between ribs on the mass transfer coefficient, it is seen that the mass transfer coefficient decreases as the spacing between ribs increases. It seems that as the ribs become more closer, their turbulence promoting ability are counteracted by the increased resistance to the oscillatory flow by virtue of the increased friction between the flow and the ribbed surface which decreases eddy intensity.

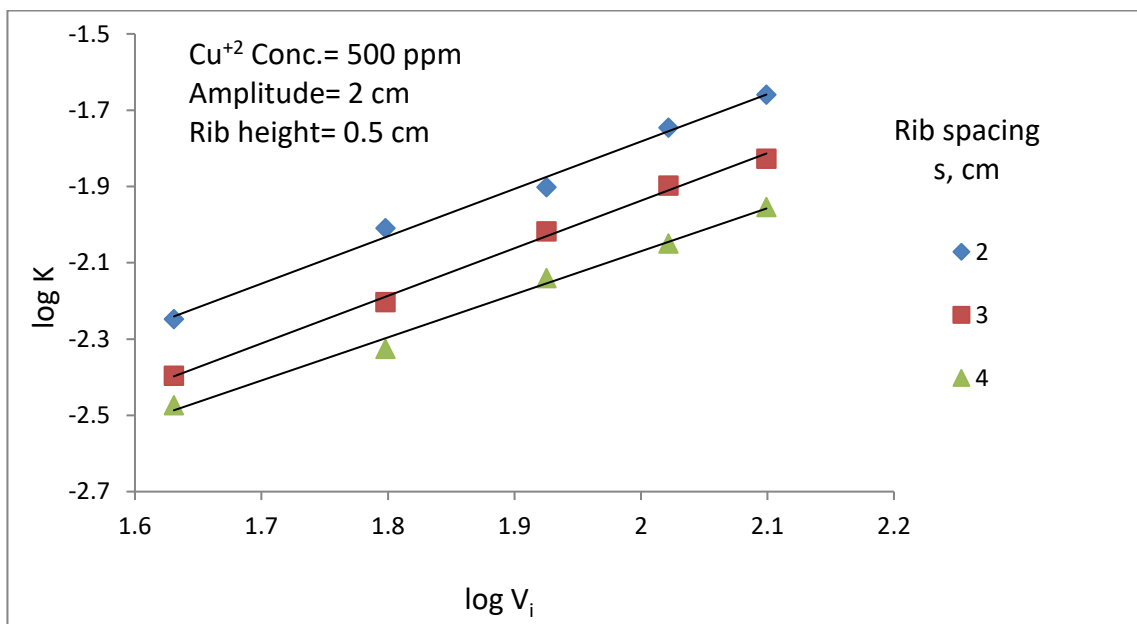


Fig (9) log K vs. log V_i at different ribs spacing

3.3.2. Effect of the ribs height

Fig (10) shows the effect of rib height on the mass transfer coefficient. The data show that the mass transfer coefficient decreases with increasing rib height. The decrease in the mass transfer coefficient with increasing rib height could be attributed to the fact the ability of the rib to promote turbulence is adversely affected by the resistance of the rib to the oscillating flow which increases with increasing rib height, increasing rib height increases the friction between the oscillating flow and the vibrating

cylinder with a consequent decrease in the intensity of the eddies which promote the rate of mass transfer.

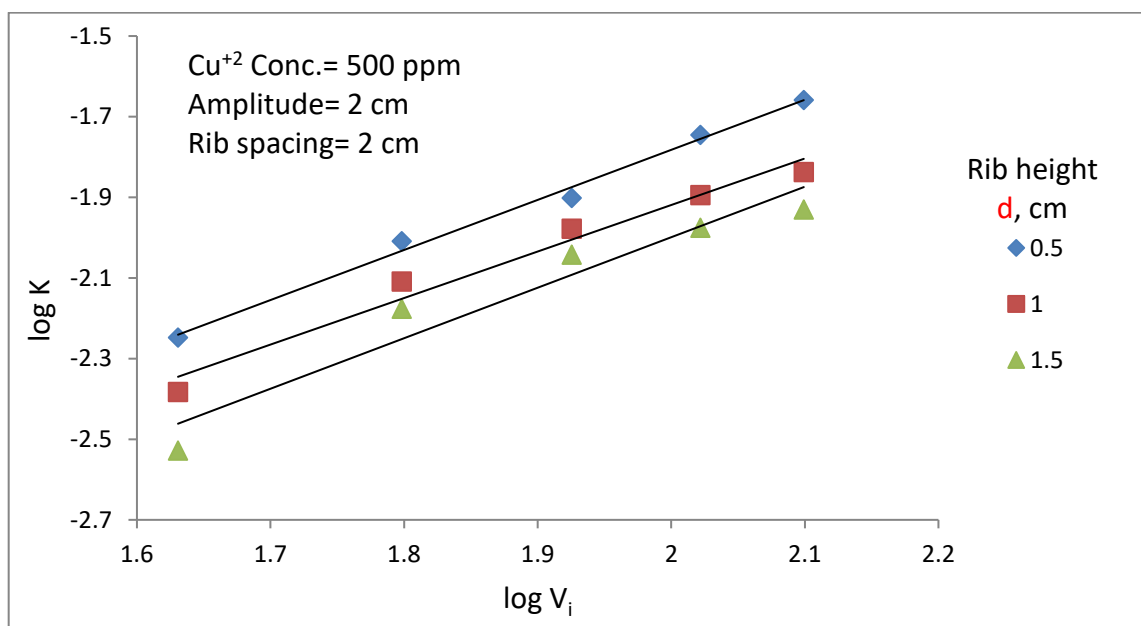


Fig (10) log K vs. log V_i at different rib height.

The present results are consistent with the finding of Gomaa and Al Taweel [24] who studied the effect of vibrating vertical flat plate fitted with TP on the rate of mass transfer by measuring the limiting current of the cathodic reduction of K₃Fe(CN)₆.

3.4. Effect of surface active agents (SAA)

As mentioned earlier SAA may exist in waste water discharged by the electroplating industry where they are used to improve the quality of the electrodeposited metal, these substances may affect the rate of cementation.

Fig (11) shows the effect of adding SAA. It is found that the cementation process is inhibited by addition of surfactants. The percentage of inhibition for the cementation reaction is calculated from the following relation

$$\% \text{ inhibition} = (K - K') / K \times 100 \quad (3)$$

Where K is the mass transfer coefficient for blank solution and K' is the mass transfer coefficient in presence of SAA. Table (3) shows the % inhibition of PEG 400 and CTAB at different concentrations and vibration intensity. It is well noted that the % inhibition ranged from 18.69 to 67.86 % depending on the type of SAA and its concentration [22]. The decrease in the mass transfer coefficient is in the following order; Surfactant free solution > PEG 400 > CTAB.

The decrease in the rate of cementation of Copper ions on Zinc in the presence of PEG 400 and CTAB may be attributed to their tendency to be accumulated and adsorbed at the interface between their

solution and adjacent phases. SAA may cause a stagnant film on the Zn surface that may hinder the convective diffusion across the diffusion layer with a consequent decrease in the rate of mass transfer [18][10].

Table (4) shows the relation between % inhibition and concentration for all SAA

Table (4) % inhibition of PEG 400 and CTAB at different concentrations and vibration intensity

Type of SAA V_i , cm/s	Concentration, ppm					
	PEG 400			CTAB		
	100	200	300	100	200	300
42.73	18.81	20.79	44.55	35.64	43.56	45.54
62.83	27.43	37.14	43.43	52.57	53.71	62.29
84.20	27.68	30.80	30.36	30.80	37.05	49.55
105.13	18.69	37.38	43.61	42.37	52.96	62.62
125.66	29.08	45.66	50.51	50.00	58.93	67.86

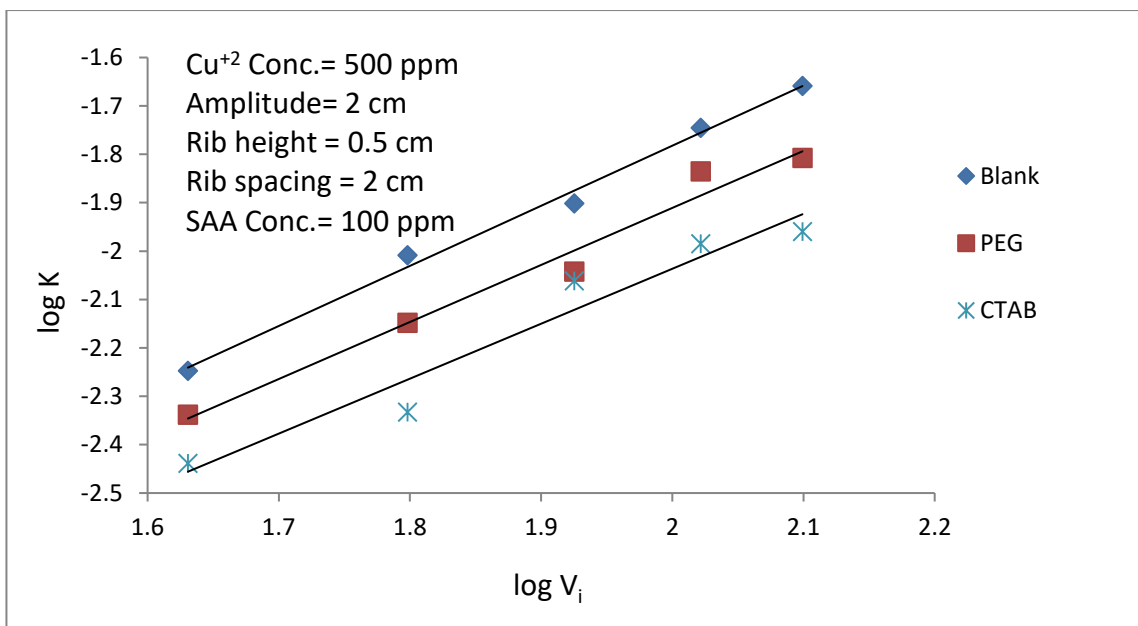


Fig (11) log K vs. log V_i at different types of SAA

Figs (12), (13) show the effect of CTAB and PEG 400 concentration on the mass transfer coefficient. In general, as the concentration of SAA increases, the mass transfer coefficient decreases. This trend is in agreement with previous studies [18][10][22].

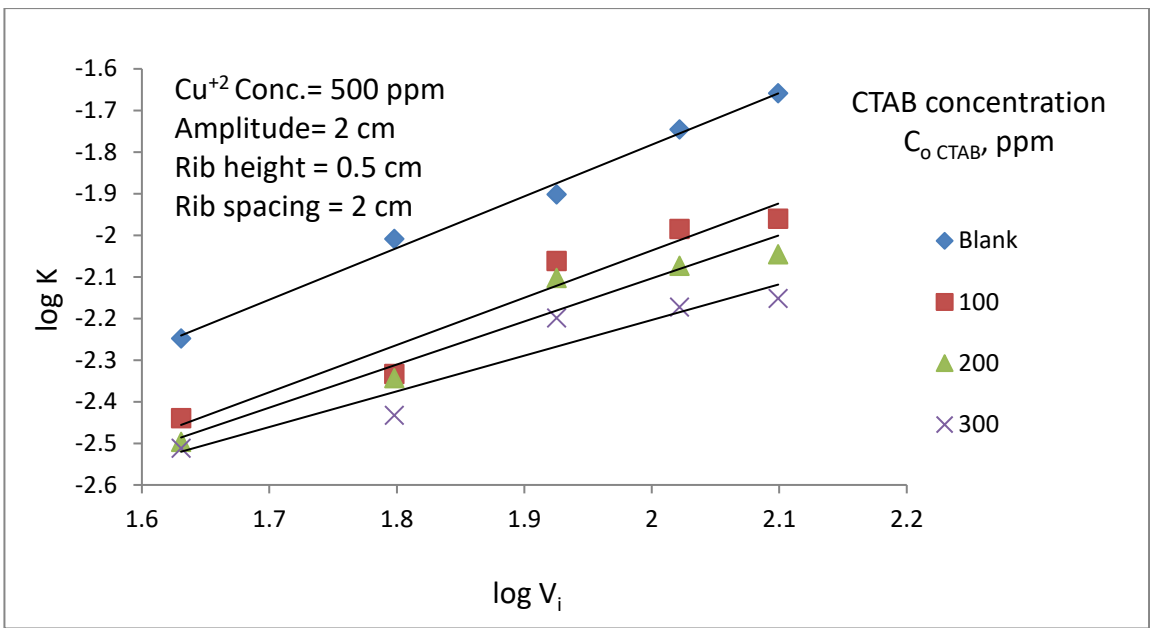


Fig (12) $\log K$ vs. $\log V_i$ at different CTAB concentrations

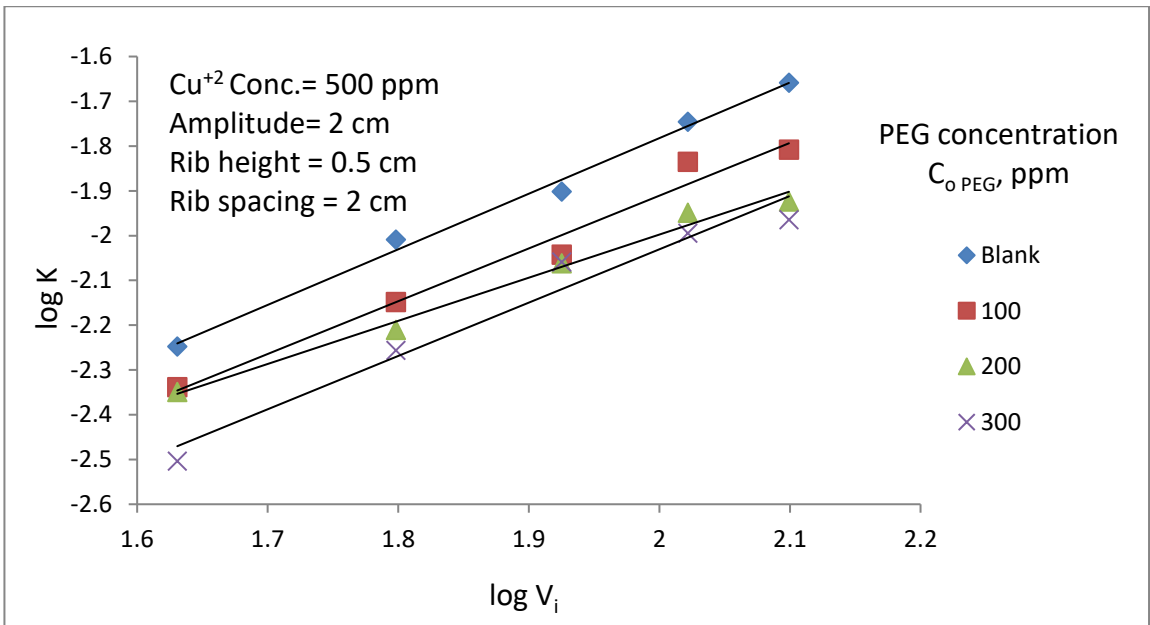
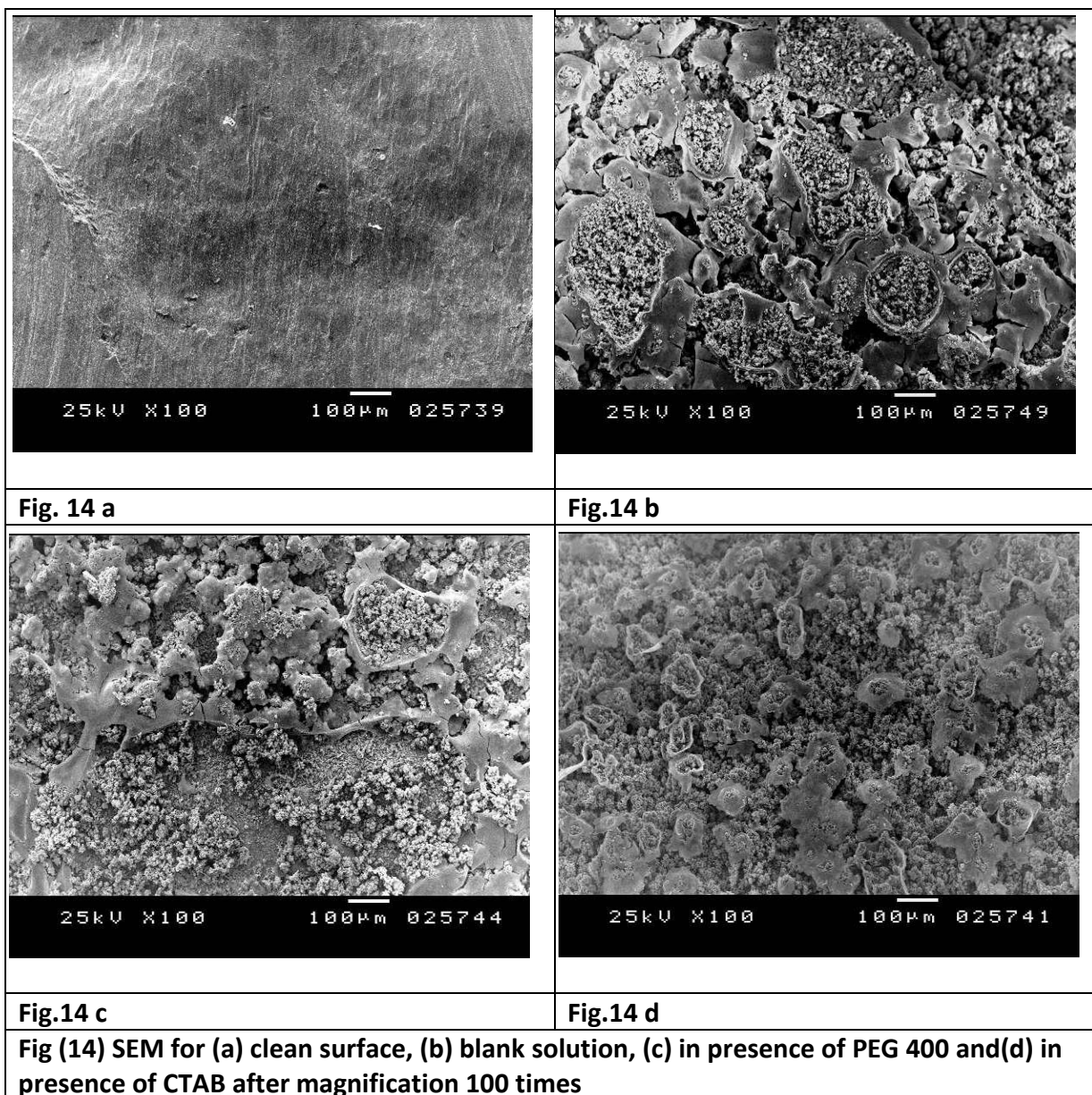


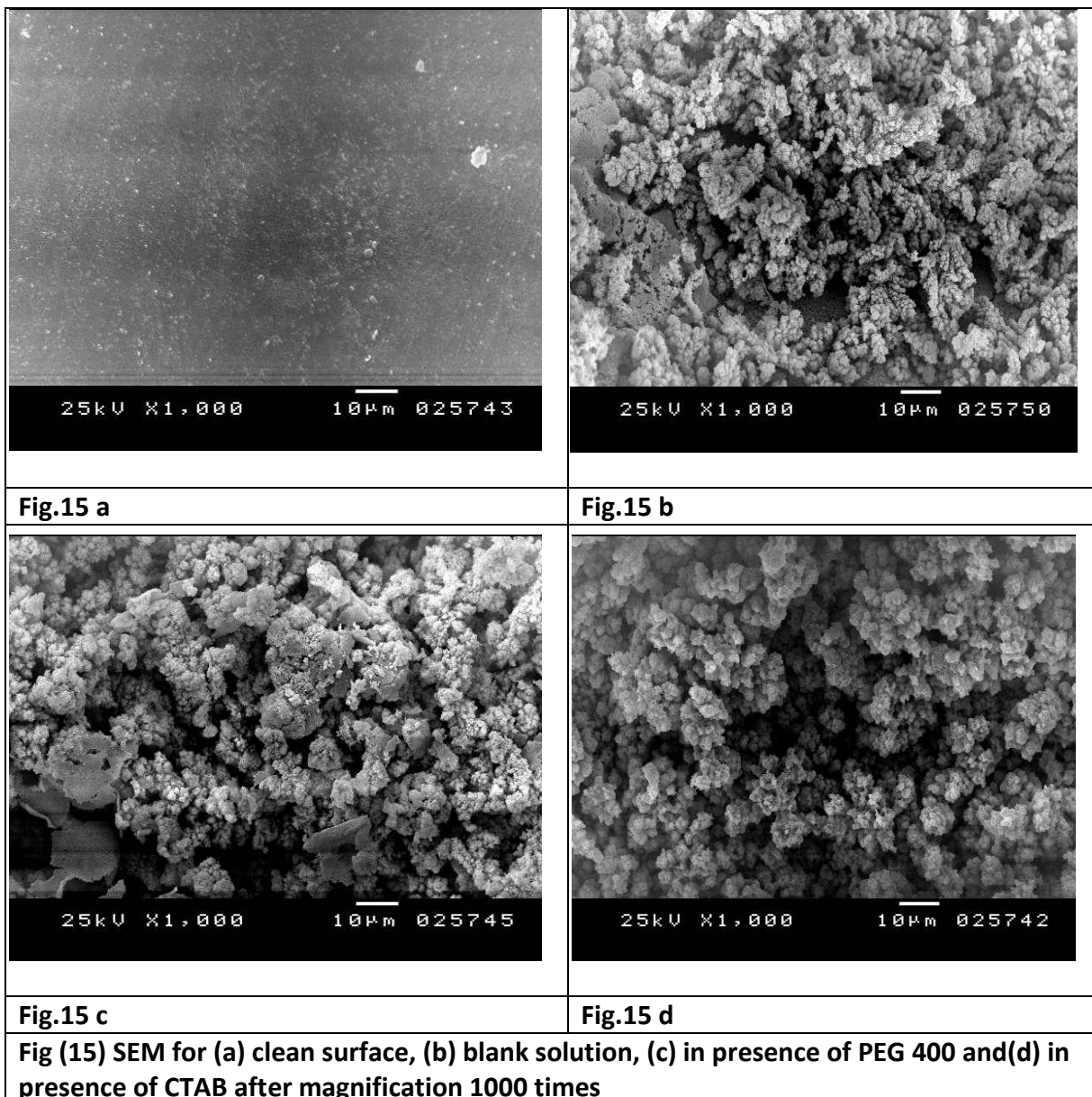
Fig (13) $\log K$ vs. $\log V_i$ at different PEG 400 concentrations

3.5. Morphology study

SEM was used to examine cementation reaction products obtained in the presence and absence of SAA. All experiments conducted at 25 ± 2 °C with a reference concentration of Copper ions concentration= 500 ppm, 400 rpm and amplitude= 2 cm. the concentration of the surfactant was 100 ppm, the time conducted for the experiments was 40 minutes.



Figs (14-a) shows a clear surface of Zinc before cementation process after pickled with 10% HCl and washed with distilled water, which was magnified 100 times. Figs (14-b) (14-c) (14-d) show Zinc surface in absence and presence of SAA (PEG 400 – CTAB) respectively, after magnification 100 times. Fig (14-b) shows the Copper deposit is not blocking the whole Zinc surface, where the gray zone is Zinc surface which did not react. Whereas Fig (14- c&d) show that the Zinc surface is almost blocked by deposit.



Figs (15-a) shows a clear surface of Zinc before cementation process after pickled with 10% HCl and washed with distilled water. Fig (15-b) shows a porous deposit which consists of irregular and non-uniform grains. Fig (15-c&d) shows a denser deposit is formed with grains which is relatively more uniform in size than the blank. A closer look at Fig (15-d) shows a denser and more compact deposit was formed in the case of CTMAB than in the case of PEG 400.

Before adding SAA. The deposit was a film of porous, non-uniform grains distributed randomly, which increase the surface roughness of the deposit, accordingly the rate of mass transfer increases. On the other hand, after adding SAA, the deposit starts to be less porous, compact uniform grains and more denser layer which results in reducing the surface roughness of the deposit and reducing the rate of mass transfer. However, in the presence of CTAB, the inhibition of Copper cementation was higher than that in presence of PEG 400. This may be attributed to that the deposit tends to be more

compact, more denser, non-porous and more uniform than in the presence of PEG 400, as a result the surface roughness of the deposit was reduced significantly. A similar results were obtained in previous study with Triton X-100 and CTAB [18].

3.6. Mass transfer data correlation

In view of the turbulence nature of the present hydrodynamic conditions, dimensional analysis was used to correlate the present data. The mass transfer coefficient can be related to the different parameters according to the following equation:

$$K = f(\rho, \mu, D, d_e, V_i, s, d) \quad (4)$$

By using dimensional analysis, the above equation can be written in terms of Sh, Re, Sc, d_e/d and d_e/s dimensionless group as follows

$$Sh = a Re^\alpha Sc^\beta (d_e/d)^\gamma (d_e/s)^\sigma \quad (5)$$

Where a , α , γ and σ are constants, which are determined from the present mass transfer data. The value of β was fixed at 0.33 according to previous studies [9][23].

Fig (18) shows the effect of Re on Sh. The Sh can be related to Re according to the following equation

$$Sh \propto Re^{1.19} \quad (6)$$

Whereas Fig (16) shows the effect of (d_e/d) on Sh. The Sh can be related to (d_e/d) according to the following equation

$$Sh \propto (d_e/d)^{0.45} \quad (7)$$

Whereas Fig (17) show that Sh can be related to (d_e/s) according to the following equation

$$Sh \propto (d_e/s)^{0.91} \quad (8)$$

Fig (18) shows that the present data for the conditions $14993 < Re < 176406$, $1374 < Sc < 1593$, $8.3 < d_e/d < 25$ and $3.1 < d_e/s < 6.3$ fit the equation:

$$Sh = 0.0001 Re^{1.19} Sc^{0.33} (d_e/d)^{0.45} (d_e/s)^{0.91} \quad (9)$$

With an average deviation of $\pm 12.3\%$. Also equation (9) can also be written in the form of:

$$K = 0.0001 \rho^{0.86} V_i^{1.19} d_e^{1.55} \mu^{-0.86} D^{0.67} d^{-0.45} s^{-0.91} \quad (10)$$

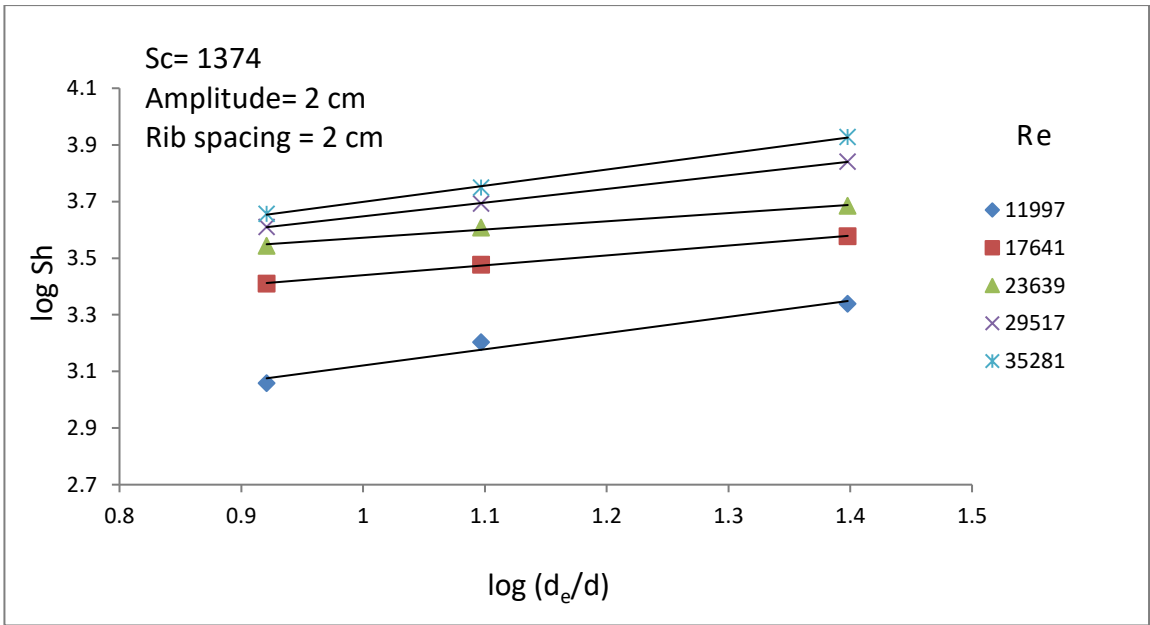


Fig (16) log Sh vs. log (d_e/d) at different Re

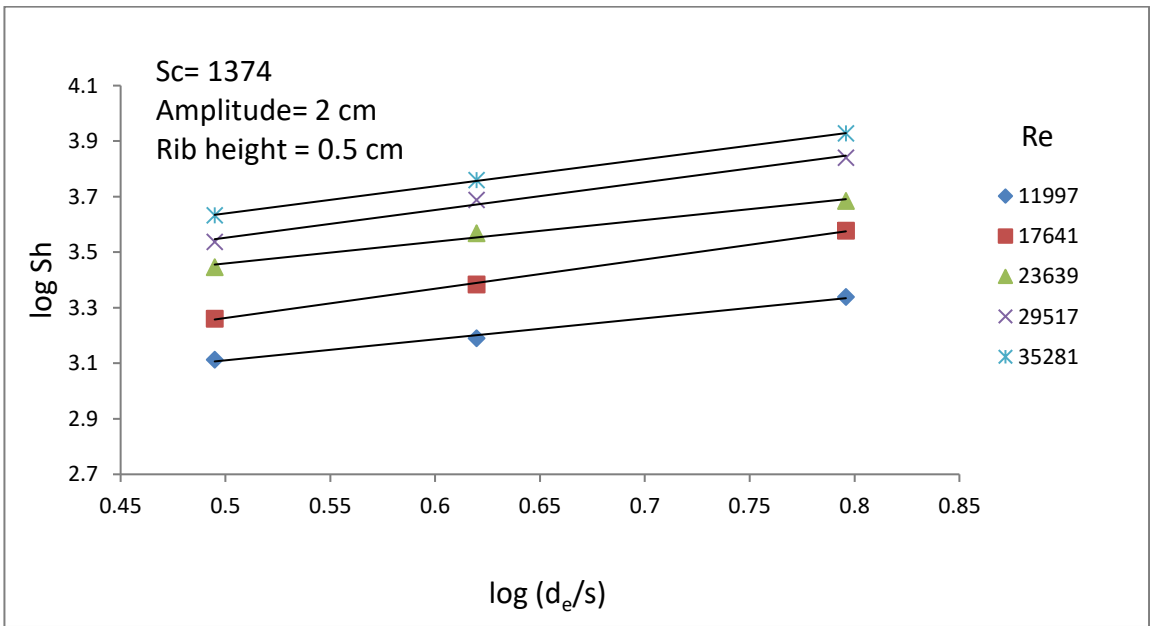


Fig (17) log Sh vs. log (d_e/s) at different Re

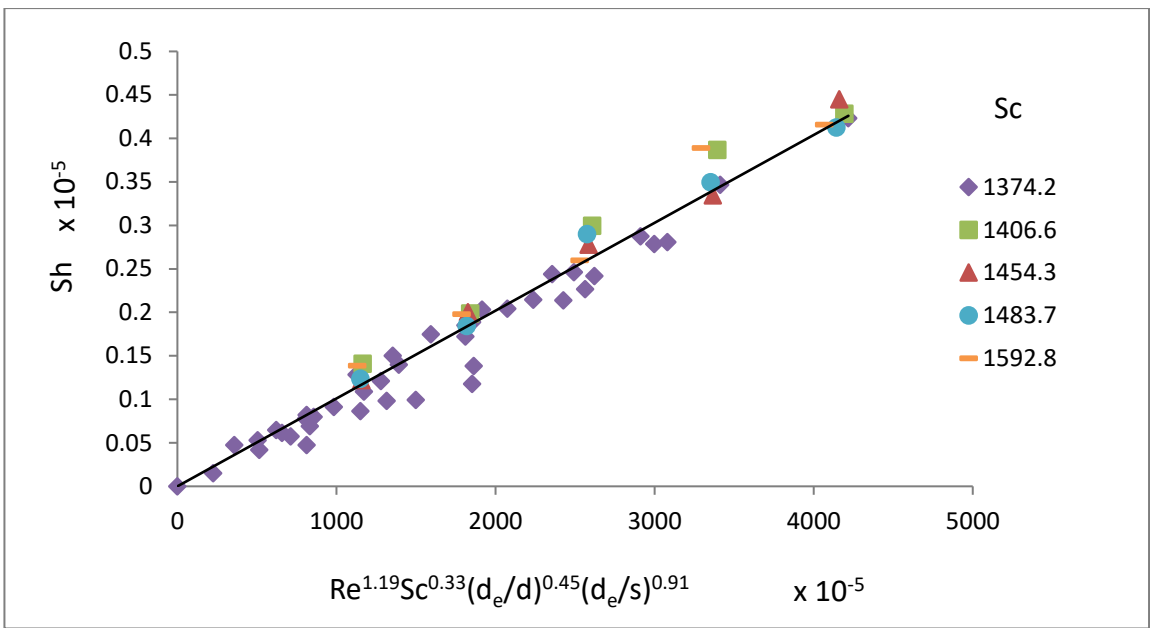


Fig (18) Overall mass transfer correlation for the cementation of Copper on oscillating Zinc cylinder fitted with turbulence promoters

4. Conclusion

The results obtained show that vibratory agitation is a powerful tool for increasing the rate of diffusion controlled cementation. Copper ions could be effectively removed from synthetic wastewater stream by cementation using oscillating Zinc cylinder fitted with non-active plastic turbulence promoters. The mass transfer coefficient was found to depend mainly on the vibration intensity, height of turbulence promoter and spacing between turbulence promoters. With increasing the initial concentration of Copper ions, the mass transfer coefficient increases with increasing concentration up to 1000 ppm then with further increasing in initial concentration the mass transfer decreases. With increasing the vibration intensity through increasing frequency and amplitude of the mechanical vibrator, the mass transfer coefficient also increases. But increasing the height of turbulence promoters and increasing the spacing between turbulence promoters show a decrease in the mass transfer coefficient. The results obtained in this investigation show that the best conditions for turbulence promoters are 0.5 cm for the TP height and 2 cm for the spacing. All variables affecting the rate of cementation were correlated in terms of dimensionless mass transfer equation which can be used in the design and operation of the suggested reactor. The effect of adding SAA has been studied. The study showed that adding SAA inhibits the mass transfer coefficient, when increasing the concentration of SAA the inhibition increases. SEM was used to examine cementation reaction products obtained in the presence and absence of SAA. The results of SEM emphasized the obtained results.

List of symbols

- a Amplitude, cm
- A Active area for oscillating Zinc cylinder, cm²

C	Concentration at any time, ppm
C _o	Initial concentration, ppm
d	Height of TP, cm
d _e	Equivalent diameter for annulus, cm
D	Diffusion coefficient, cm ² /s
f	Frequency, rpm
K	Mass transfer coefficient, cm/s
K'	Mass transfer coefficient in presence of SAA, cm/s
Re	Reynolds number ($\rho V_i d_e / \mu$)
s	Spacing between TP, cm
Sc	Schmidt number ($\mu / \rho D$)
Sh	Sherwood number ($K d_e / D$)
t	Time, s
T	Temperature, k
V _i	Vibrating intensity, cm/s
V _s	Solution volume, cm ³
μ	Solution viscosity, g/cm.s
ρ	Solution density, g/cm ³
δ	boundary layer thickness

References

- [1] J.-F. Silvain, A. Veillère, Y. Lu, Copper-Carbon and Aluminum-Carbon Composites Fabricated by Powder Metallurgy Processes, *J. Phys. Conf. Ser.* 525 (2014) 12015. doi:10.1088/1742-6596/525/1/012015.
- [2] M. Samim, N.K. Kaushik, A. Maitra, Effect of size of copper nanoparticles on its catalytic behaviour in Ullman reaction, *Bull. Mater. Sci.* 30 (2007) 535–540. doi:10.1007/s12034-007-0083-9.
- [3] N.K. Amin, E.-S. El-Ashtouky, O. Abdelwahab, Removal of copper powder from aqueous solution by cementation using an agitated vessel, *Environ. Technol.* 35 (2014) 1208–1218. doi:10.1080/09593330.2013.865062.
- [4] A. Ekmekyapar, M. Tanaydin, N. Demirkiran, Investigation of copper cementation kinetics by rotating aluminum disc from the leach solutions containing copper ions, *Physicochem. Probl. Miner. Process.* 48 (2012) 355–367.
- [5] N.K. Amin, E.S.Z. El-Ashtoukhy, Kinetic study of copper cementation onto zinc using a rotating packed bed cylindrical reactor, *Can. J. Chem. Eng.* 89 (2011) 609–616. doi:10.1002/cjce.20443.
- [6] B. Dönmez, F. Sevim, H. Sarac, A kinetic study of the cementation of copper from sulphate solutions onto a rotating aluminum disc, *Hydrometallurgy.* 53 (1999) 145–154.
- [7] Y.J. Hsu, M.J. Kim, T. Tran, Electrochemical study on copper cementation from cyanide liquors

using zinc, *Electrochim. Acta.* 44 (1999) 1617–1625.

- [8] A.H. El-Shazly, A.A. Mubarak, H.A. Farag, A.G. Fadl, Improving the rate of Cu²⁺ recovery from industrial wastewater using a vertical array of reciprocating perforated zinc discs, *Alexandria Eng. J.* 54 (2015) 71–76. doi:10.1016/j.aej.2014.10.002.
- [9] A.A. Mubarak, A.H. El-Shazly, A.H. Konsowa, Recovery of copper from industrial waste solution by cementation on reciprocating horizontal perforated zinc disc, *Desalination.* 167 (2004) 127–133.
- [10] M.A. Zarraa, Effect of surface-active substances on the rate of production of copper powder from copper sulphate solutions by cementation on zinc rods in gas sparged reactors, *Hydrometallurgy.* 41 (1996) 231–242. doi:10.1016/0304-386X(95)00058-O.
- [11] M. Arousseau, N.T. Pham, P. Ozil, Effects of ultrasound on the electrochemical cementation of cadmium by zinc powder, *Ultrason. Sonochem.* 11 (2004) 23–26. doi:10.1016/S1350-4177(03)00130-5.
- [12] K. Tojo, K. Miyanami, H. Mitsui, Vibratory agitation in solids-liquid mixing, *Chem. Eng. Sci.* 36 (1981) 279–284. doi:10.1016/0009-2509(81)85006-3.
- [13] A.I. Vogel, *Vogel's Text Book of quantitative Inorganic Analysis*, 3rd ed., Longmans, London, 1961. doi:10.1016/0160-9327(90)90087-8.
- [14] R.H. Perry, C.H. Chilton, S.D. Kirkpatrick, *Chemical Engineering Handbook*, 4th ed., McGraw-Hill, New York, 1963.
- [15] D.G. Miller, J.A. Rard, L.B. Eppstein, R.A. Robinson, Mutual Diffusion Coefficients, Electrical Conductances, Osmotic Coefficients, and Ionic Transport Coefficients *ij* for Aqueous CuSO₄ at 25 °C, *J. Solution Chem.* 9 (1980) 467–496.
- [16] E.Z. El-ashtoukhy, M.H. Abdel-aziz, Removal of copper from aqueous solutions by cementation in a bubble column reactor fitted with horizontal screens, *Int. J. Miner. Process.* 121 (2013) 65–69. doi:10.1016/j.minpro.2013.03.001.
- [17] A.H. Konsowa, Intensification of the rate of heavy metal removal from wastewater by cementation in a jet reactor, *Desalination.* 254 (2010) 29–34. doi:10.1016/j.desal.2009.12.018.
- [18] A.A. Taha, S.A.H.A. El-ghani, Effect of surfactants on the cementation of cadmium, *J. Colloid Interface Sci.* 280 (2004) 9–17. doi:10.1016/j.jcis.2004.07.023.
- [19] N.K. Amin, E.S.Z. El-Ashtoukhy, O. Abdelwahab, Rate of cadmium ions removal from dilute solutions by cementation on zinc using a rotating fixed bed reactor, *Hydrometallurgy.* 89 (2007) 224–232. doi:10.1016/j.hydromet.2007.07.007.
- [20] Y.A. Eltaweel, E.M. Nassef, R.A. Hazza, Recovery of Copper from Wastewater by Cementation Technique, *World Environ.* 4 (2014) 199–205. doi:10.5923/j.env.20140405.01.
- [21] R.M. Lamy, L. Lorenzen, A study of factors influencing the kinetics of copper cementation during atmospheric leaching of converter matte, *J. South African Inst. Min. Metall.* 105 (2005)

21–28.

- [22] M. El-batouti, Removal of copper metal by cementation using a rotating iron cylinder, *J. Colloid Interface Sci.* 283 (2005) 123–129. doi:10.1016/j.jcis.2004.08.185.
- [23] A.H. El-Shazly, A.A. Mubarak, H.S. Bamufleh, Improving the Diffusion Controlled Cementation of Cadmium Ions Using Reciprocating Fixed Bed of Zinc Rings, *Defect Diffus. Forum.* 312–315 (2011) 694–699. doi:10.4028/www.scientific.net/DDF.312-315.694.
- [24] H.G. Gomaa, A.M. Al Taweel, Intensification of inter-phase mass transfer : the combined effect of oscillatory motion and turbulence promoters, *Heat Mass Transf.* 43 (2007) 371–379. doi:10.1007/s00231-006-0110-1.

A Model Of New Polishing Process to Fused Deposition Modeling Parts

Eng. Mohamed Adel ^{a, *}, Prof. Abu Bakr Nasr^a, prof. AboelMakaram Khalil ^a

^a Department of Mechanical Engineering, Assiut University, Assiut, 71516, Egypt

*The corresponding author:

E-mail address: m.a.abdelhakeem@aun.edu.eg, Tel: +201007379579, Fax: +20 88 2335572

Abstract:

The present paper presents a heat transfer model to a new polishing process that smoothens the surface of products manufactured by fused deposition modeling (FDM) technology. FDM is one of the most common additive manufacturing techniques which, unfortunately, results in very rough surfaces when compared to similar technologies. This high roughness results from the stepped surface (stair like surface) caused by the technology nature of depositing several 2D layers to form the final 3D product. To smooth the surface, it is heated up till melting which trigger surface tension force to smooth the surface. To achieve surface melting, the surface is exposed to a localized hot air jet with certain temperature and velocity from a moving nozzle with appropriate translational velocity; this introduces three main process parameters: air jet temperature, air jet velocity and air nozzle translational velocity over the product surface. Two analytical heat transfer models were derived using

different process parameters and proved to be in agreement with each other. Also, a part of the obtained experimental results verifies model results. Moreover, the effect of entrained air on the heated jet was considered in the model. It can be concluded that we have an analytical model fits the experimental one and represents the modeled process.

Keywords: FDM, modeling of polishing process, hot air, impinging jet, Surface Roughness

List of symbols:

d_i	inner diameter of annular nozzle	Nu	The local Nusselt number, the dimensionless convective heat transfer
L_W	The plane wall half thickness	Nu_{aver}	The value of average Nusselt number mentioned by [6].
L	The distance in z direction between the nozzle face and the impinged surface	\overline{Nu}_R	The average Nusselt over a circular area of dimensionless radius R. $\overline{Nu}_R = \frac{\overline{h}_{av} \cdot L_c}{K_{air}}$
L_c	Characteristic length, for pipe flow it equal D of the pipe	\overline{h}_{av}	Average convective heat transfer value over area of R=1.8
d_o	The outer diameter of annular nozzle	m_{sur}	The fused or melted mass from the part surface
R	Dimensionless radial distance, $R = \frac{r}{d_i}$, r is the radial distance	ν	Kinematic viscosity of air
$A_{1.8}$	The circular area over dimensionless R=1.8	η^*	The dimensionless jet temperature at parts surface with the definition of Hollworth and Wilson
α	Thermal diffusivity, $\alpha = \frac{k}{\rho \cdot C_p}$		

1. Introduction:

FDM is the most common additive manufacturing technologies owing to its low cost simple fabrication technique and ability to manufacture complicated 3D closed contour parts. The technology deals with wide range of polymer base material which found its way in industrial application and may also non-polymer materials under research phase like ceramic or metal. Its manufacturing process is extruding a semi molten material from a nozzle carried in a 3-axis automated machine. FDM machine manufactures parts by extruding a semi-molten filament material through a robotically controlled nozzle in machine head; the nozzle heats and extrudes the material while the machine head is moving to deposit the layers of the part, see fig.1.

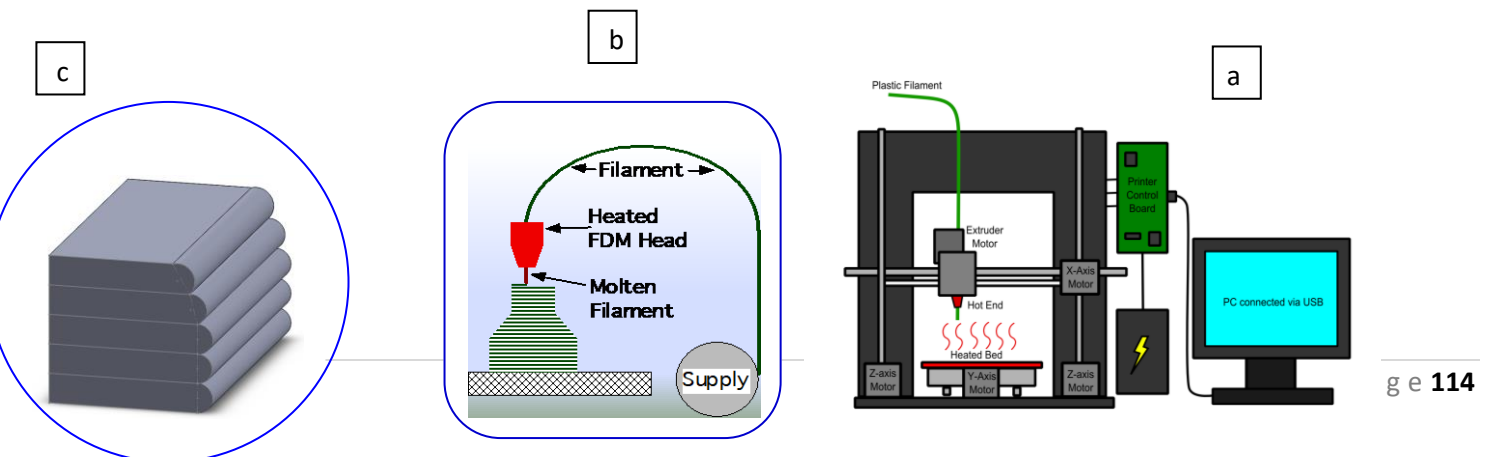




Figure 1: description of FDM technology (a) the machine [17] (b) the nozzle within manufacturing (c) the resulting surface roughness

Owing to this layer wise manufacturing technique, a stair like surface will result and this effect is the source of the elevated roughness which additive manufacturing characterized with, see fig.1b. Unfortunately, FDM has high product roughness between additive technologies [1] and a post-processing (machining) Method are generally employed for smoothing FDM parts.

The investigated post-processing technique employs mainly a heat transfer process where a hot air jet impinges the surface of FDM parts in order to melt locally the surface (the outer layer) - Figure 2 shows a schematic and experimental result of this polishing process. Melting triggers surface tension force which flattens the surface and finally leaves it smoother after naturally cooled down in free air. In a microscopic scale, the surface stairs will collapse to fill or heel the gaps in between these melted stairs.

The technique is similar to laser polishing which generally employed to smooth hard alloys with a significant roughness reduction. The difference between the two techniques is that laser heats surfaces up by radiation while hot air employs convection. Also, the polished materials for laser are metal or ceramic alloys while it is polymer material for hot air (material of FDM parts). The process requires impinging a jet of hot with proper temperature and velocity. In order to provide continuous machining, the hot air nozzle moves with a proper translational velocity over the surface that is lower enough to cause melting. Similar to laser polishing, it was also found that much lower nozzle velocity cause overheating and surface deterioration. In other hand, high nozzle velocity causes insufficient heating and no smoothening to the surface and hence, proper tuning to the process parameter is required. Another important point is that the process response depends to several parameters and a prediction to process behavior is required when a change in process parameters or part material is introduced.

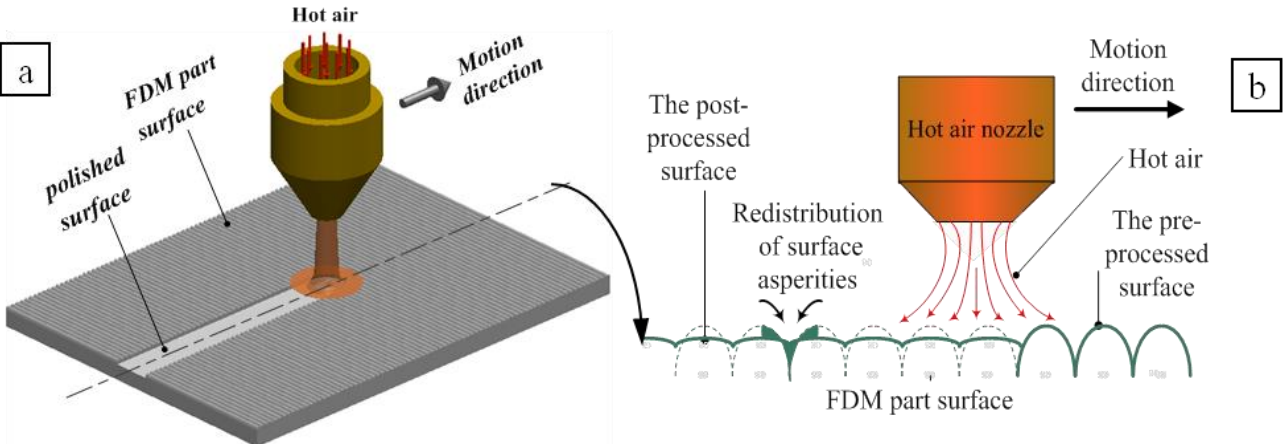


Fig. 2: (a) 3D general description of the polishing process (b) 2D description of finishing phenomena at line shown- a sintering phenomenon

Also air polishing will provide lower machining cost and safer processing condition for possible manual applications. For impinging jet application, the process generally can deliver a surface density of thermal power transfer rate up to $1\text{Gw}/\text{m}^2$ [2] like in cooling of turbine blade making the process applicable in this process. The hot air heating process has its potentials over using laser process as the process has low initial cost. Also the most appropriate laser used in polymer based materials as our technology is CO_2 laser owing to its appropriate absorptivity (wavelength $\approx 10600\ \mu\text{m}$) and so less reflectivity, but it has low efficiency (a common value 15%) in its high voltage power supply which may make hot air processing more safe and probable efficient solution -as will be seen- especially if used with amateur application.

Fortunately, FDM uses low melting material (polymer materials) making the method applicable. Furthermore, beside surface tension force, additional forces related to the developed process help moving (flattening) the fused stair tips to the corresponding valleys around which are stagnation pressure/force and shear flow force that help flattening the surface.

Impinging of hot air jet is a forced convection heat transfer problem. Its main input output parameter is jet exit velocity and the corresponding convective heat transfer coefficient respectively. The jet impinges the FDM part surface with a certain temperature as an input. With a certain convective heat transfer coefficient (h) and at certain temperature, the surface takes an optimum amount of time (or optimum nozzle translation velocity) to be heated to melting. When surface melting is reached, the effect of different forces stated appears naturally and redistribution to its topography happens leaving the surface smoother as shown in see [fig.2a](#).

2. Modeling of the finishing process:

[Figure 1c](#) shows the surface profile of the parts manufactured by FDM process. At the surface of the product, the stairs appear physically which can be recognized by eye in real world. The polishing process intended to melt the shell of the FDM product surface. Melting will be achieved by exposing the surface to a hot air jet. The jet is impinged to the surface with proper temperature and velocity and for a certain appropriate exposure time (certain nozzle velocity). [Figure 3](#) shows a description of model parameters.

The process model starts with a heated jet exit from a nozzle opening and then, passes through a stagnant fresh air for certain distance till impinges the processed surface for a certain amount of time (or velocity). This time (or the corresponding velocity) is the time required to melt a certain amount of material from the surface. In this study, the investigated parameters will be jet temperature, jet

velocity, and processing time/velocity. This process sequence is investigated in the three following sections: heat transfer of impinging jet, entrainment effect on heated jets, and a convenient heat transfer model of the polishing process. The following two sections will investigate the equations describing these stages beginning from determining the convective heat transfer of the jet and the jet temperature at part surface. The result of these two sections will be feed to the third one which is a 2-D transient –forced convection heat transfer model. The third section will and the required processing time/velocity based on two transient –forced convection heat transfer models.

2.1 Heat transfer from the impinging jets:

Impinging jet is an advanced topic in heat transfer and less amount of work presented to determining the dimensionless heat transfer coefficient (Nu number). The process contains different process parameters including type of flow, nozzle shape, fluid type, surrounding conditions, nozzle configurations and hard to be determined in generalized equation form. This section handles the circular impinging jet (CIJ) while Figure 3a process parameters for CIJ. CIJ is simply generated from a nozzle with circular cross section (pipe type). CIJ is the common type between impinging jets owing to its simple nozzle section and high resulting Nusselt number over small area. On the negative side, almost all experimental studies presented in CIJ are using non laminar flow application or related to certain fluid or conditions which is not our case [3]–[5]. Turbulence flow results to high stagnation pressure which may deteriorate the polished surface upon melting. ; Hence, only laminar flow

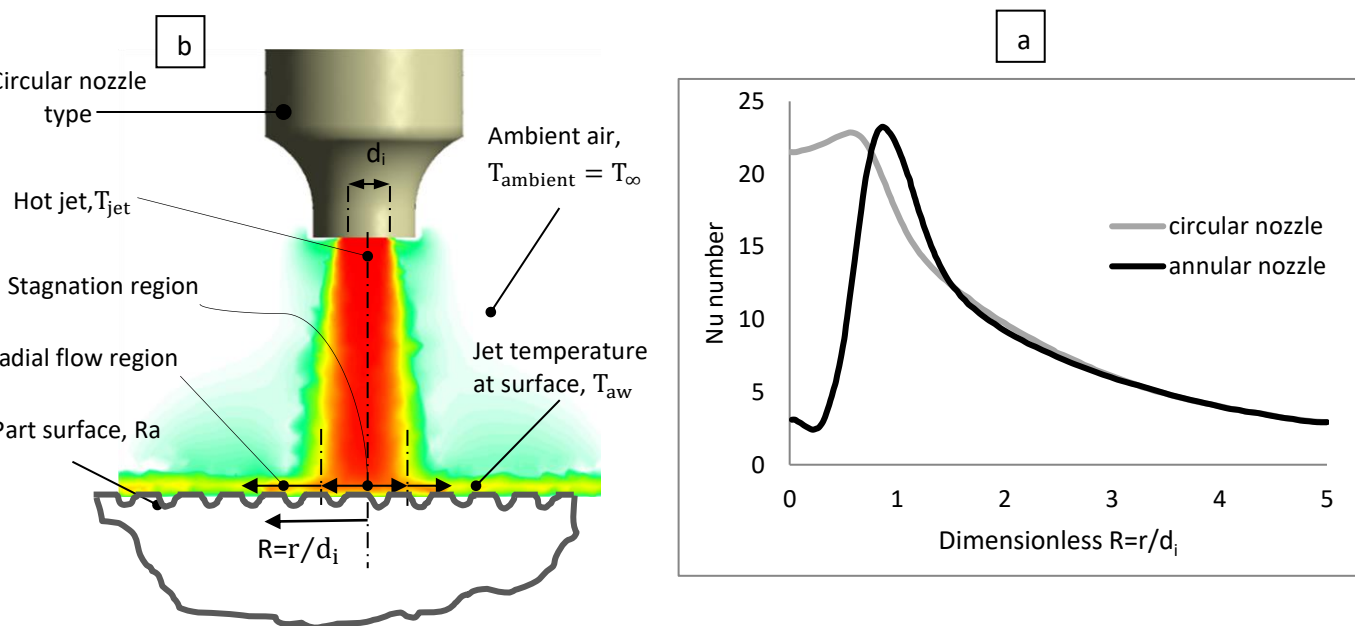


Figure 3: (a) the parameters of circular impinging jet (b) Nu number for annular jets at different Re number, (regenerated with permission from Elsevier publisher with license number 3699481203810)

will be employed in the study. [Greene et al \[3\]](#) (chapter 2) presents a good review for CIJ and provides analytical for laminar flow (based on laminar flow theories), but it employs either uniform surface temperature or uniform heat flux which is not our case.

[Chattopadhyay \[6\]](#) presents the most related study to our model conditions. The study presents a numerical results for CIJ compared with annular impinging jet in the resulting Nusselt number for an investigated domain of $R=5d_i$. the study reported Nu values for from 250 up to 1000. [Figure 3b](#) shows the data obtained from [Chattopadhyay](#) for AIJ and CIJ. It can be noted that the average Nusselt values given in the study calculated by $Nu_{aver} = \frac{1}{R} \int_0^R Nu. dr$. To obtain the average Nu value over circular area of radius $R=r/d_i$, we calculated $\overline{Nu}_R = \frac{2}{R^2} \int_0^R Nu. r. dr$. [Table1](#) contains the \overline{Nu}_R values for different Re number integrated numerically over the area of interest of $R= 1.8$; this area is about the double of the stagnation region which is about at $R= 0.9$ at [figure 3a](#); also, this area was considered as the heat-affected zone while Nu values at radius larger than $R=1.8$ will be small and usefulness for melting and will be omitted. [Table 1](#) also shows the [Chattopadhyay](#) results and the calculated numerical results provided with the best fit equations.

[Chattopadhyay](#) model conditions are jet height "h" -from impinged surface - is two times the characteristic length ($L_c = 2d_i$). Also, the ambient temperature is equal to jet temperature (cooling process) and/or no entrainment effect. Also uniform velocity gradient in the output from the nozzle was assumed. Our model will follow up the

Table1: results of Nusselt number with Reynolds number before and after perform numerical integration to the result given in [\[6\]](#) using our operating parameter.

Reynolds number	The study result		the numerically calculated results		
	Circular	Difference ratio	Annular	Circular	Difference ratio
	$Nu_{aver} = \frac{1}{R} \int_0^R Nu. dr, R=5d_i$		$Nu_{aver} = \frac{2}{R^2} \int_0^R Nu. r. dr, R=1.8d_i$		
1000	10.16	19.6%	15.7	7.2%	
500	6.88	21.4%	11.5	9.6%	
250	4.49	25.6%	8.1	16.7%	
Best fit curve	---	---	$\overline{Nu}_{1.8} = 0.584Re^{0.4774} (1)$		---

study conditions assuming it prevails except the two conditions that $T_j = T_\infty$ (or cooling process) and the other condition that the effect of "entrainment effect" is neglected – as investigated in the following.

2.2 Entrainment effect:

When an impinging jet crosses its nozzle opening to a stagnant medium, an amount of fresh air entrained with the perimeter of the jet. [Figure 4](#) presents a schematic to the phenomenon. This mix between the ambient fresh air and the high jet temperature causes decrease in jet temperature when reached to part surface for both axial and radial flow directions. When the jet cuts longer distance in the ambient, the entrainment effect becomes more significant and so, the nozzle exit temperature is no longer the actual processing temperature.

[Jambunathan et al \[7\]](#) presents a review in entrainment effect. A dimensionless jet parameter -named effectiveness- is studied to indicate jet actual temperature at any axial and radial position. These studies state that effectiveness is independent to Reynolds number and jet temperature. Also, the effectiveness is near unity (approximate no change in jet temperature) at small apparent distance between nozzle and target surface – length to diameter ($L/d_{noz.}$) <4 . For larger apparent distances $L/d_{noz.}$, the effectiveness in stagnation region become significant for larger $L/d_{noz.}$ while radial flow region, it is still independent on all values $L/d_{noz.}$. Moreover, the value of resulting Nu number is independent to the temperature difference between jet and ambient air. [Goldstein \[8\]](#) presents a correlation of (η^*) by Hollworth and Wilson definition as:

$$\eta^* = \frac{T_{aw} - T_{\infty}}{T_{jet} - T_{\infty}} \cong 0.38 + 0.6e^{-0.01(\frac{L}{d_i}-2)^{2.2}-0.1(r/d_i)^{2.5}} \quad (2)$$

And hence, the average effectiveness value over the studied area of $R=1.8$ will be:

$$\bar{\eta}_{av}^* = \frac{\bar{T}_{aw} - T_{\infty}}{T_j - T_{\infty}} = \frac{2}{(r/d_i)^2} \int_0^{r/d_i=0.1.8} \eta^* \cdot \left(\frac{r}{d_i}\right) \cdot d\left(\frac{r}{d_i}\right) = 0.879 \quad \text{where } \frac{L}{d_i} = 2, r/d_i = 1.8 \quad (3)$$

The value of $\bar{\eta}_{av}^*$ in [eq.3](#) was used to obtain the average jet temperature over the polished surface with respect jet exit temperature T_j . This temperature will be feed to the model at [section 2.3](#).

2.3 heat transfer models of the Polishing process:

This section will presents the employed heat transfer models to use to model the process. As previously state, laser Polishing is the closest process to our developed one; it is more commonly applied in metal based additive manufacturing technology [\[9\]](#), [\[10\]](#). [Figure 4](#) illustrates the similarities between laser and air polishing processes.

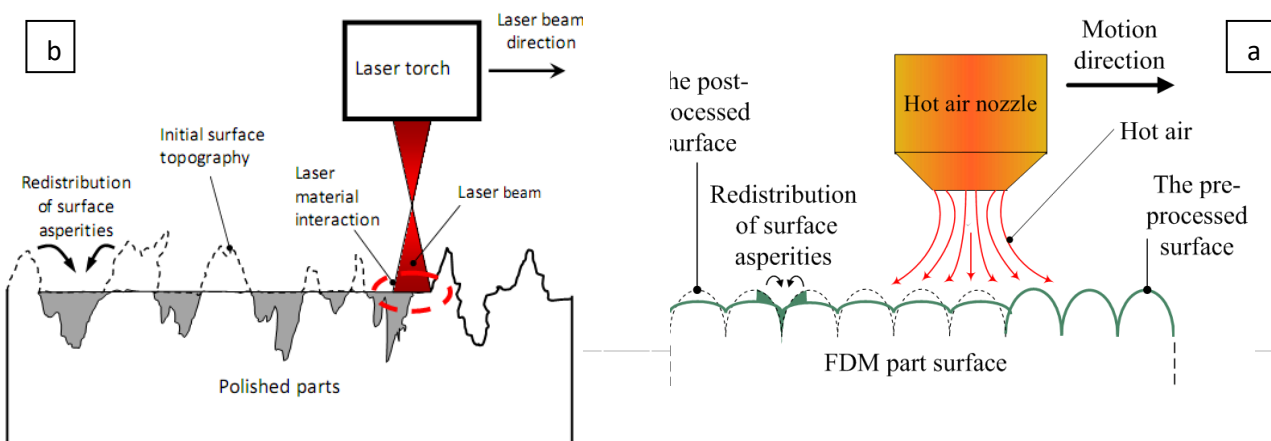


Figure 4: comparison between the developed polishing process in (a) and laser polishing process in (b).

This similarity helps developing the model with guidance to similar studies in laser polishing process. [Bordatchev et al \[11\]](#) represent a review to the process including the modeling studies. He concluded that almost all were based on some of the classical theories developed for heat transfer by conduction. [Ramose et al \[12\]](#) presents an analytical model laser polishing process to selective laser sintering processed parts (SLS). The SLS technology is one of additive manufacturing technology with similar characteristics to the used one. For the analytical model, the studies present an energy balance equation for laser beam where a part of energy input in the surface will melt and superheat a certain mass from surface and the other part of energy will heat up another amount of surface material but below melting temperature. In our process, the surface will pass with the same sequence with the aid of impingement of hot air instead of laser. [Sections 2.1 and 2.2](#) presents the equivalent Nu number (the convective heat transfer) and air jet temperature at the surface respectively. This section will determine the third parameter which is the processing time (or the corresponding velocity) to melt the surface. This processing time is required to melt the outer microscopic layer which contains the staircase (the rough topography). This processing time is the required to heat up the surface to melting (t_{heating}) and the time required for phase change of the surface to liquid ($t_{\text{phase change}}$) as in [eq. 4](#).

$$t_{\text{processing}} = t_{\text{heating}} + t_{\text{phase change}} \quad (4)$$

The term $t_{\text{phase change}}$ depends on thickness of the molten layer to successfully melt the staircase in this layer. This thickness is about the measured surface roughness value R_a which is extremely small - in order of 1E-6 meter- and hence, the term $t_{\text{phase change}}$ is neglected. Therefore, the term $t_{\text{processing}}$ is reduced to t_{heating} . This time (t_{heating}) can be obtained by solving this transient conduction problem. The best model fits this circumferences is a semi-infinite solid model exposed to temperature of $T_{\infty}=T_{\text{jet}}, \bar{h}_{\text{av}}$. this model fits polymer or insulating materials like earth. the book [\[13\]](#) (chapter5, equation 5.63) presents the model equation as follows:

$$\frac{T(x, t_{\text{heating}}) - T_i}{T_{\infty} - T_i} = \text{erfc}\left(\frac{x}{2\sqrt{\alpha t_{\text{heating}}}}\right) - \left[\exp\left(\frac{\bar{h}_{\text{av}} \cdot x}{k} + \frac{\bar{h}_{\text{av}}^2 \cdot \alpha t_{\text{heating}}}{k^2}\right)\right] \left[\text{erfc}\left(\frac{x}{2\sqrt{\alpha t_{\text{heating}}}} + \frac{\bar{h}_{\text{av}}\sqrt{\alpha}}{k}\right)\right]$$

The value of x is considered zero and α and k is the thermal diffusivity and thermal conductivity of the FDM part material respectively. The model valid within treated part thickness more than the penetration depth δ_p at which $\frac{T_{\delta_p} - T_{\text{surface}}}{T_{\text{initial}} - T_{\text{surface}}} = 0.9$ which is reasonable thickness for polymer materials that has much low thermal diffusivity is the case for FDM material.

The data output from the model will also validated with data results from considering the surface as one dimensional transient conduction problem in plane wall of thickness $2 L_w$ where $\delta_p > L_w$. The model equation is:

$$\frac{T(x, t_{\text{heating}}) - T_{\infty}}{T_{\text{initial}} - T_{\infty}} = \sum_{n=1}^{\infty} C_n \exp(-\zeta_n^2 F_0) \cos(\zeta_n [\frac{x}{L_w}]) \text{ where } C_n = \frac{4 \sin \zeta_n}{2\zeta_n + \sin(2\zeta_n)} \quad (6)$$

Eq.7 [13] (equations 5.63 and 5.42a) is the infinity Fourier series where $F_0 = \frac{\alpha * t_{\text{heating}}}{L_w^2}$.

The thermo-physical properties used in the model (along figure 6, 7) are averaged and presented in table 2 for poly(lactic acid) (PLA). Also, air properties are averaged over it operating temperature. The properties are taken from [14], [15].

Table2: Properties of PLA used. Values are averaged in operating temperature range 35°C to 175°C

Item	Density ($\bar{\rho}$) Kg/m ³	Specific heat (\bar{C}_p) J/Kg.K	Thermal conductivity (\bar{K}) w/m.K	heat of fusion ΔH_m j/kg	Melting temperature T_m °C
PLA	1192	2227	0.205	45000	175

3. Results and discussion:

This section will present the study results divided into two subsections. The first one section presents the obtained results after operating different model equation based on table 2. The second subsection will present the model verification with experimental results based on table 3 after implementing the exact material properties and the actual experiment conditions.

3.1 modeling results:

Using the equations previously presented from 1 through 6, the relation between different process parameter is obtained by the two proposed models. The two

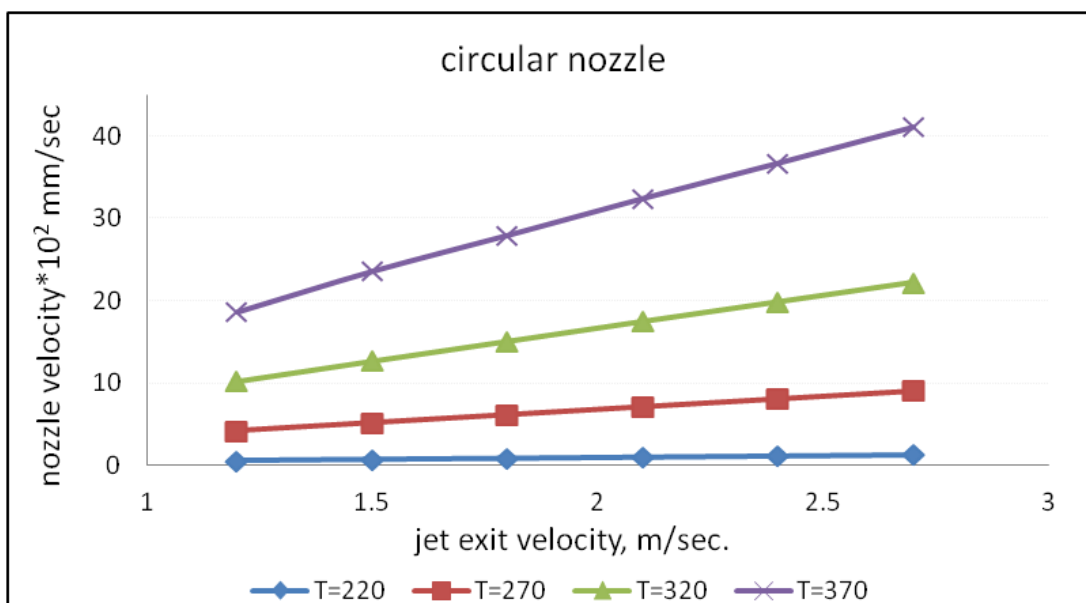


Figure 5: the relation between processing time and velocity at constant temperature for circular impinging jet

models were matched with maximum error of 2.6% and average of 1.1% and presented in Figures from 5 to 6.

Fig 5 shows the model results with different processing parameters. The polished area has a dimensionless radius $R = 1.8$ ($r = 1.8d_i$) and hence, the process velocity can be computed by dividing the diameter of area of interest by the obtained time. Figure 5 shows the relation between jet exit velocity and nozzle velocity for different jet exit temperature. Figure 6 shows the relation between jet exit temperature and nozzle Velocity for different jet exit velocity. it appears from both figures that jet temperature has more effect than jet velocity in accelerate the process. A worth noting is that the model was feed with much lower jet velocity which results to much lower nozzle velocity as shown in figures 5,6. These results help us to predict and work at higher jet velocity and hence, higher nozzle velocity as will be presented in the experiment section.

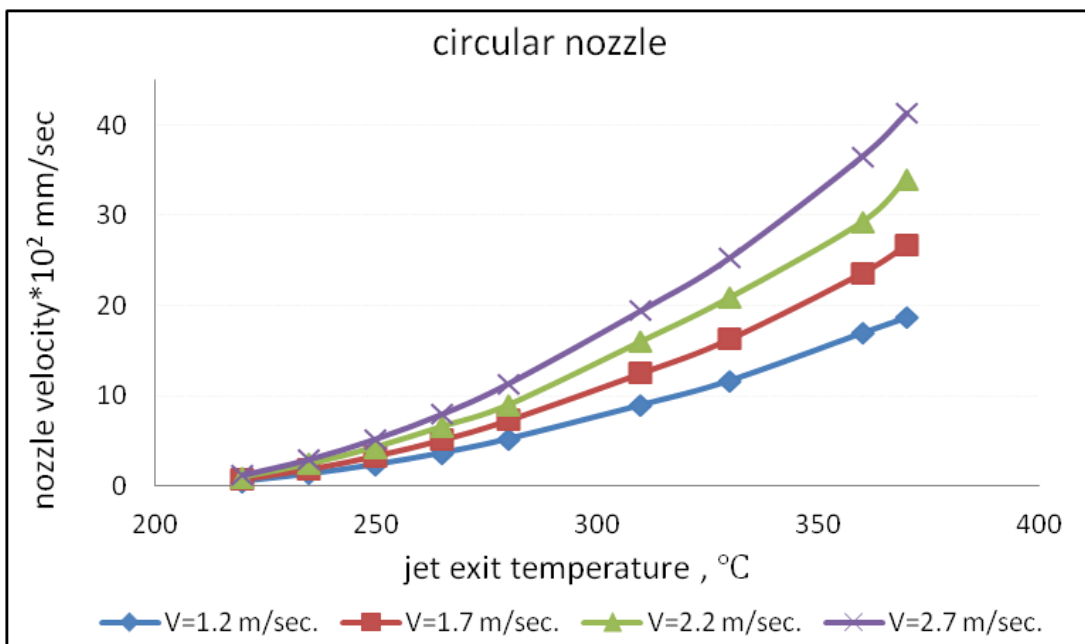


Figure 6: the relation between processing time and temperature at constant velocity for circular impinging jet and

3.2 experimental verification:

This section presents the experimental data obtained for the investigated polishing process. This section was held after modeling studies where more accurate and related properties were obtained as shown in [table 3](#); The site of Ultimachine cites the common PLA type of PLA4043D-Natureworks [16]. The peak melting temperature is 145-165 °C which with average of 153 °C as in [table 3](#).

Table3: Properties of PLA used. Values are averaged in operating temperature range 35°C to 153°C

Item	Density ($\bar{\rho}$) Kg/m ³	Specific heat (\bar{C}_p) J/Kg.K	Thermal conductivity (\bar{K}) w/m.K	heat of fusion ΔH_m j/kg	Melting temperature T_m °C
PLA	1256	2227 ¹	0.165	45000	153

[Figure 7a](#) shows the experimental test rig while [figure 7b](#) show an experimentally polished surface with magnification to the boundary region between the polished and the unpolished region.

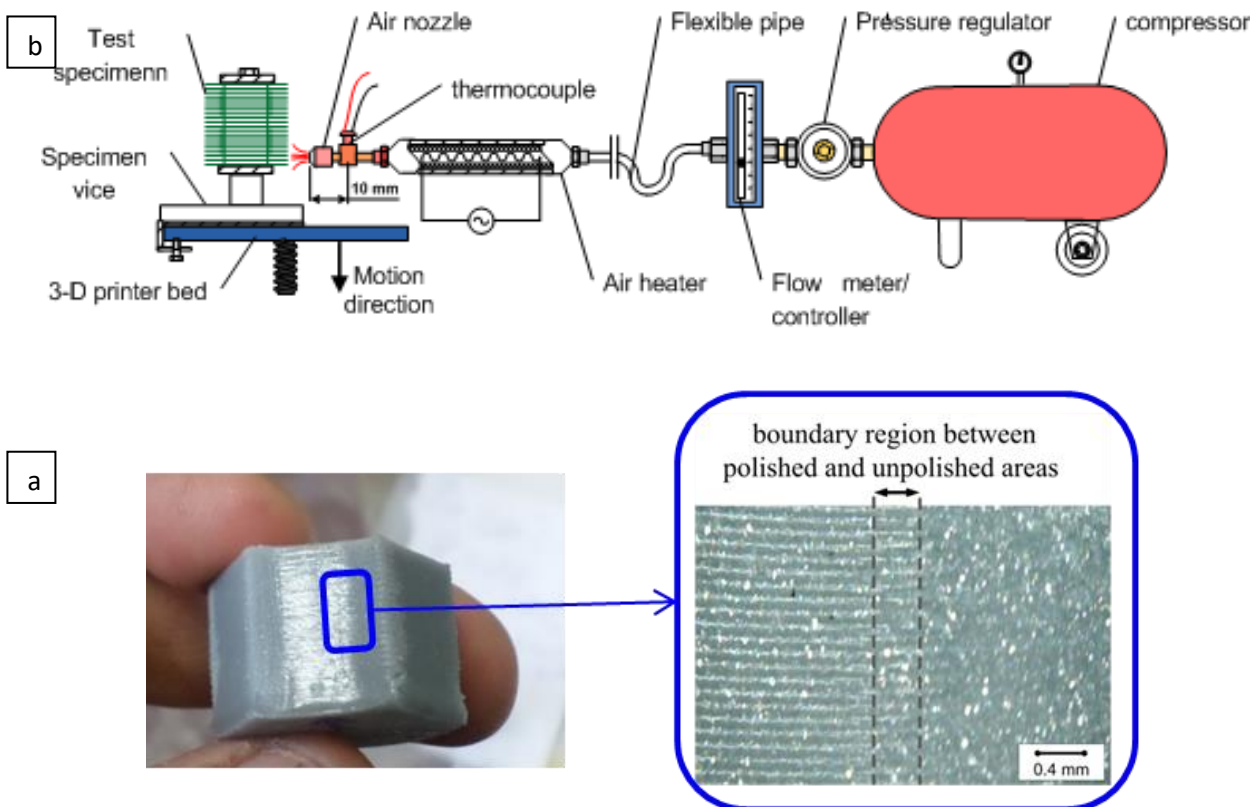
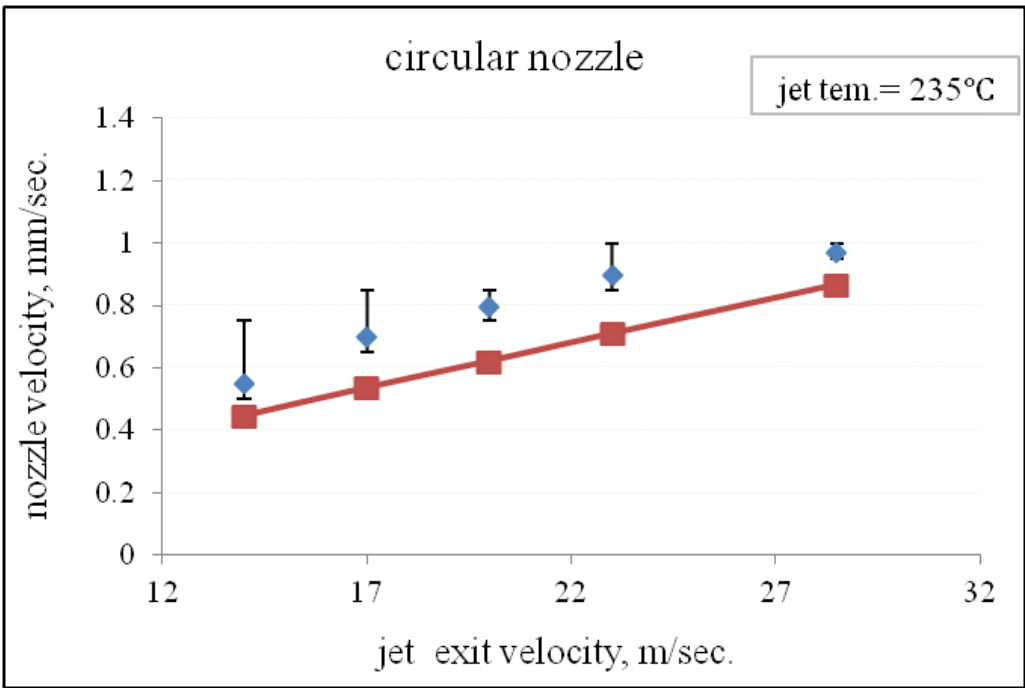


Figure 7: (a) schematic of the constructed test rig (b) experimentally polished surface with magnification at the boundary region showing the polished and the unpolished surfaces

Figure 7b shows the experimentally polished surface and demonstrate the concept shown in figure 2b. A ninety one different tested surface under different testing parameters was held. Figure 8 shows the comparison between the model data represented by continuous line and the experimental one represented by discrete points. The model data is obtained corresponds to properties at table 3. Also the experimental processing conditions are: jet velocity from 14 to 28.5 m/sec. and jet temperature from 215 to 265°C. The experimental data corresponds to the highest achieved surface roughness reductions (smoothest surface) which introduce sufficient melting to the surface as derived in the model. This roughness reduction is from 85% to 66% which from initial range of surface roughness from 7 to 8 μm .

a



b

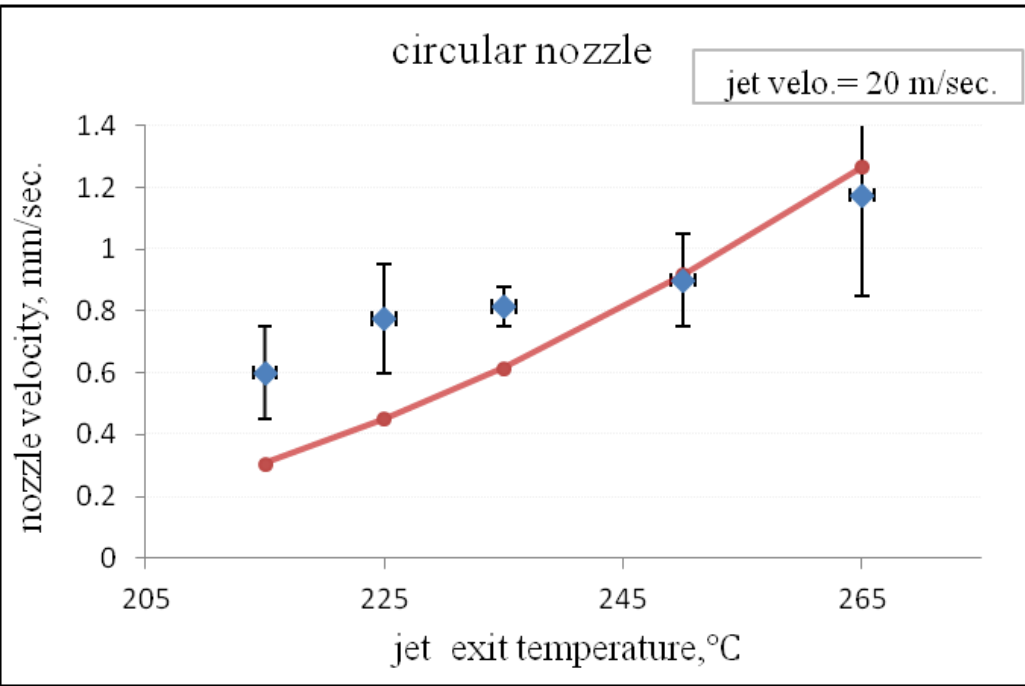


Figure 8: the model and the experimental results for the relations between nozzle translation velocity and (a) jet exit velocity (b) jet exit velocity

The deviation of model from experimental results is considered acceptable compared with similar studied published in polishing. The difference between the model and the experimental results may be owing to the deviation between the exact material properties and the averaged one. This material properties are more four with other approximations at Nu value. Also the exit temperature was measured 1cm apparent from the exit opening which may contribute in this deviation. A worth noting is that the model can fit the experiment better than it be by a bit change in the thermo physical proprieties that at [table3](#) while we committed to the thermo physical properties obtained from [\[16\]](#) while it is known that PLA properties dependent on the molecular weight and stereo-chemical makeup of its backbone [\[14\]](#).

4. Conclusion:

A modeling to a new polishing process is presented to improve the surface roughness of FDM parts. The developed polishing process replaces the laser as heating source by an impinging hot air jet to melt the outer surface layer to improves the surface roughness. An analytical model was developed by studying impinging jet heat transfer, entrainment in impinging jet, and 2-D transient conduction models to relate the main process parameter: jet temperature, jet velocity, and nozzle translational velocity. The model data was validated using two heat transfer model giving the same results and verification experimentally with a good agreement. Furthermore, the model can predict the effect of other process parameters including material properties. It is found that jet temperature can accelerate the polishing process more than jet velocity. base on the developed model, we can predict the behavior of different process parameters.

Reference:

- [1] D. Pal and B. Ravi, "Rapid tooling route selection and evaluation for sand and investment casting," *Virtual Phys. Prototyp.*, vol. 2, no. 4, pp. 197–207, Dec. 2007.
- [2] D. T. H. New and S. C. M. Yu, "Vortex Rings and Jets," 2015.
- [3] G. Greene, Y. Cho, J. Hartnett, and A. Bar-Cohen, *Advances in heat transfer*, Volume 26, vol. 26. Elsevier, 1995.
- [4] H. Maki and A. Yabe, "Heat Transfer By the Annular Impinging Jet," *Exp. Heat Transf.*, vol. 2, no. 1, pp. 1–12, Jan. 1989.

- [5] K. Ichimiya, "Heat transfer characteristics of an annular turbulent impinging jet with a confined wall measured by thermosensitive liquid crystal," *Heat Mass Transf.*, vol. 39, no. 7, pp. 545–551, Jul. 2003.
- [6] H. Chattopadhyay, "Numerical investigations of heat transfer from impinging annular jet," *Int. J. Heat Mass Transf.*, vol. 47, no. 14–16, pp. 3197–3201, Jul. 2004.
- [7] K. Jambunathan, E. Lai, M. Moss, and B. Button, "A review of heat transfer data for single circular jet impingement," *Int. J. Heat ...*, vol. 13, no. 2, pp. 106–115, 1992.
- [8] R. Goldstein, "Effect of entrainment on the heat transfer to a heated circular air jet impinging on a flat surface," *J. Heat Transfer*, vol. 112, no. August 1990, 1990.
- [9] a. Lamikiz, J. a. Sánchez, L. N. López de Lacalle, and J. L. Arana, "Laser polishing of parts built up by selective laser sintering," *Int. J. Mach. Tools Manuf.*, vol. 47, no. 12–13, pp. 2040–2050, Oct. 2007.
- [10] M. Rombouts, G. Maes, W. Hendrix, E. Delarbre, and F. Motmans, "Surface Finish after Laser Metal Deposition," *Phys. Procedia*, vol. 41, pp. 803–807, Jan. 2013.
- [11] E. Bordatchev, "Performance of laser polishing in finishing of metallic surfaces," *Int. J. Adv. Manuf. Technol.*, vol. 73, no. 1, pp. 35–52, 2014.
- [12] J. Ramos, J. Murphy, and K. Wood, "Surface roughness enhancement of indirect-SLS metal parts by laser surface polishing," *Proc. 12th ...*, pp. 28–38, 2001.
- [13] T. Bergman, F. Incropera, and A. Lavine, *Fundamentals of heat and mass transfer*, Seventh ed. John Wiley & Sons, 2011.
- [14] D. Garlotta, "A literature review of poly (lactic acid)," *J. Polym. Environ.*, vol. 9, no. 2, pp. 2005–2008, 2001.
- [15] M. Pyda, R. . Bopp, and B. Wunderlich, "Heat capacity of poly(lactic acid)," *J. Chem. Thermodyn.*, vol. 36, no. 9, pp. 731–742, Sep. 2004.
- [16] "Moldflow Material Testing Report - NatureWorks LLC." [Online]. Available: http://www.natureworksllc.com/~media/Technical_Resources/Properties_Documents/PropertiesDocument_7000DMoldFlowReport_pdf.pdf. [Accessed: 18-Mar-2017].
- [17] "3Dprintingtech.cc - news and more about 3d printing." [Online]. Available: <http://www.3dprintingtech.cc/how-does-a-3d-printer-work/fdm-tecnologia-stampanti-3d-stampa-3d-forum/>. [Accessed: 13-Nov-2015].

Adsorption of cationic dye from aqueous solution onto activated carbon derived from waste newspaper

M.T. Hamdy^{a,*}, S.A. Nosier^b and M. Hussein^c

^{a,b,c}Chemical Engineering Department, Faculty of Engineering, Alexandria University, Alexandria, Egypt.

*E-mail: Mohamed91.tarek@gmail.com

Abstract

Carbonaceous wastes are considered to be a cheap source of activated carbon for the treatment of waste water. Present study is to convert waste newspapers (WNP) to activated carbon by using physical activation and chemical activation on different conditions of carbonization temperatures and times. In case of chemical activation, ZnCl₂ is used as an activating agent in different reagent to sample ratios. Batch adsorption experiments were performed to study its effectiveness of removing methylene blue (MB) from aqueous solution. Equilibrium adsorption capacity of activated carbon under each condition was then determined to indicate the sample which has the highest adsorption capacity. Also Adsorption isotherms of this sample were indicated and modeled with Langmuir and Freundlich equations. It was found that Activated carbon which was chemically prepared by ZnCl₂ activation and under different conditions show higher Equilibrium adsorption capacity than that of physical activation. Afterwards, the best activated carbon obtained was used as an adsorbent in a fixed bed adsorption column to study the effect of different methylene blue feed flow rates and different activated carbon bed heights on the break through characteristics of the adsorption system. The results revealed that WNP can be used as a low-cost alternative in waste water treatment for dye removal.

Keywords: Waste newspaper, Activated carbon, Methylene blue, Adsorption, Isotherms, Fixed bed.

1 Introduction

Many environmental problems can be caused by dye contaminated waste water. Plant's life can be affected by colored water. Therefore, Humans can retroactively be affected by the contamination of dyes in water^[1]. One of the important dyes is methylene blue. Methylene blue has many uses, it may be seen in medical treatments^[2] and some industrial aspects. With expanding the interests on eco-friendly industry, it is crucial to find inexpensive and competent ways for treating waste water^[3]. Various techniques have been performed for removing dyes from waste water including photo catalytic degradation^[4] and cation exchange membrane^[5]. One of the most effective and widely used technique is adsorption by activated carbon. Activated carbon is well known by its large surface area, it can be structured in different forms and its pores can be easily modified. On the other hand, it has some economical problems due to its high cost^[6]. Therefore, several researches have been done to find a cheap source of activated carbon such as agricultural wastes^[7] including coconut shell^[8], rice husks^[9], almond hulls^[10] and date stones^[11]. Others can be prepared from carbonaceous waste like wood and coal^{[12] [13]}.

Carbonaceous materials have been anciently used as adsorbents, also activated carbon can widely be prepared from carbonaceous raw materials such as waste rubber tires^[14] and lignite^[15] either by physical or chemical methods. In this study, activated carbon was prepared from waste newspaper by physical and chemical activation ($ZnCl_2$ as an activating agent) on different conditions. The equilibrium adsorption capacities of the prepared activated carbon samples were then investigated using MB adsorption from aqueous solution to indicate the sample with the highest equilibrium adsorption capacity. Furthermore, the adsorption prospect of the WNP based activated carbon was evaluated through removing MB from aqueous solution using a small scale fixed-bed adsorption column including the effect of MB feed flow rates and activated carbon bed heights on the adsorption capacity of the bed.

2 Material and Methods

2.1 Preparation of activated carbon

For physically activated carbon, The WNPs were cut into equal small square pieces of size 1-1.5 cm length and then were dried at 110 °C for 2 hours to remove any moisture. After that, the samples were placed in 315 stainless steel covered tubes of 12 cm height and 5 cm inner diameter and were put in the muffle furnace to be subjected to a thermal activation by carbonization. The samples were physically activated and carbonized in the absence of air at different carbonization temperatures (600°C, 700°C, 800°C, 900°C) and different carbonization times (1, 1.5, 2, 2.5 hr.). After carbonization the samples were left to cool then they were crushed and sieved to particle size of 125 µm.

For chemically activated carbon by $ZnCl_2$ activation, After the WNP was cut and dried, activation was carried out by impregnation the samples in three different $ZnCl_2$ to WNP samples mass ratios of 0.5, 1 and 1.5. Afterwards, this impregnated paste was left over night before carbonization. After impregnation for one night the impregnated WNPs were dried in vacuum oven for 4 hours at 110°C. The samples were then placed in the stainless steel covered tubes and were put in the muffle furnace. Carbonization was done on different carbonization temperatures (600°C, 700°C, 800°C, 900°C) and different carbonization times (1, 1.5, 2, 2.5 hr.). After carbonization the samples were left to cool then they were crushed and sieved to particle size of 125 µm as well as physical activation. The samples were then washed to remove any chemical residuals by stirring them in 500 ml of 1 N HCL for 30 minutes followed by continuous rinsing with hot distilled water till the PH of the washed solution ranged between 6 -7.

2.2 Adsorption procedures

For physical activation, the experiments were carried out by mixing 150 ml of Different methylene blue concentration (10, 30, 50, 70 and 100 ppm) with 0.5 grams of activated carbon in different conical flasks. The flasks were then put in isothermal water bath Shaker at 150 rpm and $25 \pm 1^\circ C$ for one hour until equilibrium occurred. Then the samples were taken from conical flasks and the solutions were centrifuged for 15 minutes at 1000 rpm in order to separate the solid particles of the activated carbon

from the MB solution. The concentrations of MB before and after adsorption were determined using spectrophotometer (shimadzu Model: UV 1601). For chemically activated carbon, the experiments were carried out by mixing 100ml of 500 ppm MB solution with activated carbon samples of different doses (0.1, 0.2, 0.3, 0.4, 0.5 g) in different conical flasks. The conical flasks were then agitated in isothermal water bath Shaker at 150 rpm and $25 \pm 1^\circ\text{C}$ for one hour, followed by the same procedures as the physical activation.

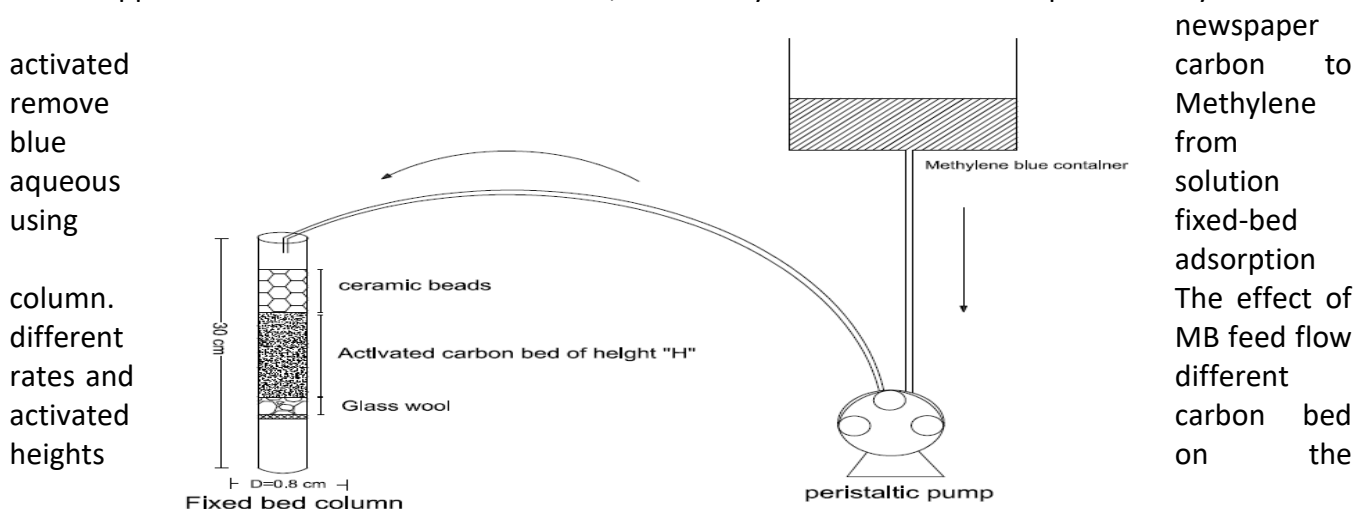
In order to determine the sample with the highest specific surface area, the equilibrium adsorption capacity of each sample was calculated from the following equation^[7]:

$$q_e = \frac{C_i - C_e}{m} \times V \quad (1)$$

Where, q_e is the equilibrium amount of MB adsorbed by the adsorbent (mg/g), C_e is the equilibrium concentration of methylene blue, C_i is the initial concentration of the MB which (ppm), V is the volume of solution in liters and m is the weight of the adsorbent in grams.

2.3 Fixed bed adsorption studies

As an application of WNP activated carbon, this study observed the adsorption ability of Waste newspaper



breakthrough properties of the adsorption system were determined. As shown in figure 1, the adsorption experiments were carried out in a Pyrex glass column tube of 0.8 mm inner diameter and 30 cm height. At the top and the bottom of the column, a layer of glass wool. The column was then filled up with 2 mm size ceramic beads above the adsorbent bed. These beads are to serve a uniform distribution of the MB solution through the column. Moreover, 500 ppm of methylene blue entered the column from the top at different bed heights (1, 2, 3 and 4 cm) and different feed flow rates (11.5, 17 and 20 ml/min), the feed flow rates were controlled by a peristaltic pump. The concentrations of the outlet methylene blue solutions were measured by collection the samples of MB solution at time intervals and the concentrations were measured by the UV spectrophotometer at maximum wavelength of 662 nm.^[22]

Figure 16 Diagram for the fixed bed experiment setup

3 Results and discussion

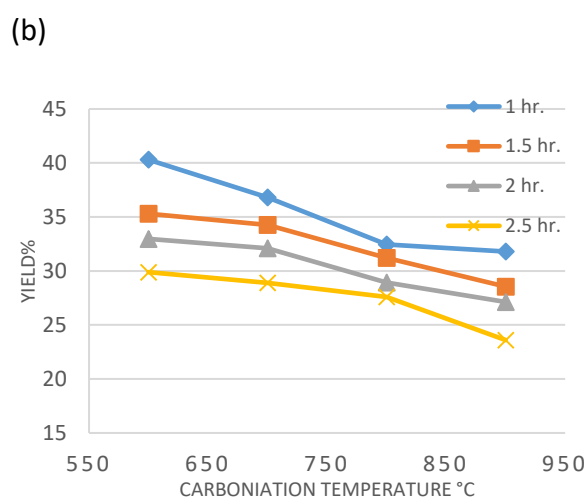
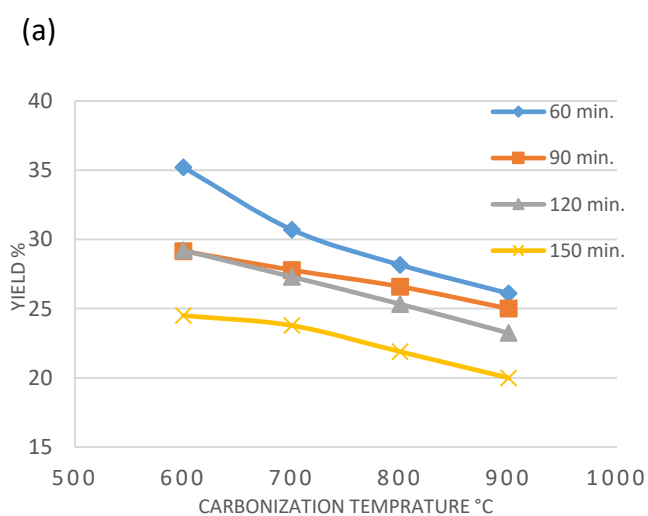
3.1 Characterization of activated carbon

3.1.1 Yield WNP activated carbon

The Yield was obtained by weighting the WNP samples before and after carbonization at different temperatures and times, then it was calculated from the following equation^[15]:

$$\text{Yield \%} = \frac{W_f}{W_0} \times 100 \quad (2).$$

Where, W_f and W_0 are the weight of the final activated carbon (g) and the weight of the dried WNP samples before Carbonization (g), respectively. The effect of carbonization temperature and time on the yield of activated carbon is shown in Figure 2. Figure 2 (a) shows the yield of physically activated carbon and indicates that the yield was decreased from 35.2% to 20% with increasing the carbonization temperature from 600°C to 900°C due to the loss of volatile material by increasing the carbonization temperature, while figure 2 (b) shows the yield of chemically prepared activated carbon at various carbonization temperatures and carbonization times using ZnCl_2 as activating reagent of reagent to sample mass ratio=0.5. At this ratio of activator the yield decreased from 40.3% to 23.6%. It is clear from this figure that there is a gradual decrease in the yield with increasing carbonization times and carbonization temperature. Similar, although not as clear behavior, was observed for ratio = 1 figure 2 (c). The yield in this case decreased from 42.2% to 26.1%. In case for ratio=1.5, the yield in this case decreased from 44.37% to 28.91% as shown in figure 2 (d).^[16]



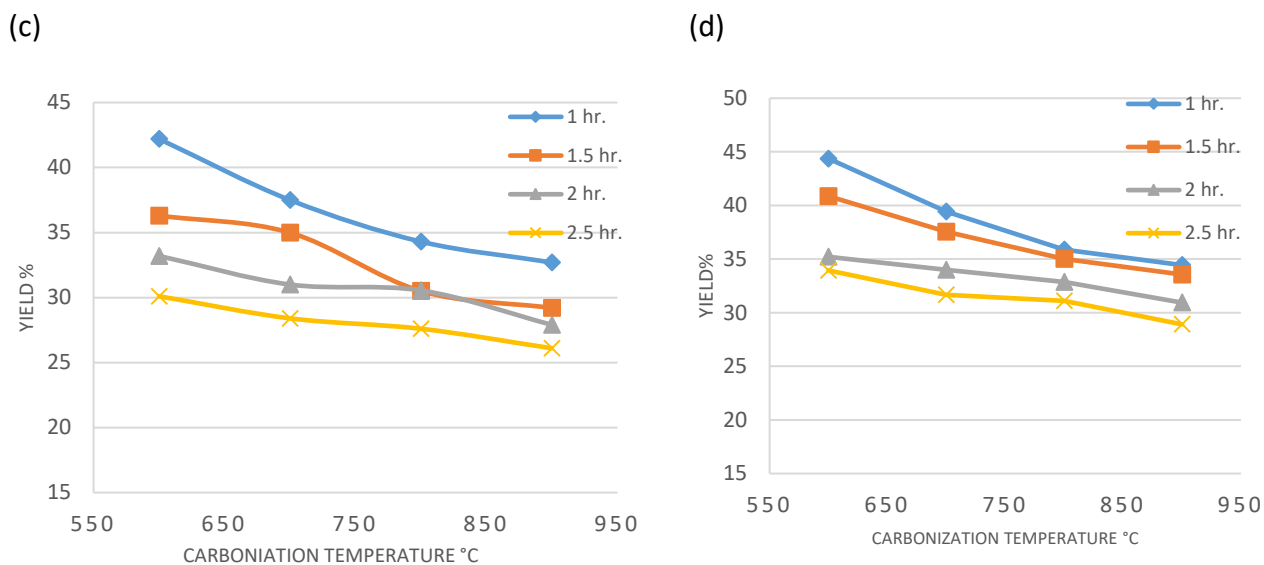
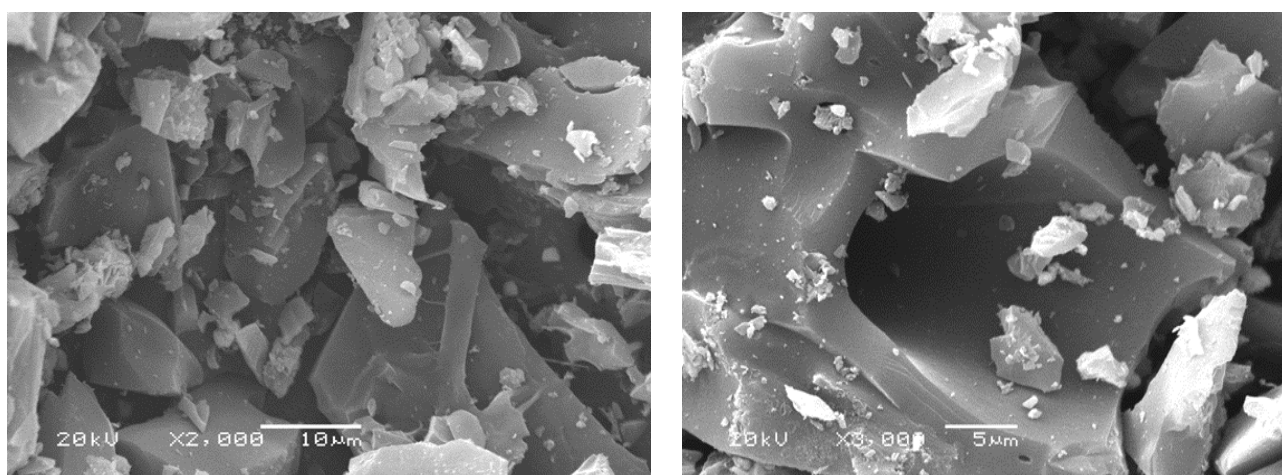


Figure 2 Effect of carbonization temperature on yield of activated carbon at different activation times. (a) Physical activation, (b) ZnCl₂ activation by ZnCl₂ to sample ratio=0.5, (c) ZnCl₂ activation by ZnCl₂ to sample ratio=1 and (d) ZnCl₂ activation by ZnCl₂ to sample ratio=1.5

3.1.2 Scanning electron microscope

In order to identify the microstructure of the chemically activated WNP activated carbon, SEM images were investigated. Figure 3 (a)-(b) show SEM micrograph of chemically activated WNP carbon produced at 900°C carbonization temperature, 2.5 hours Carbonization time and ZnCl₂ to sample impregnation mass ratio = 1.5 at two different magnifications. The images of the SEM display well noticeable porosity, with a series of sequence active sites distributed along the surface.



(a)

(b)

Figure 3 SEM of chemically activated carbon prepared from WNP (a) Magnification 2000 (b) magnification 3000

3.1.3 FTIR analysis

Figure 4 shows the FTIR of the chemically activated WNP activated carbon. The band around 3400 cm^{-1} can indicate O–H stretching mode of Hydroxyl groups. The band around 2900 cm^{-1} can indicate C–H stretching mode of Alkyl groups. The band around 1600 cm^{-1} can indicate C=C bending vibration mode of alkenes groups. The band around 1103 cm^{-1} can indicate C–O stretching mode of alcohols, ethers and anhydrides groups and the small band around 740 cm^{-1} can indicate =C–H bending mode of aromatic groups or indicates C–Cl stretching vibration mode of alkyl halides.^[10]

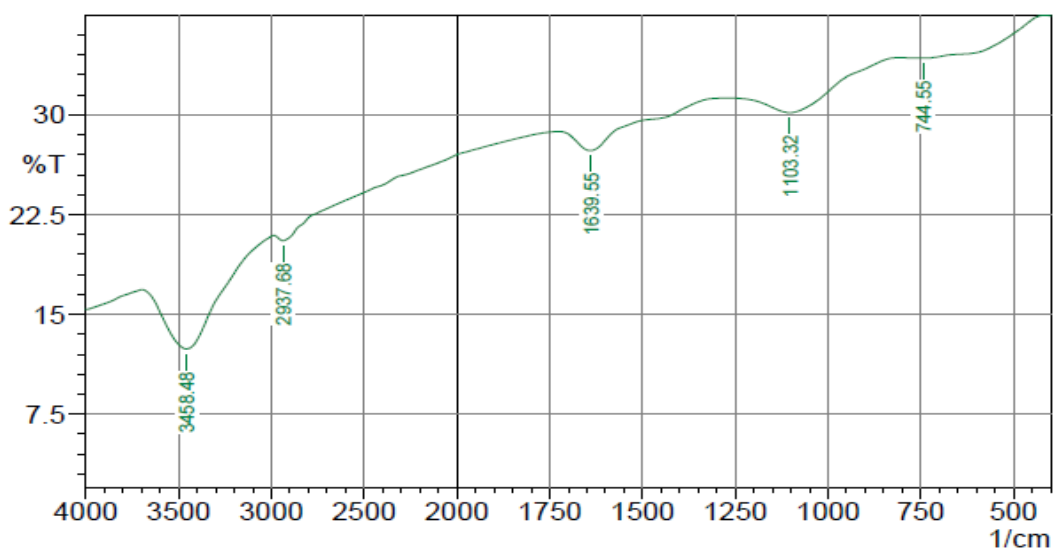


Figure 4 FTIR for chemically activated carbon prepared at ZnCl_2 activation by ZnCl_2 to sample ratio=1.5

3.2 Determination of equilibrium Adsorption capacity

In case of Physical activation, Figures 5(a)-(d) show The equilibrium adsorption capacities for Physically activated carbon that were studied at different carbonization temperatures (600°C , 700°C , 800°C , 900°C) and different carbonization times (1, 1.5, 2, 2.5 hr.). Figure 5(a) shows that the maximum equilibrium adsorption capacity of activated carbon prepared at 600°C and different activation times reached 11.2 mg/g , while in case of activated carbon prepared at 700°C , the maximum equilibrium adsorption capacity reached 11.9 mg/g as shown in figure 5(b) and in case of activated carbon prepared at 800°C and 900°C , the maximum equilibrium adsorption capacities reached 11.8 mg/g and 12 mg/g respectively from figures 5(c) and 5(d). Overall, the physically activated carbon which is prepared at 900°C and 2.5 hours activation time has the highest equilibrium adsorption capacity.^[17]

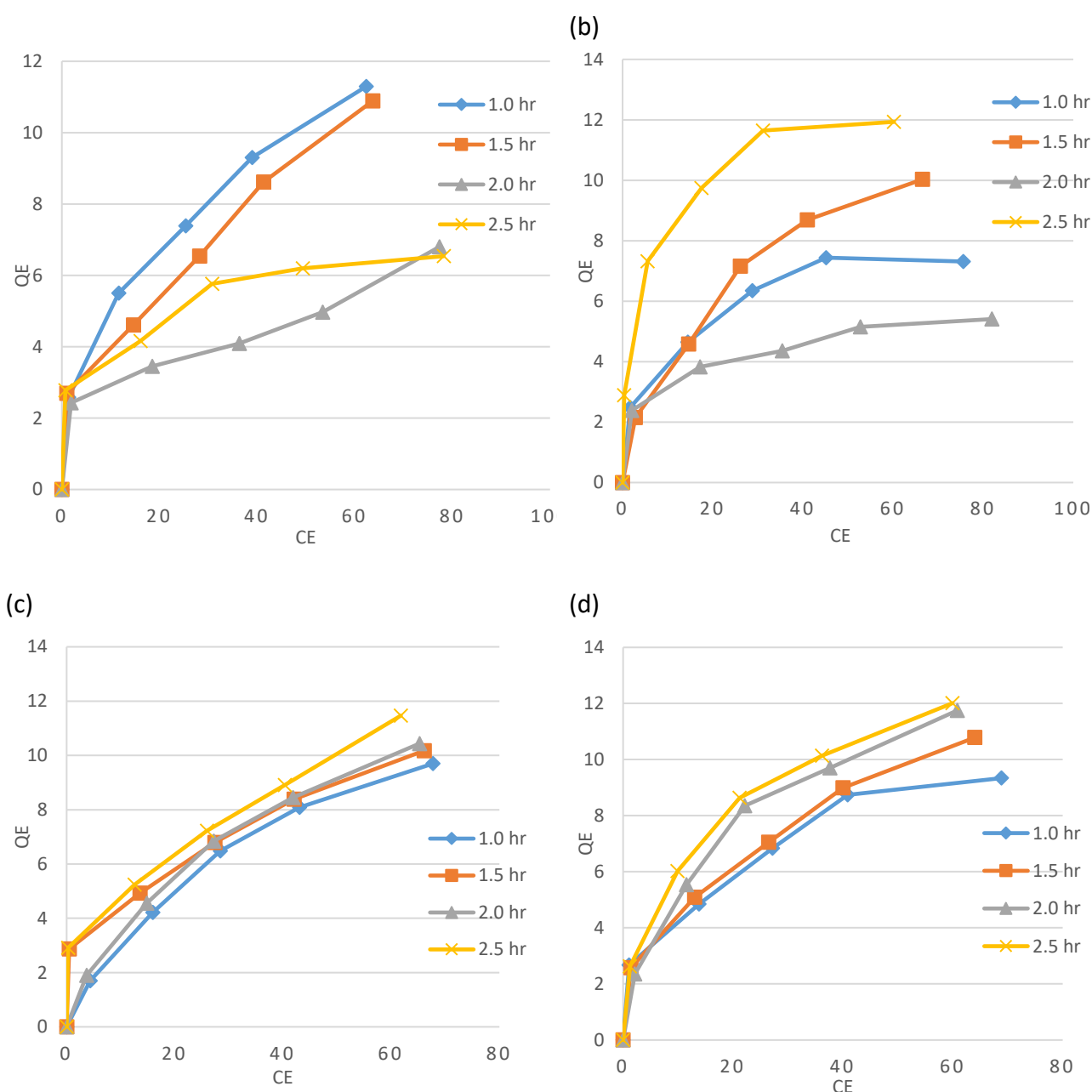


Figure 5 Adsorption isotherm of physically activated carbon at different carbonization times (a) carbonization temperature 600°C (b) carbonization temperature 700°C (c) carbonization temperature 800°C (d) carbonization temperature 900°C

In case of chemical activation, for different activated carbon doses (0.1, 0.2, 0.3, 0.5 and 0.5 grams). The equilibrium adsorption capacities were obtained at different activation temperatures (600, 700, 800 and 900°C), reagent to sample ratios (0.5, 1 and 1.5) and activation times (1, 1.5, 2 and 2.5 hours). Figures 6 (a)-(c) show the equilibrium adsorption capacities of activated carbon prepared at 600°C, different carbonization times and different ZnCl₂ to sample ratios, it is obvious that the activated carbon which is prepared from ZnCl₂ to sample mass ratio=1.5 and 2.5 hours has the highest equilibrium adsorption capacity which is 237 mg/g, while Figures 7 (a)-(c) show the equilibrium

adsorption capacities of activated carbon prepared at 700°C, different carbonization times and different ZnCl₂ to sample ratios, this show that the equilibrium adsorption capacity is at its maximum for the activated carbon which prepared at ZnCl₂ to sample mass ratio=1 and 1 hour which is 276 mg/g. Figures 8 (a)-(c) and Figures 9 (a)-(c) show the equilibrium adsorption capacity for activated carbon prepared at 800°C and 900°C respectively at different conditions which indicates that maximum equilibrium capacity of each temperature reached 196 and 278 mg/g respectively. It is obvious that there is great difference of MB adsorption between the chemically and the physically activated carbons, this is due to the presence of ZnCl₂ which enhanced the active sites onto the chemically activated carbon^[17]. Generally, the figures show that the activated carbon which is prepared at 900°C, 2.5 hours Carbonization time and ZnCl₂ to sample ratio=1.5 has the highest equilibrium adsorption capacity of all which reached 278 mg/g and this indicates that this sample has the highest specific surface area. These results agreed with the previous work reported on the Adsorption of MB by waste newspaper^{[18][19]}.

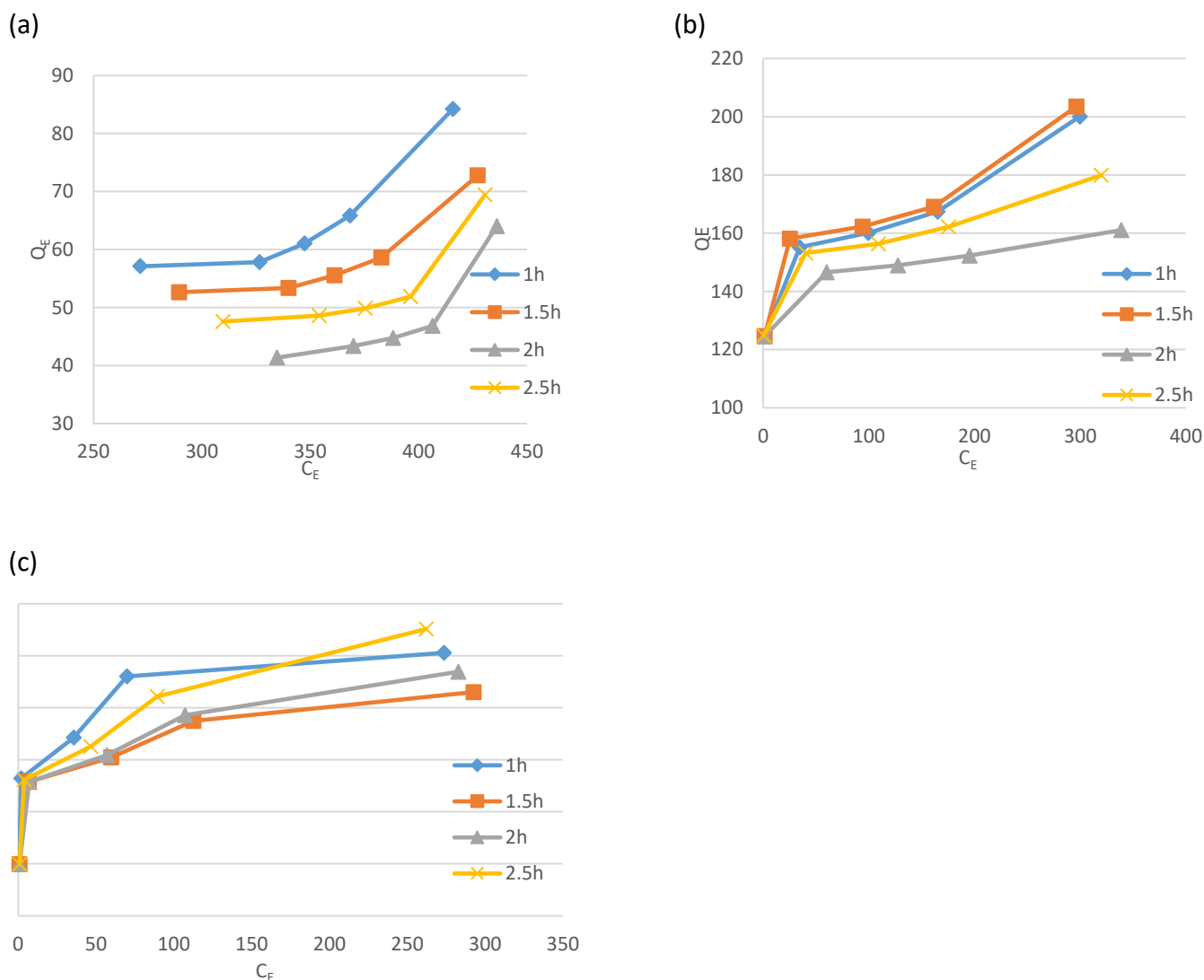


Figure 6. Adsorption isotherms of MB at 25°C onto chemically activated carbon prepared at activation temperature 600°C (a) zncl₂ to sample ratio 0.5 (b) zncl₂ to sample ratio 1 (c) zncl₂ to sample ratio 1.5

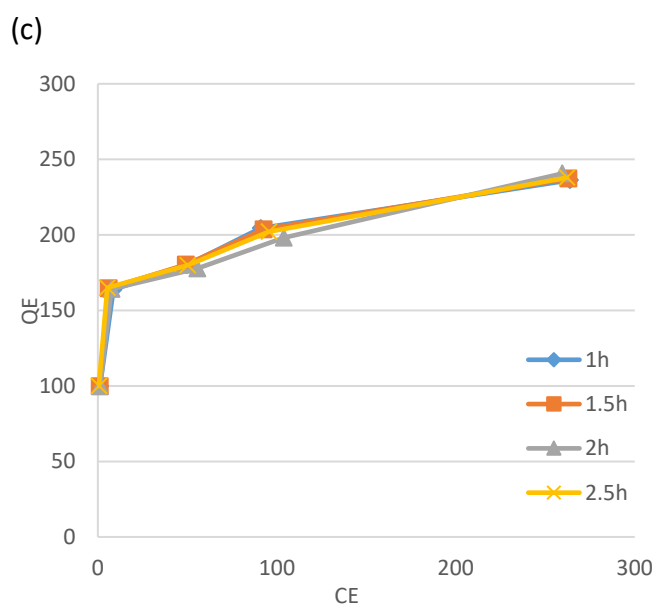
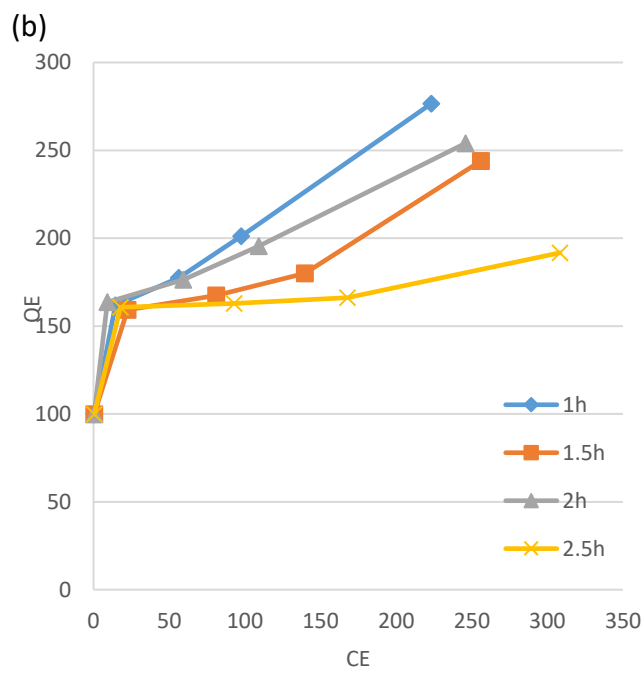
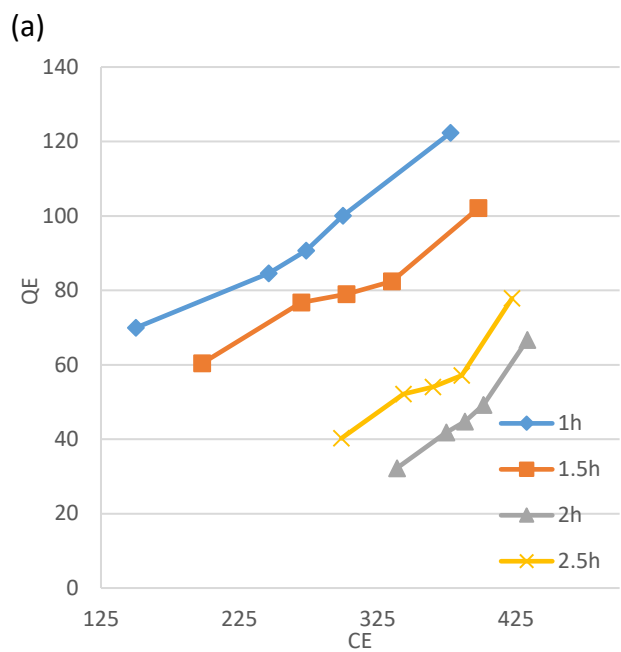


Figure 7 Adsorption isotherms of MB at 25°C onto chemically activated carbon prepared at activation temperature 700°C (a) zncl₂ to sample ratio 0.5 (b) zncl₂ to sample ratio 1 (c) zncl₂ to sample ratio 1.5

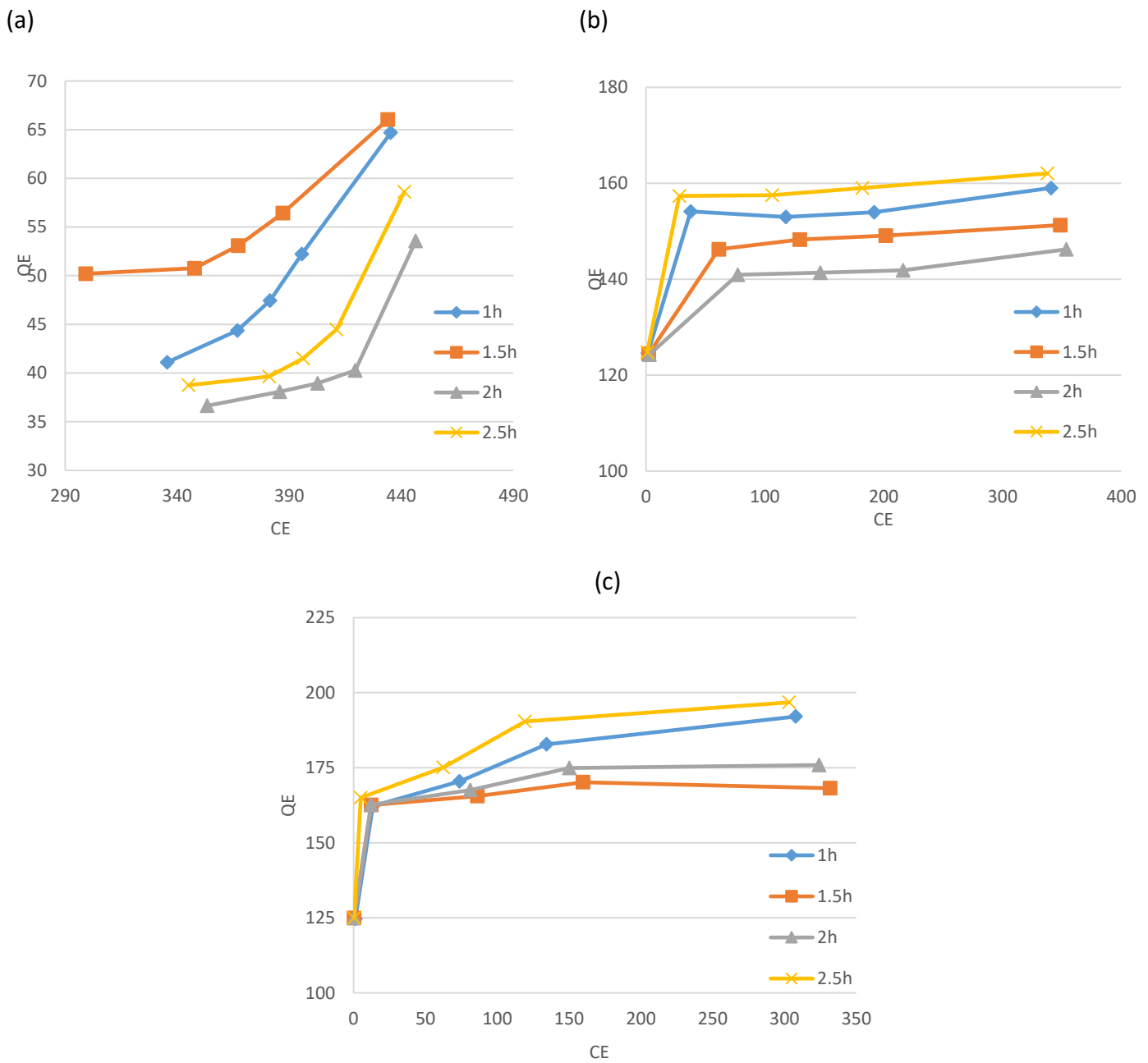


Figure 8. Adsorption isotherms of MB at 25°C onto chemically activated carbon prepared at activation temperature 800°C (a) zncl₂ to sample ratio 0.5 (b) zncl₂ to sample ratio 1 (c) zncl₂ to sample ratio 1.5

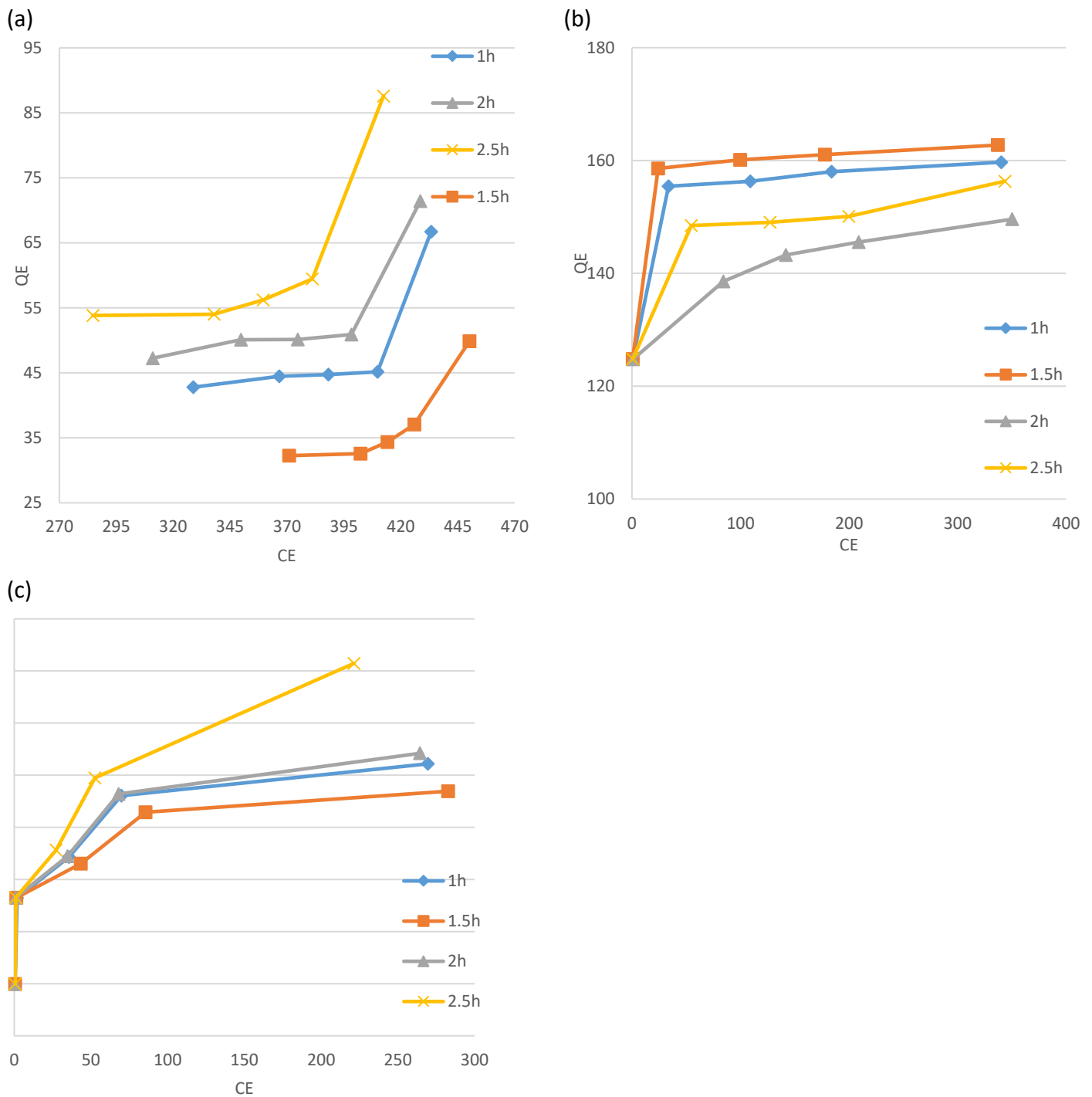


Figure 9. Adsorption isotherms of MB at 25°C onto chemically activated carbon prepared at activation temperature 900°C (a) zncl₂ to sample ratio 0.5 (b) zncl₂ to sample ratio 1 (c) zncl₂ to sample ratio 1.5

3.3 Adsorption isotherms

The adsorption isotherms indicate the distribution of the molecules between the adsorbent and the adsorbate when reaching equilibrium. The adsorption isotherms were carried out on both Langmuir and Freundlich models on the Activated carbon sample which has the highest adsorption capacity (carbonization temperature=900°C, carbonization time=2.5 hours and ZnCl₂/sample=1.5).

The Langmuir isotherm indicates a monolayer adsorption onto the surface of the adsorbent, the linear form of Langmuir isotherm is given as: ^[16]

$$\frac{C_e}{q_e} = \frac{1}{Q_m K_L} + \frac{1}{Q_m} C_e \quad (4)$$

Where, q_e is the equilibrium amount of MB adsorbed by the adsorbent (mg/g), C_e is the equilibrium concentration of methylene blue, K_L is the Langmuir adsorption constant (Lmg⁻¹) and Q_m is the theoretical maximum adsorption capacity(mgg⁻¹). While the Freundlich isotherm indicates non uniform heterogeneous distribution over the surface of the adsorbent, the linear form of Freundlich isotherm is given as: ^[21]

$$\log q_e = \log K_f + \frac{1}{n} \log C_e \quad (5)$$

Where, K_f is the Freundlich adsorption constants related to the adsorption capacity, n is the intensity of the adsorbent. The Error analysis (X^2) is statistical Data which is performed to evaluate the error between the experimental data and the calculated values of the adsorption capacity and it is calculated from the following equation: ^[20]

$$X^2 = \sum_{i=0}^n \frac{(q_{e,exp} - q_{e,calc})^2}{q_{e,exp}} \quad (6)$$

Where $q_{e,exp}$ is the experimental equilibrium adsorption capacity (mg/g), $q_{e,calc}$ is the calculated equilibrium adsorption capacity (mg/g) and n is the number of observations in the experimental isotherms. Table 1 and figure 10 (a), (b) show the comparison between the isotherm models of the WNP activated carbon which gives the highest equilibrium adsorption capacity (carbonization temperature=900°C, carbonization time=2.5 hrs. and ZnCl₂ to sample mass ratio= 1.5). From the table, it is illustrated that R^2 value of Langmuir isotherm is higher than that of Freundlich isotherm, while the error analysis of Langmuir isotherm is much lower than that of Freundlich isotherm. Therefore, these results indicate that the activated carbon fits more on Langmuir isotherm.

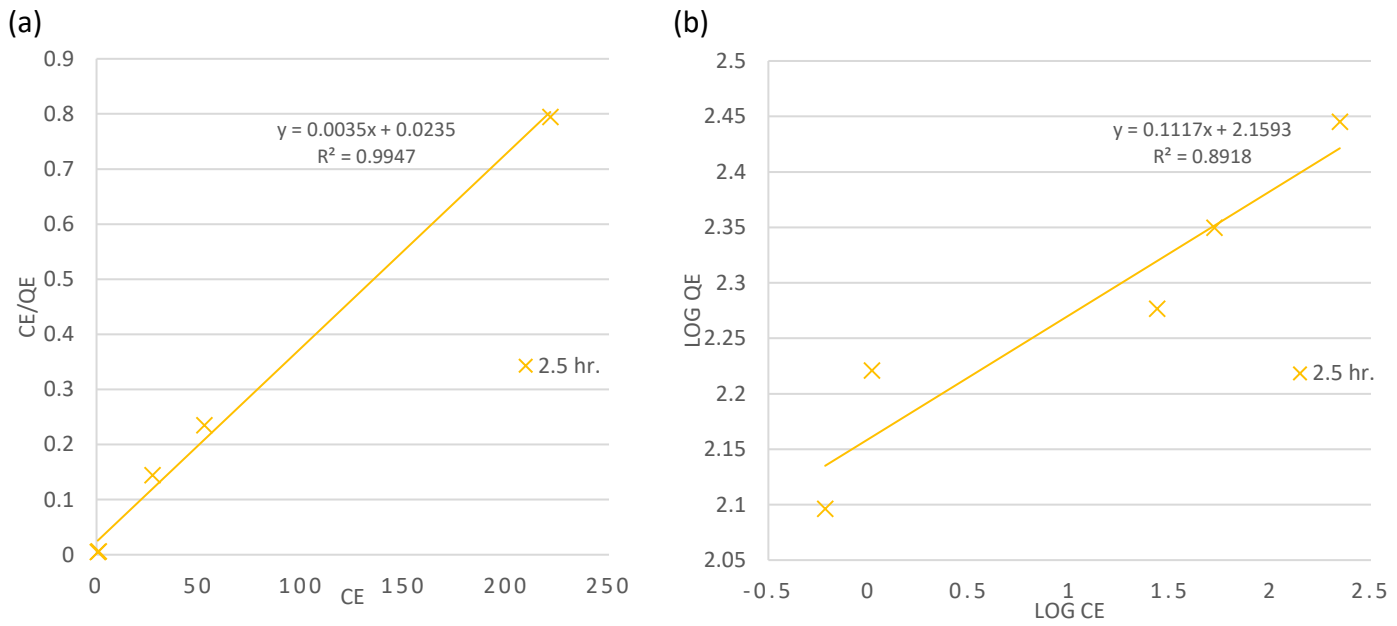


Figure 10. Adsorption isotherms fitting of methylene blue onto WNP activated carbon (a) Langmuir isotherms (b) Freundlich isotherm.

Isotherm models	Isotherms parameters	
Langmuir $\frac{C_e}{q_e} = \frac{1}{Q_m K_L} + \frac{1}{Q_m} C_e$	Q_m	13.514
	K_L	0.103
	R^2	0.995
	χ^2	2.316
Freundlich $\log q_e = \log K_f + \frac{1}{n} \log C_e$	K_f	2.443
	$1/n_f$	0.396
	R^2	0.892
	χ^2	6.687

Table 3 adsorption isotherm parameters and correlation coefficients for MB adsorption onto WNP activated carbon

3.4 Fixed bed adsorption

The MB adsorption results on the waste newspaper activated carbon using fixed-bed were exhibited in the form breakthrough curves. The curves illustrated the adsorption behavior of MB from the aqueous solution along time interval till saturation of the bed occurs, and this was showed as the ratio of outlet concentration to inlet concentration as a function of time (C/C_0 versus t). The maximum capacity of the column (q_t) was shown in Eq. (7) as the total amount of MB adsorbed (mg) in the column at the time when saturation of the bed occurs. Table (2) listed the adsorption parameters including the breakthrough times and bed capacities that are obtained from all the adsorption systems. [22]

$$q_t = \int_{t=0}^{t=\text{total}} (C_i - C_t) dt \times V \quad (7)$$

Where C_i is the initial concentration of MB in ppms, C_t is the concentration of MB at time where equilibrium occurs, V is the feed volumetric flow rate (liter/min) and t is the total flow time (min). Figures 11(a)-(d) show the effect of MB feed flow rates on the breakthrough curves obtained at different bed heights, it was found that the activated carbon bed exhaust faster at higher MB feed flow rates at the same bed height leading to earlier breakthrough due to the quicker saturation of the active sites.

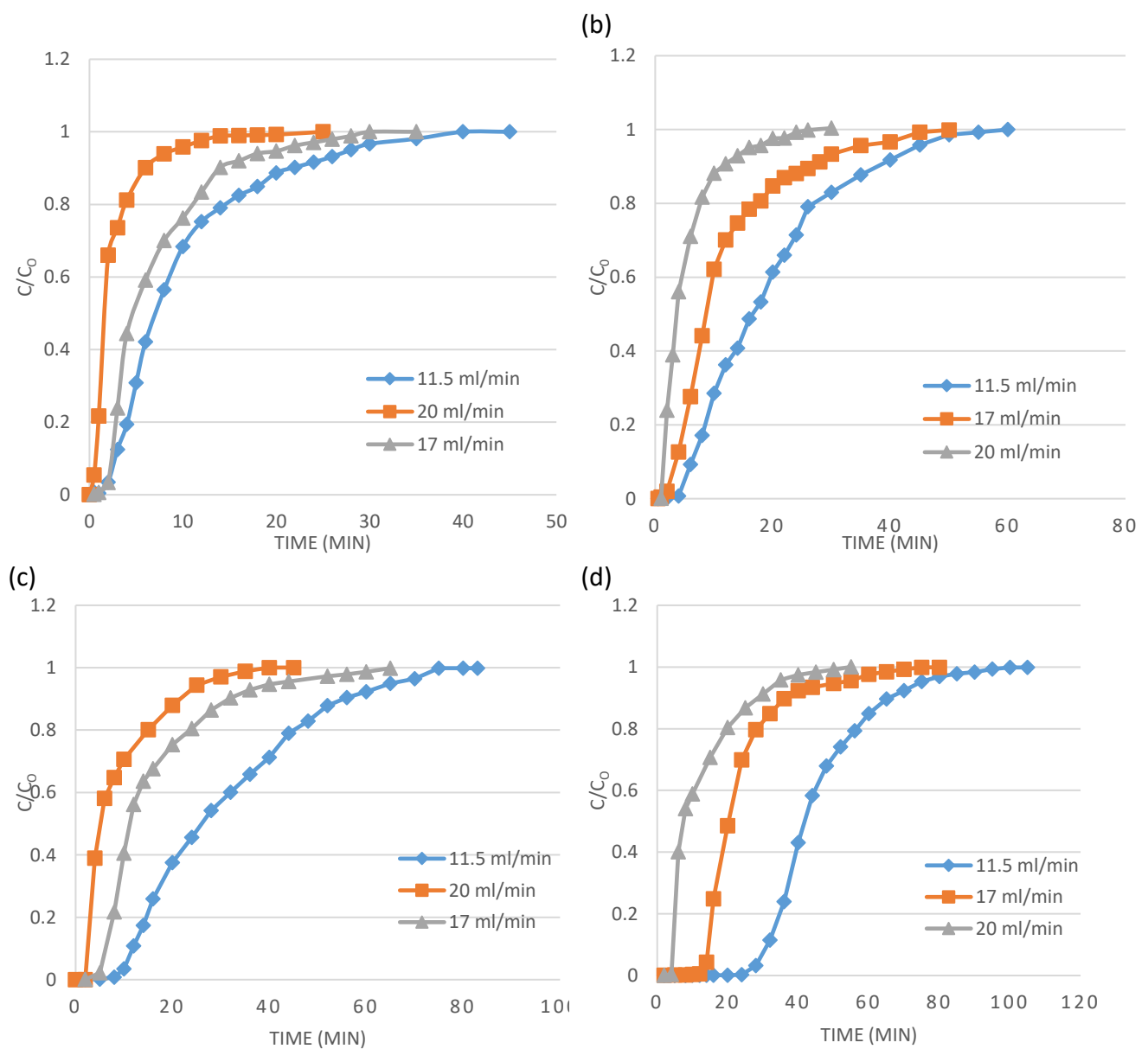


Figure 11. break through curves for MB adsorption at different MB feed flow rates (a) fixed bed of activated carbon bed height 1 cm (b) fixed bed of activated carbon bed height 2 cm (c) fixed bed of activated carbon bed height 3 cm (d) fixed bed of activated carbon bed height 4 cm

Table (2) shows that by increasing the bed height, the maximum adsorption of the column increases and this indicates that by increasing the mass of the adsorbent in the form of higher bed height, it provide a greater surface area of adsorption. Therefore, an increase in the adsorption capacity will occur. The table also shows that by increasing the MB feed flow rate, the adsorption capacity of the bed decreases due to shorter contact time of the MB with the adsorbent, this caused the diffusion of the MB into the pores of the activated carbon to be insufficient. These results agreed with previous work done on fixed bed adsorption system of different activated carbon source ^[23].

Activated carbon bed height (cm)	MB feed flow rate (ml/min)	break through time (min)	bed capacity q_t (mg)
1	11.5	45	86.21
1	17	35	81.43
1	20	25	75.26
2	11.5	60	110.34
2	17	50	103.16
2	20	30	100.25
3	11.5	83	136.17
3	17	65	129.18
3	20	45	124.82
4	11.5	105	205.82
4	17	80	165.42
4	20	55	156.74

Table2 fixed bed adsorption parameters for adsorption of MB on activated carbon prepared from waste newspaper

4 Conclusions

Activated carbon prepared from waste newspaper has been proved as an adsorbent for removal MB from aqueous solutions. MB adsorption was found to be higher in the chemically prepared activated carbon than in the physically prepared activated carbon. The Chemically activated carbon carried out at carbonization temperature 900°C, carbonization time 2.5 hrs. and ZnCl₂ to sample mass ratio=2.5 appeared to be the best activated carbon in terms of equilibrium adsorption capacity which reached 278 mg/g. Equilibrium data were fitted by Langmuir Isotherm model. It was found that the fixed-bed adsorption system become more efficient by decreasing MB feed flow rates and increasing the activated carbon bed height. The present study illustrated that activated carbon prepared from waste newspaper can be an alternative adsorbents for removal MB from aqueous solution.

5 References

- [1] A. Reife, H. S. Freeman. Environmental chemistry of dyes and pigments. John Wiley & Sons, 1996.
- [2] J. Pelgrims, F. De Vos, J. Van den Brande, D. Schrijvers, A. Prové, J. B. Vermorken. "Methylene blue in the treatment and prevention of ifosfamide-induced encephalopathy: report of 12 cases and a review of the literature." *British journal of cancer* 82.2 (2000): 291.
- [3] S. Wang, Z.H. Zhua, A.Coomes, F. Haghseresht, G.Q. Luc "The physical and surface chemical characteristics of activated carbons and the adsorption of methylene blue from wastewater." *Journal of Colloid and Interface Science* 284.2 (2005): 440-446.
- [4] Sohrabi, M. R., and M. Ghavami. "Photocatalytic degradation of direct red 23 dye using UV/TiO₂: effect of operational parameters." *Journal of Hazardous Materials* 153.3 (2008): 1235-1239.
- [5] J. S. Wu, C. H. Liu, K. H. Chu, S. Y. Suen. "Removal of cationic dye methyl violet 2B from water by cation exchange membranes." *Journal of membrane science* 309.1 (2008): 239-245.
- [6] M. Rafatullah, O. Sulaiman, R. Hashim, A. Ahmad. "Adsorption of methylene blue on low-cost adsorbents: a review." *Journal of hazardous materials* 177.1 (2010): 70-80.
- [7] K. Kadirvelu, K. Thamaraiselvi, C. Namasivayam. "Removal of heavy metals from industrial wastewaters by adsorption onto activated carbon prepared from an agricultural solid waste." *Bioresource technology* 76.1 (2001): 63-65.
- [8] J. Laine, S. Yunes. "Effect of the preparation method on the pore size distribution of activated carbon from coconut shell." *Carbon* 30.4 (1992): 601-604.
- [9] D. Kalderis, S. Bethanis, P. Paraskeva and E. Diamadopoulos . "Production of activated carbon from bagasse and rice husk by a single-stage chemical activation method at low retention times." *Bioresource technology* 99.15 (2008): 6809-6816.
- [10] D. Mohan, A. Sarswat, V. K. Singh, M. Alexandre-Franco, C. U. Pittman. "Development of magnetic activated carbon from almond shells for trinitrophenol removal from water." *Chemical Engineering Journal* 172.2 (2011): 1111-1125.
- [11] C. Bouchelta, M. S. Medjram, O. Bertrand, J. P. Bellat. "Preparation and characterization of activated carbon from date stones by physical activation with steam." *Journal of Analytical and Applied Pyrolysis* 82.1 (2008): 70-77.
- [12] T. Wang, S. Tan, C. Liang. "Preparation and characterization of activated carbon from wood via microwave-induced ZnCl₂ activation." *Carbon* 47.7 (2009): 1880-1883.
- [13] L. I. Xiaobing, C. ZHANG, and L. I. U. Jiongtian. "Adsorption of oil from waste water by coal: characteristics and mechanism." *Mining Science and Technology (China)* 20.5 (2010): 778-781.

- [14] V. K. Gupta, B. Gupta, A. Rastogi, S. Agarwal, A. Nayak. "A comparative investigation on adsorption performances of mesoporous activated carbon prepared from waste rubber tire and activated carbon for a hazardous azo dye—Acid Blue 113." *Journal of Hazardous Materials* 186.1 (2011): 891-901.
- [15] M. M. Saleh, A. A. Atia. "Removal of some surfactants from dilute aqueous solutions using charcoal." *Adsorption Science & Technology* 17.1 (1999): 53-63.
- [16] R. Hazzaa, M. Hussein. "Adsorption of cationic dye from aqueous solution onto activated carbon prepared from olive stones." *Environmental Technology & Innovation* 4 (2015): 36-51.
- [17] K. Okada, N. Yamamoto, Y. Kameshima and A. Yasumori. "Porous properties of activated carbons from waste newspaper prepared by chemical and physical activation." *Journal of Colloid and Interface Science* 262.1 (2003): 179-193.
- [18] N. R. Khalili, M. Campbell, G. Sandi, J. Golaś. "Production of micro-and mesoporous activated carbon from paper mill sludge: I. Effect of zinc chloride activation." *Carbon* 38.14 (2000): 1905-1915.
- [19] K. Okada, N. Yamamoto, Y. Kameshima and A. Yasumori. "Adsorption properties of activated carbon from waste newspaper prepared by chemical and physical activation." *Journal of colloid and interface science* 262.1 (2003): 194-199.
- [20] W. Konicki, D. Sibera, E. Mijowska, Z. Lendzion-Bieluń, U. Narkiewicz. "Equilibrium and kinetic studies on acid dye Acid Red 88 adsorption by magnetic ZnFe 2 O 4 spinel ferrite nanoparticles." *Journal of colloid and interface science* 398 (2013): 152-160.
- [21] M. R. Sohrabi, and M. Ghavami. "Photocatalytic degradation of direct red 23 dye using UV/TiO 2: effect of operational parameters." *Journal of Hazardous Materials* 153.3 (2008): 1235-1239.
- [22] A. A. Ahmad and B. H. Hameed. "Fixed-bed adsorption of reactive azo dye onto granular activated carbon prepared from waste." *Journal of hazardous materials* 175.1 (2010): 298-303.
- [23] I. A. W Tan, A. L. Ahmad, and B. H. Hameed. "Fixed-bed adsorption performance of oil palm shell-based activated carbon for removal of 2, 4, 6-trichlorophenol." *Bioresource technology* 100.3 (2009): 1494-1496.

The Role of Users` Participation in the Landscape Design of Business Parks

Sara M. Atwa^{1*}, Mona G. Ibrahim², Ahmed M. Saleh³

¹ Ph.D. student at School of Energy Resources and Environmental Engineering, Egypt-Japan University of Science and Technology (E-JUST), Alexandria, Egypt

² Dean of school of Energy Resources, Environment, Chemical and Petrochemical Engineering, (E-JUST) - Professor of Environmental Engineering, Environmental Health Department, High Institute of Public Health, Alexandria University, Alexandria, Egypt

³ Lecturer in Architecture and Urban Planning Department, Suez Canal University (SCU), Al-Ismailia, Egypt

*E-mail: sara.atwa@ejust.edu.eg or archi_1003@hotmail.com

Keywords: Life quality – Open spaces – Virtual Reality – Mobile Devices

Abstract

Inside the Business park`s open spaces, landscape improves the employees` quality of life and enhances the environmental quality of the community. Occupants play an important role in landscape design and decision-making which is an important key to the correct prediction of the space performance and users` satisfaction. The traditional ways of getting the users` opinion are unreliable as they give a bigger space to the user`s imagination. Virtual reality (VR) helps landscape architects as well as clients to overcome the gap between the virtual design and the real world thus, to enhance the creativity of designers through the development and use of virtual technologies. The main research problem is no clear framework of the design requirements inside Business parks` open spaces was followed in Egypt. Three different landscape design alternatives have been implemented in VR form, then have been explored and evaluated by a sample of users. Another questionnaire for experts was conducted to weigh the users` feedback. The study determines the essential guidelines for sustainable landscape design inside Business parks, which achieve workers` needs, depending on the highest score alternative with specific design criteria. The outcome of this paper offers vital insights on the preferences and community values towards successful Business parks.

Introduction

The renaissance of countries depends on their economy; which confirms the need for convenient office buildings. Business buildings appeared more than 100 years ago, they have been subjected to a lot of developmental stages influenced by subsequent technological changes. The increasing demand for wider offices has necessitated the need for higher buildings, which causes negative impacts on both the ecological balance and demographical balance. Buildings are responsible for the most carbon emissions, followed by transportation and industry. It is estimated that constructions in the Middle East consume 20–25% of primary energy use, 40–45% of electricity consumption and 20–25% of carbon emissions [1]. Not all office tall buildings are compatible with the environmental, social and economic dimensions of sustainability so that they do not contribute significantly to the sustainable development [2]. Therefore, a new worldwide trend newly appears to accommodate business offices, and light industrial corporations grouped together which is called Business park in England, Canada, Australia, China, and Netherlands. Since 2000, Business parks have appeared as a new office buildings` development in the Egyptian cities such as: Smart Village on Alexandria desert road with a total plot area of 3 million m², Cairo Business park in New Cairo with a total plot size of 75,615 m² and Capital

Business park in Al Sheikh Zayed City with a total plot area of 35,000 m²; they allow escaping from the crowd of the capital cities areas to provide a solution for the centralization problem in major cities. They promote a healthy lifestyle and provide employees the opportunity to use a safe and clean workspace through the landscaped areas that are designed within and surrounding the buildings [2]. The significance of Business park, which is a collection of similar architecturally arranged office buildings designed within a large green landscaped area, are usually situated outside the City-Centre where land cost is cheaper and the city pollution is much less. Business parks have positive effects on both employees` health and wellbeing since they provide relaxation, save time and effort, minimize noise pollution, create safe places for work [2]. There is a considerable difference between office environments that are simply not harmful and the positive environments that support health and wellbeing, and encourage productivity [3]. Designing comprehensive, mixed-use communities with appropriate access to employment, education, shopping, recreational opportunities, and health care will help reduce car tours and promote a healthier and more active lifestyle [4].

It is well known that building design, construction, and landscape design are such expensive processes. Any change to layout or materials when built means extra costs, so the clients should have an accurate vision of any structure before the construction process. As to guarantee an efficient workplace for employees, the participation of users become an important issue that should be considered while designing the landscape of Business parks` layout [5]. When the users do not participate in the design process and decision making, the results become unpleasant as architects` vision may be in contrary with the customers` own needs in the spaces. Public involvement is valuable for helping to create improved decisions and a more considerate community plan. Public Participation is significant when persons have more opportunities to influence the decision-making process and feel a sense of ownership for the design plan [6].

Recently published studies start to focus on the importance of users` participation in decision-making of sustainable landscape design process in parks. The most straightforward and common method to describe the design to users is using reports [7], which leave the user to his imagination to construct the project in his own mind. This makes the evaluation more prone to his capability of perception and his cultural background which have an effect on the reliability of the final feedback. Other alternative approaches are proposed to reduce the effect of users` imagination such as supporting the reports with maps [8] or images [5].

The evolution of maps and images leads to use computer simulation as to help the users to realize better the design alternatives which is considered a more reliable method. A computerized visualization technique, either on a computer or mobile devices, offers landscape architects some new ways to support and facilitate policymaking. Designers need a tool to improve the efficiency of communication in the landscape process and users` involvement. Computer Simulated Visualization of the built environment can be the instrument which has an effective means of enhancing the users` participation in evaluating landscape design alternatives [5]. Simulations have always been used for public participation instead of the form of photos, sketches, and models [9]. VR is the most common trend in the modern technologies in various fields like entertainment, medicine, and engineering. This paper proposes the use of VR technology for architects to acquire more accurate feedback to help for taking the right decision of the design criteria.

This paper discusses the design of a sustainable landscape area of suggested Business park in New Borg El Arab City in Egypt. The research can contribute to being a part of the feasibility study of the New Borg El Arab Eco-City (Eco NBC) project. The scope of the study is analyzing the most applicable

solutions for different sectors (industrial, residential, commercial, business and transportation) in NBC for turning the city into an Eco-City [10]. The research approach consists of three different trends in landscape design; Traditional formal design in the first case, while in the second case the design follows the Xeriscape concepts and Biomimicry design for the third one. The study main objective is to use the outputs of public participation using VR technology as a reliable feedback which can help landscape architects in future decision-making to optimize the design to be enhanced for meeting consumers` needs and preferences. Besides, this study utilizes this approach to envision the sustainable landscape guidelines. Furthermore, the research aims to identify the most appropriate simulation software tools in the market and develop an approach to augment users` participation in the process of landscape design of Business parks.

1 Background Literature

(ア) Role of Landscape design in Business Park

Business park`s landscape plays a significant role in the workplace areas which brings people the enjoyment of the beautiful nature, interaction, and recreation [5]. One could say that “landscape is everything” because although over the years, some authors [8] have presented various types and concepts of landscape, they are simply definitions of analytical value, based on a whole in which the human being is an integral part and comprising a specific identity. The user`s knowledge, the landscape formation processes, and the methods it can be influenced become essential in landscape assessment performs. Landscape design, construction, and management should no longer be the result of superficial approaches based exclusively on ideas of designers and planners. In order to measure accurately, the assessment should be supported by the application of users` participation techniques about their opinion and perceptions of the site, not only depending on the experts` attitude [8].

(イ) User`s participation as a decision tool

Public participation is the involvement of people in the creation and management of their built and natural environments [11]. Its strength is that it cuts across traditional professional boundaries and cultures. The activity of user/visitor participation is based on the principle that the surrounding environments work better if people are active and engaged in its formation instead of being treated as passive consumers [5]. Participation is challenging but it is necessary to help planners make better judgments and a more thoughtful community plan. The Public contribution plan can make the most effective use of limited general budgets and time [6]. The previous results demonstrated the strong willingness towards participation despite socioeconomic variations.

Ikhwan, Saruwono et al. [7] discussed that it is important to identify who participates and who will be affected by the decisions made particularly by the professionals. Although the public is engaged in the difficult design process, it may not be a representation of the “public” itself. Shan [12] conducted face-to-face questionnaire surveys at 24 green sites across urban China with 595 respondents successfully interviewed. The positive findings supported driving the local governments to be more open, inclusive and develop effective governance strategies and mechanisms to promote public participation in urban green spaces decision-making. Jausus [13] introduced the community sharing as a strategic approach in landscape maintenance in order to create vibrant open spaces in Malaysian towns. He identified the barriers that cause lack of users` participation in landscape maintenance, the factors that encourage public involvement in landscape maintenance; and the development concept of public participation as a tool in landscape maintenance.

Borazjani and Abedi [14] proposed a systematic guideline to find participant's requirements and the relationship between the design and the contribution in the 3 stages of the project process. In order to develop a sustainable landscape design, the model was established to meet sustainability in architecture and planning, which was examined in the case of Iran, Tehran. A Qualitative Research Method was adopted which was being supported by depth interview technique with a questionnaire. Therefore, they set the users' requirements according to the main criteria which are access and connection, safety, health, sociability, and vitality. Shuib, Hashim et al. [15] recommended that employing Q-methodology in getting public opinion on issues relevant to the research would increase awareness among the local community groups to preserve the values and amenities of the park and its environmental setting which offer essential insights on the community values towards successful parks.

(ウ) Visualization by Computer Simulation and Mobile Devices

The difficulties in communication between the users and the decision makers lead to uncertainty and lack of consistency in landscape processes. The audience can accept a simulation if they are aware of the fact that it is only a limited visualization and when there is a model involved, there is always a reduction [5]. The visualization in landscape projects is needed in order to support communication between designers and consumers. Design changes are easier and less expensive for the architect than with hand drawings, builders can avoid expensive mid-project changes, clients get a realistic image of the final product allowing them to understand and move forward with the project, and the design team can observe their project within a safe environment and make changes as and where it is necessary [5]. Landscape visualization is an image of the real world that can be displayed as 3D simulations with various levels of realism, also it always saves both time and money [9]. Landscape imagining makes it possible to display scenes that are non-existing, these can be represented as static, animated or interactive scenes and immersive or outside of context. The findings from the previous studies suggested that visualizations can enhance public participation by allowing people to meet experts and professionals for proposed projects [9].

W. Shen and Q. Shen introduced an outline of a user activity simulation and evaluation model (UASEM), which aims to mimic and predict the scenario of customers' actions in 3D virtual environments. Users and architects can evaluate the geometrical and topological attributes of the spaces in office buildings during the early design phase. Thus the suggestions were generated after the evaluation, which can be used to optimize the space planning of the office building. For the aim to facilitate the users and architects to specify their requirements and evaluate the design, an assessment system containing subjective and objective indicators was also introduced [16]. Various tools have been adopted and improved by this transformation process as technology advances.

The advances in the computing field and mobile platform have led improvements in landscape visualization and interactivity on Mobile Devices (MDs). MDs become a vital part of our daily life owing to the advantages in many fields ranging from communication to navigation [9]. MDs are still not as capable as computers for performing tasks because of their weakness and limitations in display, detail and realism, immersion, connectivity, speed & processing capability, small size screen, and usability (as a mobile device usually allows only one person to display the visualizations unlike larger panoramic screens that can serve multiple audiences simultaneously) [17]. Also, they have the advantages of ubiquity, portability, availability, accessibility, interactivity and being lightweight, and context-aware compared to their predecessors. Unlike computers, MDs give more freedom to users without requiring any kind of dedication for place and time of use. The simulation techniques can be supported by the

new capabilities of mobile devices; these advancements with the help of interactivity on mobile devices, support engagement during a visualization process [9]. MDs also give users a better understanding of a space or plan by letting them move between and beyond different environments or contexts in order to investigate and evaluate them [17]. Although pre-prepared visualizations have a positive influence on involving the public and enhancing their understanding, there is still need for future research to decide which specific mobile visualization technique is advantageous compared to the rest of other techniques [9]. Bilge, Hehl-lange et al. used iPads, views of stakeholders including hard-to-reach groups, students and professionals are sought regarding the mobile device technology and regarding the new urban park design in Sheffield, UK. Participants were shown a short animated video of a 3D model of the site study and they were asked questions about the mobile device visualization. The study shows that visualization using mobile devices can contribute to enhancing the understanding of the general public; thus creating a broader base for decision-making [18].

From the related studies, it is clear that Virtual Reality (VR) is a suitable computer simulated visualization tool for Landscape design. VR models add interactivity and immersion to landscape but require an appropriate technical input and management [5].

2 Materials and Methods

(A) Case Study Area

The study was conducted in New Borg El Arab City (NBC) as shown in Figure 17, coordinates: 30°51'37"N, 29°34'29"E [19], is situated around 45 kilometers southwest Alexandria downtown area and in the range of seven kilometers from the Mediterranean coast. North of the city is King Marriott resort and Marriott Lake, the atmosphere in the site area is semi-dry Mediterranean atmosphere [20]. This kind of atmosphere is described by a brief, gentle, moderate downpour in winter and long warm summer months with no downpour [21]. NBC is one of the new urban areas whose foundation is commanded in the national arrangement of the Arab Republic of Egypt for the foundation of new urban groups, with the point of retaining the present and future ascent in the populace in Alexandria city. The total area is 47.403 thousand acres of which 30 thousand acres are built up area (residential areas - services - industrial -tourism and recreation ...). The city is surrounded on all sides by a green belt with a surface area of 18,000 acres [19]. New Borg El Arab is regarded as a major urban center because it is a residential-industrial city with a full range of facilities and services [20].



Figure 17: Borg Al Arab location

([http://www.mcit.gov.eg/Egypt Maps](http://www.mcit.gov.eg/Egypt_Maps) , <https://www.google.com.eg/maps/place/>)

This research introduces the design of sustainable landscape area of a suggested Business park nearby the planned Smart Village as shown in Figure 18, with regard to the climate of New Borg El Arab City. In the first case, the design is Traditional-Formal landscape (Figure 19, Figure 20) which is characterized by clean, clear, symmetrical, and rectilinear forms. The design consists of large green areas, lawns, trees, flowers, shrubs, pergolas, high quality seating decks, pedestrian paths, fountains, trash bins, and services like Restaurants. While in the second case, the design is called Xeriscape (Figure 21, Figure 22) which is asymmetric where cactus, palms, native trees, and rocks are commonly used. The plants used need less water and less maintenance. The design contains sandy areas like the desert's nature to minimize the water usage, the seating decks are from recyclable materials, pedestrian paths, recycle trash bins, and Cafés. Otherwise, the third design follows Biomimicry trend in landscape (Figure 23, Figure 24) which is characterized by modern look, informal appearance, curved lines, mixed borders, natural, wild, native and colorful aspects. The used landscape elements are inspired from natural forms. From the sustainability point of view, Xeriscape design, the proposed Alternative 2, is fulfilling mostly of the sustainable landscape concepts in which the used plants require less water for irrigation, need less-maintenance, and are from native species. The materials applied to the park facilities are eco-friendly, the waste is recycled and the garbage is collected in separated trash bins.

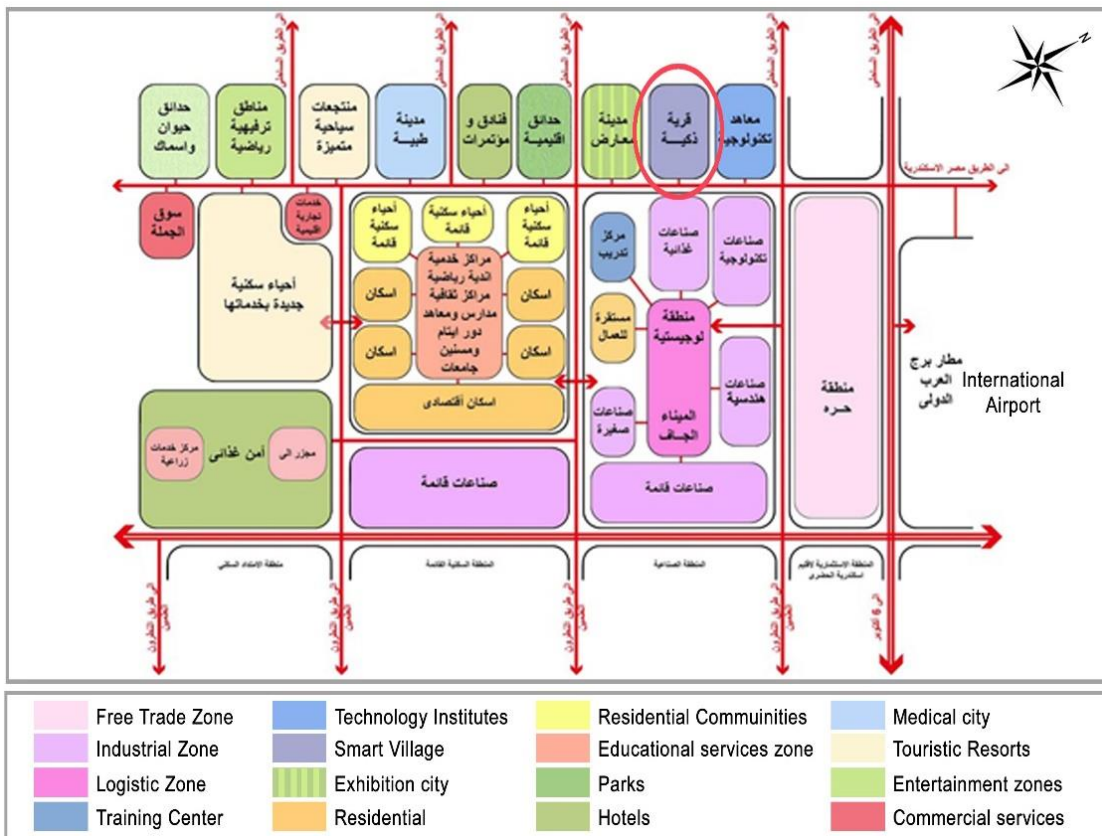


Figure 18: General strategic plan of New Borg Al Arab City

(<http://mmohsen.weebly.com/professional.html>)



**Figure 19: Layout,
Alternative 1**



Figure 20: Perspective, Alternative 1



**Figure 21: Layout,
Alternative 2**



Figure 22: Perspective, Alternative 2



**Figure 23: Layout,
Alternative 3**



Figure 24: Perspective, Alternative 3

(1) Modeling Setup and Preparation

The proposed Virtual Reality consists of 4 phases as shown in Figure 25, the first phase is data collection, determining the design aims, and determining the design alternatives, then phase two is 2D drawing and 3D modeling, the third phase is to generate Virtual Reality model and finally, the fourth phase is navigation through the virtual model using Virtual Reality browser on Mobile Devices wearing VR box.

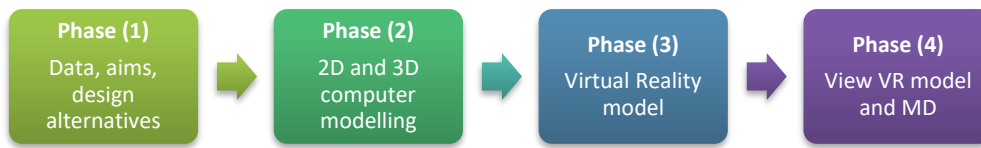


Figure 25: The four phases of Virtual Reality landscape modeling

As shown in Figure 26; firstly, the researcher (or the landscape architect and the designer) creates the three landscape design alternatives on AutoCAD 2015® [22], then are exported to Trimble SketchUp 2015 pro® [23] to produce 3D models of the area owing to the software easy access and easy-to-use interface. After that, all the landscape elements; which are green lush, trees, shrubs, flowers, seating decks, pavement tiles, lighting units, trash bins and other amenities are added to the 3 landscape design models. On SketchUp 2015 pro® [23], the models are rendered by v-ray plugins to get the nearest image to reality and then, they are converted to 360 Panoramic images (Figure 27, Figure 28, Figure 29) to make interactive models that help the participants to visualize the different alternatives before answering the prepared questionnaire, thus to evaluate the 3 alternatives of the case study of landscape design. Afterward, the models are uploaded on a virtual tour website [24] so as to be converted into VR images that can be opened on iPhone mobile devices (Figure 30) or any other mobile device, which enables the user to explore the landscape design through wearing the VR glasses (Figure 31, Figure 32).

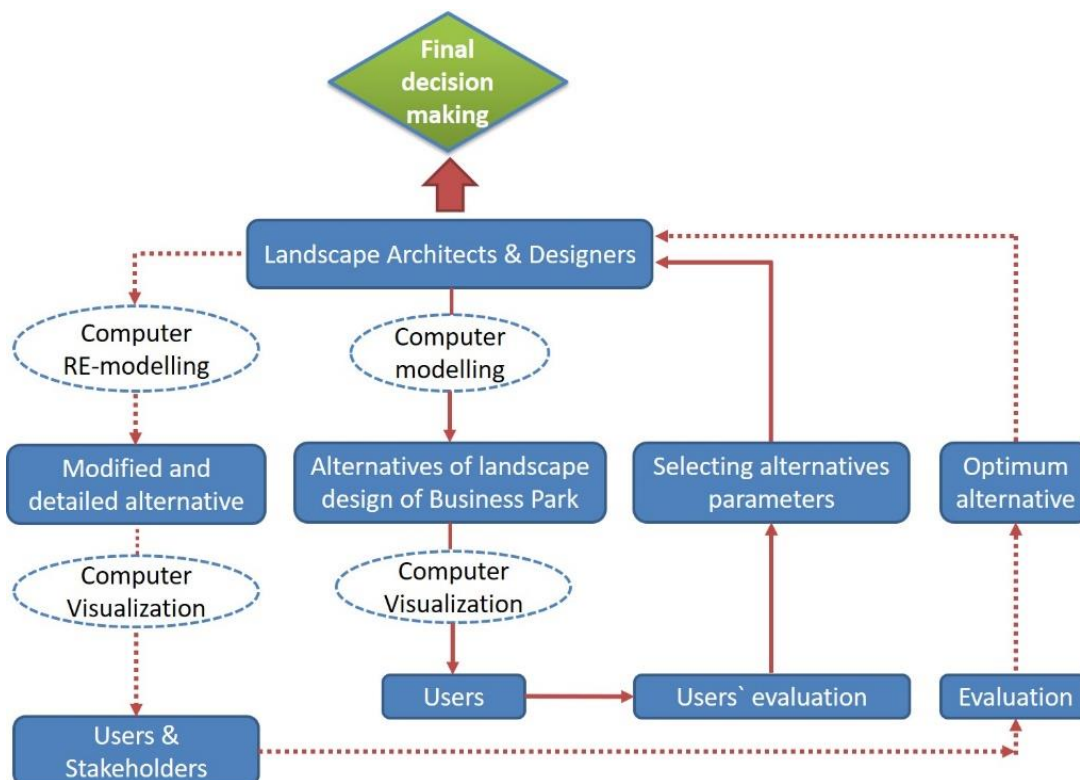


Figure 26: Methodology application framework



Figure 27: 360 panoramic image – Alternative (1)



Figure 28: 360 panoramic image – Alternative (2)



Figure 29: 360 panoramic image – Alternative (3)



Figure 30: Presentation of VR 3D



Figure 31: VR Glasses



Figure 32: Exploring

**model on an iPhone device to
participants**

**the models on VR
Glasses**

The evaluation is based firstly on the experts, ten landscape architects and urban designers who introduce their method of enhancing users` participation. A questionnaire sheet was prepared for professionals which contains general questions related to the function, the suitable mood, and the appropriate style of landscape areas in Business parks. Besides, questions about the four main evaluation criteria of different landscape models in which all are evaluated with specified marks. The evaluation is following the quantitative analysis method that based on scores from 1-5 means poor to excellent then the results were collected and analyzed to give each criterion and sub-criteria a relative weight. The list of sub-criteria groups is mentioned in the below Table 4:

Criteria	Sub-criteria
Access and Connection (AC)	AC1: Accessible and welcoming entry AC2: Walkable, safe and convenient AC3: Private paths for handicapped people AC4: Connection between paths and water AC5: Improve visual access AC6: Having continuity diverse AC7: Enhance lighting at night
Comfort (C)	C1: Safety and security C2: Privacy C3: Harmony with nature C4: Attractiveness C5: Sense of beauty C6: Flexibility of spaces C7: Landscape elements high quality
Activities (A)	A1: Enhance passive and active uses A2: Variety of recreational uses A3: Enough spaces for activities A4: Functional landscape A5: Attraction of users A6: High-quality landscape amenities A7: Availability of cafes, stores, Gym
Sociability (S)	S1: Welcoming places S2: Liveliness spaces S3: Create cooperative environment S4: Improve participation S5: Interactivity between users S6: Improve health and wellbeing S7: Feeling with space ownership

Table 4: The evaluation criteria and sub-criteria of Landscape Design of Business Parks

The targeted users are between varieties of socioeconomic characteristics. The sample consists of teaching staff, employees, accountants, engineers, architects, urban planners, and landscape designers. The participants are between the ages of 25-50 years old, males and females. While the user is wearing the VR glasses, he should answer some questions in the prepared questionnaire. The sheet is designed to ask the sample after completing the navigation through every model from the three virtual reality models, so the survey sheet will be filled three times. Before the navigation, the questionnaire begins by a simple introduction informing the users about the main aim of the research and asks the sample some personal questions about name, age, job title, and address. The next step presents a typical questionnaire sheet, which consists of questions related to the expected function, the preferred landscape style, the suitable mood, the favorable plant type and color, and the compatible paving materials. The following part presents questions related to the four main evaluation criteria for the 3 alternatives which are: access & connection, comfort, activities, and sociability.

(ウ) Statistical analysis

After finishing the survey, the answers were collected and exported to statistical software to analyze the participants' feedbacks based on the experts' ones to determine the preferred alternative. The analysis procedure is detailed below based on well-known statistical concepts [25].

When analyzing landscape elements it can be noticed that not all elements have the same criteria and each criterion does not have the same relative weight. Those weights are deduced from the experts' questionnaire answers. Let the total number of sub-criteria from all the four categories to be denoted by L . The weight of a sub-criteria (i) is calculated from (M) experts' answers as follows:

$$w_i = \frac{1}{M} \sum_{k=1}^M e_k(i)$$

Where $e_k(i)$ is the feedback of expert k for the sub-criteria i . This absolute weight is normalized over all the weights to be converted into the percentage from, the normalized weight for a sub-criteria i is given by:

$$W_i = \frac{w_i}{\sum_{i=1}^L w_i} \times 100\%$$

The previous equation calculates the relative weights to be multiplied by the users' feedback. The average feedback from all the N users for a certain sub-criteria i is calculated by:

$$U_i = \frac{1}{N} \sum_{k=1}^N u_k(i)$$

Where $u_k(i)$ is the feedback of user k for sub-criteria i . Hence, the weighted evaluation of a sub-criteria i of an alternative a :

$$E_i(a) = W_i U_i$$

The final accumulated score of an alternative a is produced by a simple addition process, other accumulation criteria may be applied:

$$S_a = \sum_{k=1}^L E_k(a)$$

3 Results and Discussion

When participants were asked if they are willing to use mobile devices (iPhone, iPad, smartphone, tablet etc.) as part of designing and the decision-making process, 86% of them deeply preferred. This means that they are completely compatible with the new technologies application in the design process. It is more easy and time-saving to use the smart developed simulation software on users for accurate judgment. For a better illustration of all sub-criteria evaluation, a radar format of the results is shown in Figure 33, the chart plots the absolute average of each sub-criteria evaluation on a scale from 1 to 5. This chart introduces a good representation so that the results can be visually analyzed and the points of strength and weakness of each alternative are observed clearly. As noticed, Access and Connection (AC) aspect is the most dominant, about 27%, followed by Activities (A) criterion, about 26%. The percentage ratios among all criteria are considered approximately close; which means that the four criteria are relatively important and essential in landscape design assessment. The participants give high marks to the paths that should be safe and convenient, and the importance of the high-quality appearance of landscape elements. They are interested in the features of improving the visual access to the park and being welcoming and liveness space.

The relation between the three alternatives and the total gained scores according to the users' opinion is represented in Figure 34, which shows the final scores of all alternatives reveals that alternative 3 has the highest score succeeded by alternative 1 then finally alternative 2 with scores approximately 39%, 34%, and 27% respectively. Even though alternative 2 is the most sustainable design for the landscape case study, most users preferred alternative 3 which was designed mainly targeting high sense of beauty and to be like a piece of nature. Biomimicry landscape design makes the users feel more comfortable, as they declared, due to the rich colorful elements, high-quality amenities, and cheerful aspects. Besides, alternative 2 is designed giving a higher priority for applying the sustainability concepts over the other aspects. A result is that its sustainable-oriented components do not satisfy the users' preferences and needs. As known, the sustainability is a worldwide trend nowadays in landscape architecture design. However, it seems that the Egyptians who are targeted by this case study have less awareness of the important sustainable design concepts found in alternative 2. The way of thinking of the mentioned sample is not developed enough to cope with the trendy sustainable landscape design concepts. The effect of such way of mind perception makes them find their comfort and relief in the components of rich luxurious design, such as colorful elements, wide open areas, water elements, high-quality landscape amenities ... etc. Sustainable design elements did not acquire the attention of the selected sample of users as much as the unsustainable ones that basically focus on providing recreation using a lot of green areas with higher water consumption. People preferred the new modern landscape style with the organic curved lines more than the traditional formal design although both designs afford the same elements and services.

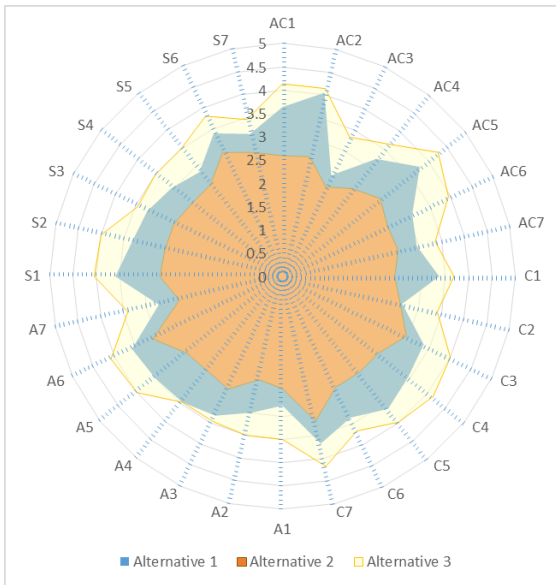


Figure 33: Radar technique format for comparing the 3 alternatives, displaying how public users evaluate in details the criteria of the landscape assessment in the participation process

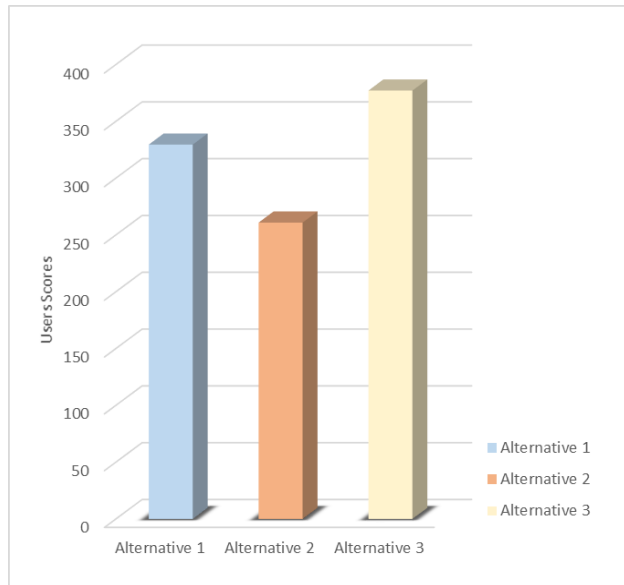


Figure 34: Alternatives evaluation by users, the selected one is Alternative (3)

It can be concluded that a new approach can be formed in landscape design of Business parks in Egypt. For applying the sustainability concepts in the Egyptian society, the design should be covered by an outer layer of the favorable design elements to achieve the integration between the sustainable core and the best visual scene. For example, the rocks should have a colorful texture and the green areas could be expanded but with less water consumption elements. The trees and palms would be from native species with variable colors. The water channels ought to appear which can serve the irrigation process and generate energy or electricity for the lighting units and cafés. Therefore, the optimum design is achieved by merging the highest score alternative scene with the sustainability aspects from alternative 2 in the design core. The future work includes implementing this suggestion in a design model and evaluates it using the same followed ways in this paper to figure out if the new design approach is promising. A list of main design guidelines for sustainable landscape elements for Business parks are conducted as shown in the following Table 5:

Element	Aspects
Layout	Prepare a long-term 'master plan' be able to control and adapt the environment
	Compliance with environmental regulations
	Minimize energy demand for the site through orientation
Vegetation	Implement a plan for natural flora and fauna to maintain the ecological balance of the site
	Use of deciduous plantings for shading purposes
	Plant trees for heating or cooling needs

	Use local and adaptive plants
	Use plants need less maintenance
	Replant existing trees or plants in site
Water	Design water flows to conserve resources
	Collect rainwater for re-use
	Use irrigation systems for water rationalization
	Use gray water for irrigation
Soil	Use safe soil that doesn't need harmful pesticides
	Use the local and native soil
	Use soils that need less water
	Use long term soils without decaying
Waste	Establish a plan for solid waste management
	Reduce toxic materials risks through integrated site-level waste treatment
	Use wastes as potential products to be reused within the park
	Use separated trash receptacles
Materials	Ensure maximum re-using and recycling of materials
	Create space for sorting and storing recyclable materials
	Use local and recyclable materials
	Use materials that need less maintenance
	Use durable materials

Table 5: List of design guidelines for sustainable landscape elements of Business parks

4 Conclusions

Three different landscape design alternatives have been conducted on 2D and 3D software program, then are converted into interactive VR images. A sample of users evaluate the alternatives while exploring the designs using a VR box and a mobile device (iPhone) succeeded by answering a questionnaire to select the best chosen one. Previously, a prepared experts' questionnaire were applied to give relative weights to the landscape design evaluation criteria and sub-criteria. The public interacts well with VR box, that is proved to be an easy and a successful method to reach the accurate opinion of workplace's users, which helps to enhance the whole design process. VR boxes and mobile devices save time in spreading the alternatives faster among a large number of participants through social media. Sharing the virtual experience improves the participation among designers, users, and other stakeholders in the landscape design project; thus achieves transparency in the design procedures and decision-making and consequently, reduce any misunderstanding in the design development. There is a strong potential for 3D mobile device visualization to contribute to the public participation enhancement and design scenarios including social employees, stakeholders, professionals, and businesses. The outputs of users' evaluation are used as a feedback to help landscape architects in decision-making to get the optimum design alternative fitting the users' preferences. The research creates a methodology, from landscape experts and users, should be tracked while evaluating the sustainability of landscape design in the new and future workplaces environment. The analysis considering both the users' participation questionnaire and the landscape assessment by specialists allowed the researcher to determine new ways of merging sustainability concepts within visual amenities that people mostly feel comfortable. The obtained results show that it

is more efficient not to depend only on landscape architects` point of view but also should involve the space users.

Acknowledgements

The first author would like to thank the Egyptian Ministry of Higher Education (MoHE) for providing the financial support (Ph.D. scholarship) for this research, as well as the Egypt-Japan University of Science and Technology (E-JUST) for offering the facility and tools needed to conduct this work. I, also, would give my appreciation to Eng. Osama Talaat Ibrahim (Lecturer assistant and Ph.D. student at Computer Science and Engineering Department in E-JUST) for doing the statistical model analysis and for his valuable support. Furthermore, deep thanks for all cooperated landscape designers and my colleagues who involved into discussions and participation in the questionnaire.

References

- [1] I. A. Gelil, Energy Demand Profile in Arab Countries. Energy Today, 2015.
- [2] S. M. Atwa, M. G. Ibrahim, and A. M. Saleh, "Green Business Parks towards Sustainable Cities," in 8th Conference on Sustainable Development & Planning, 2017.
- [3] AMRP, "Sustainable business parks (Strategies and actions)," 2012.
- [4] D. Stone, "Health and Nature : the sustainable option for healthy cities," no. August, 2016.
- [5] A. Saleh and U. Nassar, "The use of new visualization Tools to Enhance Public Participation in Riverfronts` Landscape regeneration Case Study of Nile riverfront in Cairo," in Green Cities: a Path to Sustainability, 2011, no. December, pp. 10–13.
- [6] D. Miskowiak, "Crafting an Effective Plan for Public Participation," 2004.
- [7] M. Ikhwan, N. Anuar, and M. Saruwono, "Obstacles of Public Participation in the Design Process of Public Parks," Journal of Asian Behaviour Studies, Volume 3, Number 8, 2013.
- [8] L. Loures, A. Loures, J. Nunes, and T. Panagopoulos, "Landscape Valuation of Environmental Amenities throughout the Application of Direct and Indirect Methods," pp. 794–810, 2015.
- [9] G. Bilge, S. Hehl-lange, and E. Lange, "The Use of Mobile Devices in Participatory," Digital Landscape Architecture, pp. 234–242, 2016.
- [10] F. Reda, P. Tuominen, Å. Hedman, M. Gamal, and E. Ibrahim, "Low-energy residential buildings in New Borg El Arab : Simulation and survey based energy assessment," Energy Building, vol. 93, pp. 65–82, 2015.
- [11] J. Wiley, Planning and Urban Design Standards. Canada: John Wiley & Sons, 2007.
- [12] X. Shan, "Attitude and willingness toward participation in decision-making of urban green spaces in China," Urban Forestry and Urban Green., vol. 11, no. 2, pp. 211–217, 2012.
- [13] N. B. Jausus, "Public Participation as a Tool in Public Space Maintenance in Malaysian," Malaysia.
- [14] V. N. Borazjani and M. Abedi, "The Rule Of Public Participation in Sustainable Design Process," International Journal of Asian Society Science., vol. 4, no. 12, pp. 1191–1201, 2014.
- [15] K. B. Shuib, H. Hashim, and N. A. M. Nasir, "Community Participation Strategies in Planning for Urban Parks," in Asia Pacific International Conference on Environment-Behaviour Studies, 2015, vol. 168, pp. 2014–2016.
- [16] W. Shen and Q. Shen, "User Activity Simulation and Evaluation Model for the Improvement of Space Planning in Office Buildings."
- [17] A. Lovett, K. Appleton, B. Warren-kretschmar, and C. Von Haaren, "Using 3D visualization

methods in landscape planning: An evaluation of options and practical issues,” *Landscape and Urban Planning*, pp. 309–314, 2015.

- [18] G. Bilge, S. Hehl-lange, and E. Lange, “Use of Mobile Devices in Public Participation for the Design of Open Spaces,” in *Digital Landscape Architecture*, 2014, pp. 309–314.
- [19] New Urban Communities Authority, “New Urban Communities Authority Portal,” 2015. [Online]. Available: http://www.newcities.gov.eg/english/New_Communities/Borg_Arab/default.aspx. [Accessed: 22-Apr-2017].
- [20] Ghada Elshafei, A. Negm, M. GamalEldin, and M. Bady, “Towards a Green Building : a Preliminary Study of Natural Ventilation on Thermal Comfort and its Impact on Residential Building in the City of New Borg El Arab,” in *ICESA*, 2017, no. May 2016, pp. 210–215.
- [21] K. S. Essa and S. M. Etman, “On the relation between cloud cover amount and sunshine duration,” *Meteorol. Atmos. Phys.*, vol. 240, pp. 235–240, 2004.
- [22] Autodesk, “AUTODESK,” 2015. [Online]. Available: <http://www.autodesk.com/education/free-software/autocad>. [Accessed: 21-Apr-2017].
- [23] Trimble, “SketchUp,” 2015. [Online]. Available: <https://www.sketchup.com/>. [Accessed: 21-Apr-2017].
- [24] Easypano Holdings, “Easypano,” 2017. [Online]. Available: <http://www.easypano.com/>. [Accessed: 21-Apr-2017].
- [25] W. Feller, *An introduction to probability theory and its applications*, vol. 2. John Wiley & Sons, 2008.

Improving Water Management inside the Middle East Oil Refinery "MIDOR"

S.ElSherbini^a, H.A.Farag^b, E.Ashtoukhy^c

^aMiddle East Oil Refinery, Amreya Free Zone, El King Marriott, Alexandria, Egypt

^bAlexandria University, Faculty of Engineering, Lotfy El-Sied st. Alexandria

^cAlexandria University, Faculty of Engineering, Lotfy El-Sied st. Alexandria

E-mail address: ssherbini@eprom-midor.com.eg, phone +201005031793

Abstract

This work involves applying water management inside MIDOR oil refinery. MIDOR Plant was designed with water optimization concept, but there is always a gap of improvement and modification after plant operation. The study targets the use of recent and updated technologies and modifications in water treatment to achieve optimization of water use. This was done in three steps; The first step is water conservation which focuses on reducing water consumption by optimizing plant operation to reach the design condition and upgrading current equipment to enhance the water reduction process, the second step is the re-use of effluent from one stream in another areas without any change in its quality and the last step is the recycling of water by reusing from plant streams or final effluent as make up or feed to specific streams after improving its quality. These were done by applying a specific treatment program like treating the final effluent (end of pipe) with Reverse Osmosis (RO), Ultra Filtration (UF), Nano Filtration (NF) or other technologies. 5 schemes were studied & involved the use of Zero Liquid Discharge (ZLD) package after using a primary first stage RO which means that no water is going to leave the plant boundary. The Process involves a brine concentrator and/or crystallizer and processing all the wastewater to solids. The study aimed to achieve the highest possible water recovery, and economically wise like low capital investment and reasonable operating, maintenance costs and payback period. The best scheme chosen involves the use of Brine Concentrator followed by Crystallizer then land filling with 99.8% water recovery, in addition to the lowest capital investment, operating and maintenance costs.

Keywords: Water Management in Oil Refineries ; Water Conservation-Reuse-Recycling ; Applying Zero Liquid Discharge in MIDOR Refinery; End of pipe treatment ; Environmental awareness.

5 Introduction

There are many water related challenges facing Egypt. As the population continues to grow steadily and development efforts intensify in order to produce food and raise standards of living, As applying the National Water Resource Plan placed on 2010 by the Egyptian government to face water scarcity, ministry of petroleum gave an order to the petroleum processing companies (petrochemical, gas and refining) to make a study of water management inside each company. This study targets the decrease of water used in the industrial applications, MIDOR oil refining uses from 540 to 570 m³/hr in different refinery applications like Demi-water, Fire water, Service water and cooling water. So, there were few areas where optimization can be applied, utilized to gain water savings and reduce water discharge. The water optimization can be divided into three steps like Water Conservation, Water Re-Use and Recycling.

During the lab analysis it was found that the temperature of non oily sewer needs to be decreased at the final collecting sump, so a decision was taken to treat the effluent after mixing with oily water one

which has a lower temperature, to reach 230 m³/hr total flow. It is worth to mention that, non oily water analysis found small traces of oil after mixed together in the non oily final sump.

It is proposed to introduce the 230 m³/hr to a filtration package followed by a conventional first stage Reverse Osmosis Unit [1]; the feed must be free of any oil after passing through the activated carbon filters. The treated water total dissolved solids TDS is about 2000 ppm as appeared in the lab analysis. This feed with the lab analysis result was simulated in more than one (reverse osmosis design model) to know the normal and maximum permeate recovery that appeared to reach TDS figure between (12000-16000) ppm. the concentrate is then introduced to zero liquid discharge package which means: No water leaving the plant boundary, this Process involves a brine concentrator and/or crystallizer of wastewater all the way to solids.

6 Technical Schemes and Methods used for the study comparison

There are five general commercial processing schemes used in many wastewater ZLD facilities with individual processing steps for treating wastewater in these schemes include: (Brackish RO -Lime softening -Thermal brine concentrator -Thermal crystallizer-Spray dryer (used only for small flows) - Evaporation pond- Landfill). Product water is produced from the 1st stage RO, brine concentrator, and crystallizer process steps, followed by a processing step for the wastewater treatment, beginning with concentrate (conc), are as follows:

Scheme 1A: conc → BC → EP

Scheme 1B: conc → BC → CRYST → LF

Scheme 2A: conc → LS → RO → BC → EP

Scheme 2B: conc → LS → RO → BC → CRYST → LF

Scheme 3: conc → LS → RO → EP

Solids produced from lime softening also go to a landfill. Possible small-volume purge from the crystallizer would go to an evaporation pond. The capacity of RO and the filtration package are 1 Mgd in addition to this a 0.4 Mgd Concentrate capacity directed to zero liquid package.

7 Results and discussion

6.1. Proposed and Implemented Modifications

6.1.1. Implemented Modifications:

- Conservation: partially implemented by reducing cooling water (C.W) blow down by increasing the cycle of concentration (C.O.C) to 2.8. (3D TRASSAR Monitoring system +Recovery of quenched blow down (B.D) from boilers) [2].

- Reuse: Reuse of stripped water instead of service water in Flare seal pot for gas absorption purposes.
- Recycle: Recycle treated effluent waste water to the Coke dust suppression system and to the irrigation system.

6.1.2. Proposed Modifications in the near Future:

- Reuse/ Conservation: Reuse of stripped Water instead of service water for Coker quench water /cutting water.
- Reuse: Replacing Clean Condensate used as Wash Water in Hydro-treating units with Stripped Water.
- Recycle: Recycle Treated Effluent, after treatment (UF-NF/RO) and use it as a source for demineralization or cooling system make up, which represent more than 75% of plant water consumption ,but the more economic solution will be directing the permeate towards the Cooling tower to achieve the 2.8 C.O.C as mentioned in the implemented modifications. See Figure 1

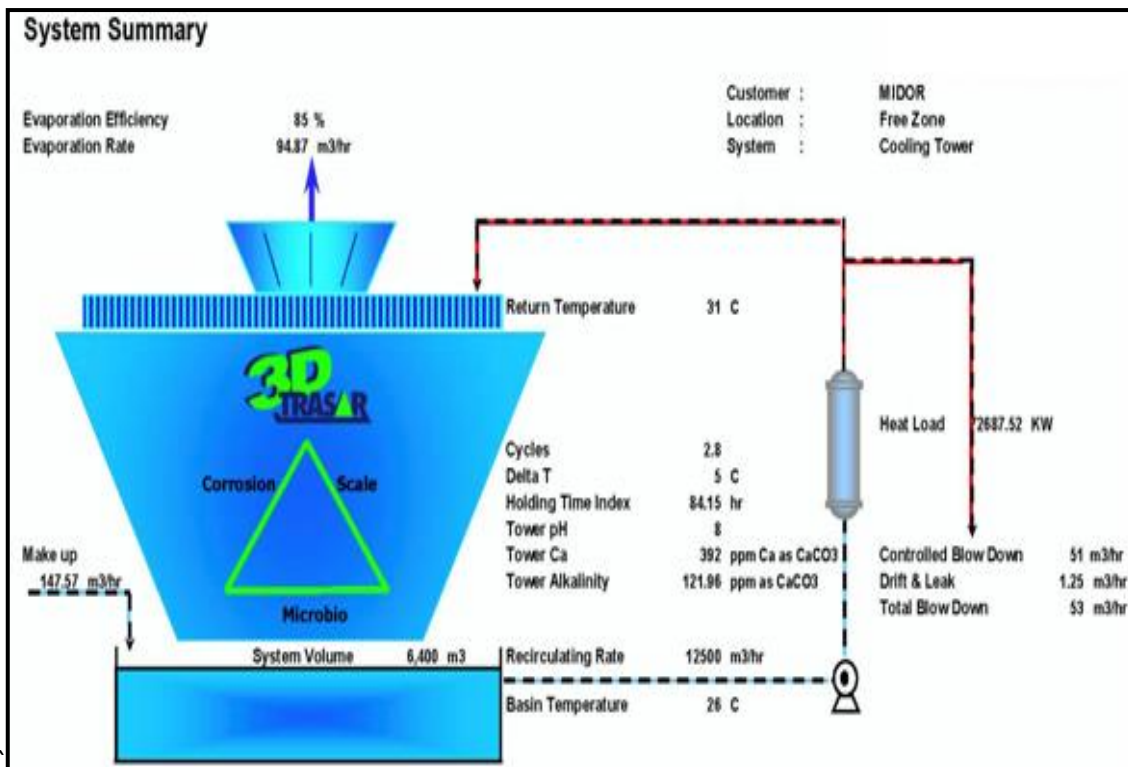


Figure 1 Cooling tower system summary for 2.8 cycle of concentration

6.2. ZLD System Costs

System size has a relatively small effect on unit system costs (dollars per MGD). Large system sizes require multiple equipment modules for RO, brine concentrator, and crystallization components, thus minimizing the economy-of-scale factors more typically associated with increasing the size for individual modules. Evaporation ponds and landfills have a minimum economy of scale. Thus, overall

there was little economy of scale influencing the total costs. Negotiated cost reductions on large orders of equipment may change this picture somewhat, but this possibility was not taken into consideration.

Probably the most widely known cost index to the general public is the Consumer Price Index (CPI) generated by the U.S. Department of Labor, Bureau of Labor Statistics. While the CPI could probably serve our needs, more specific data is available for use in engineering and technical applications. Cost indices are useful when basing the approximated cost on other than current prices. If the known cost of a piece of equipment is based on, for instance 1991/2006 prices, this cost must be multiplied by the ratio of the present day index (2015/2016) to the 1991/2006 base index in order to proportion the value to present day in dollars (See equation number 1 which represents the Cost Indices for updating the cost estimation). The Rule of Six-tenths was used to get an approximate cost of a similar item of different size or capacity is known. A rule of thumb developed over the years known as the rule of six-tenths gives very satisfactory results when only an approximate cost within plus or minus 20% is required as represented in equation number 2 for updating the unit capacity [3,4].

- **Cost Indices equation**

$$C_2 = C_1 (\text{Index}_2 / \text{Index}_1) \quad (1)$$

C_2 = Required cost of facility in required year

C_1 = Known historical cost of facility in reference year

Index_2 = Required year cost index

Index_1 = Reference year cost index

- **Rule of Six-tenths equation**

$$C_B = C_A (S_B / S_A)^{0.6} \quad (2)$$

C_B = the approximate cost \$ of equipment having size S_B

C_A = the known cost \$ of equipment having corresponding having size S_A in reference year

S_B = Required cost of facility in required year

S_A = Known historical cost of facility in reference year where S_B/S_A is the ratio known as the size factor, dimensionless

6.2.1. Relation between salinity and economics:

Concentrate salinity and composition had significant effects on unit capital costs (dollars per MGD), operating costs (dollars per year per MGD) for the five processing schemes. The significant effects of salinity and composition on individual process step performance translate into wide variations in equipment size and capital costs as well as operating costs. The result of adding up capital and

operating costs for the five processing schemes and normalizing these costs based on process size (feed MGD) revealed the following:

1. The processing (Scheme 2B) with crystallizer was more expensive than the processes without the crystallizer step.
2. The processing schemes with lime softening and second-stage RO (Schemes 2A, 2B, and 3) were nearly less expensive than the cases without a second-stage RO. Volume reduction prior to the application of thermal brine concentrators is nearly always cost-effective.
3. The processing scheme most consistently of lowest operating and maintenance cost was Scheme 3, where there was no thermal evaporation equipment used. This was due to the fewest processing steps and the low operating cost of evaporation ponds.
4. The processing scheme most consistently of lowest capital cost was Scheme 1B than scheme 2A&2B, in which volume reduction by lime softening and second-stage RO preceded further volume reduction by the brine concentrator.
5. Scheme 3, without any thermal evaporative steps, had a relatively high capital cost due to the relatively larger evaporation pond acreage.
6. The processing scheme most consistently of lowest annualized cost was Scheme 2A, the system with lime softening, second-stage RO, and brine concentration.
7. Costs for the original ZLD processing Schemes 1A and 1B may be cost-competitive for higher-salinity feed waters.
8. Capital costs for evaporation ponds and landfills can be significant. They were frequently the highest individual capital cost process step and the highest source of capital cost variability among the processing schemes and cases studied.

Table 1 Summary of all capital, operating, costs for all processing schemes

Scheme No. versus Recovery	Scheme 2A		Scheme 1A		Scheme 2B		Scheme 1B		Scheme 3	
	Nelson &	CEPCI	Nelson &	CEPCI						
Capital Cost M\$	19.68	16.66	19.82	16.77	21.19	20.61	19.61	16.60	24.53	20.91
Annual O&M Cost M\$	2.11	2.06	1.87	1.82	2.27	2.22	1.84	1.80	1.53	1.50
Water Recovery %	92.3		95.4		100		99.8		81	

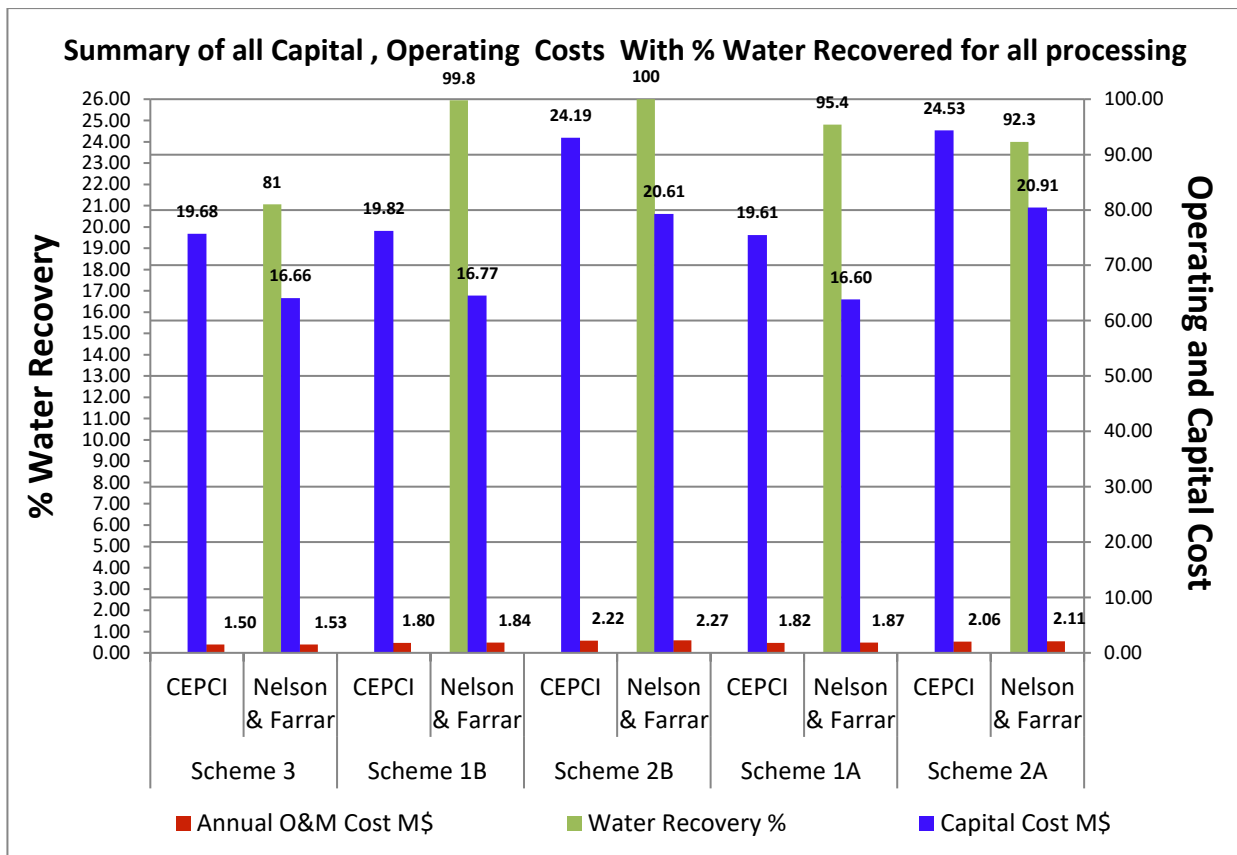


Figure 2 Summary of all Capital, Operating Costs With % Water Recovered

8 Conclusions

As Represented in Table 1, and Figure2 the choice was dependent on:(%Water recovery-lower total capital cost-lower operating and maintenance cost Between 3 schemes: (Scheme 1A-Scheme 2B - Scheme 1B)

The 3 schemes have the best water Recovery among the 5 schemes [5], the % water recovery was 95.4, 100, and 99.8 respectively. The other 2 schemes the water recovery scheme 2A and scheme 3 were discarded due to low water recovery% (92.3, 81) and high capital-operating and maintenance cost.

The capital costs for the 3 schemes were 16.77 M\$, 20.61M\$ and 16.60 M\$ respectively (Referenced to CEPCI Cost index which is closer towards water treatment technology than Nelson and Farrar Cost index).

The operating and maintenance costs were 1.82 M\$, 2.22 M\$ and 1.80 M\$ respectively (Referenced to CEPCI Cost index which is closer towards water treatment technology than Nelson and Farrar Cost index).

The payback period, depreciation and return on investments for scheme 1B was the best among the five schemes.

The total money saving (income cash) from the overall project was 2.99 M\$/year including:

- The water saving from the source with amount of 1.46 M\$/Year (0.85\$/M³).
- Cooling tower chemicals saving achieved by reducing cycle of concentration to 2.8 wasf 0.092 M\$/Year.
- The saving amount of condensate when replaced with stripped water was 1.43 M\$/Year. (Condensate cost 5 \$/M³). As mentioned before in the proposed projects item 3.1.2.
- The water management and Zero Liquid Discharge scope expected to be applied in MIDOR oil refinery is the government and ministry of petroleum strategy in order to decrease the effect of water scarcity in the upcoming days. Also applying this project will give an advantages as:
 - Avoid any pollutant pay policy due to violation of discharging treated waste water towards the Nubaria canal.
 - Gives good reputation to MIDOR oil refinery as applying the latest environmental standards.
 - The water cost for industrial application is expected to be increased 3 times in the upcoming years ^[6].

From all the above points the scheme 1B is the best choice for MIDOR oil refinery that has a high water recovery, the lowest total capital /operating and maintenance.

Abbreviations and Acronyms

BC	Brine Concentrator
CRYST	Crystallizer
C.O.C	Cycle of Concentration
EP	Evaporation Pond
LS	Lime Softener
NF	Nanofiltration
RO	Reverse Osmosis
UF	Ultra Filtration
ZLD	Zero Liquid Discharge

Acknowledgements

It is my great pleasure to express my thoughtful and sincere gratitude to people who assisted, supported and involved to make this case study possible, and I would like to express my sincere appreciation to **Dr. Mohammed Abdel Aziz**, MIDOR Chairman and **Ch. Medhat Bahgat**, EPROM Chairman who provided me the worthwhile support and discussions opportunity to run my experiments, to sample and audit all water drains and wastewater treatment plant all over MIDOR Oil Refinery site. I would like to thank **Dr. Hemdan Noor Eldin** MIDOR Chairman Assistant, who assisted me in choosing the topic of my case study, may his sole rest in peace. **Another special thank** goes to **Eng. Amgad El Ahmady**, Eprom Chairman Assistant for Operation and Technical Studies and **Eng. Sherif Magdy** Technical Assistant General Manger MIDOR site for their technical supports, kind

encouragement, and useful suggestions. Also, I would like to gratitude my wife, parents, father and mother in law, brother, and my relatives for their moral support, endless inspiration, and encouragement in my entire Master study period, as my success as today is a huge contribution from them.

References

1. Anantha P.R. Koppola, Miguel J. Bagajewicza,* , Brian J. Dericksb, Mariano J. Savelskib, On zero water discharge solutions in the process industry, © 2002 Elsevier Science Ltd.
2. James P. McIntyre, Industrial Water Reuse and Wastewater Minimization, 2006, gewater.com, E-mail: custhelp@ge.com.
3. Randall W. Whitesides (CPE) PE 5 ,Process Equipment Cost Estimating by Ratio and Proportion ,© 2012, ,<http://www.pdhone.com/courses>
4. Fredrick T. Moore, economies of scale: some statistical evidence, quarterly journal of economics, volume 73, Issue 2 (May, 1959), 232-245.
5. Alexander Robertson Long D., Treatment of high TDS liquid waste: Is zero liquid discharge feasible?, Nghiem University of Wollongong, longn@uow.edu.au,2011.
6. Thesis (M.SC.) Faculty of Engineering-Department of Chemical Engineering, Improving Water Management inside the Middle East Oil Refinery (MIDOR), Egyptian universities libraries connections © 2016, http://srv4.eulc.edu.eg/eulc_v5/Libraries.

Experimental Investigation of the Air Flow Characteristics through Helical-Spiral Inlet Port having Shrouded Inlet Valve in Diesel Engine under Steady Flow Conditions

A. Abd El Sabor. Mohamed (Corresponding author)

Teaching assistant
Department of mechanical engineering, Faculty of engineering, Assuit university
Egypt, Assuit-71516
eng_ahmedabdelsabor@eng.au.edu.eg

Saleh Abo-Elfadl

Doctor
Department of mechanical engineering, Faculty of engineering, Assuit university
Egypt, Assuit-71516
salehaboelfadl2@gmail.com

Abd El Moneim M. Nassib

Associate Professor
Department of mechanical engineering, Faculty of engineering, Assuit university
Egypt, Assuit-71516
amnassib@yahoo.com

Keywords: Air Flow, Swirl, Discharge coefficient, Helical-Spiral Port, Shrouded Valve.

Abstract

Swirl generation is an important parameter inside the diesel engine cylinder as it achieves good mixing of air and fuel which has a great influence on the combustion efficiency, engine emissions, and soot formation. The generated swirl intensity by the inlet port and the inlet valve configuration is usually measured on a steady flow test rig using an impulse torque meter. In this paper, an experimental investigation using steady flow test rig was performed on an engine cylinder having a helical-spiral inlet port and shrouded inlet valve. Three valve shrouds were used, they are; 120°, 150° and 180°. With each shroud, four orientation angles were used; they are 0°, 30°, 60° and 90°. The experiments were performed under constant cylinder vacuum pressure of 350 mm H₂O. The results showed that using shrouded inlet valve increases the swirl number at all valve shroud and orientation angles except for valve shroud angle of 180° and orientation angle of 90°. Also, using of shrouded inlet valve decreases the mass flow rate and the discharge coefficient at all valve shroud and orientation angles.

Introduction

The inlet port and inlet valve designs are very important parameters in internal combustion engines. The inlet port and inlet valve configuration effect on the volumetric efficiency and the charge flow motion (tumble and swirl) inside the cylinder. Swirl motion has a great influence on the fuel-air mixing process inside the engine cylinder and hence on the combustion process. Increasing swirl ratio improves the combustion process reduces the fuel consumption and the engine emissions.

Many researchers performed experimental and theoretical studies on the effect of the inlet port and the inlet valve geometries on the flow characteristics through the engine cylinder. The most important flow characteristic in ICE are the inlet valve mass flow rate and the discharge coefficient besides the swirl and tumble motion inside the engine cylinder. In diesel engines, swirl motion is a very important parameter in the fuel-air mixing process. The effect of inlet port geometry on the swirl generation studied by CFD simulation in [1-4]. C. Arcoumanis et al. [5] performed an experimental study under steady operating conditions for investigating the effect of using helical inlet port on the flow pattern through the inlet valve flow area and the in-cylinder swirl by using LDA. Razavi and Rabiei [6] studied the effect of the valve lift profile and valve opening duration on the swirl generation and engine performance. A. Maier et al. [7, 8] studied the effect of the inlet valve geometry parameters like valve cone angle, valve seat angle and fillet radius on the flow characteristics through the valve flow area and the discharge coefficient. The results showed that small changes in the valve geometry have a great effect on the flow regimes through the valve flow area. J. Rabault et al. [9] performed an experimental study using the PIV technique for investigating the effect of using two inlet valves on the swirl structure inside the engine cylinder. The results exhibited a clear difference in swirl intensity for high and moderate valve lifts. Many researchers studied the shrouded inlet valve effect with a direct inlet port on flow characteristics specially swirl generation inside the engine cylinder [10-16]. M. Krishna and J. Mallikarjuna [16] performed an experimental study using PIV for investigating the effect of using shrouded inlet valve and the shroud orientation angle about the valve axis on the in-cylinder turbulent kinetic energy and tumble ratio. Yungjin et al. [17] studied the swirl generation and the flow coefficient variations experimentally using four configurations of helical and tangential inlet ports having bypass between them. They used swirl control valve on the tangential port. The results showed

that the swirl control valve has a great effect on swirl generation and using the bypass increases flow coefficient. The effect of swirl ratio on the in-cylinder flow, the heat release rate and soot emissions was studied experimentally and numerically in [18-20]. It was found that increasing of swirl enhances the heat release rate and decreases soot emissions.

Swirl can be measured by impulse swirl meter or by vane swirl meter. D. Heim and J. Ghandhi [21] performed an experimental investigation for studying the performance of both impulse and vane swirl meters under different swirl conditions. Impuls-type swirl meter achieved better agreement between the measured and the known swirl values than the vane-type meter.

However, the inlet port and the inlet valve configurations still need more study for achieving higher values of swirl ratio with a little effect on the mass flow rate and the valve discharge coefficient. In this study, A helical-spiral inlet port and shrouded inlet valve configuration are examined under steady flow condition by using the impulse-type meter. Three shrouded valves having different shroud angles are used at different orientation angles for achieving high swirl ratio and mass flow rate.

The Experimental Setup

A helical-spiral inlet port of single cylinder, Four-stroke diesel engine is chosen as a case study. Figure 1 shows the port design. Three shrouded inlet valves having different shroud angles are examined; the shroud angles are 120° , 150° and 180° . With each shroud angle, the shrouded valve is oriented by four orientation angles; they are 0° , 30° , 60° and 90° . With each valve condition (orientation angle and shroud angle), four valve lifts are considered; they are 3, 6, 9, and 12 mm. Also, an ordinary valve is examined at the same valve lifts and is taken as a reference case. Figure 2 illustrates the ordinary and the shrouded valves. Figure 3 shows the valve position with respect to the cylinder axis, the valve shroud angle α , and the orientation angle β . The mass flow rate, the impulse meter torque, the pressure drop across the inlet valve and the atmospheric conditions are measured at each condition for evaluating the port and the valve configuration. For achieving these measurements, a steady flow test rig setup is constructed as shown in Fig. 4. In this setup, an impulse torque meter is used for evaluating the swirl generation. Table 1 shows the elements of the experimental setup.

In this work, constant value pressure drop across the inlet valve of 350 mm H₂O is achieved through the whole experiments. The swirl meter and the orifice meter are calibrated and the following results are set after taking the calibration process into consideration.

Air flows through the inlet port, passing through the valve flow area due to the evacuation which is produced by the blower. The port and the valve geometries cause a swirl generation inside the cylinder. The swirling air passes through the honeycomb causing it to rotate against the tension springs and rotating the pointer. The tension springs resist the honeycomb rotation and the pointer indicates the resisting torque. The orifice meter measures the mass flow rate and the manometer measures the pressure drop across the port-valve configuration. The control valve achieves a constant pressure drop of 350 mm H₂O through the whole experiments.

Results and discussion

The valve lift and the valve shroud besides the port and the valve configuration have a great influence on the flow characteristics through the valve flow area and through the cylinder. The considered flow characteristics are mass flow rate, discharge coefficient, and the swirl number.

Figures 5 to 7 illustrate the mass flow rate of air through the inlet valve for the ordinary and the shrouded valve cases at the four orientation angles and at the different valve lifts. The horizontal axis is registered in the form (L_v/D_v) which is recommended in flow analysis through the inlet valve. The corresponding values of (L_v/D_v) for the valve lifts of 3, 6, 9, and 12 mm are 0.06, 0.12, 0.18, and 0.24. The solid line represents the ordinary valve and the other lines represent the shrouded valve at the orientation angles of 0°, 30°, 60° and 90°. From these Figs., it is obvious that increasing the shroud valve angle decreases the mass flow rate at all valve orientation angles and valve lifts with respect to the ordinary valve. The maximum decrement occurs at valve condition of 90°-180° and valve lift of 9 mm where the mass flow rate is 38.5 g/s and the corresponding mass flow rate through the ordinary valve is 63.5 g/s with a percentage decrement of 39.5% as shown in Fig. 7. Increasing the orientation angle shifts the valve shroud toward the cylinder middle (see Fig. 3). So, the flow resistance increases which reduce the mass flow rate. The maximum decrement in the mass flow rate occurs at valve orientation angle of 90°.

The discharge coefficient is a dimensionless measure of the inlet valve and the inlet port configuration performance. It is defined as the ratio of the actual inlet mass flow rate divided by the theoretical mass flow rate through the same geometric area under the same pressure drop.

$$C_D = \frac{m'_{act}}{m'_{th}} \quad (1)$$

Where m'_{act} is measured through the orifice meter in Fig. 4 and m'_{th} is calculated according to the one-dimensional isentropic flow of ideal gas from a reservoir through a restrictive area at subsonic flow conditions.

$$m'_{th} = A_{ref} \times \left\{ 2P_o \rho_o \frac{\gamma}{\gamma - 1} \left(\frac{P_c}{P_o} \right)^{2/\gamma} \left[1 - \left(\frac{P_c}{P_o} \right)^{(\gamma-1)/\gamma} \right]^{1/2} \right\} \quad (2)$$

Where P_o and ρ_o are the stagnation pressure and density (the atmospheric conditions) and γ is the specific ratio. A_{ref} is a reference area, it is taken in this paper the valve curtain area as [7, 8].

$$A_{ref} = \pi D_v L_v \quad (3)$$

Figures 8 to 10 represent the discharge coefficient variations with respect to the valve lift for the ordinary valve and the shrouded valve at the previous different orientations. It is obvious that, the discharge coefficient for both the ordinary valve and the shrouded valve is decreased with the increase of the valve lift at all shroud angles. This decrement occurs due to the inlet flow separation from the valve and the port seats. Also, the shrouded valve achieves lower values of discharge coefficient with respect to the ordinary valve at all valve shroud angles and orientation angles due to the shroud resistance for the inlet flow. Moreover, increasing the valve shroud angle decreases the discharge coefficient at all valve orientation angles due to the decrement in the effective area. The minimum discharge coefficient values occur at orientation angle of 90 and valve lift of 12 mm. Their values are 0.33, 0.3 and 0.27 at valve shrouds of 120°, 150° and 180°, respectively.

The swirl number is defined as the flow angular momentum divided by the flow axial momentum. The swirl number is calculated according to the following equation.

$$S_N = \frac{8 T}{m'_{act} v_o B} \quad (4)$$

Where: v_o is the axial flow velocity through the inlet valve flow area under the pressure difference between the engine cylinder and the atmosphere.

$$v_o = \sqrt{\frac{2 \Delta P}{\rho}} \quad (5)$$

Where: T is the torque, which is measured by the torque meter in Fig. 4, \dot{m} is the actual mass flow rate of air and B is the cylinder diameter.

Figures 11 to 13 represent the swirl number variations with respect to the valve lift at shroud angles of 120°, 150°, and 180° respectively. The swirl number of the ordinary valve is plotted in each figure as a reference case. The swirl number increases with the increase of the valve lift due to the increase in mass flow rate. Swirl is created by bringing the inlet flow into the cylinder with an initial angular momentum by the helical-spiral inlet port. The swirl enhanced by using the shrouded inlet valve the shroud forces the entering flow to inlet the cylinder tangentially. Figure 11 illustrates the swirl variation for valve shroud angle of 120° at orientation angles of 0°, 30°, 60° and 90°. The swirl number increases by increase the orientation angle till 60°. At valve orientation angle of 90°, the movement of the valve toward the cylinder middle increases more and more. So, the flow resistance increases and hence the mass flow rate is reduced. As the swirl number represents the angular momentum of the flow inside the cylinder, the decrease of the mass flow rate reduces the angular momentum in spite of the increase of the tangential velocity. So, the swirl number at the orientation angle of 90° is smaller than that at 30° and 60°. Using valve shroud angle of 150° and 180° increases the distance of the valve circumference that covered by the shroud which reduced the valve effective flow area. Also, increasing the orientation angle of these shrouds moves the shroud toward the cylinder middle. So, the flow resistance increases and hence the mass flow rate is decreased. This effect reduces the swirl number with increasing the orientation angle at these shrouds. At the valve condition (90°-180°), the mass flow rate and the discharge coefficient in Figs. 7 and 10 are in their lowest level due to the shroud flow resistance. So, the swirl number at this condition is reduced lower than the ordinary valve case.

Conclusions

An experimental setup based on the impulse torque meter is constructed for investigating the flow characteristics through the inlet port and inlet valve configuration. The measurements are performed under a constant vacuum pressure of 350 mm H₂O. The results can be concluded in the following points.

- 1- Increasing the shroud valve angle decreases the mass flow rate at all valve orientations and valve lifts with respect to the ordinary valve. The maximum decrement occurs at valve orientation 90° .
- 2- The shrouded valve achieves lower values of the discharge coefficient relative to the ordinary valve at all valve shroud angles and orientation angles due to the shroud resistance for the inlet flow.
- 3- Using of valve shroud increases the swirl ratio at the different orientation angles and valve lifts relative to the ordinary valve except the valve condition of (90° - 180°).

References

- [1] S. E. Razavi, S. M. Lashkarpour, and S. Marami, "Enhancement of a Diesel Engine Inlet Port for Pollutant Reduction and Performance Optimization," *J. Engine Res.*, vol. 22, pp. 39–49, 2011.
- [2] A. Rahiman, A. R. R. K, M. S. a D, and M. K. Ramis, "CFD Analysis of Flow Field Development in a Direct Injection Diesel Engine with Different Manifolds," vol. 4, no. 3, pp. 102–113, 2014.
- [3] B. Paul and V. Ganesan, "Effect of Manifold Configuration in Turbulence Inside the Cylinder of a Direct Injection Diesel Engine by CFD Simulation," *Proc. 3rd BSME-ASME Int. Conf. Therm. Eng. 20-22 December, 2006, Dhaka, Bangladesh, 2006*.
- [4] B. Paul and V. Ganesan, "Flow Field Development in a Direct Injection Diesel Engine with Different Manifolds," *Int. J. Eng. Sci. Technol.*, vol. 2, no. 1, pp. 80–91, 2010.
- [5] C. Arcoumanis, C. Vafidis, and J. H. Whitelaw, "Valve and In-Cylinder Flow Generated by a Helical Port in a Production Diesel Engine," *J. Fluids Eng.*, vol. 109, no. December 1987, 1987.
- [6] S. E. Razavi, "The Effect of Valve Lift on In-Cylinder Flow, Performance and Emissions in a Turbocharged DI Diesel Engine," *J. Engine Res. Vol. 18*, vol. 18, pp. 3–11, 2010.
- [7] A. Maier, T. Sheldrake, and D. Wilcock, "Geometric Parameters Influencing Flow in an Axisymmetric IC Engine Inlet Port Assembly: Part I—Valve Flow Characteristics," *J. Fluids Eng.*, vol. 122, no. December 2000, pp. 650–657, 2000.
- [8] a Maier, T. Sheldrake, and D. Wilcock, "Geometric Parameters Influencing Flow in an Axisymmetric IC Engine Inlet Port Assembly: Part II—Parametric Variation of Valve Geometry," *J. Fluids Eng.*, vol. 122, no. December 2000, pp. 658–665, 2000.
- [9] J. Rabault, J. A. Vernet, B. Lindgren, and P. H. Alfredsson, "A Study Using PIV of the Intake Flow in a Diesel Engine Cylinder," *Int. J. Heat Fluid Flow*, vol. 0, pp. 1–12, 2016.

- [10] C. Crnojevic, F. Decool, and P. Florent, "Swirl Measurements in a Motor Cylinder," *Exp. Fluids*, vol. 26, no. 6, pp. 542–548, 1999.
- [11] B. Khalighi, "Intake Swirl Process Generated by an Engine Head - a Flow Visualization Study," *J. Eng. Gas Turbines Power-Transactions Asme*, vol. 113, no. 3, pp. 433–439, 1991.
- [12] P. Baker, S. F. Benjamin, N. S. Girgis, A. W. Newman, and W. A. Seeley, "Characterisation of Barrel Swirl Motion Under Steady Flow Conditions," *SAE Tech. Pap. Ser. Int. Congr. Expo. Detroit, Michigan*, no. 412, 1995.
- [13] B. H. Ramadan, J. Charles L. Gray, J. S. Harold, J. H. Fakhri, and H. H. Karl, "Design of Engine Intake Systems Using Computer Simulations," *2002 Fall Tech. Conf. ASME Intern. Combust. Engine Div.*, pp. 1–8, 2002.
- [14] M. Haghgooei, J. C. Kent, and R. J. Tabaczynski, "Intake Valve Cylinder Boundary Flow Characteristics in an Internal Combustion Engine," *Combust. Sci. Technol.*, vol. 38, no. 1–2, pp. 49–57, 1984.
- [15] B. Roy, R. D. Misra, and K. M. Pandey, "Characterization of Shrouded Intake Valve in terms of Mean Flow Coefficient and Swirl Ratio," *Int. J. Appl. Eng. Res.*, vol. 11, no. 1, pp. 273–277, 2016.
- [16] M. K. B and J. M. Mallikarjuna, "Experimental Investigations of In-Cylinder Flows of Engine with Intake Shrouded Valve," *Int. J. Eng. Technol. Manag. Appl. Sci.*, vol. 3, no. November, pp. 85–91, 2015.
- [17] Y. Kim, Y. Han, and K. Lee, "A Study on the Effects of the Intake Port Configurations on the Swirl Flow Generated in a Small D.I. Diesel Engine," *J. Therm. Sci.*, vol. 23, no. 3, pp. 297–306, 2014.
- [18] F. Bonatesta, A. La Rocca, P. J. Shayler, and E. Wahab, "The Influence of Swirl Ratio on Soot Quantity and Distribution in the Cylinder of a Diesel Engine," *Third Eur. Combust. Meet. ECM*, pp. 1–6, 2007.
- [19] J. Kim, E. Yim, C. Jeon, C. Jung, and B. Han, "Effect of Injection Condition and Swirl on D.I. Diesel Combustion in a Transparent Engine System," *Int. J. Automot. Technol.*, vol. 9, no. 5, pp. 535–541, 2008.
- [20] H. W. R. Dembinski, "The Effects of Injection Pressure and Swirl on In-Cylinder Flow Pattern and Combustion in a Compression-Ignition Engine," *Int. J. Engine Res.*, vol. 15, no. 4, pp. 444–459, 2014.
- [21] D. M. Heim and J. B. Ghandhi, "Investigation of Swirl Meter Performance," *Proc. Inst. Mech. Eng. Part D J. Automob. Eng.*, vol. 225, no. 8, pp. 1067–1077, 2011.

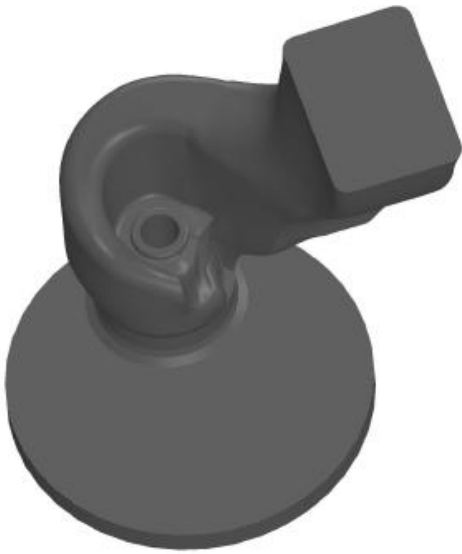


Figure 35 The helical-spiral inlet port design.

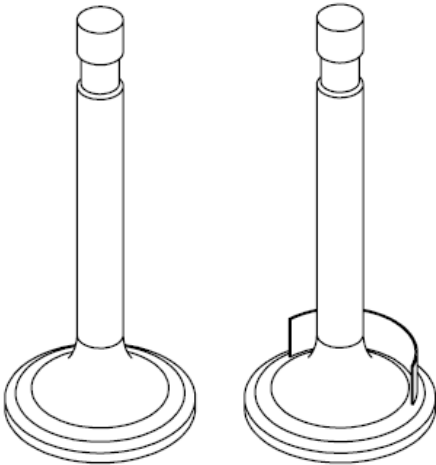


Figure 36 The ordinary and the shrouded valves.

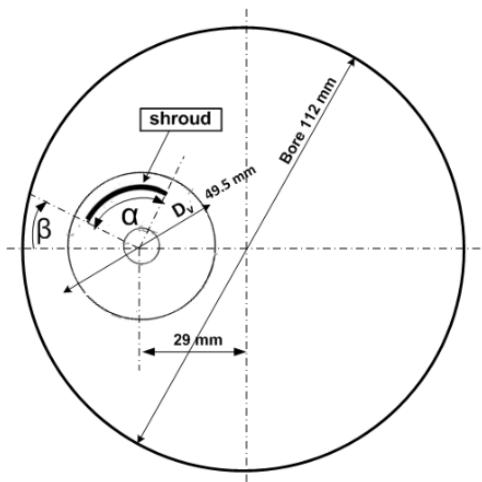


Figure 37 The location of the inlet valve and angles α and β .

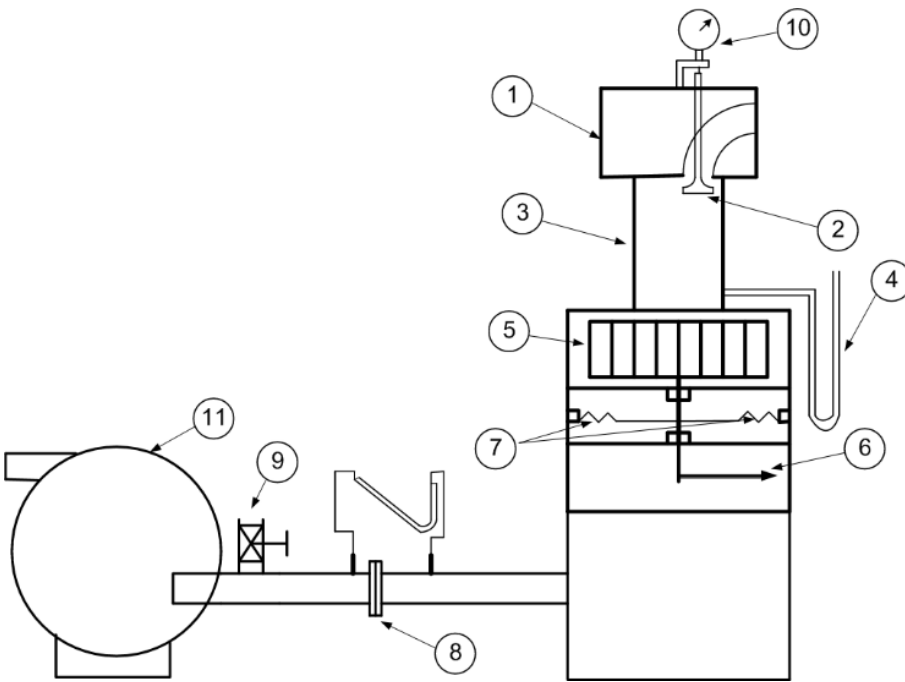


Figure 38 Schematic diagram of test rig.

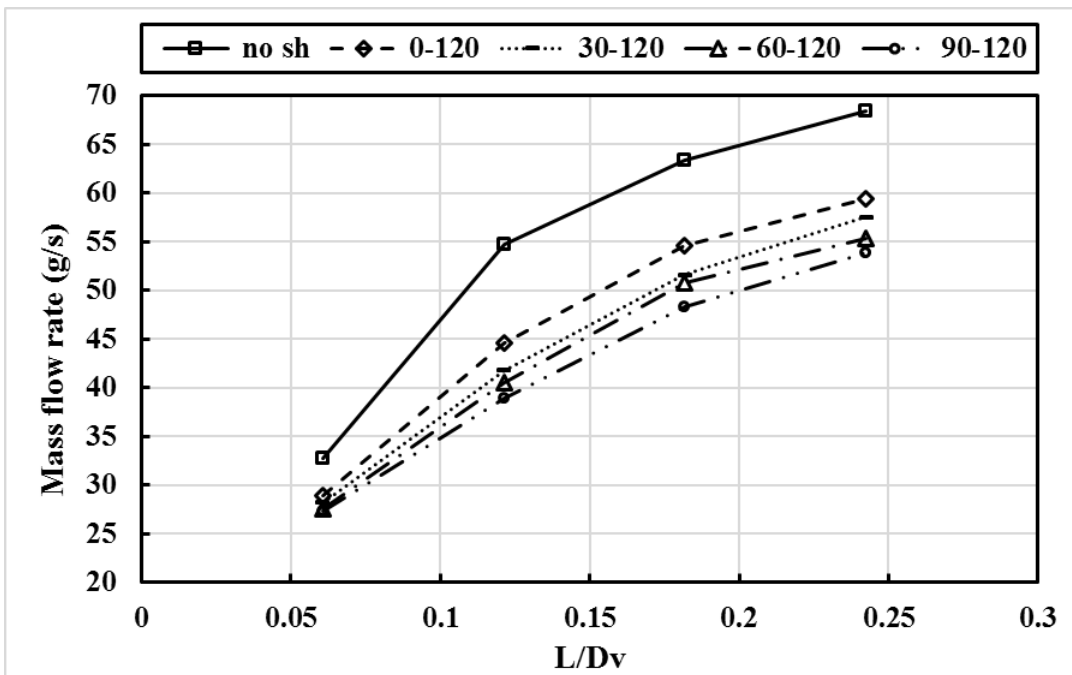


Figure 39 Mass flow rate through 120° shroud valve.

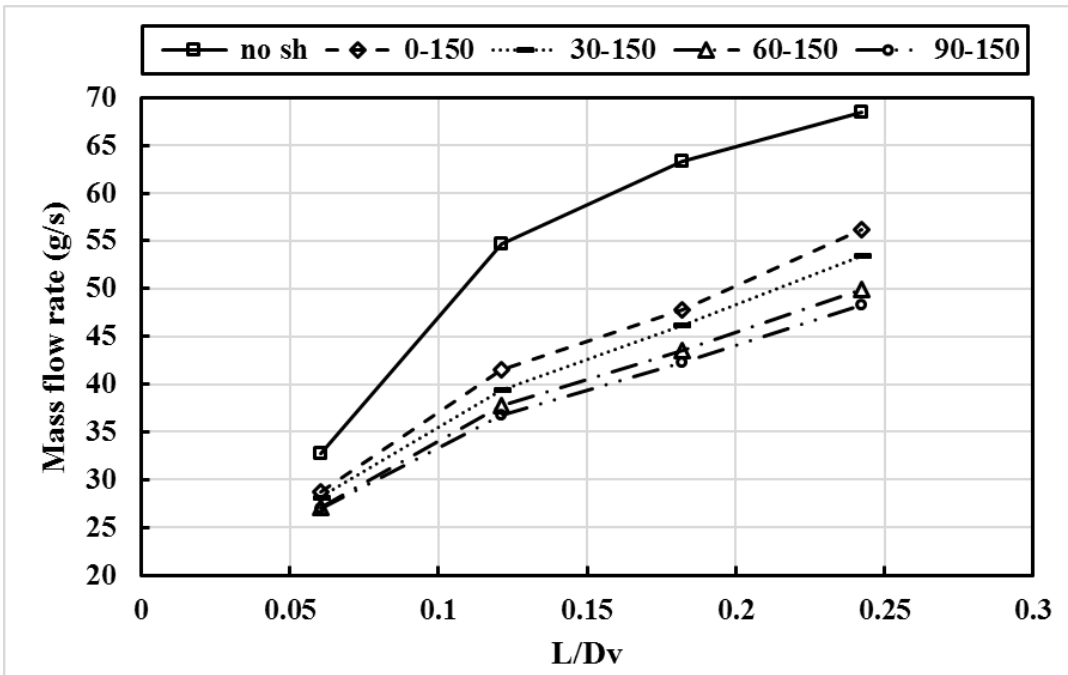


Figure 40 Mass flow rate through 150° shroud valve.

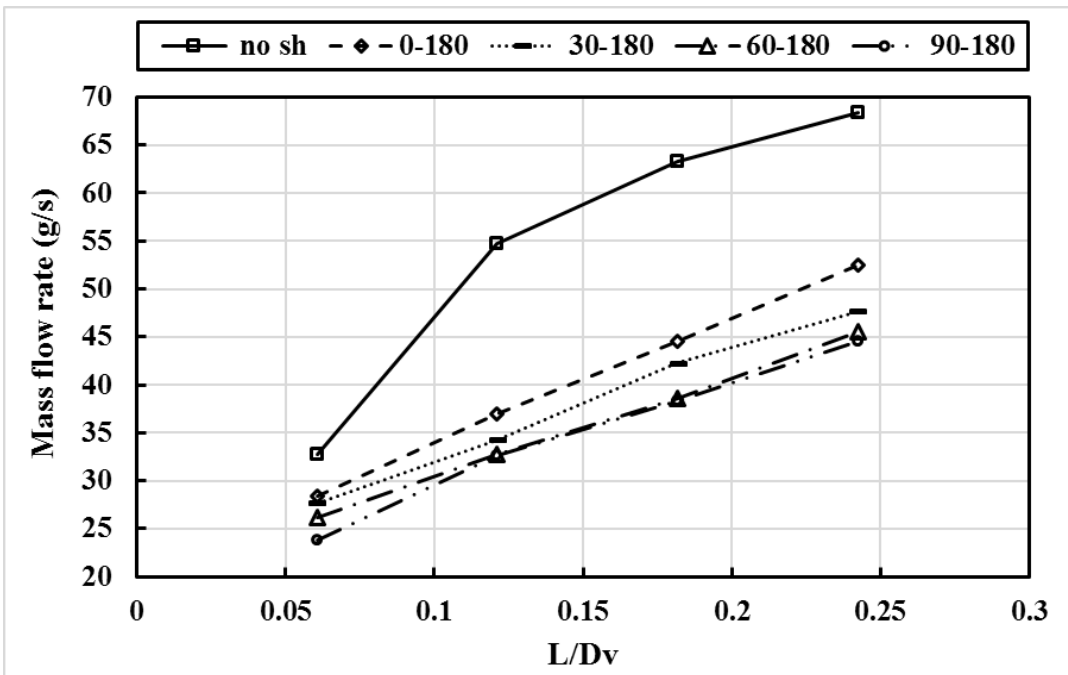


Figure 41 Mass flow rate through 180° shroud valve.

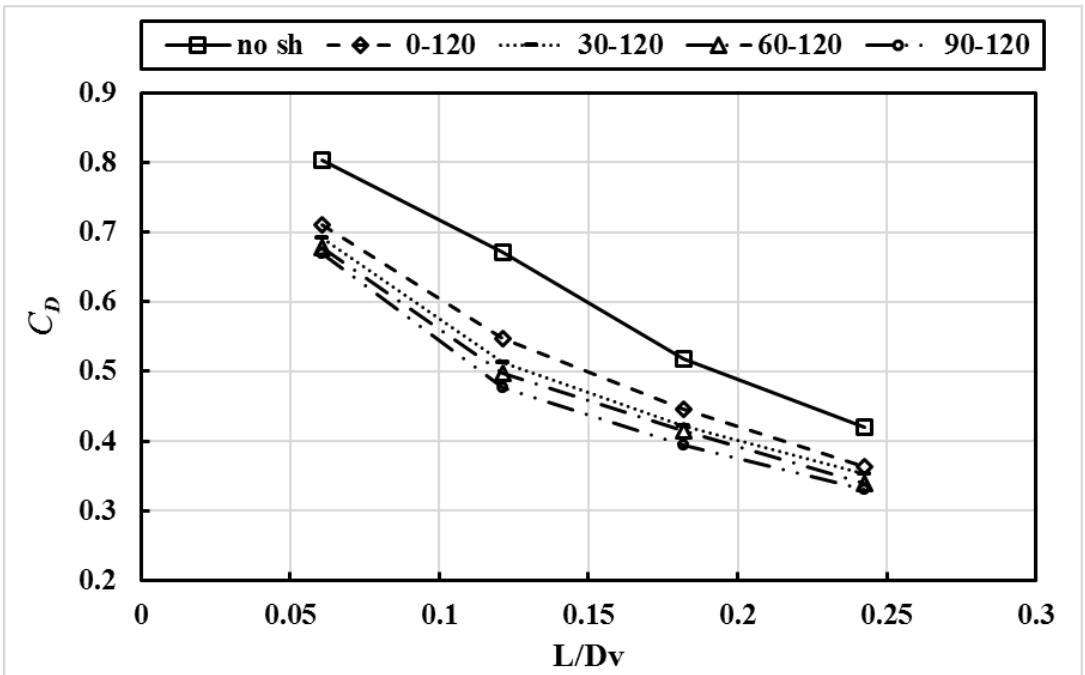


Figure 42 Discharge coefficient for 120° shroud valve.

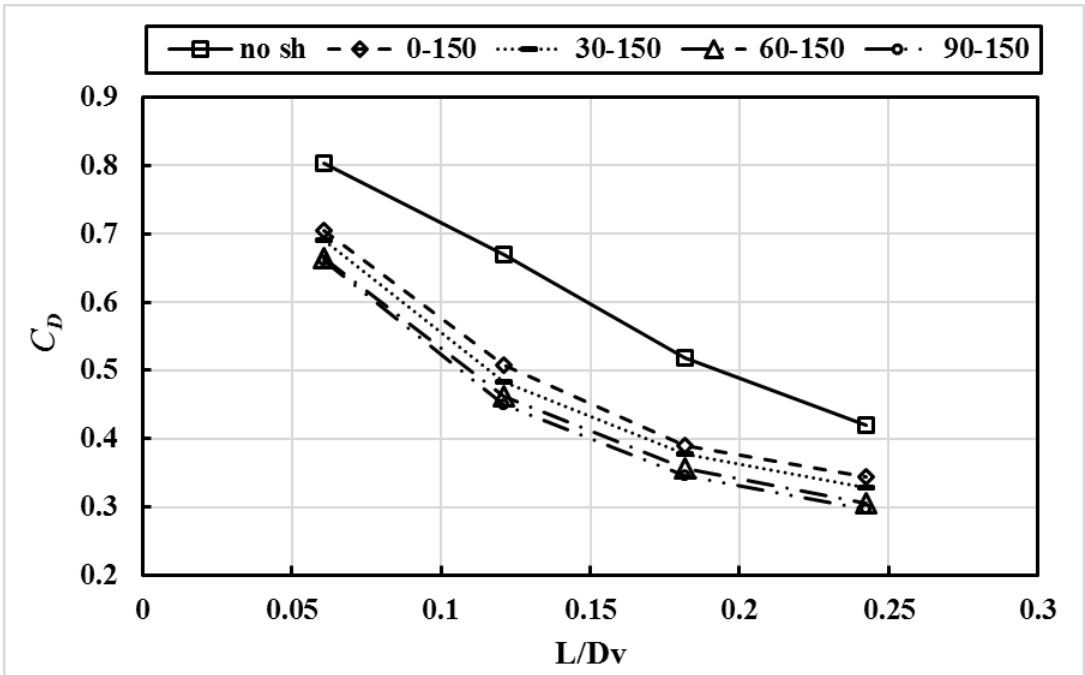


Figure 43 Discharge coefficient for 150° shroud valve

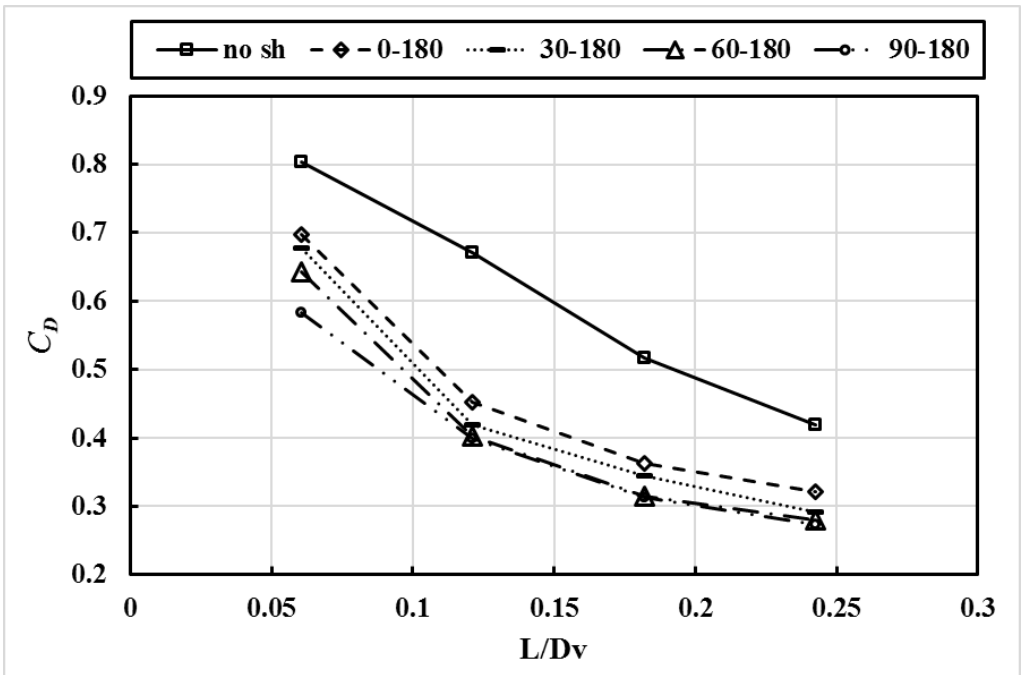


Figure 44 Discharge coefficient for 180° shroud valve.

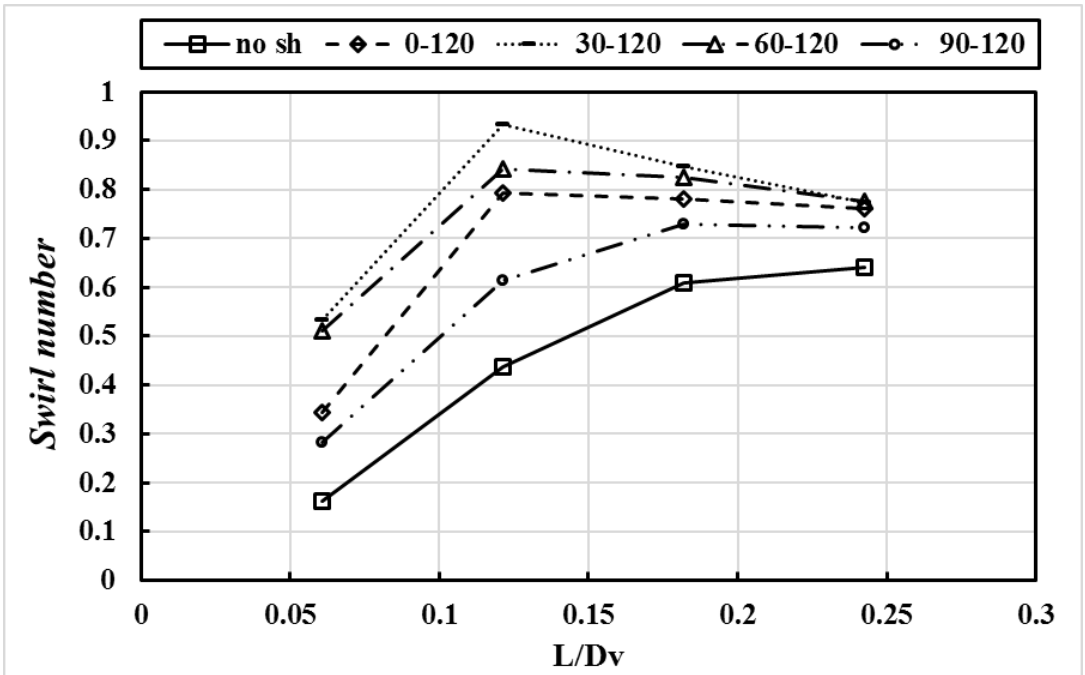


Figure 45 Swirl number for 120° shroud valve

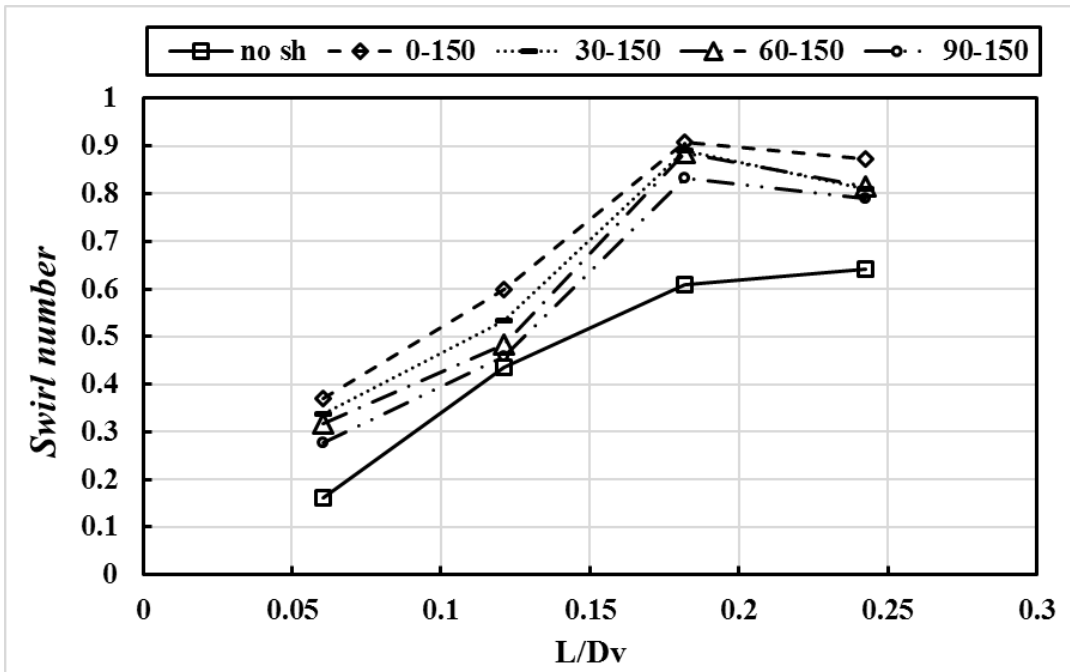


Figure 46 Swirl number for 150° shroud valve.

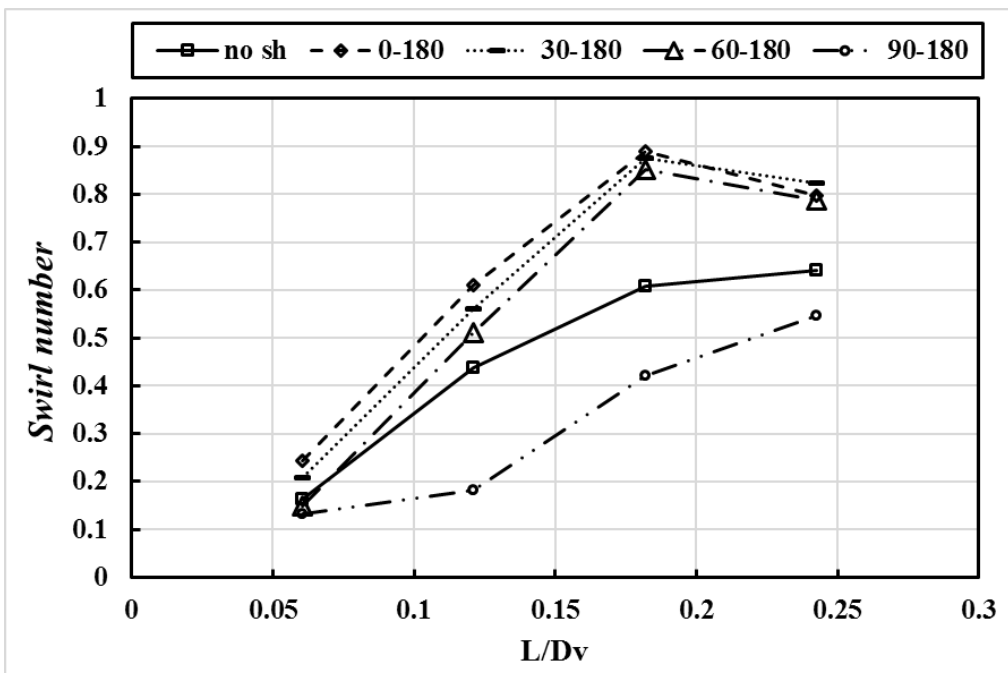


Figure 47 Swirl number for 180° shroud valve.

Table 1. The test rig components.

No.	Component	No.	Name
1	Inlet port: helical-spiral	7	Tension springs
2	Inlet valve: ordinary and shrouded valve	8	Orifice meter
3	Engine cylinder	9	Control valve
4	Manometer	10	Dial gauge
5	Honeycomb	11	Blower
6	Pointer		

Evaluation of CO₂ emissions from electricity generation in Egypt: Present Status and Projections to 2030

Lamiaa Abdallah^{a,*}, Tarek El-Shennawy^b

^a Alexandria higher Institute for Engineering and Technology (AIET), Alexandria, Egypt

^b Alexandria National Refining and Petrochemicals Co. (ANRPC), Alexandria, Egypt

Abstract:

Egypt emitted 225,000 tons of CO₂ in 2015, ranking number 27th of the world. Approximately 50% of CO₂ emissions in Egypt is from the electricity generation sector. Egypt announced its 2030 Vision in March 2016. Energy is the main driver for the planned vision. To achieve its goals of development, Egypt plans to build new power plants to add 51 GW to the existing 35 GW electrical grid. Almost 67% of these 86 GW will be from fossil sources (natural gas – oil – coal). About 33% of this power will be from renewables (wind and solar), hydroelectric and nuclear energy. This situation will improve the present status of 91% oil and gas, 8% hydroelectric and 1% renewables, as of 2016.

During last year, several discoveries of natural gas proven reserves were announced that might shift Egypt's vision towards a more dependence on the natural gas, with agreements between the Egyptian government and Siemens, one of the major German companies in the power industry, to add three new - gas fueled - power stations with a total capacity of 14.4 GW. Together, with another agreement with RosAtom, governmental nuclear company of Russia, to build and operate a nuclear power station with four reactors, with a total capacity of 4.8 GW. The picture is completed with tendering seven power plants fueled with coal, with a total capacity of 17 GW. The missing part of the picture is the renewables. Very small contributions were made to support this direction, which might lead to increased percentage of fossil fuel, with introducing one of the most polluting fuels, the coal, to the Egyptian energy mix. This will release huge amounts of CO₂ (and other pollutants) to the atmosphere. This paper examines the CO₂ emissions from electricity generation under various futuristic scenarios. The main issues to be discussed are business as usual, coal, nuclear power and renewables. Several activists are against coal, doubting the deployment of Clean Coal Technologies. Nuclear plants are subject to political externalities with the supplier, with major concerns regarding funding very high capital costs required, in addition to national security issues and management of nuclear wastes. Although Egypt is blessed by generous Renewable sources (Solar & Wind), the authors strongly doubt that Egypt can reach its renewable goals based on current indicators.

KEYWORDS

CO₂ Emissions –Electricity Generation – Fuel Mix – Egypt 2030

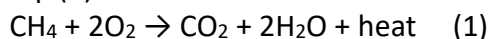
* Corresponding author: Lamiaa_Abdallah@yahoo.com, 01223695552

1. Introduction

Energy is a key issue for development of any nation. However, using energy consumes finite fossil fuels (coal, petroleum and natural gas), causes air pollution, environmental damage, global warming and costs money. Among the many human activities that produce greenhouse gases, the use of energy represents by far the largest source of emissions.

To generate electricity by conventional methods, a fossil fuel is burned (oxidized) to generate heat (transforming chemical energy in the fuel to heat energy). This heat energy is used either to convert water into steam in a steam turbine or in a combustion chamber to revolve a gas turbine using the combustion gases (transforming heat energy to mechanical rotating energy). This rotating turbine serves as the prime mover for an electric generator (transforming kinetic energy into electrical energy), with an overall thermal efficiency approximately equal to 40%.

Let us assume that we have a certain amount of natural gas (or methane CH₄). Since methane is a hydrocarbon, a common way to convert its chemical energy into work is to combine it with oxygen from the atmosphere and burn it to release its chemical energy in the form of heat. Accordingly, methane and oxygen undergo a chemical reaction and produce water and carbon dioxide, as shown in eq. (1):



The amount of CO₂ released in order to generate 1 kWh of electric energy depends on the carbon content in the fuel as shown in Table I [1].

Table I. Amount of CO₂ in kg released to generate 1 kWh of electricity

Fuel	Coal	Petroleum Oil	Natural Gas
CO ₂ released in kg/kWh	0.95 ~ 1	0.75 ~ 0.8	0.55

Despite the growth of non-fossil energy (such as nuclear, hydropower, solar and wind), the share of fossil fuels within the world energy supply is relatively unchanged. In 2016, fossil sources accounted for 80% of the world energy production. According to the International Energy Agency (IEA), the annual CO₂ emissions from fuel combustion reaches 36 GtCO₂ in 2016, the hottest year recorded ever, with CO₂ concentration of the atmosphere reaching 400 ppm [2].

For the first time in the history of climate negotiations, an agreement among the leaders of the world was signed on December 2015 at the United Nations (UN) 21st session of the Conference of the Parties (COP21) on climate change in Paris. The agreement main goal was to limit global warming to an increase of maximum of 1.5°C to 2°C by the year 2100 above the 20th century level. Global warming of more than 2°C would have serious consequences, such as an increase in the number of extreme climate events such as rise in sea level, droughts, etc. [3].

The United Nations declares 17 Sustainable Development Goals (SDG's) to be achieved by 2030. The 7th goal is concerned about energy: ensure universal access to affordable, reliable, and modern energy services, increase the share of renewable energy in the global energy mix and double the global rate of improvement in energy efficiency [4].

International negotiations and national targets seek to reduce greenhouse gas (GHG) emissions significantly and limit the risks of dangerous climate change. Climate Change Mitigation Actions require a reduction in emissions of 50%-80% by 2050 compared with 1990 levels [5].

The electricity sector has a key role to play in meeting these targets. Average emissions from electricity generation worldwide is in the range of 500 gCO₂eq/kWh in 2016 [6].

These figures consider only the emissions caused directly at the point of electricity generation, such as when coal is burnt in a coal-fired power station. To provide a more complete picture of the emissions

caused by generation technologies, all stages of their life cycles must be considered. These include their construction and maintenance, the extraction, processing and transport of their fuels (if applicable), and their ultimate decommissioning and disposal [7].

2. CO₂ Emissions in Egypt

Egypt emitted 225,000 tons of CO₂ in 2015, ranking number 27th of the world, with a share of 0.63% and 2.7 tons of CO₂ emissions per capita [8].

The emissions of CO₂ in Egypt are continuously monitored since 1960. The European Commission [8], the World Bank [9] and British Petroleum [10] publish historical emission trends. There are slight differences among these bodies; however, average milestone emissions are presented in Figure (1).

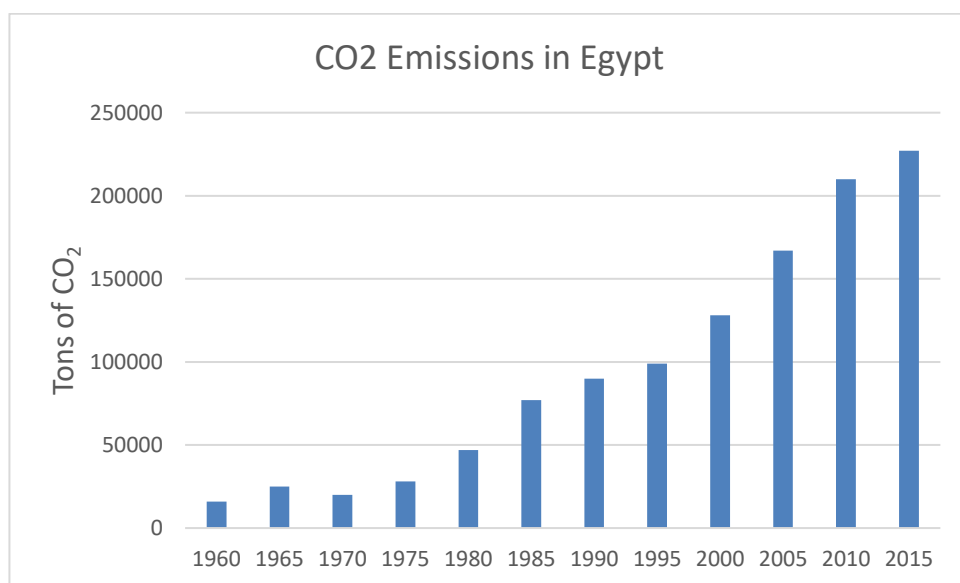


Fig. (1) CO₂ emissions in Egypt

The World Data Atlas estimated that the electrical power generation in Egypt is responsible for approximately 48.3% of the total CO₂ emissions in 2013, followed by transport (24.5%), industry (15%), residential buildings (8.4%) and others (3.8%), as shown in Figure (2) [11].

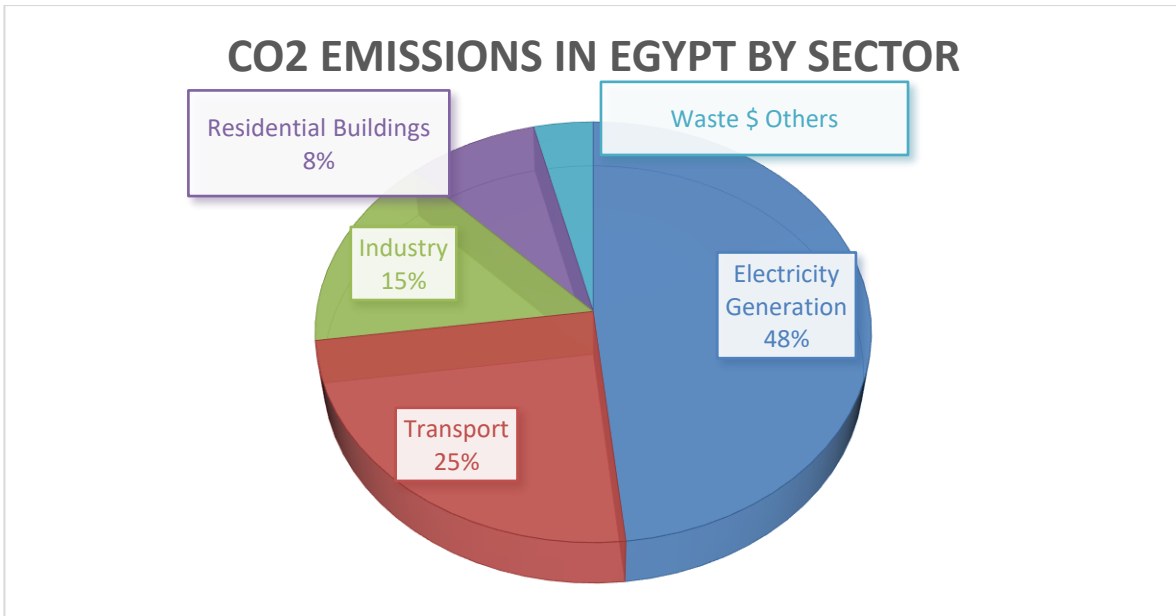


Fig. (2) Sources of CO₂ emissions in Egypt (2013)

The Egyptian Electric Utility and Consumer Protection Regulatory Agency publishes a monthly issue under the name of “Electricity Observer”. Table II summarizes some of the relevant figures published in these monthly reports during 2015, 2016 [12].

Table II. Electricity and CO₂ in Egypt during 2015 & 2016

Year	2015	2016	Change	% Change
Generating capacity (GW)	33	35	2	6 %
Peak demand (GW)	28.2	29.1	0.9	3.2 %
Generated Energy (GWh)	180,150	187,500	7,350 GWh	4.1 %
Natural Gas (%)	67.24 %	67.22 %	4,900 GWh	4 %
Mazout (%)	24.03 %	24.52 %	2,700 GWh	6.2 %
Hydroelectric (%)	7.78 %	6.99 %	- 900 GWh	- 6.4 %
Renewables (%)	0.96 %	1.27 %	650 GWh	37.5 %
CO ₂ emitted (tons)	112,000	118,000	6,000	5.35 %
CO ₂ Intensity (gm/kWh)	624	630	6	1 %

The energy mix in Egypt through 2016 is shown in Figure (3), where approximately 92% from the total energy generated is from thermal fossil fuel, 7% from hydropower and 1% from renewables (wind and solar).

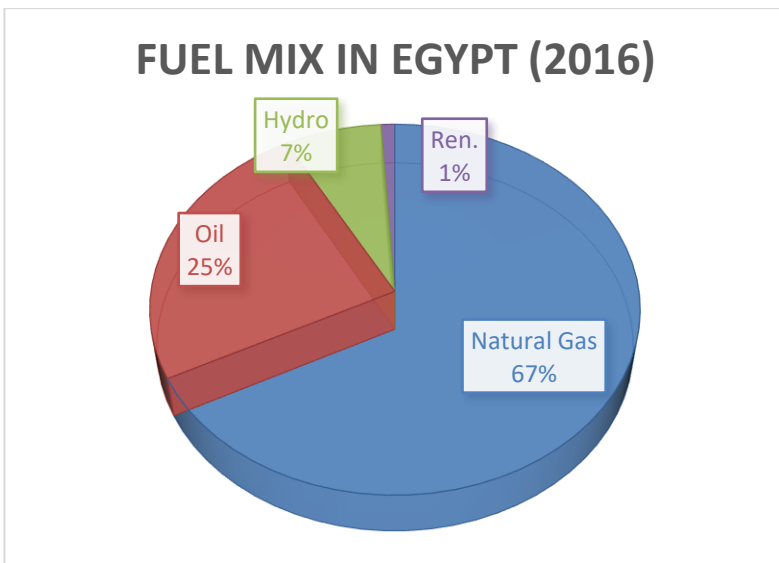


Fig. (3) Energy mix in Egypt (2016)

Approximately 50% of CO₂ emissions in Egypt (112,000 tons of out of 227,000 tons of CO₂ in 2015) are from the electricity generation sector. The total emissions of CO₂ in 2016 in Egypt are not available when this paper is prepared.

3. Effects of Climate Changes on Egypt

Egypt's climate has already changed. Sandstorms, rainstorms, unusual and untimely temperature fluctuations have noticeably become more frequent over the past few years.

According to the Fifth Assessment Report of the Intergovernmental Panel on Climate Change (IPCC), Egypt was identified as one of the most vulnerable regions to climate change such as sea level rise, temperature rise, Alteration of weather patterns, fresh water resources evaporation, and agricultural crop deficiency [13].

According to the report, this vulnerability stems from Egypt's unique combination of geography, population distribution, land-use and economic activity. It manifests in potentially massive impacts on Egypt's sectors of water resources, agricultural resources and food security, economy, tourism, and health. This is due to the fact that Egypt's lifelines are constrained to five percent of its land area, the Nile Valley and its Delta.

A rise in sea levels, perhaps the most direct effect of global warming, can have potentially devastating effects on Egypt's income-generating coastal cities and agricultural haven, the densely populated Nile Delta.

Alexandria for example, a major economic center where 40 percent of Egypt's industry and some of the nation's richest historic and architectural heritages are located, is one of the lowland cities most threatened.

The study estimated that just a one-meter sea level rise could displace 10 percent of Egypt's population, as more than half of the nation's inhabitants live within 100 kilometers of the Mediterranean coast. The IPCC predicts that the Mediterranean will rise that one meter within this century.

Not only do rising seas threaten the lives of the millions who live in these areas, they pose serious threats for their economy and tourism, as well as agricultural crop production in the Nile Delta.

Another highly vulnerable city, for example, is Port Said, an important harbor and the second largest tourist and trade center on the Mediterranean.

Further studies show that climate change will not solely take its toll on the Mediterranean, but it can also affect the Nile. Egypt’s Third National Communication to the United Nations Framework Convention on Climate Change (UNFCCC) report presented studies that conclude that natural flows in the River Nile Basin as a whole, and in separate sub-basins, are extremely sensitive to change in precipitation and temperature increase caused by climate change [14].

In conclusion, Climate change can affect Egypt’s most important water resource, and subsequently its food production and security.

4.Reducing CO₂ emissions from Electricity Sector in Egypt

4.1. Switching to low/no carbon fuels

Switching to low carbon fuels or to “carbon free” generation (hydroelectric – nuclear – solar – wind). This can be achieved by modifying the existing Energy Mix. A recent study of the optimal power generation mix in Egypt points out that, according to resource availability and the future expected electricity needs, new power plants could be based on renewable resources or nuclear power plants. Nuclear power plants in addition to 20% integration of renewables in the generation mix can reduce the CO₂ emission of the Egyptian power sector by almost 25 million tons per year. Although the renewable sources of power generation can be used efficiently at very decentralized and local scales, yet intermittent nature of these technologies does not permit to provide a large-scale continuous base-load power. Therefore, a power generation strategy based on a gradual integration of nuclear and renewable is suggested. A power generation mix, based on an optimal choice of fossil, nuclear, hydraulic and other renewable energy, is considered to be the most appropriate way of electricity production in Egypt [15].

4.2. Use Combined Cycle generation

The type of power generation technology also affects the CO₂ emissions. According to the 2013-2014 fiscal year report by the Egyptian Electricity Holding Company (EEHC), the combined cycle gas turbines have the lowest fuel consumption and CO₂ emitted per kWh generated, whereas the steam turbines have the worst indicators. It should be noted also that power plants with larger capacities are generally of higher efficiency. Table III summarizes the outcomes of the report [16].

Table III. Effect of Generation Technology on CO₂ Emissions

Technology	Steam Turbines				Gas Turbines		Combined Cycle	
	< 100	100:300	300:600	> 600	< 50	> 50	< 400	> 400
Power (MW)								
No. of Units	10	16	26	4	29	20	7	13
Total Power (MW)	400	2400	8600	2600	800	2600	1400	8700
Fuel Consumption (gm oil/kWh)	281	265	229	214	385	266	222	167
CO ₂ Intensity (gmCO ₂ /kWh)	724	722	606	591	923	612	510	384

4.3. Capturing CO₂ and storing it.

Among CO₂ mitigation options, carbon capture and storage (CSS) is considered the only technology that can significantly reduce the emissions of CO₂ from existing fossil fuel power plants. CO₂ can be captured either after combustion (CO₂ is separated from the flue gas) or before combustion (CO₂ is removed from the fuel before combustion). A third method to capture CO₂ uses oxy-fuel combustion (uses nearly pure oxygen for the combustion of fuel, then CO₂ is removed from the generated gases, formed principally from water vapor and CO₂). Unfortunately, all these application may increase the cost of electricity by 30-70%. After capturing the CO₂, it can be stored in geological formations such as mines, mountains and in the deep water in oceans [17].

This technology does not exist in Egypt. The authors of this paper do not expect it to be implemented in the near future due to its complicated technology and high associated expenses.

5. Prediction of CO₂ emissions in Egypt from 2017 to 2030

5.1. Egypt Vision 2030 (Energy)

Egypt announced its 2030 Vision in March 2016. Energy is the main driver for the planned vision. To achieve its goals of development, Egypt plans to build new power plants to add approximately 51 GW to the existing 35.7 GW electrical grid [18].

Table IV compares the Existing 35.7 GW generation capacities (2016) to the proposed 87 GW (2030). Figure (4) shows the proposed energy mix in 2030, to be compared with Figure (3).

Table IV. Electricity Mix in Egypt 2016 versus 2030

Year	2016	2030
Natural Gas	23.6	35
Mazout	8.6	2.6
Hydroelectric	2.8	2.8
Solar	0.2	16
Wind	0.5	9.4
Coal	0	16.8
Nuclear Energy	0	4.8
Generating capacity (GW)	35.7	87.4

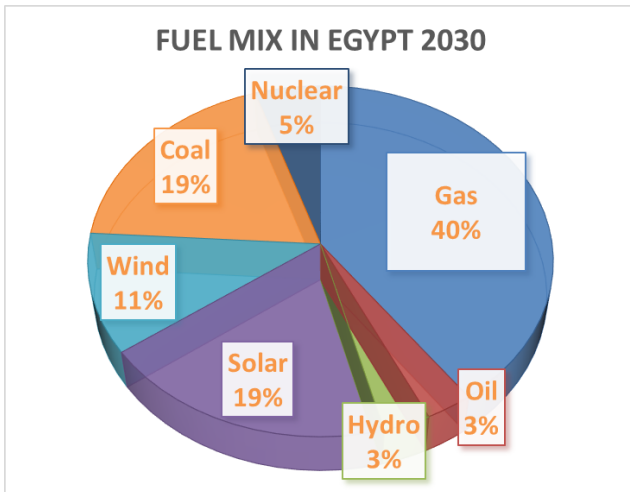


Figure (4) Fuel Mix according to Egypt Vision (2030)

5.2. Calculation of CO₂ intensity

CO₂ intensity (gmCO₂/kWh) can be calculated using equation (2) [19]:

$$\text{CO}_2 \text{ intensity} = \frac{\sum \left(\frac{P_i * C_i}{E_i} \right)}{\sum P_i} \quad (2)$$

Where P_i = Electrical Energy Produced from Fuel (i) in kWh
 C_i = Emission Factor of Fuel (i) in g/kWh
 E_i = Generation Efficiency during production of P_i

6. Results

6.1. Proposed (Optimistic) Scenario

The government had announced that by 2022, the renewables would supply 20% of the electric energy needs in the country. This share includes the hydroelectric energy. The share of the wind energy will be 12%. An agreement with RosAtom Company was signed to build a nuclear power plant with 4*1.2 GW nuclear reactors. The 1st reactor ought to start operation by 2024, the 2nd by 2025, the 3rd by 2026 and the 4th by 2027. Seven coal-fired power plants are being built and the first one will start operation by 2019. Using interpolation, data from [20] and applying equation (2), results in Table V.

Table V. Proposed Scenario for electric generation until 2030

	Installed Powers (GW)								
	2016	2018	2020	2022	2024	2026	2028	2030	%
Nat. Gas	23.6	29.6	31.0	32.6	32.6	32.6	35.0	35.0	40.0%
Oil	8.6	8.0	7.4	6.4	5.6	4.8	3.6	2.6	3.0%
Hydro	2.8	2.8	2.8	2.8	2.8	2.8	2.8	2.8	3.2%
Wind	0.5	2.0	4.8	7.2	7.2	8.4	8.4	9.4	10.8%
Solar	0.2	0.6	1.2	2.0	6.0	9.0	12.0	16.0	18.3%
Coal	0.0	0.0	7.2	9.0	11.0	12.8	14.8	16.8	19.2%
Nuclear	0.0	0.0	0.0	0.0	1.2	3.6	4.8	4.8	5.5%
Total Power (GW)	35.7	43.0	54.4	60.0	66.4	74.0	81.4	87.4	
Total Energy (GWh)	190,635	221,856	285,138	305,461	340,011	379,028	421,233	445,236	
CO2 emissions (ktons)	119,583	134,851	203,493	219,897	234,323	246,872	266,537	279,878	
CO2 intensity (gCO2/kWh)	627	608	714	720	689	651	633	629	

6.2. Business As Usual (BAU) Scenario:

- New Natural Gas Discoveries

During last year, several discoveries of natural gas proven reserves were announced that might shift Egypt's vision towards a more dependence on the natural gas, with agreements between the Egyptian government and Siemens, one of the major German companies in the power industry, to add three new - gas fueled - power stations with a total capacity of 14.4 GW.

- Renewables

Although the government announced a Feed-In-Tariff (FIT) to encourage investors to invest in renewable energy, and availed several lands blessed with high rates of solar irradiation and wind speeds, negligible powers are being added from wind & solar.

- Falling Oil Prices

Growing interest in renewables worldwide, coupled with political situation had led to falling prices of oil (40-50 US \$/barrel).

These circumstances may shift the government interest in implementing its optimistic vision towards a Business As Usual (BAU) scenario that depends on oil & gas and may be accompanied by nuclear energy and coal, with limited contribution of renewables.

- Under this pessimistic scenario, the CO₂ emissions from the electricity sector will increase, and the CO₂ intensity will worsen (increase). Table VI is a new run-out of the interpolation and calculation procedure with new feed data based on this pessimistic scenario. Figures (5) & (6) compare the CO₂ emission and intensity from the electricity sector under both scenarios.

Table VI. Pessimistic Scenario for electric generation until 2030

	Installed Powers (GW)								
	2016	2018	2020	2022	2024	2026	2028	2030	%
Nat. Gas	23.6	29.6	31.3	33.1	35.5	37.2	41.3	43.7	56.2%
Oil	8.6	8.0	7.4	6.4	5.6	4.8	3.6	2.6	3.3%
Hydro	2.8	2.8	2.8	2.8	2.8	2.8	2.8	2.8	3.6%
Wind	0.5	1.0	2.0	3.0	3.5	4.0	4.5	5.0	6.4%
Solar	0.2	0.4	0.8	1.2	1.4	1.6	1.8	2.0	2.6%
Coal	0.0	0.0	7.2	9.0	11.0	12.8	14.8	16.8	21.6%
Nuclear	0.0	0.0	0.0	0.0	1.2	3.6	4.8	4.8	6.2%
Total Power (GW)	35.7	41.8	51.5	55.5	61.0	66.8	73.6	77.7	
Total Energy (GWh)	190,635	221,172	285,427	305,487	340,300	379,133	421,155	445,420	
CO2 emissions (ktons)	119,583	134,851	204,419	221,441	243,278	261,077	285,991	306,742	
CO2 intensity (gCO2/kWh)	627	610	716	725	715	689	679	689	

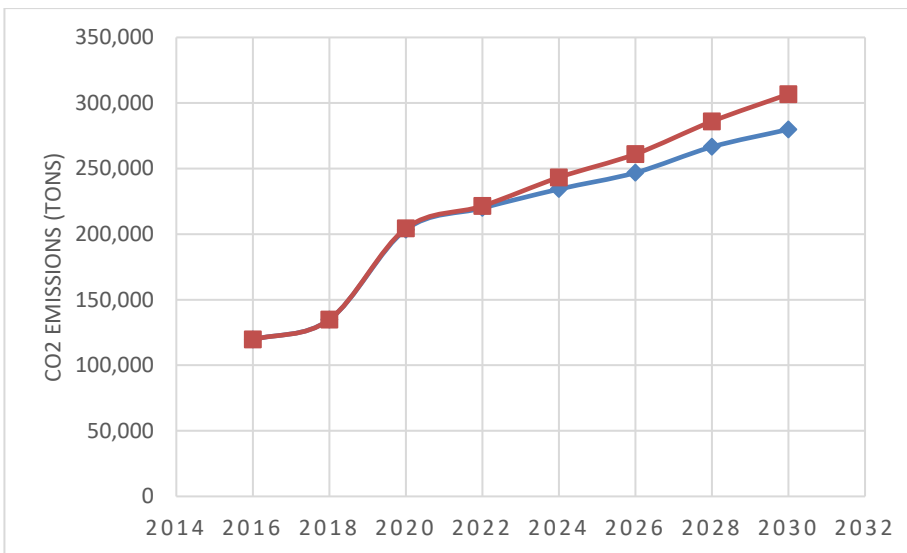


Figure (5) CO₂ emissions from electricity sector Planned (Blue) Vs. BAU Scenario (Red)

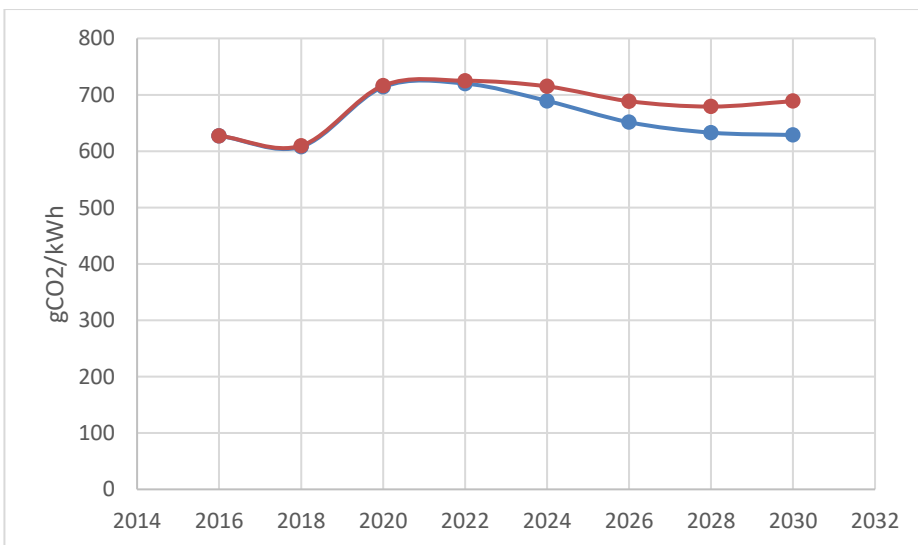


Figure (6) CO₂ intensity: Planned Vision (Blue) Vs. Business As Usual Scenario (Red)

7. Conclusions

New natural gas discoveries can modify Egypt's vision towards more dependence on natural gas in place of renewables. Although natural gas is the cleanest fossil fuel, yet, this will increase the total CO₂ emissions and the CO₂ intensity from electricity generation. This will have hidden costs on water resources, agriculture, sea level rise and severe climate changes in Egypt.

References

- [1] International Energy Agency (IEA), "Energy, Climate Change and Environment: 2016 Insights", IEA Publications, France, November 2016.
- [2] International Energy Agency (IEA), "CO₂ Emissions from Fuel Combustion: 2016 Highlights", IEA Publications, France, October 2016.
- [3] United Nations (UN), "Report of the Conference of the Parties on its twenty-first session, held in Paris from 30 November to 13 December 2015.
- [4] United Nations (UN), "Transforming Our World: The 2030 Agenda for Sustainable Development", A/RES/70/1, 2015.
- [5] World Bank Group Climate Change Action Plan, April 7, 2016
- [6] European Commission, Joint Research Centre (JRC) / PBL Netherlands Environmental Assessment Agency, "Trends in Global CO₂ emissions: 2016 report", 2016.
- [7] R. Turconi, A. Boldrin and T. Astrup, "Life cycle assessment (LCA) of electricity generation technologies", Renewable and Sustainable Energy Reviews, Vol. 28, pp. 555–565, 2013.
- [8] European Commission, Joint Research Centre (JRC) / PBL Netherlands Environmental Assessment Agency, "Emission Database for Global Atmospheric Research (EDGAR)", release version 4.3.2. <http://edgar.jrc.ec.europa.eu>, 2016
- [9] World Bank (WB), TheGlobalEconomy.com
- [10] British Petroleum (BP), "Statistical Review of World Energy", 2016.
- [11] World Data Atlas, "Egypt CO₂ emissions from electricity and heat production", 2013. Available at: www.knoema.com/atlas/Egypt
- [12] Egyptian Electricity Utility and Consumer Protection Regulatory Agency, "Electricity Observer", Issue 17 (Jan. 2015) through Issue 40 (December 2016). Available at <http://egyptera.org>
- [13] Intergovernmental Panel on Climate Change (IPCC), "Fifth Assessment Report (AR5): Working Group II: Climate Change 2014: Impacts, Adaptation, and Vulnerability", 2014.
- [14] Egypt's Third National Communication to the United Nations Framework Convention on Climate Change (UNFCCC) report, 2016.
- [15] A. Farnoosh and F. Lantz, "De-carbonization of Electricity Generation in an Oil and Gas Producing Country: A Sensitivity Analysis over the Power Sector in Egypt", Journal of Fundamental Renewable Energy and Applications, Vol. 5, issue (5), 2015.
- [16] Egyptian Electricity Holding Company (EEHC), "Annual Report, 2013-2-14", 2015.
- [17] D. Cebrucean, V. Cebrucean and I. Ionel, "CO₂ Capture and Storage from Fossil Fuel Power Plants", Energy Procedia, Vol. 63, pp. 18-26, 2014.
- [18] Ministry of Planning, Cairo, Egypt, "Sustainable Development Strategy: Egypt's Vision 2030", 2016.
- [19] C. Hussy, E. Klaassen, J. Koornneef and F. Wigand, "International comparison of fossil power efficiency and CO₂ intensity", ECOFYS Netherlands B.V., 2014.
- [20] The Egyptian Center for Economic and Social Rights & the Heinrich Böll Foundation, "80 Gigawatts of Change: Egypt's Future Electricity Pathways", 2016.

Modeling Human Factors in the Probabilistic Safety Assessment of Nuclear Power Plants

Mai A. Radwan^{1*}, Mohamed H. Hassan², Ezzat A. Eisawy¹, Ahmed E. Mohamed²

1 Nuclear and Radiological Regulatory Authority, Egypt

2 Nuclear and Radiation Engineering Department, Alexandria University, Egypt

ABSTRACT

Human performance plays a central role in overall safety of Nuclear Power Plants (NPPs). Human interactions with equipment occur during operations, response to accidents, surveillance testing, and maintenance. Humans are more perceptive and flexible in performance than machines; hence, during adverse situations, crew members are expected to be able to deal with complex situations and system interactions. Human interactions may cause initiating events through errors. Human machine interactions can also mitigate the effects of accidents through recovery and control actions. However, in the response to accidents, errors may be committed that not only do not correct the situation but actually exacerbate it.

Because human errors can be important contributors to risk, this study represents the inclusion of human error in analyzing a NPP Station Blackout (SBO) accident. The Fault Tree Analyzer CAFTA** was used to predict the SBO probability with and without human errors. The top event probability value increased from $8.20E-07$ in the basic SBO fault tree (without human error) to $2.59E-04$ in the SBO fault tree including the human error probabilities. Importance measures were used to identify the most important human factor contributing to the SBO.

Key words: Probabilistic Safety Assessment, Human Reliability Analysis, Fault tree analysis, CAFTA, Station Blackout accident.

1. INTRODUCTION

Since the beginning of the nuclear power generation, human performance has been a very important factor in all phases of the plant lifecycle: design, commissioning, operation, maintenance, surveillance, modification, decommissioning and dismantling [1].

Any problems arising at a nuclear power plant originate in some way due to human error. Probabilistic Safety Analysis (PSA) studies of nuclear power plants have found both beneficial and detrimental contributions of human interactions with machines. The overall objective of treating human reliability in a PSA is to ensure that the key human interactions of typical crews are accurately and systematically incorporated into the study in a traceable manner [2]. The area witnessed more assessment and analysis especially after the Fukushima, Daiichi accident [3]

2. HUMAN RELIABILITY ANALYSIS

Human Reliability Analysis (HRA) is an iterative process for determining the probability that human actions required for system performance. HRA results are often used as inputs to PSA that

analyze the reliability of entire systems by breaking each system down into its constituent components, including hardware, software, and human operators [4].

* Corresponding author. Postal address: Nuclear and Radiological Regulatory Authority, 6 the pilot Mahmud Shaker st., Alexandria, Egypt

E-mail address: mai_nuc@yahoo.com.

** CAFTA: Computer Aided Fault Tree Analysis

The HRA process, as described in NUREG-1792, includes a lot of activities paralleling the requirements found in the ASME PRA Standard and endorsed in NRC Regulatory Guide 1.200 [5]. These activities are described beginning with the makeup of the HRA team, continuing with how to identify human failure events (HFEs) and model them within the PSA, how to obtain screening and nominal HEPs, and how to model recovery, and concluding with documenting the HRA. [6]

Most of HRA methods address only a subset (often only quantification) like “Standardized Plant Analysis Risk Human Reliability Analysis (SPAR-H)” which is a simplified HRA method for quantifying Human Error Probabilities (HEPs) and it is not a full-scope HRA method in the sense that it does not provide guidance for identifying or modeling Human Failure Events (HFEs) within the context of the PRA. Some of HRA methods address all of the previous process elements such that “Technique for Human Error Rate Prediction (THERP)” which is considered a complete approach to HRA, and has been used more than any other HRA methods [7]. Plant specific human reliability data of NPP generally, consists of (i) simulator runs, (ii) expert judgment and, in a few cases, of (iii) real life experience. [4]

3. HUMAN ACTIONS IN PSA

In the past years human behavior and performance in organizations received an increasing attention [1].

In NPP, the study of human factors is the scientific study of how human beings interact with the plant and respond to the systems, culture and environment at work. The correct application of Human Factors helps to match the capabilities of the human operator to the design and operation of the plant, optimizing human performance and minimizing the potential for human error [8].

Human interactions that can affect both the cause and the frequency of an event sequence can take place before, during or after the initiation of the event sequence and can either mitigate or exacerbate an accident. Human errors are classified into two basic types’ errors of omission and errors of commission. An error of omission is not doing a correct action and an error of commission is doing an incorrect action [9, 10].

There is a need to analyze all the possible failure mechanisms in complex systems, also perform probabilistic analyses for the expected rate of failures and estimate probabilities of events that are modeled as logical combinations or logical outcomes of other random events [11]. The fault tree is extremely suitable for PSA purposes because of the clear structure. It is a logic diagram based on the principle of multi-causality, which traces all branches of events which could contribute to an accident or failure [12].

The human failure is considered as an integral part of a fault tree analysis (FTA). Human errors in PSA fault trees are usually presented in the form of anormal basic event, similarly to component failures. FTA can help identifying the most important consequences of human failures to a system [9, 13]. The CAFTA code is one of the codes usually used for developing reliability models of large complex systems, using fault tree methodology. [14]

4. STATION BLACKOUT CASE STUDY

The station blackout accident (SBO) is chosen as a case study to analyze the impact of human factors. SBO is the total loss of alternating current (ac) electrical power to the essential and nonessential equipment at a nuclear power plant. [15, 16]. The accidents in the Chernobyl and Fukushima Daiichi NPP support the PSA results regarding the importance of the AC power and the impact of an SBO on the safety of NPP [17, 18].

In this case study, a calculation of an SBO (representing a particular failure) is assumed to happen without the electric power not being restored for a period of time longer than the plant's capability to cope with the event, using the example of the Millstone Unit 3 Pressurized Water Reactor [2].

4.1 Evaluation of SBO fault tree without human error events:

Fig. 1 shows a simplified fault tree showing all possible combinations of events which could result in Station Blackout. Note that failures of critical support systems have been screened out based on the plant specific design.

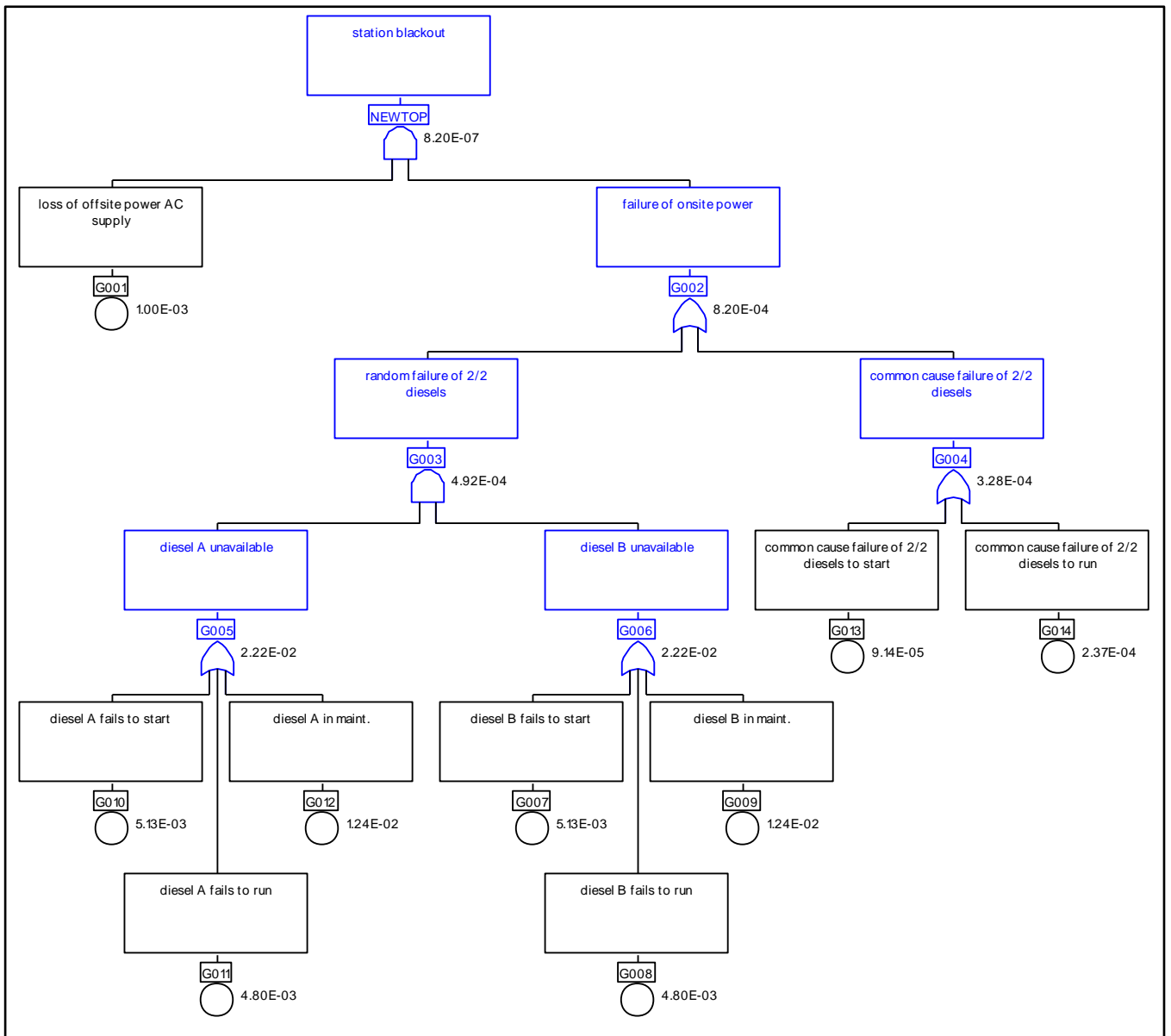


Fig. 1 Station blackout fault tree [2]

Once the fault tree model was built, it was evaluated using The Fault Tree Analyzer CAFTA [14]. This was done after inserting the failure probabilities of the different components. One can either calculate probabilities for every gate in the fault tree, or can generate cutsets for the top event using the cutset generating module, as shown in figures 2 and 3.

```

maigto - Notepad
File Edit Format View Help
Gate Probability Report
Input Filename: D:\mai\mai.gtp

Name           Min           Point Est.    Max
-----
G005           2.22E-02     2.22E-02     2.22E-02 ( 0.000E+00)
G006           2.22E-02     2.22E-02     2.22E-02 ( 0.000E+00)
G003           4.92E-04     4.92E-04     4.92E-04 ( 0.000E+00)
G004           3.28E-04     3.28E-04     3.28E-04 ( 0.000E+00)
G002           8.20E-04     8.20E-04     8.20E-04 ( 0.000E+00)
NEWTOP        8.20E-07     8.20E-07     8.20E-07 ( 0.000E+00)

Execution Time : 0.4 sec.
Input Filename : D:\mai\mai.gtp
Database Name  : D:\mai\mai.rr
Date & Time    : 06/11/16 23:55:50
Truncation Limit : 0.00e+000

GTPROB32 ver. 4.0b
SOURCE set to :GTPROB 06/11/16
Database successfully updated.

```

Fig. 2 SBO Gate probability report

It is worth noting that the point estimate is the geometric average of the minimum and maximum values. The range of the minimum and maximum values is controlled with the Truncation Probability value. In this study truncation probability value was taken to be zero, so the minimum, maximum and point estimated probabilities have the same value.

```

cut1 - Notepad
File Edit Format View Help
Cutset Report
NEWTOP = 8.27E-07 ( Probability )

Prob.  %      Class  Inputs...
2.37E-07  28.7%  G001  G014
1.54E-07  47.2%  G001  G009  G012
9.14E-08  58.3%  G001  G013
6.36E-08  66.0%  G001  G007  G012
6.36E-08  73.7%  G001  G009  G010
5.95E-08  80.9%  G001  G008  G012
5.95E-08  88.1%  G001  G009  G011
2.63E-08  91.3%  G001  G007  G010
2.46E-08  94.2%  G001  G007  G011
2.46E-08  97.2%  G001  G008  G010
2.30E-08  100.0% G001  G008  G011

Report Summary:
Filename: C:\Users\moha\Documents\final.cut
Print date: 12/21/2016 10:51 AM
Not sorted
Printed in full

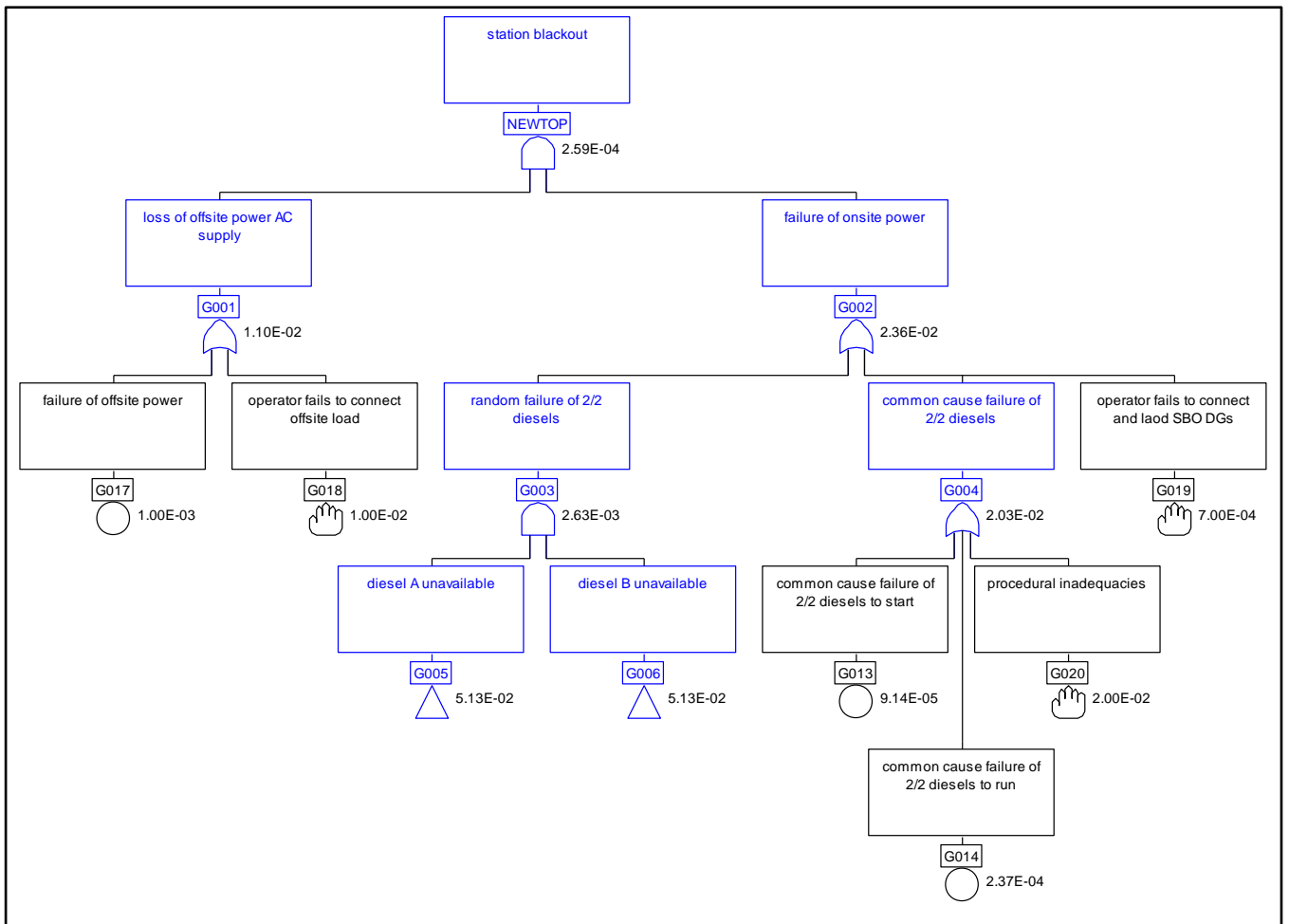
```

Fig. 3 SBO Cutset report

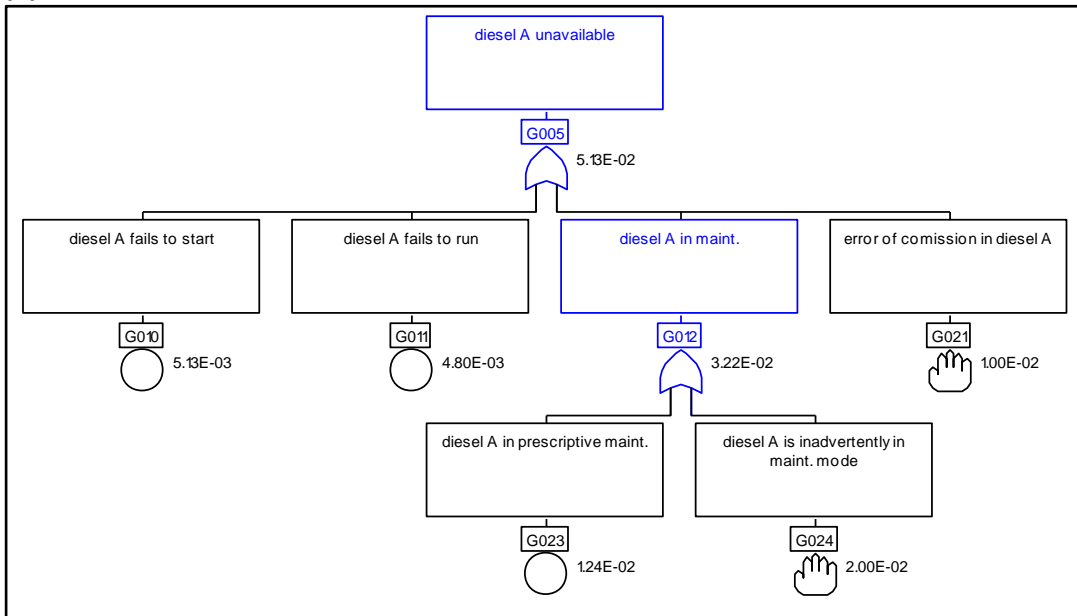
The fault tree was reduced to the form of cutsets using the CAFTA cutset generator CQUANT. A cutset is a (minimal) set of basic events that lead to the failure of the fault tree top event. These cutsets provide insights to the functionality of the system, as well as a quantification of the top event probability [14].

4.2 Evaluation of SBO fault tree including probable human error events:

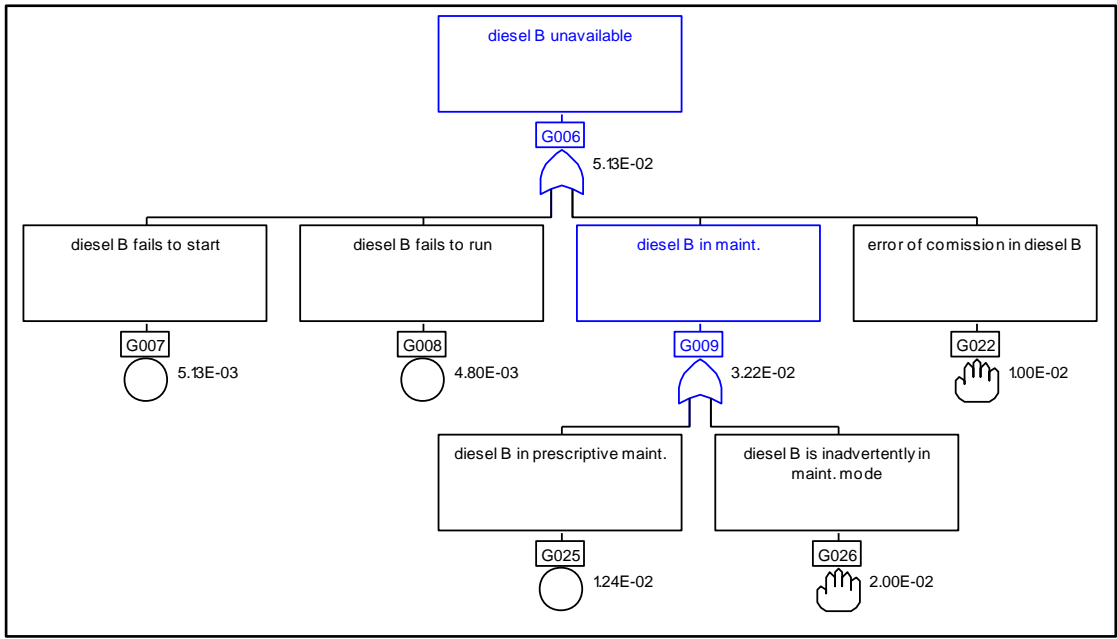
Different human errors are incorporated in the same SBO fault tree which was modeled and evaluated in the previous section to illustrate the important effect of the human errors on the SBO accident. The steps executed in the previous section would be repeated here. Different human errors were included at the different levels of the fault tree. This is shown in figures 4: a, b, and c.



(a)



(b)



(c)

Fig. 4 (a) SBO fault tree including human errors, (b) the gate of “diesel A unavailable” and related human errors, and (c) the gate of “diesel B unavailable” and related human errors

Name	Min	Point Est.	Max	
G001	1.10E-02	1.10E-02	1.10E-02	(0.000E+00)
G012	3.22E-02	3.22E-02	3.22E-02	(0.000E+00)
G005	5.13E-02	5.13E-02	5.13E-02	(0.000E+00)
G009	3.22E-02	3.22E-02	3.22E-02	(0.000E+00)
G006	5.13E-02	5.13E-02	5.13E-02	(0.000E+00)
G003	2.63E-03	2.63E-03	2.63E-03	(0.000E+00)
G004	2.03E-02	2.03E-02	2.03E-02	(0.000E+00)
G002	2.36E-02	2.36E-02	2.36E-02	(0.000E+00)
NEWTOP	2.59E-04	2.59E-04	2.59E-04	(0.000E+00)

Execution Time : 0.4 sec.
 Input Filename : C:\Users\moha\Documents\final.gtp
 Database Name : C:\Users\moha\Documents\final.rr
 Date & Time : 12/21/16 23:36:08
 Truncation Limit : 0.00e+000
 GTPROB32 ver. 4.0b
 SOURCE set to :GTPROB 12/21/16
 Database successfully updated.

Fig. 5 SBO gate probability report including human error events

As shown in figure 5, the Station Blackout probability increased from 8.20E-07 in the basic case to 2.59E-04 when human errors were taken into consideration. The values and the number of the gates increased after including the human errors.

Prob.	%	Class	Inputs...
2.00E-04	76.5%	G018	G020
2.00E-05	84.2%	G017	G020
7.00E-06	86.8%	G018	G019
4.00E-06	88.4%	G018	G024 G026
2.48E-06	89.3%	G018	G023 G026
2.48E-06	90.3%	G018	G024 G025
2.37E-06	91.2%	G014	G018
2.00E-06	91.9%	G018	G021 G026
2.00E-06	92.7%	G018	G022 G024
1.54E-06	93.3%	G018	G023 G025
1.24E-06	93.8%	G018	G021 G025
1.24E-06	94.2%	G018	G022 G023
1.03E-06	94.6%	G007	G018 G024
1.03E-06	95.0%	G010	G018 G026
1.00E-06	95.4%	G018	G021 G022
9.60E-07	95.8%	G008	G018 G024
9.60E-07	96.1%	G011	G018 G026
9.14E-07	96.5%	G013	G018
7.00E-07	96.7%	G017	G019
6.36E-07	97.0%	G007	G018 G023
6.36E-07	97.2%	G010	G018 G025
5.95E-07	97.5%	G008	G018 G023
5.95E-07	97.7%	G011	G018 G025
5.13E-07	97.9%	G007	G018 G021
5.13E-07	98.1%	G010	G018 G022
4.80E-07	98.3%	G008	G018 G021
4.80E-07	98.5%	G011	G018 G022
4.00E-07	98.6%	G017	G024 G026
2.63E-07	98.7%	G007	G010 G018

2.48E-07	98.8%	G017	G023	G026
2.48E-07	98.9%	G017	G024	G025
2.46E-07	99.0%	G007	G011	G018
2.46E-07	99.1%	G008	G010	G018
2.37E-07	99.2%	G014	G017	
2.30E-07	99.3%	G008	G011	G018
2.00E-07	99.3%	G017	G021	G026
2.00E-07	99.4%	G017	G022	G024
1.54E-07	99.5%	G017	G023	G025
1.24E-07	99.5%	G017	G021	G025
1.24E-07	99.6%	G017	G022	G023
1.03E-07	99.6%	G007	G017	G024
1.03E-07	99.6%	G010	G017	G026
1.00E-07	99.7%	G017	G021	G022
9.60E-08	99.7%	G008	G017	G024
9.60E-08	99.8%	G011	G017	G026
9.14E-08	99.8%	G013	G017	
6.36E-08	99.8%	G007	G017	G023
6.36E-08	99.8%	G010	G017	G025
5.95E-08	99.9%	G008	G017	G023
5.95E-08	99.9%	G011	G017	G025
5.13E-08	99.9%	G007	G017	G021
5.13E-08	99.9%	G010	G017	G022
4.80E-08	99.9%	G008	G017	G021
4.80E-08	100.0%	G011	G017	G022
2.63E-08	100.0%	G007	G010	G017
2.46E-08	100.0%	G007	G011	G017
2.46E-08	100.0%	G008	G010	G017
2.30E-08	100.0%	G008	G011	G017

Report Summary:
Filename: C:\Users\moha\Documents\final.cut
Print date: 12/22/2016 12:34 AM
Not sorted

Fig. 6 SBO Cutsets report including human error events

The number of cutsets increased as a result of the human error events as shown in figure 6. This means that there are a lot of minimal sets of basic events which include human error events that lead to the failure of the fault tree top event.

Event importance measures

Importance measures rank events by their importance (contribution) to the top event probability and are used to provide a quantifiable ranking of this contribution. Four common quantitative importance measures are calculated by the Cutset Editor. They are Fussell- Vesely, Birnbaum, Risk Achievement Worth and Risk Reduction Worth [14].

As shown in figure 7, the human error “operator fails to connect offsite load” is the main contributor to the SBO accident, according to the different methods of importance measure. In the meantime, the human error “procedural inadequacies” is an important event and effective contributor to the SBO accident.

Event	Probability	Fus Ves	BirnBm	Red W	Ach W	Description
G007	5.13E-3	0.01130	5.7535E-4	1.0114	3.190	diesel B fails to start
G008	4.8E-3	0.01057	5.7535E-4	1.0107	3.190	diesel B fails to run
G010	5.13E-3	0.01130	5.7535E-4	1.0114	3.190	diesel A fails to start
G011	4.8E-3	0.01057	5.7535E-4	1.0107	3.190	diesel A fails to run
G013	9.14E-5	0.00385	1.0987E-2	1.0039	43.025	common cause failure of 2/2 diesels to start
G014	2.37E-4	0.00997	1.0987E-2	1.0101	43.019	common cause failure of 2/2 diesels to run
G017	1.0E-3	0.09091	2.3679E-2	1.1000	91.489	failure of offsite power
G018	1.0E-2	0.90911	2.3684E-2	10.9995	90.690	operator fails to connect offsite load
G019	7.0E-4	0.02945	1.0987E-2	1.0303	42.999	operator fails to connect and load SBO DGs
G020	2.0E-2	0.84154	1.099E-2	6.3093	42.196	procedural inadequacies
G021	1.0E-2	0.02202	5.7535E-4	1.0225	3.179	error of comission in diesel A
G022	1.0E-2	0.02202	5.7535E-4	1.0225	3.179	error of comission in diesel B
G023	1.24E-2	0.02730	5.7535E-4	1.0281	3.174	diesel A in prescriptive maint.
G024	2.0E-2	0.04404	5.7536E-4	1.0461	3.157	diesel A is inadvertently in maint. mode
G025	1.24E-2	0.02730	5.7535E-4	1.0281	3.174	diesel B in prescriptive maint.
G026	2.0E-2	0.04404	5.7536E-4	1.0461	3.157	diesel B is inadvertently in maint. mode

Fig. 7 SBO importance measurers report

5. CONCLUSIONS

- Human performance plays a central role in the overall safety of Nuclear Power Plants since human interactions with equipment occur during operations, response to accidents, surveillance testing, and maintenance. In the mean time, Human machine interactions can mitigate the effects of accidents through recovery and control actions.
- The loss of the electric power supply from the external grid is a major contributor to station blackout accident (SBO) which is considered as one of the main areas in the analysis of severe accidents in nuclear reactors especially after the Fukushima accident.
- The Fault Tree Analyzer CAFTA was used to analyze the impact of human factors on the analysis of an SBO accident. The top event probability value increased from 8.20E-07 in the basic SBO fault tree (without human errors) to 2.59E-04 in the SBO fault tree including the human error probabilities.
- The human error events affected the gate probability analysis since they increased the number of gates and raised the probability values of all the gates.
- On the other hand, the number of the cutsets increased dramatically in the case of considering the human errors compared with the basic case without the human errors. In this case, many minimal sets of basic events that lead to the top event failure include effective human errors.
- The human error “operator fails to connect offsite load” is the main contributor to the SBO accident according to Fussell-Vesely Measure and increases the associated risk as illustrated by the Birnbaum measure. So when this human error probability is reduced to zero, the risk is reduced and The Risk Reduction Worth measures a peak value. When this human error is sure to happen (probability = 1), the risk increased and The Risk Achievement Worth reached high values.
- The human error “procedural inadequacies” is also an important event. It is an effective contributor to SBO accident according to Fussell-Vesely Measure. When its probability is reduced to zero, the risk is also reduced.

REFERENCES

- [1] Giustino Manna, "Human and Organizational Factors in Nuclear Installations", DG JRC – Institute for Energy, the Netherlands, 2007, pp. 8-10
- [2] IAEA, Case study on the use of PSA methods: Station blackout risk at Millstone Unit 3, VIENNA, 1991, pp. 31
- [3] International Experts Meeting, Human and Organizational Factors in Nuclear Safety in the Light of the Accident at the Fukushima Daiichi Nuclear Power Plant, Vienna, 21-24 May 2013
- [4] PekkaPyy, "Human reliability analysis methods for probabilistic safety assessment", VTT PUBLICATIONS 422, FINLAND, 2000, pp. 8-9, 16- 24, 36- 40
- [5] U.S. Nuclear Regulatory Commission, "An Approach for Determining the Technical Adequacy of Probabilistic Risk Assessment Results for Risk-Informed Activities," Draft Regulatory Guide 1.200, Washington, DC, February 2004.
- [6] Anthony J. Spurgin, "Human Reliability Assessment Theory and Practice", CRC Press, Taylor & Francis Group, Boca Raton, 2010, pp.9, 24- 29
- [7] U.S. Nuclear Regulatory Commission Office of Nuclear Regulatory Research, Evaluation of Human Reliability Analysis Methods against Good Practices, NUREG-1842, Final Report, Washington, DC 20555-0001, pp. 45-49
- [8] Office for Nuclear Regulation An agency of HSE, "Nuclear Research Index", Section J, Human Factors, pp. 2.
- [9] Swiss Federal Institute of Technology Zurich, "Human Reliability Analysis (HRA)", Donnerstag, Mai 2011, pp.1-3, 12.
- [10] Bill Vesely, Fault Tree Analysis (FTA): Concepts and Applications, NASA HQ, Mission Success Starts with Safety, pp. 86-89, 91
- [11] M. Pandey, Fault Tree Analysis, University of Waterloo, CIVE 240 – Engineering and Sustainable Development
- [12] Fault Tree Analysis (FTA) and Event Tree Analysis (ETA), NEBOSH National Diploma - Unit A | Managing Health and Safety, RRC Training
- [13] PekkaPyy& Bjorn Wahlstrom, Modeling the Human in PSA Studies, Electrical Engineering Laboratory, Technical Research Centre of Finland, Otakaari 7B, 02150 Espoo, Finland, 1988, pp. 285 – 287
- [14] CAFTA Software Manual, Fault Tree Analysis System, Version 6.0 Demo, 2013, pp. v, 34-35, 73-76, 83-84
- [15] L.S. de Carvalho, J. M de Oliveira Neto, Advanced Technology Application Station Blackout Core Damage Frequency Reduction – The Contribution of AN AC Independent Core Residual Heat Removal System, BRASIL, 2011, pp. 1-2

[16] U.S. Nuclear Regulatory Commission, Common-Cause Failure Event Insights, Emergency Diesel Generators, Washington, 2003, pp. 3, 7,19,32,38,44

[17] AndrijaVolkanovski, Andrej Prošek, Station Blackout and Nuclear Safety, “Jožef Stefan” Institute, Slovenia, 2011, pp. 1-3.

[18] Andrija Volkanovski, Antonio Ballesteros, DuškoKančev, Events related to loss of offsite power and station blackout at NPPs Topical Study, European Commission, Joint Research Centre, Institute for Energy and Transport, 2015, pp. 58, 62-63.

EXPERIMENTAL STUDY ON THE PRODUCTIVITY OF SOLAR STILL COUPLED WITH PARABOLIC TROUGH COLLECTOR

Mohamed Fathy¹, M.Salem.Ahmed^{2*} Hamdy Hassan^{3,4} and El-Desouki Eid⁵

¹Teacher at Technical Industrial Institute, Sohag, Egypt

² Mech. Department, Faculty of Industrial Education, Sohag University, Sohag, Egypt

³ Mech. Engineering Department, Faculty of Engineering, Assiut University, Assiut, Egypt

⁴Egypt-Japan University of science and Technology, Alexandria, Egypt

⁵ Dean Of Faculty of Industrial Education, Suez University, Suez, Egypt

* *Corresponding author: M. Salem Ahmed*

Email address: mahmoudsalem.ahmed@yahoo.com

Abstract

The present paper studies an experimental work for the distillation of saline water using solar still. The experimental work aims to investigate the production of double acting conventional solar still (CDSS) and CSS with fixed parabolic trough collector (FPTC). The study has been implemented for a depth of water of 20mm and 30 mm inside the solar still and comparing them on the production. The study also investigates the performance of solar still on the production for the case of solar still with FPTC and comparing them without FPTC. The experimental results revealed that the production rises with decreasing of depth of saline water. The solar still temperatures and production of CSS with FPTC are greater than the production and temperatures of CSS.

*Corresponding author : Email : mahmoudsalem.ahmed@yahoo.com

Key words: Double slope; Solar Still; Fixed Parabolic trough collector (FPTC); Fresh water production

1. Introduction

In the recent days, the crises decay of energy resources and a shortage of fresh water are the two main challenges for the world where they play a crucial role in the overall economic development of any country [1]. Fresh water is essential for all life forms on earth; plants, animals and human being, etc. The fresh water presented on the earth is limited and does not meet the accelerated rise in population and rapid industrialization. Industrial wastes and sewage discharges are mostly mixed in the rivers, so the available fresh water availability is reduced. Oceans are the only available source of large amount of water but they contain high levels of salt. This requires means to remove salts. Desalination represents the solution to remove salts and hence to obtain fresh water. Desalination is one of humankind's most primitive forms of water treatment and it is still a popular treatment solution throughout the world today. In natural desalination process solar radiation is absorbed by the sea and causes water to evaporate. The evaporated water rises above the earth's surface and moved by the wind. Once this vapor cools down to its dew point temperature, condensation occurs and the fresh water comes down as a rain. This same principle is used in all distillation systems using alternate sources of heating and cooling. Solar still is considered one of the important solutions for the distillation of brackish water and it is driven by the

solar energy since it is easy in operation and low cost in construction. However, the solar still production is low. So, there are many efforts exerted to enhance its production from researchers [2-9]. But there is more attention given to enhancement depending on the solar energy. Solar still is one means for desalination process, which is used for desalination purpose. Solar still is of two type's namely passive solar still and active solar still. Singh et al. [10] have been designed solar stills integrated with N identical partially covered photovoltaic thermal (PVT) compound parabolic concentrator (CPC) water collectors known as PVT-CPC active solar distillation. The average daily thermal, exergy, electrical, overall exergy, overall thermal efficiencies and average daily production have been evaluated for optimum number of collectors and mass flow rate. The results show that single slope performs better than double slope PVT-CPC active solar still on the basis of average daily thermal efficiency, overall thermal efficiency and production if depth of water in the basin is more than 0.31 m and vice versa. In the active solar still, the thermal energy is provided to the basin of solar still through some external source either directly by incorporating flat plate collector (FPC)/PTC/evacuated tube collector (ETC) or indirectly by the use of heat exchangers. A lot of researches by various researchers are available for active solar still [11-13]. But there is more attention given to enhancement depending on the solar energy. The parameters affecting the production of solar still have been studied and these include; depth of water, glass cover temperature, and phase change materials, solid materials in the basin and extra [14-16].

The present paper studies an experimental work for the distillation of salty water using solar still. The experimental work aims to investigate the production of solar still with and without FPTC. The study has been implemented for a depth of water of 20mm and 30 mm inside the solar still and comparing them on the production. The study also investigates the performance of solar still on the production for the case of solar still with FPTC and comparing them without FPTC. The FPTC produces high temperature on its tube receiver which is used as an extra heating source to the salty water in solar still basin. The collected solar radiation on the FPTC is transferred to the solar still by using an oil pipes formed a heat exchanger inside the solar still basin.

2. Experimental work

The system using consists of FPTC coupled with still as shown in Fig.1. The solar still unit consists of salty water basin has area of 1.5 m^2 ($1\text{m} \times 1.5 \text{ m}$) and 0.1m high. The basin still is made from a galvanized iron sheet of 1.5 mm thick. The whole inside surface of the basin still is coated with black paint. The basin is fitted inside the wooden frame of 0.03m thick and 0.20 m height and the external dimensions $1.70 \text{ m} \times 1.20 \text{ m}$ the void between the basin and the wooden frame is filling by insulating foam layer of thickness of 0.07 m. The double slope solar still is covered with a clear glass sheet of 4 mm thickness inclined at 26.5° horizontally, which is the latitude of Sohag, Egypt. The silicon used as a bonding material to prevent any leakage between the basin box and the glass cover. There is one distillate channel for each side of two solar still sides. The distillate channel made of reinforced plastic (Aquatherm) of 4.0 mm thickness. It is tilted with enough slopes for each side to collect the water condensate in the inside glass cover. The salty water tank is placed 1 m above the basin still to feed salty

water to the basin still by water pipe line. A check valve is integrated at the pipe line entrance to regulate the salty water flow rate.

The FPTC used as the external heat source to rise the temperatures of the basin water through the finned oil pipes heat exchanger fitted on the bottom of basin water. The solar parabolic trough collector system consists of a cylindrical parabolic concentrator with focal pipe, oil heat exchanger, absorber surface, and measuring devices. A cylindrical parabolic concentrator used as a reflector system that concentrates sunlight on the receiver tube. It is manufactured from reflective stainless steel sheet of 0.4 mm thickness, 1.2 m wide and 2.5 m long with effective aperture area 3m^2 and geometrical concentration ratio 28.6. The receiver consists of copper tube 2.5 m long and 25.4 mm diameter covered by glass evacuated tube 2.5 m long and 42 mm diameter. Oil heat exchanger consists of a single copper tube with 18 passes, the oil flow inside the copper tube 0.8 cm diameter and 20 m long. Oil heat exchanger is painted by black paint to rise the absorptivity of solar radiation during sunlight. In the present experimental work the intensity of solar radiation (I), and temperatures of ambient air (T_a), glass cover (T_g), salty water (T_w), vapor (T_v), absorber plate (T_b), inlet heat exchanger oil ($T_{oil,in}$), and fresh water production are measured every 1 h by using thermocouples K-type (± 0.5) digital temperature device and flask tank. All experimental measurements aim to evaluate the performance for the double slope of conventional and modified solar still with FPTC under the ambient conditions of Sohag City, Egypt (Latitude 26.33N and longitude 31.41E).



Figure 1. An image of the experimental setup

3. Results and Discussions

The results of the present experimental work are presented for two solar still systems (CDSS and double acting solar still with fixed PTC) and for two depths of salty water 20 and 30 mm. The measurements are measured and recorded each hour from 8 AM to 5 PM in summer from 16 to 21 July 2016.

3.1 Temperatures results

The temperatures of ambient air (T_a), inside glass temperature ($T_{g,in}$), outside glass temperature ($T_{g,out}$), salty water in the basin (T_w), vapor region (T_v), fixed PTC absorber plate (T_b), oil at the inlet to the solar still ($T_{oil,in}$), and oil at the outlet from the solar still ($T_{oil,out}$) are measured.

Figure 2 showed the Evolution of temperatures and solar intensity with time for CDSS at water depth 20 mm. Figure 2 shows that the solar cell temperatures rises with time from 8 Am until 1 PM and then reduces with time until the end of the reading time at 5 PM. The solar intensity rises with time from the reading starting until about 12 PM and then it reduces with time until the end of reading time at 5 PM. The temperature of the water temperature is the greatest followed by the vapor temperature followed by the temperatures of inlet glass surface and the outlet glass temperature. The maximum temperatures of the salty water, vapor, inlet glass and outlet glass are 70, 68, 55, and 53 °C respectively. Figure 3 illustrates the evolution of temperatures and solar intensity with time for CSS at water depth 30 mm. Figure 3 shows that the solar cell temperatures rises with time from 8 Am until 1 PM and then reduces with time until the end of the reading time at 5 PM. The solar intensity rises with time from the reading starting until about 12 PM and then it reduces with time until the end of reading time at 5 PM. The temperature of the salty water is the greatest followed by the vapor temperature followed by the temperatures of inlet glass surface and the outlet glass temperature. The maximum temperatures of the salty water, vapor, inlet glass and outlet glass are 66, 64, 53, and 51 °C respectively. The solar still temperatures for 30 mm salty water depth are less than the salty water temperatures for 20 mm salty water depth. Figure 4. Shows the evolution of temperatures and solar intensity with time for modified solar still with FPTC at water depth 20 mm. Figure 4 illustrates that the solar cell temperatures rises with time from 8 Am until 1 PM and then reduces with time until the end of the reading time at 5 PM. The solar intensity rises with time from the reading starting until about 12 PM and then it reduces with time until the end of reading time at 5 PM. The temperature of the inlet oil is the greatest followed by the water temperature, followed by the temperatures of inlet glass surface and the outlet glass

temperature. The maximum temperatures of the inlet oil temperature, salty water, vapor, inlet glass and outlet glass are 104, 88, 85, 61 and 60 °C respectively. Figure 5. Shows the evolution of temperatures and solar intensity with time for modified solar still with FPTC at water depth 30 mm. Figure 5 shows that the solar cell temperatures rises with time from 8 Am until 1 PM and then reduces with time until the end of the reading time at 5 PM. The solar intensity rises with time from the reading starting until about 12 PM and then it reduces with time until the end of reading time at 5 PM. The temperature of the inlet oil is the greatest followed by the water temperature, followed by the temperatures of inlet glass surface and the outlet glass The maximum temperatures of the inlet oil, salty water, vapor, inlet glass and outlet glass are 97, 85, 82, 59 and 58 °C respectively. The solar still temperatures for 30 mm salty water depth are less than the salty water temperatures for 20 mm salty water depth and the salty water temperatures with FPTC is greater the the CSS temperatures without FPTC.

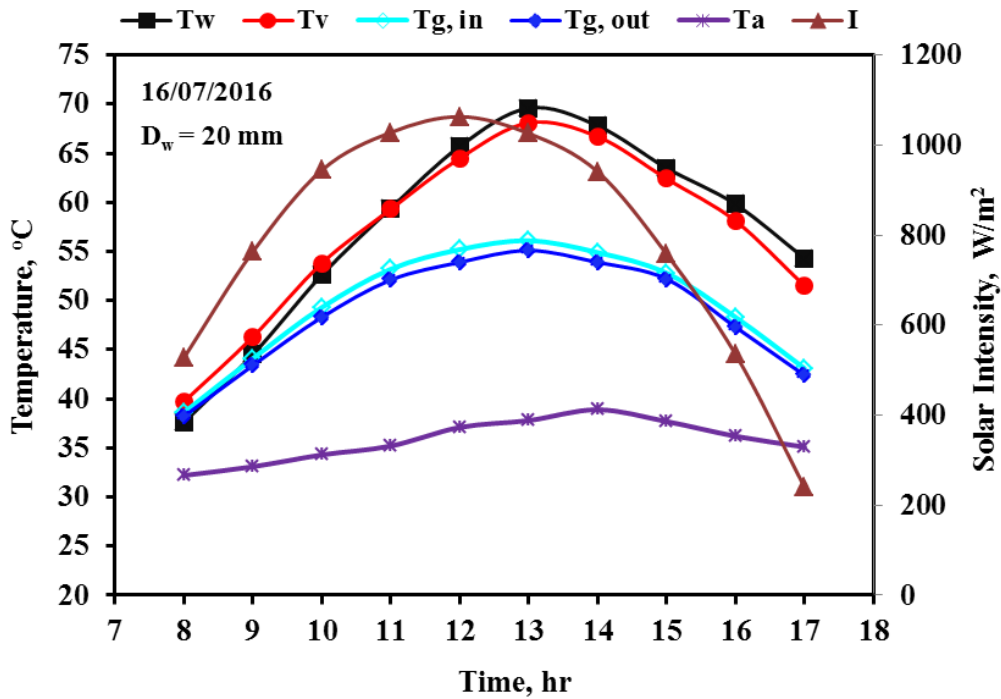


Figure 2. Evolution of temperatures and solar intensity with time for CSS at water depth 20 mm

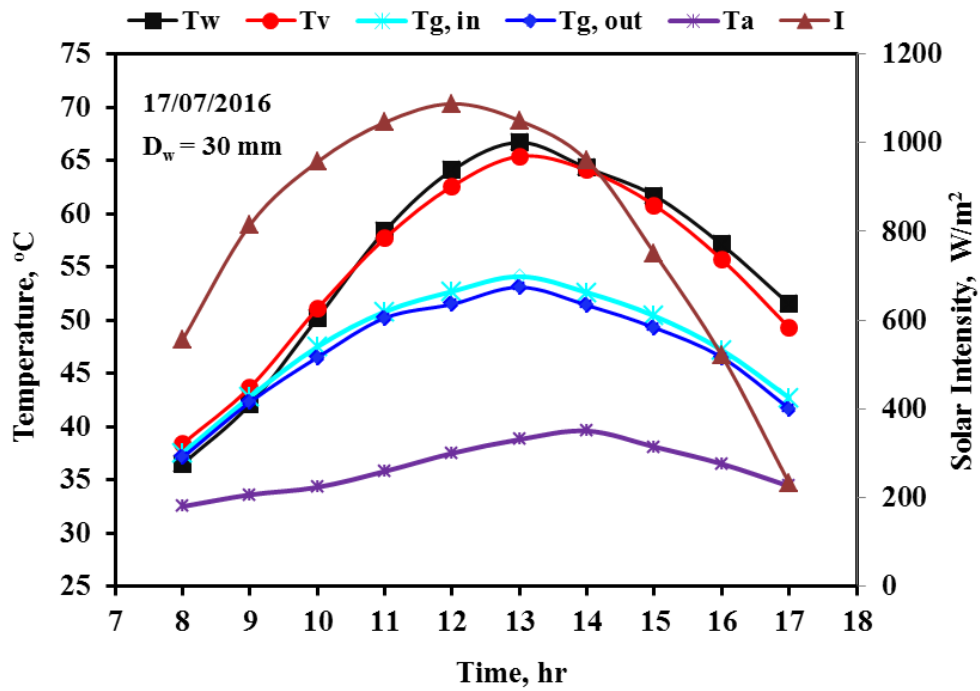


Figure 3. Evolution of temperatures and solar intensity with time for CSS at water depth 30 mm

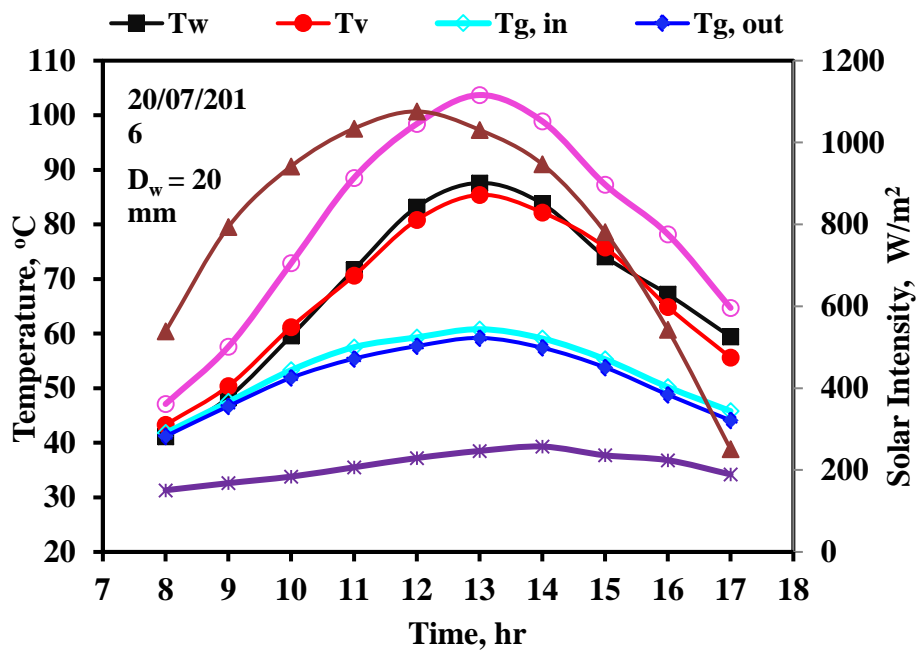


Figure 4. Evolution of temperatures and solar intensity with time for modified solar still with FPTC at water depth 20 mm

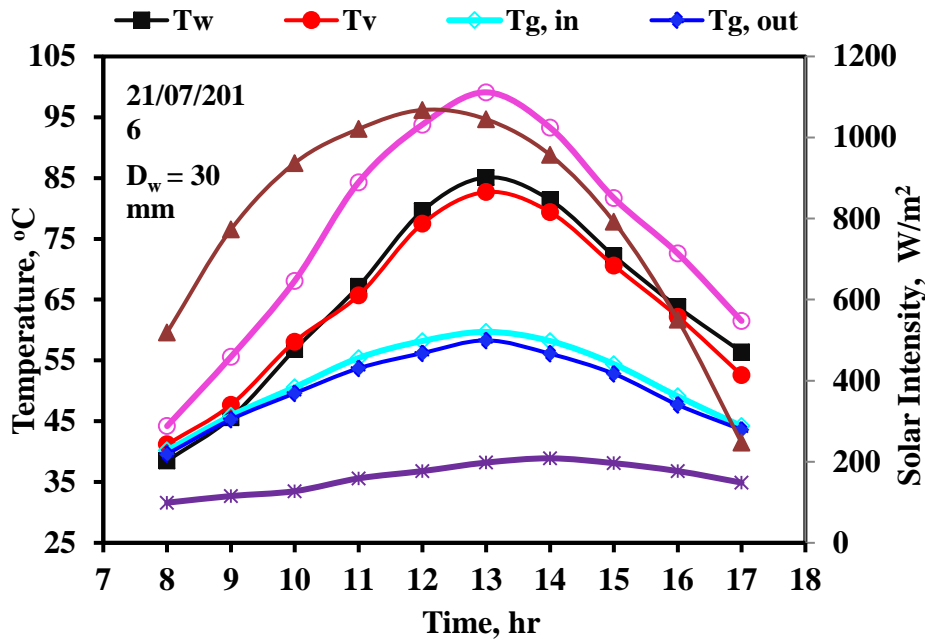


Figure 5. Evolution of temperatures and solar intensity with time for modified solar still with FPTC at water depth 30 mm

3.2 Production

Figure 6 shows the hourly production of fresh water for CDSS and solar still with FPTC. Figure 6 shows that the hourly production of fresh water for all studied cases rises from the starting of the measuring data (8 AM) until about 2 PM and then reduces with time until the end of reading (5 PM). The fresh water production of the system with 30 mm depth of the salty water in the basin is less than the production of 20 mm depth of the salty water in the basin. The production of the solar still with FPTC is greater than the production of CDSS. The maximum production of the CDSS with 30 mm thickness water salty depth, CSS with 20 mm thickness water salty depth, solar still with FPTC with 30 mm thickness salty water depth and solar still with FPTC with 20 mm thickness water salty depth are 0.92, 1.0, 1.4, and 1.63 kg/m².hr respectively. Figure 7 shows the accumulated production of fresh water for CSS and solar still with FPTC. Figure 7 shows that the total accumulated production of fresh water for all studied cases rises from the starting of the measuring data (8 AM) until the end of reading (5 PM). The total accumulated fresh water production of the system with 30 mm depth of the salty water in the basin is less than the production of 20 mm depth of the salty water in the basin. The production of the solar still with FPTC is greater than the production of CSS. The maximum production of the CSS with 30 mm thickness water salty depth, CSS with 20 mm thickness water salty depth, solar still with

FPTC with 30 mm thickness water salty depth and solar still with FPTC with 20 mm thickness water salty depth are 4.2, 5.7, 8.0, and 9.8 kg/m² respectively.

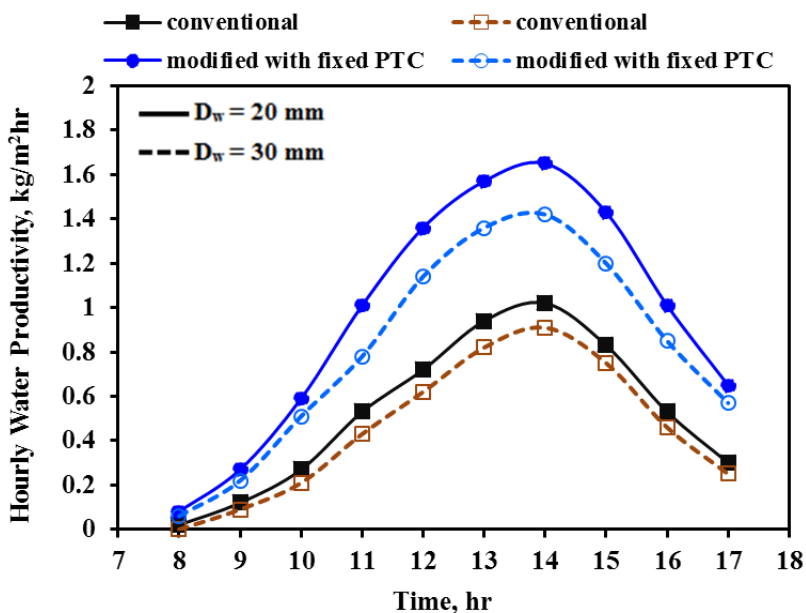


Fig.6. Hourly production of fresh water for CSS and solar still with FPTC

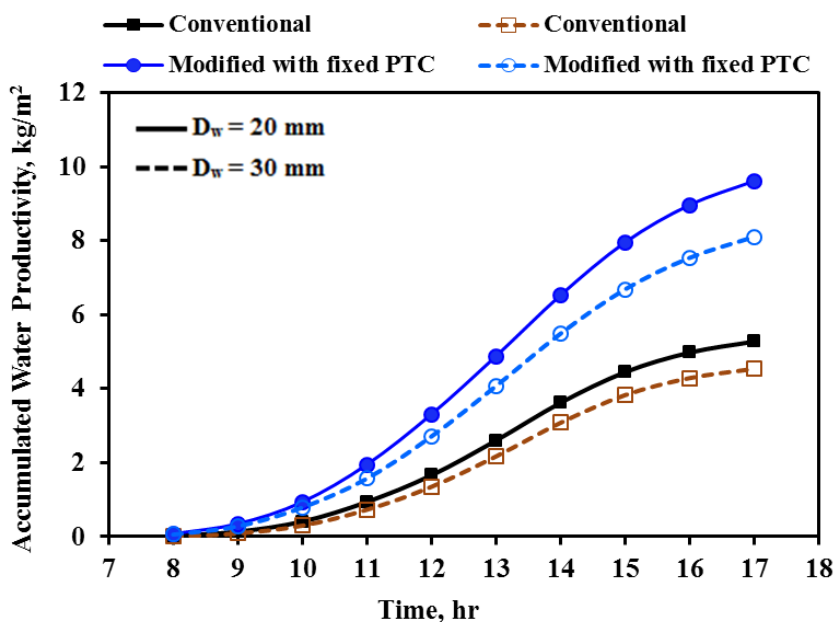


Fig.7. Comparison of accumulated production of the fresh water

4. Conclusions

The performance of a FPTC coupled with double slope solar still with finned oil pipes heat exchanger was experimentally investigated. FPTC supplies its heat to the heat exchanger in the solar still basin to rise the temperature of the basin water. The solar still temperatures in case of solar still with FPTC are higher than that of CDSS and the temperatures of solar still reduce with rise salty water depth. The production of the solar still rises with decreasing salty water depth. The daily fresh water productions at 20 mm salty water depth with sand as porous material are recorded 5.28 for conventional solar still, while 9.62 for solar still with FPTC. The fresh water production for solar still with FPTC is higher than that for conventional solar still by about 82.2% at salty water depth 20 mm in the summer.

5. References

- [1] United Nations, Water for People, Water for Life — UN World Water Development Report, Unesco Publishing, Paris, (2003).
- [2] Sushrut Shashidhar Halewadimath and C.N.Nataraj, Experimental study on the production for different depth variation – solar still, International research journal of engineering and technology (IRJET), vol. 02, pp 1890-1893 (2015).
- [3] T.Arunkumar, David Denkenberger, R.Velraj, Ravishankar Sathyamurthy, Hiroshi Tanaka and K.Vinothkumar, Experimental study on a parabolic concentrator assisted solar desalting system, Energy conversion and management, vol. 105, pp 665-674(2015).
- [4] V.Manikandan, K.Shanmugasundaram,S.Shanmugan, B.Janarthanan, and J.Chandrasekaran," Wick type solar stills: A review", Renewable and sustainable energy reviews, Vol. 20, pp 322-335(2013).
- [5] A.A.El-Sebaili and M.El-Naggar,"Year round performance and cost analysis of a finned single basin solar still", Vol.110,pp787-794(2017).
- [6] Z.M.Omara, A.E.Kabeel and A.S.Abdullah," A review of solar still performance with reflectors", Vol.68,pp638-649(2017).
- [7] A.E.Kabeel , Z.M.Omara and F.A.Essa," Enhancement of modified solar still integrated with external condenser using nanofluids: An experimental approach", Vol. 78, pp 493-498(2014).
- [8] Z.M.Omara, Mohamed A. Eltawil and Elsayed A. ElNashar," A new hybrid desalination system using wicks/solar still and evacuated solar water heater", Vol. 325,pp56-64(2013).

- [9] PankajK.Srivastava and S.K.Agrawal," Experimental and theoretical analysis of single sloped basin type solar still consisting of multiple low thermal inertia floating porous absorbers", *Desalination*, Vol.311, pp 198-205(2013).
- [10] D.B. Singh , and G.N. Tiwari, "Performance analysis of basin type solar stills integrated with N identical photovoltaic thermal (PVT) compound parabolic concentrator (CPC) collectors: A comparative study", *Solar Energy*,Vol. 142,pp144–158 (2017).
- [11] Arslan, M.," Experimental investigation of still performance for different active solar still designs under closed cycle mode", *Desalination*, Vol. 307, pp9–19 (2012).
- [12] Badran, A.A., Al-Hallaq, A.A., Eyal Salman, I.A., and Odat, M.Z., "A solar still augmented with a flat-plate collector", *Desalination*, Vol.172, pp227–234 (2005).
- [13] Calise, F., d Accadia, M.D., and Piacentino, A.,"A novel solar trigeneration system integrating PVT (photovoltaic/thermal collectors) and SW (seawater) desalination: dynamic simulation and economic assessment", *Energy*, Vol. 67, pp129– 148 (2014).
- [14] P.Prakash, and V.Velmurugan," Parameters influencing the production of solar stills-A review", *Ren. And Sustainable Energy Reviews*, Vol.49, pp585-609(2015).
- [15] V.Velruga, and K.Srithar," Performance analysis of solar stills based on various factors affecting the Production – A review", *Ren. And Sustainable Energy Reviews*, Vol.15, pp1294-1304(2011).
- [16] Hanane Aburideh, Adel Deliou, Brahim Abbad, Fatma Alaoui, Djilali Tassalit and Zahia Tigrine," An experimental stud of a solar still: Application on the sea water desalination of Fouka", Vol. 33, pp 475-484(2012).

Potassium thiocyanate as Inhibitor for the Corrosion of Copper in different acidic mediums

D.M.Sobhy^{1*}, Y.El-Taweel³, M.Abd El fattah^{1,*}, M.E. Ossman^{1,2}

¹Petrochemical Engineering Department, Faculty of Engineering, Pharos University, Alexandria, Egypt

²City for Scientific Research and Technology Application (SRTA-City), Alexandria, Egypt.

³Chemical Engineering Department, Faculty of Engineering, Alexandria University, Alexandria, Egypt

*corresponding author

Abstract

The effect of potassium thiocyanate (KSCN) on the corrosion of copper in 1 M HCl and 0.5 M H₂SO₄ was investigated by weight loss techniques, electrochemical impedance spectroscopy (EIS) and potentiodynamic polarization. EIS measurements showed that the dissolution process of copper occurs under diffusion control. The Nyquist plots of copper in acidic medium consist of distorted semicircles followed by diffusion tail indicative. Potentiodynamic polarization curves indicated that the potassium thiocyanate behaves as cathodic-type inhibitor. The corrosion rates of copper and the inhibition efficiencies of the KSCN were calculated. The results obtained show that the KSCN could serve as an effective inhibitor for the corrosion of copper in both 1 M HCl and 0.5 M H₂SO₄. Inhibition was found to increase with increasing concentration of the KSCN.

1. Introduction

Copper has been one of the preferred metals in industry owing to its excellent electrical and thermal conductivities, good mechanical workability, and its relatively noble properties. ^[1] Copper is resistant toward the influence of atmosphere and many chemicals, however, it is known that in aggressive media it is susceptible to corrosion. ^[2] Copper is used in microelectronics, fabrication of heat exchanger tubes and cooling water systems, due to its high thermal and electrical conductivities, low cost and malleability. ^[3-4] It is commonly used as a material in heating and cooling systems. ^[5] It is widely used in many applications in electronic industries and communications as a conductor in electrical power lines, pipelines for domestic and industrial water utilities including sea water, heat conductors, heat exchangers, etc. ^[6-7] It is a general consensus that the best method to protect the metal deployed in these corrosive environments is to add corrosion inhibitors. ^[8-9] The use of inhibitors is the most economical and practical method of reducing corrosive attack on metals. ^[10] To this end, the use of organic and

inorganic substances to inhibit corrosion of metals in many environments is well established. ^[11] It is generally believed that corrosion inhibitors effectively eliminate the undesirable destructive effects of aggressive media and prevent copper dissolution. ^[12] The inhibiting action of these inhibitors is usually attributed to their interactions with the copper surface via their adsorption. ^[13] Most of the well-known acid inhibitors are organic compounds containing nitrogen, oxygen and sulfur atoms. ^[14] But other types of inhibitors, such as inorganic compounds, are used in different acidic media. ^[15]

The aim of this research is to study the effectiveness of potassium thiocyanate (KSCN), which is considered to be inorganic corrosion inhibitor in controlling corrosion of copper in 1 M HCl and 0.5 M H₂SO₄ solutions using three techniques: weight loss, potentiodynamic polarization and electrochemical impedance spectroscopy (EIS) techniques for corrosion measurements.

2. Experimental

2.1. Electrochemical Measurements

The electrochemical impedance (EIS) and polarization measurements were achieved using frequency response Solatron Parstat 2263 Transfer Function Analyzer (TFA), that was controlled by a personal computer for data logging and data analysis. The frequency range for EIS measurements was 0.01 Hz - 100 kHz. The amplitude of the superimposed potential was 10 mV.

The electrochemical measurements of metals in aqueous media were carried out in an electrochemical cell of three-electrode mode; working electrode, auxiliary electrode and reference electrode. The material used for constructing the working electrode was copper that had the following chemical composition (% wt) 0.5% Ca, 99.5% Cu was used for the electrochemical corrosion studies in aqueous solutions. The working electrodes were fabricated by cutting and shaping in cylindrical forms. A long screw fastened to one end of the test cylinder for electrical connection. The samples were wet hand-polished using different grade emery papers 320, 400, 600, 800 and 1000 grit finishes starting with a coarse one and proceeding in steps to the fine grit up to a mirror finish, washed thoroughly with double-distilled water and finally dried by absolute ethanol, just before immersion in the solution. Each experiment was carried out with newly polished electrode. Three identical samples were tested for each experiment to ensure the reproducibility of the results. The results were consistent within $\pm 2\%$.

2.2. Weight loss Measurements

Coupons with area 21 cm² its dimensions 3*3*0.25 cm³ were used in the weight loss experiments. The weight loss coupons were polished, cleaned and suspended in beakers containing 100 ml of the test solutions. After definite time, the coupons were removed from the solution, washed with distilled water, ethanol and then dried by acetone and reweighed.

The weight loss was then determined (gm/cm².hr), the experiment was then repeated for different times in travels up to 96 hours. To test the reliability and responsibility of the measurements, duplicate experiments were performed in each case of the same conditions.

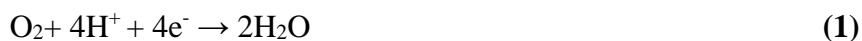
2.3. Solution preparation

The solutions of H₂SO₄, HCl and KSCN from BDH chemical company and double distilled water were used for preparing stock solutions. The aggressive solutions of 1 M HCl were prepared by dilution of analytical grade 37% HCl with distilled water. The stock solution of 0.5 M H₂SO₄ was prepared from the concentrated acid solution using double distilled water. The inorganic compound tested was potassium thiocyanate. The concentration ranges of this compound were 0.00001, 0.00005, 0.0001, 0.0005, 0.001, 0.005, 0.01, 0.05, 0.1 and 0.2 M.

3. Results and Discussions

3.1. Potentiodynamic Polarization Results

Figure 1 shows the potentiodynamic polarization curves of copper in 0.5 M H₂SO₄, in absence and presence of different concentrations of KSCN. As seen from the figure, addition of the KSCN affects the cathodic part of the polarization curve for copper rather than the anodic one indicating that KSCN could be classified as cathodic-type inhibitor and retard the reduction of oxygen gas at the cathodic areas. The cathodic polarization curves of copper in absence and in presence of the KSCN show a limiting current, indicating that the cathodic reduction of oxygen gas at the copper surface takes place under diffusion control. Cathodic reduction of oxygen can be expressed either by a direct 4e⁻ transfer as shown by equation.



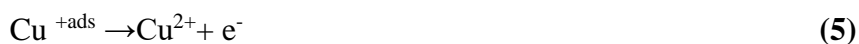
Or by two consecutive 2e⁻ steps involving a reduction to hydrogen peroxide first



Followed by a further reduction ^[10]



In absence of the KSCN the first step is probably fast reversible and the second one is the rate determining step of the reduction process of oxygen. However, in presence of the KSCN the first step is retarded by the adsorption of the active adsorbable species of the extract at the copper surface and becomes the rate determining step^[10]. The transfer of oxygen from the bulk solution to the copper solution interface will strongly affect rate of oxygen reduction reaction despite how oxygen reduction takes place, either in 4e⁻ transfer or two consecutive 2e⁻ transfer steps: Dissolution of copper in sulfuric acid is described by the following two consecutive steps:



Where Cu^{+ads} is an adsorbed species at the copper surface and does not diffuse into the bulk solution^[11]. Since KSCN act as cathodic inhibitor for the acidic dissolution of copper and the reduction process of oxygen gas at the cathodic areas take place under diffusion control, Tafel equation cannot be applied to calculate the electrochemical parameters of the corrosion reaction in this case.

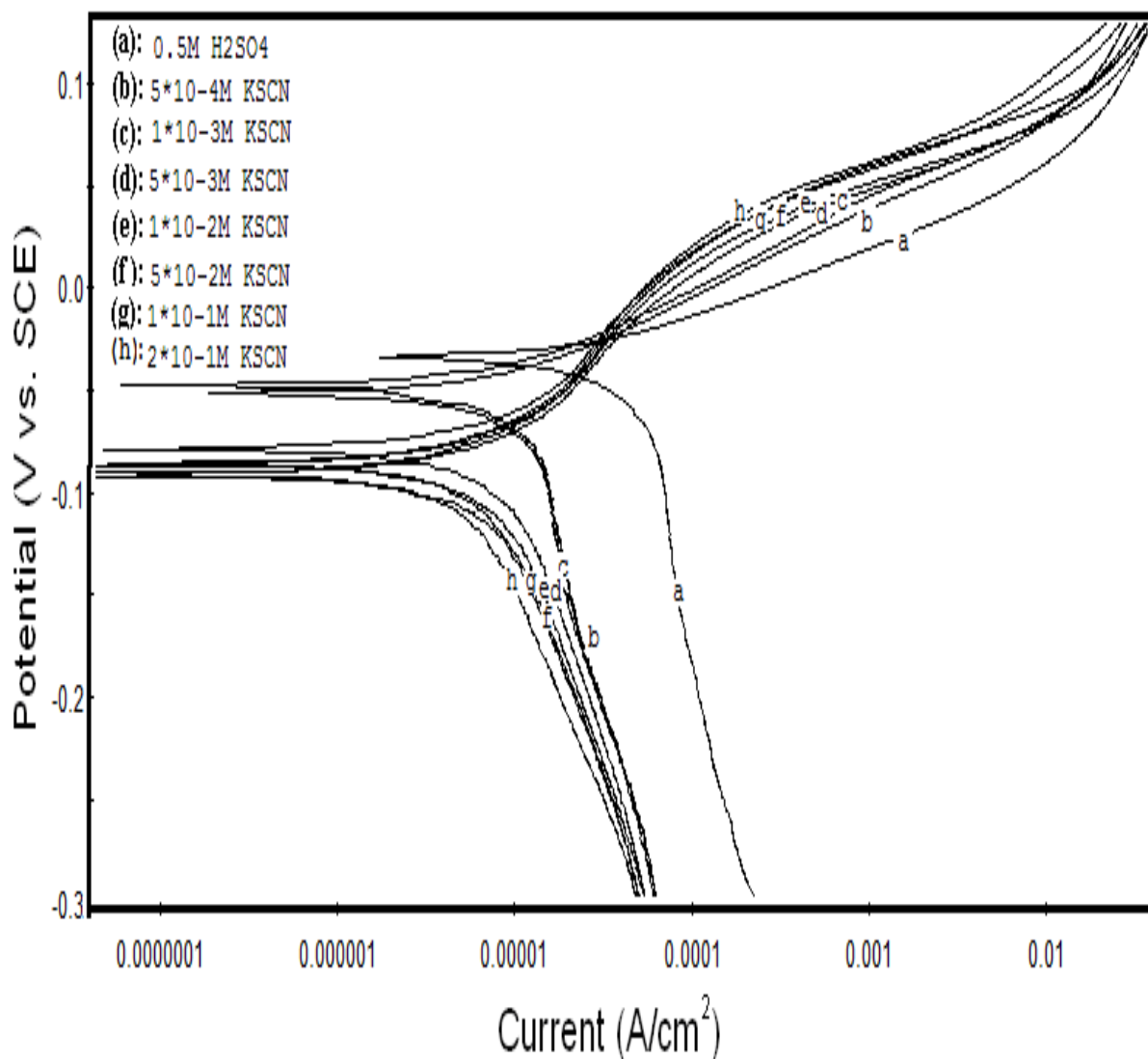


Figure 1. Potentiodynamic polarization curves for copper in 0.5 M H₂SO₄ in absence and presence of different KSCN concentrations at 30 °C after 2 hrs.

The previous curves don't obey Tafel equation due to the limiting current in cathodic parts.

3.2. Electrochemical Impedance Spectroscopy (EIS) Results

Figure 2 shows the Nyquist impedance plots of copper in 0.5 M H₂SO₄, in absence and presence of different concentrations of KSCN. The Nyquist plots of copper in acidic medium consist of distorted semicircles followed by diffusion tail indicative that the corrosion process occurs under diffusion control which confirm the results obtained from the polarization measurements. The increase in the size

of the semicircle in presence of the KSCN indicates that a barrier gradually forms on the copper surface. [12]

The impedance spectra of Nyquist plots for copper in 0.5 M H₂SO₄, in absence and presence of different concentrations of KSCN were analyzed by fitting the experimental data to the equivalent circuit model shown in figure 3. In this circuit R_s represents the solution resistance; R_{ct} is the charge transfer resistance and CPE is constant phase element related to the double-layer capacitance. The parallel combination of CPE₂ and R₂ could be equivalent to Warburg diffusion element which describes the diffusion behavior. It is noted that, the capacitances were implemented as constant phase element (CPE) during analysis of the impedance plots. [13]

Table 1: Electrochemical impedance parameters of copper in 0.5 M H₂SO₄ containing different concentrations of KSCN.

[KSCN], (mole/L)	R _s (Ohm.cm ²)	CPE (μF.cm ⁻¹)	n ₁	R _{ct} (Ohm.cm ²)	R _f (Ohm.cm ²)	CPE ₁ (μF.cm ⁻¹)	n ₂	R ₂ (Ohm.cm ²)	CPE ₂ (μF.cm ⁻¹)	n ₃	% P
0.0	1.3	41	0.8	124	138	1298	0.6	261	4498	0.6	0
5x 10 ⁻⁴	1.4	39	0.8	133	184	901	0.6	422	4380	0.6	25
1x 10 ⁻³	1.2	37	0.9	153	252	821	0.6	598	4300	0.3	45.2
5x 10 ⁻³	1.0	36	0.8	168	362	614	0.7	789	4270	0.4	61.9
1x 10 ⁻²	1.2	33	0.9	194	471	524	0.6	940	4100	0.4	70.7
5 x 10 ⁻²	1.1	31	0.8	227	566	351	0.7	1078	3840	0.4	75.6
1x 10 ⁻¹	1.4	29	0.9	257	611	290	0.6	1124	3773	0.3	77.4
2x 10 ⁻¹	1.2	27	0.7	267	691	266	0.6	1278	3576	0.4	80.0

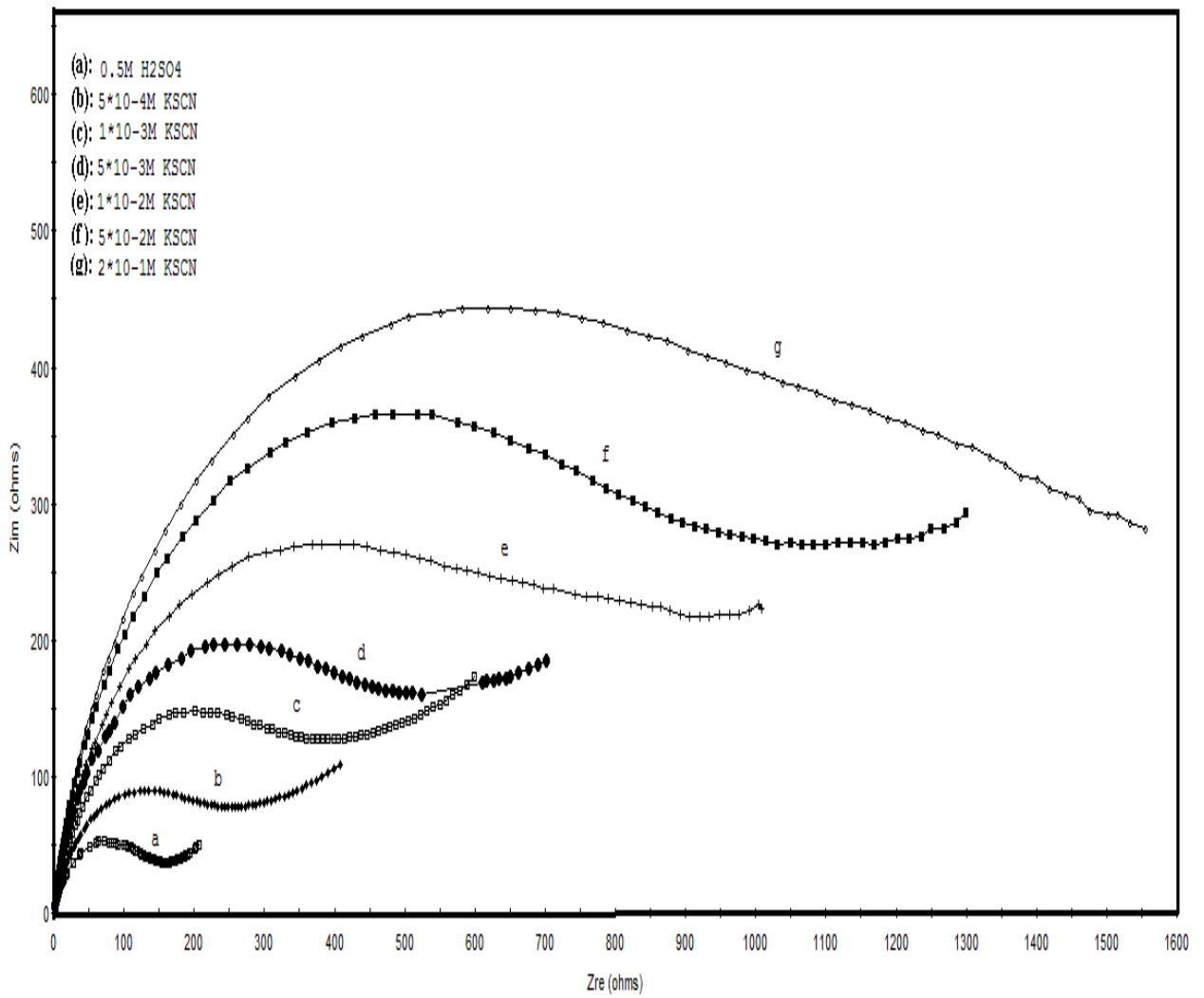


Figure 2. Nyquist plots of copper in 0.5 M H₂SO₄ in absence and presence of different concentrations of KSCN.

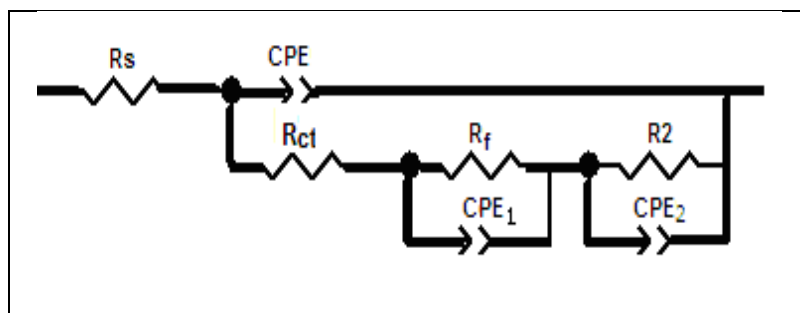


Figure 3. Schematic for the equivalent circuit of copper.

Increasing R_{ct} values with the concentration of the KSCN, suggesting decrease of the corrosion rate since the R_{ct} value, is a measure of electron transfer across the surface, and inversely proportional to the corrosion rate. The decrease in the Q_{dl} values could be attributed to the adsorption of the chemical constituents of the KSCN concentrations at the metal surface. ^[13]

The data shown in **table 1** indicate that the increase in the KSCN concentration leads to increase of the charge transfer resistance (R_{ct}) which is associated with a decrease in the non-ideal double layer capacitance. ^[13]

The percentage of inhibition efficiency (% P) was calculated from the impedance measurements using the relation:

$$\%P = [(R_{ct} - R_{cto}) / R_{ct}] \times 100 \quad (6)$$

Where R_{ct} and R_{cto} are the charge transfer resistance, in presence and absence of KSCN respectively. ^[14]

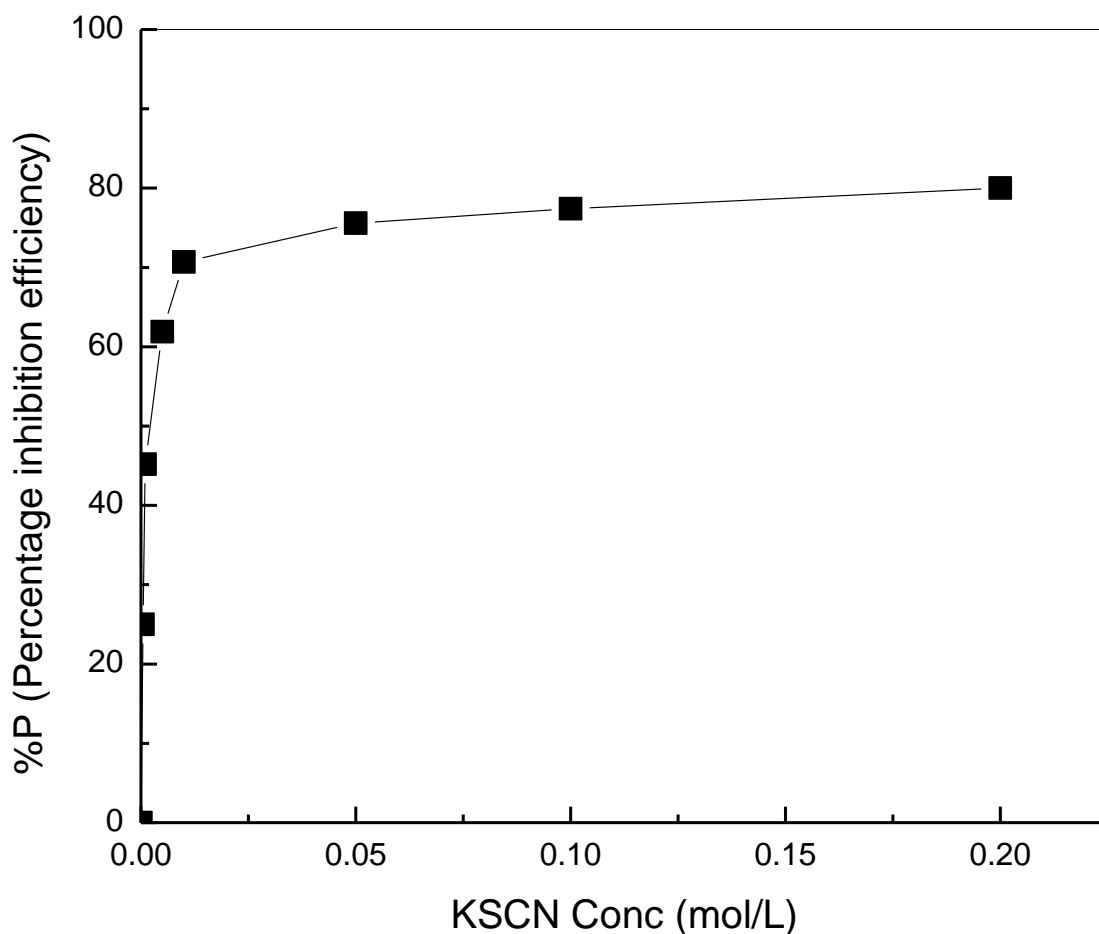


Figure 4 Relation between the percentage inhibition efficiency and concentration of KSCN for copper in 0.5 M H₂SO₄ after 2 hrs.

From table (1) the data shows that the %P increases by increase of KSCN concentrations by electrochemical impedance, as shown in figure (4).

Figure (5) shows the comparison between the percentage inhibition efficiency and concentration of KSCN for copper in 0.5 M H₂SO₄ by using two different methods (weight loss and electrochemical impedance). The curves show a good agreement with results obtained using the weight loss and electrochemical impedance techniques.

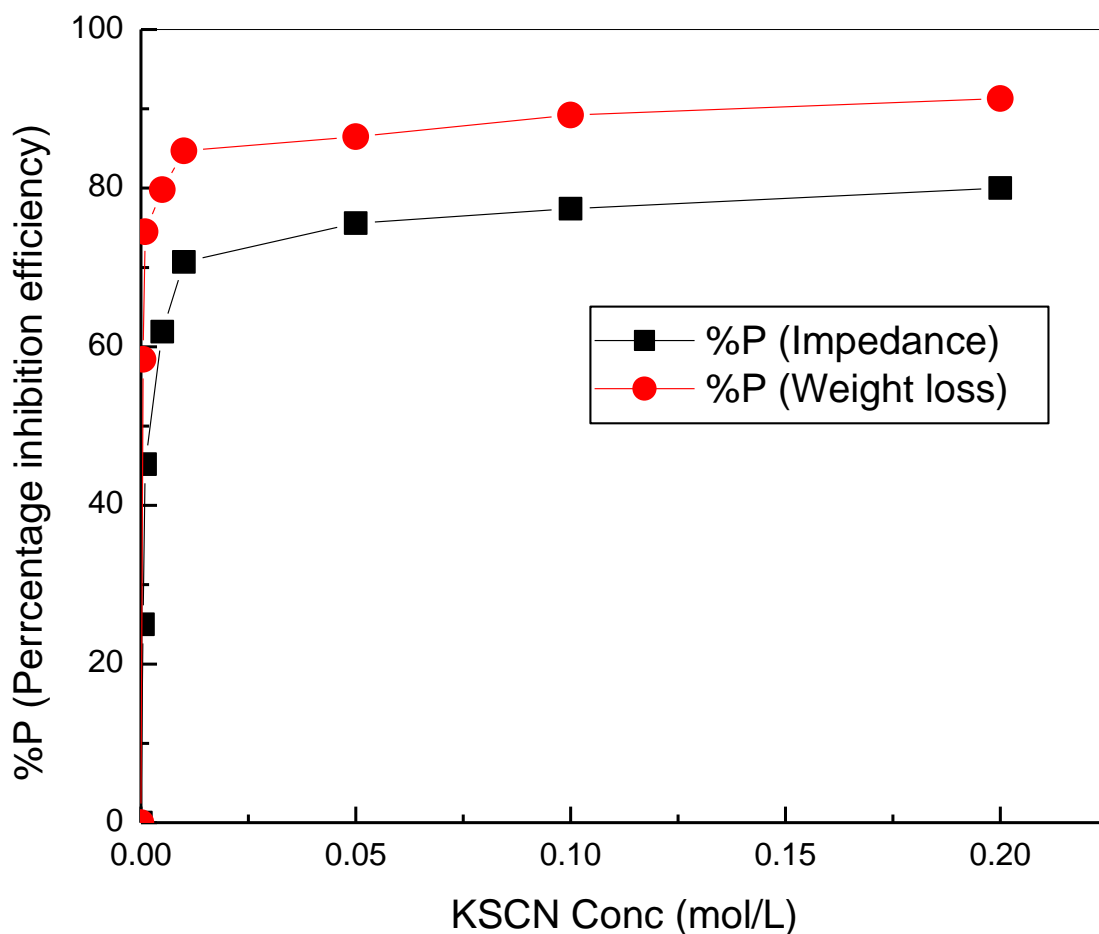


Figure 5 Comparison between the percentage inhibition efficiency and concentration of KSCN for copper in 0.5 M H₂SO₄ after 2 hrs.

The polarization and electrochemical impedance spectroscopy (EIS) tests haven't been done on 1 M HCl because the potentiodynamic polarization curves don't obey tafel equation for copper in 0.5 M H₂SO₄ and the behavior will be the same in 1 M HCl.

3.3. Weight Loss Results

Figures (6) and (7) show the relation between the percentage inhibition efficiency, and concentrations of the KSCN in 0.5 M H₂SO₄ and 1 M HCl respectively. As seen, the inhibitor efficiency of KSCN concentrations at certain fixed time of immersion increases with increasing the concentration of the KSCN.

The percentage inhibition efficiency (% P) was calculated using the relation:

$$\%P = [(w_0 - w) / w_0] \times 100 \quad (7)$$

Where w_0 and w are the weight loss in $\text{g.cm}^{-2}.\text{hr}^{-1}$, in absence and presence of KSCN.

Tables (2) and (3) showed that the KSCN is a good corrosion inhibitor for the acid corrosion of copper and showed also good inhibition efficiency along the immersion times.

Table 2: Effect of the concentration of the KSCN and immersion period on the corrosion of copper in 0.5 M H_2SO_4 at 30°C .

KSCN Conc. (mol/L)	Immersion period					
	2 h		4 h		24 h	
	W (g cm^{-2})	%P	W (g cm^{-2})	%P	W (g cm^{-2})	%P
0.00000	1.3316	---	1.3892	---	1.4118	---
0.00001	0.5707	57.1	0.6299	54.7	0.6515	53.8
0.00005	0.5540	58.4	0.5837	57.9	0.6396	54.7
0.00010	0.5201	60.9	0.5443	60.8	0.6226	55.9
0.00050	0.4218	68.3	0.4692	66.2	0.4879	65.4
0.00100	0.3392	74.5	0.4036	70.9	0.4364	69.1
0.00500	0.2682	79.8	0.3216	76.8	0.3308	76.6
0.01000	0.2029	84.7	0.2863	79.4	0.2889	79.5
0.05000	0.1790	86.5	0.1984	85.7	0.2286	83.8
0.10000	0.1413	89.2	0.1683	87.8	0.2115	85.0
0.20000	0.1160	91.3	0.1492	89.3	0.1767	87.5
KSCN Conc. (mol/L)	Immersion period					
	48 h		72 h		96 h	
	W (g cm^{-2})	%P	W (g cm^{-2})	%P	W (g cm^{-2})	%P
0.00000	1.4324	---	1.4373	---	1.4617	---
0.00001	0.6680	53.4	0.6740	53.1	0.6870	52.9
0.00005	0.5197	63.7	0.5315	63.0	0.5507	62.3
0.00010	0.4929	65.6	0.5153	64.1	0.5056	65.4
0.00050	0.4821	66.3	0.4915	65.8	0.5030	65.5
0.00100	0.4604	67.9	0.4703	67.3	0.4875	66.6
0.00500	0.3463	75.8	0.3542	75.4	0.3751	74.3
0.01000	0.2915	79.6	0.2935	79.6	0.3227	77.9
0.05000	0.2513	82.5	0.2628	81.7	0.2760	81.1
0.10000	0.2440	83.0	0.2589	82.0	0.2632	81.9
0.20000	0.1872	86.9	0.1905	86.7	0.2045	86.0

Table 3: Effect of the concentration of the KSCN and immersion period on the corrosion of copper in 1 M HCl at 30°C .

KSCN Conc.	Immersion period		
	2 h	4 h	24 h

(mol/L)	W (g cm ⁻²)	%P	W (g cm ⁻²)	%P	W (g cm ⁻²)	%P
0.00000	1.2996	---	0618.1	---	002.61	---
0.00001	0.6306	51.5	0.8942	50.5	1.2999	50.2
0.00005	0.5590	56.9	0.7889	56.3	1.1867	54.5
0.00010	0.4366	66.4	0.6188	65.7	0.8938	65.6
0.00050	0.3406	73.8	0.4985	72.4	0.7485	71.3
0.00100	0.2199	83.1	0.3356	81.4	0.4869	81.3
0.00500	0.1454	88.8	0.2112	88.3	0.3105	88.1
0.01000	0.1001	92.3	0.1580	91.3	0.2326	91.0
0.05000	0.0760	94.2	0.1220	93.2	0.1750	93.2
0.10000	0.0671	94.8	0.0928	94.9	0.1400	94.6
0.20000	0.0511	96.1	0.0761	95.8	0.1213	95.3
KSCN Conc. (mol/L)	Immersion period					
	48 h		72 h		96 h	
	W (g cm⁻²)	%P	W (g cm⁻²)	%P	W (g cm⁻²)	%P
0.00000	2.6228	---	2.6398	---	2.6612	---
0.00001	1.3333	49.2	1.3914	47.3	1.5127	43.2
0.00005	1.2524	52.2	1.2759	51.6	1.4108	46.9
0.00010	0.9157	65.1	0.9999	62.1	1.0593	60.2
0.00050	0.7848	70.1	0.8134	69.2	0.8902	66.5
0.00100	0.5690	78.3	0.6406	75.7	0.7374	72.2
0.00500	0.3521	86.6	0.4503	82.9	0.4661	82.5
0.01000	0.2893	88.9	0.3470	86.9	0.3161	88.1
0.05000	0.2541	90.3	0.3086	88.3	0.3007	88.7
0.10000	0.1740	93.4	0.2496	90.5	0.2808	89.4
0.20000	0.1315	94.9	0.1568	94.1	0.1976	92.6

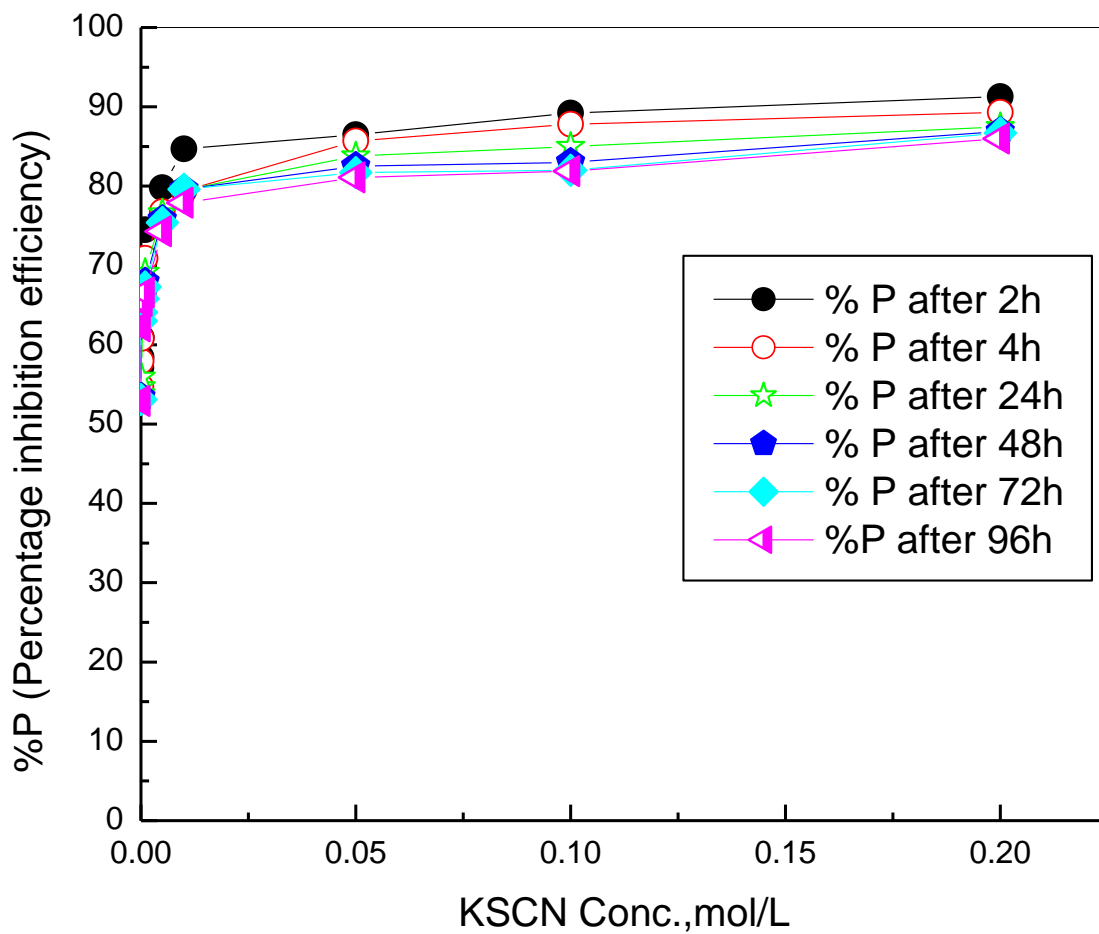


Figure 6 Variation of percentage inhibition of the copper in 0.5 M H₂SO₄, in absence and presence of different concentrations of KSCN with different exposure time at 30 °C.

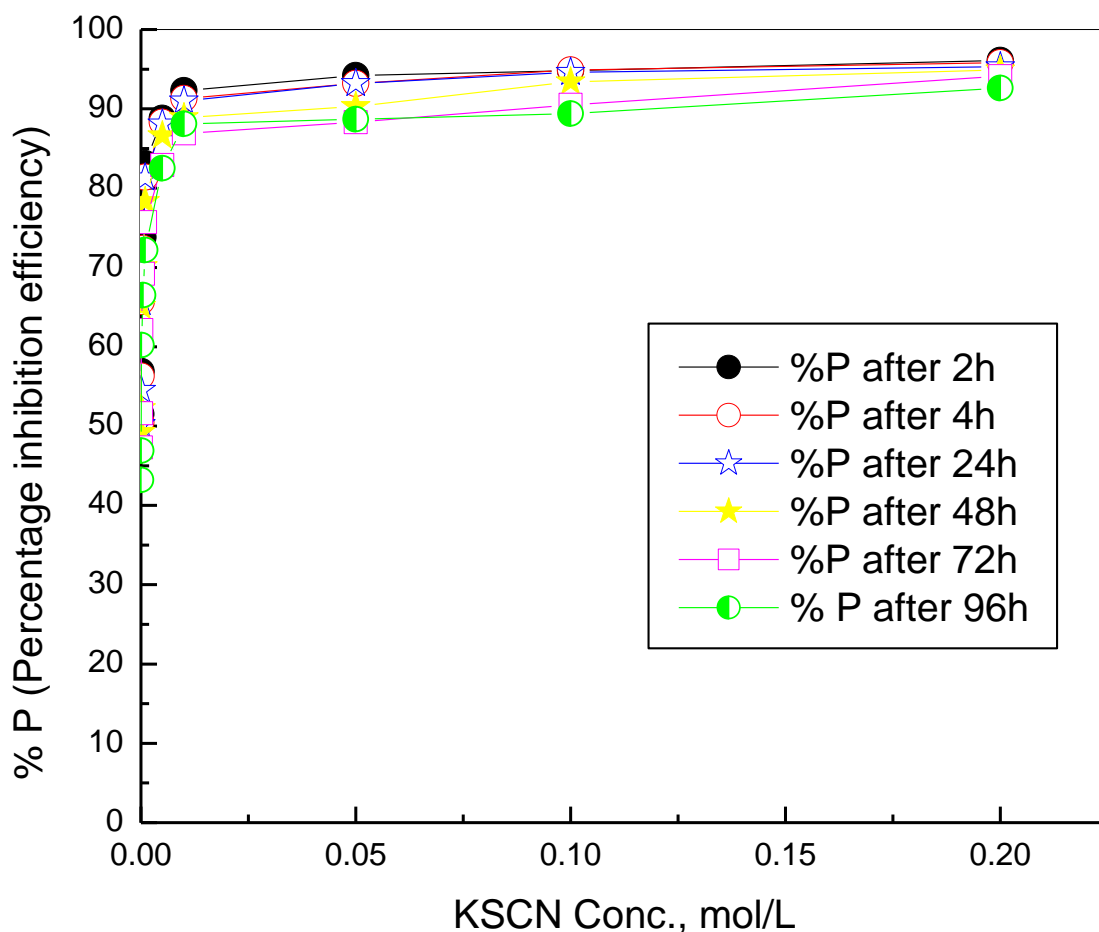


Figure 7 Variation of percentage inhibition of the copper in 1 M HCl, in absence and presence of different concentrations of KSCN with different exposure time at 30 °C.

Figures (8) and (9) show the variation of the inhibition efficiency of solutions of different concentrations of the KSCN with the immersion time in 0.5 M H₂SO₄ and 1 M HCl respectively. However, the dependence of the inhibition efficiency of the KSCN on the immersion time in presence of certain concentration of the KSCN shows a slight decrease in the efficiency with increasing the immersion time for the solutions containing low concentrations of the KSCN, but in presence of high concentrations of KSCN the efficiency is nearly constant. This behavior is probably discussed on the basis that in the presence of high concentration of the KSCN the surface of the metal becomes saturated with inhibitor molecules and the equilibrium between the adsorption and desorption processes of the inhibitor molecules at the metal surface is attained. ^[12]

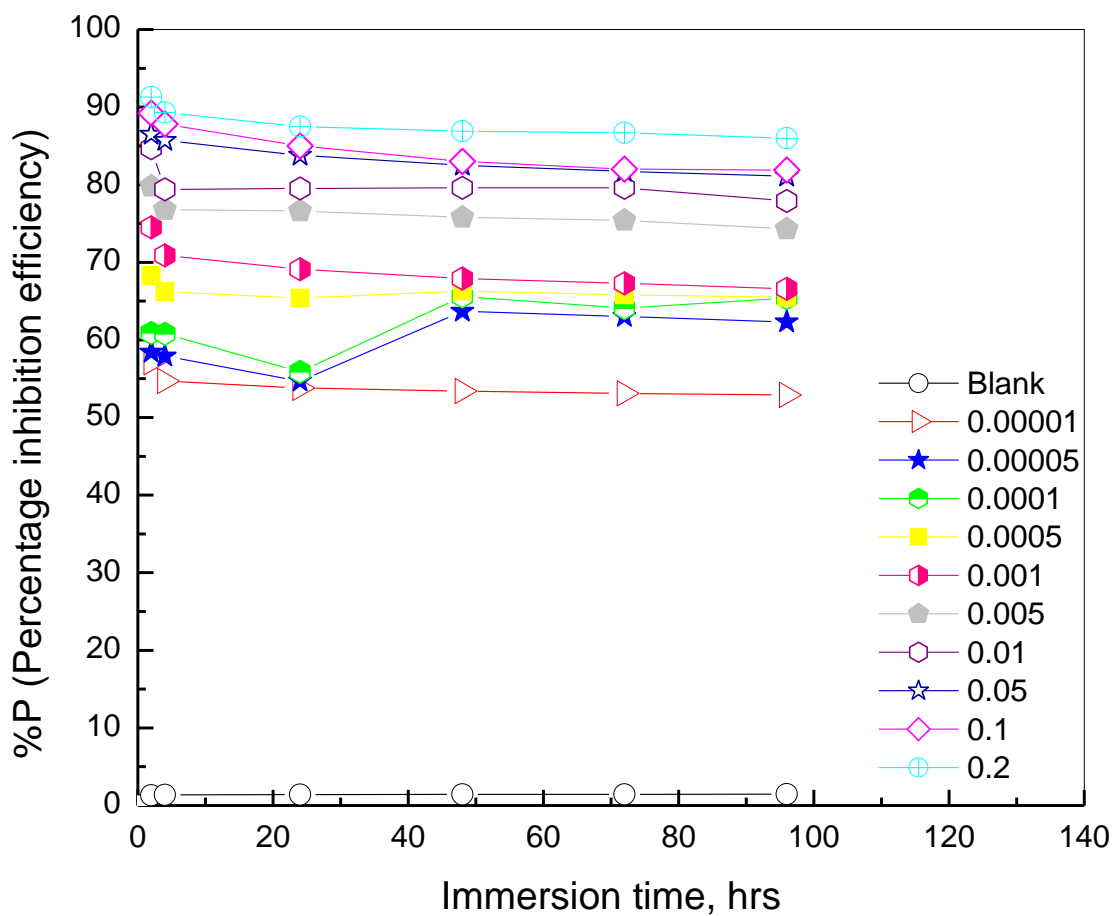


Figure 8 Dependence of the percentage inhibition efficiency (%P) of KSCN of copper in 0.5 M H₂SO₄ on the immersion time at 30 °C.

KSCN Concentrations (mole/L) [0.00001,0.00005,0.0001,0.0005,0.001,0.005,0.01,0.05,0.1,

0.2]

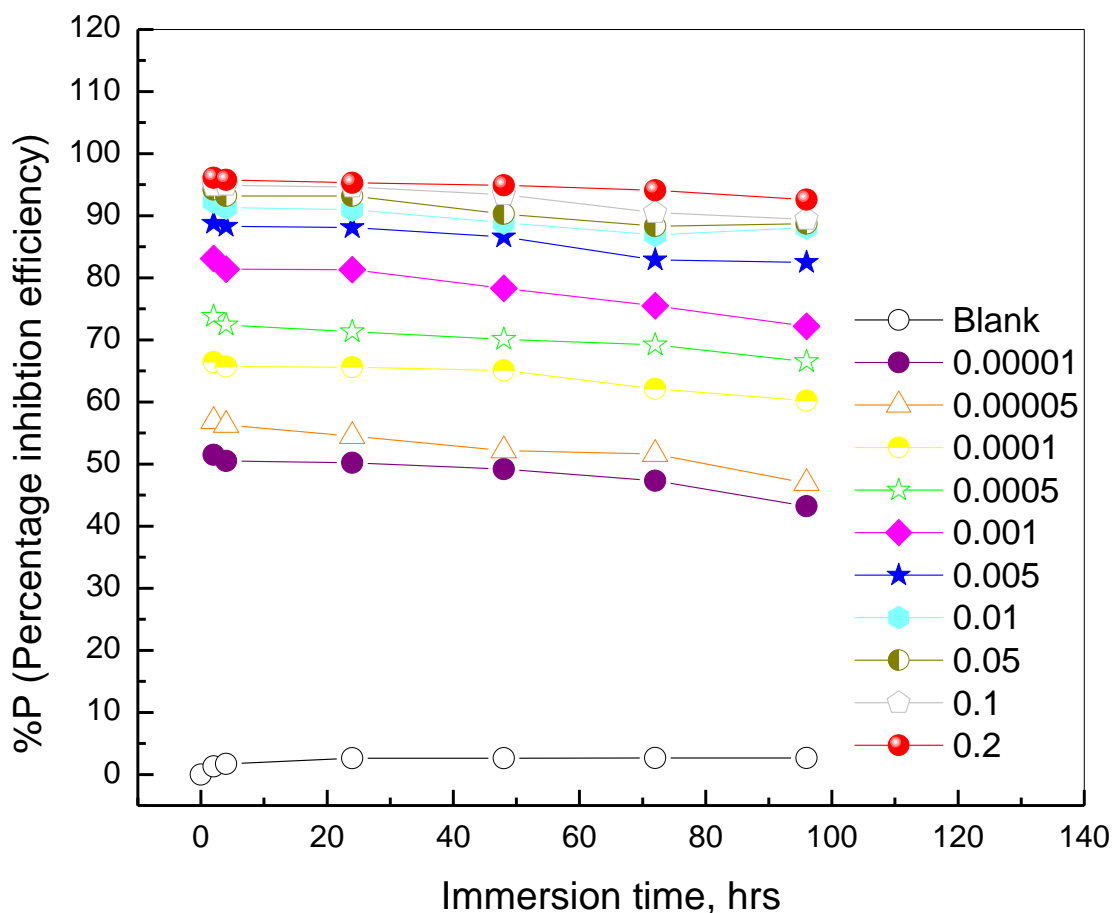


Figure 9 Dependence of the percentage inhibition efficiency (%P) of KSCN of copper in 1 M HCl on the immersion time at 30 °C.

KSCN Concentrations (mole/L) [0.00001,0.00005,0.0001,0.0005,0.001,0.005,0.01,0.05,0.1,0.2]

4. Conclusions

- The investigated concentrations of KSCN act as inhibitors for the corrosion of copper in both 1 M HCl and 0.5 M H₂SO₄ solution.
- Inhibition was found to increase with increasing concentration of the KSCN.
- Weight loss method has shown that inhibition efficiency of KSCN increases with increasing inhibitor concentration over the range 0.00001mol./L to 0.2 mol. /L. The maximum inhibition efficiency reached 91% for copper in 0.5 M H₂SO₄ and 96.1% in 1 M HCl.

- Polarization data showed that the KSCN act as cathodic type inhibitor for corrosion of copper in 0.5 M H₂SO₄.
- EIS results showed that the dissolution process of copper occurs under diffusion control.
- The Nyquist plots of copper in acidic medium consist of distorted semicircles followed by diffusion tail indicative.
- There is a good agreement between the values of inhibition efficiency of the KSCN concentrations obtained using the three techniques, weight loss, potentiodynamic polarization and electrochemical impedance spectroscopy.

References

- 1- K.F. Khaled, N. Hackerman, *Electrochem. Acta* 49 (2004) 485.
- 2- Antonijevic M. M., and Petrovic M. B., *Int. J. Electrochem. Sci.*, 2008, 3, 1.
- 3- Kane Jennings, G., Laibins, P.E., 1996. *Colloids and Surfaces A: Physicochem& Eng Asp.* 116, 105.
- 4- Sayed, E.I., Sherif, M., 2006. *Appl. Surf. Sci.* 252, 8615.
- 5- S.A. Abd El-Maksoud, *J. Electroanal. Chem.* 565 (2004) 321.
- 6- Hoepner, T., Lattemann, S., 2003. *Desalination* 152, 133.
- 7- Bellakhal, N., Dachraoui, M., 2004. *Mater. Chem. Phys.* 85, 366.
- 8- Zarrok, H., Oudda, H., Zarrouk, A., Salghi, R., Hammouti, B., Bouachrine, M., 2011. Weight loss measurement and theoretical study of new pyridazine compound as corrosion inhibitor for C38 steel in hydrochloric acid solution. *Der Pharm. Chem.* 3 (6), 576– 590.
- 9- Salghi, R., Bazzi, L., Hammouti, B., Kertit, S., 2000a. Electrochemical behavior of aluminum alloys a deaerated carbonate solution in presence of pyrazolic compounds. 272. *Bull. Electrochem.* 16 (6), 272–276.
- 10- Singh AK, Quraishi MA. Effect of Cefazolin on the corrosion of mild steel in HCl solution. *Corros Sci* 2010; 52:152–60.
- 11- Mihit, M., Laarej, K., Abou El Makarim, H., Bazzi, L., Salghi, R., Hammouti, B., 2010. Study of the inhibition of the corrosion of copper and Zinc in HNO₃ solution by electrochemical technique and quantum chemical calculations. *Arab. J. Chem.* 3, 55–60.

- 12- E. Geler, D.S. Azambuja, *Corros. Sci.* 42 (2000) 631.
- 13- M.G. Fontana, K.W. Staehle, *Advances in Corrosion Science and Technology*, vol. 1, Plenum Press, New York, 1970.
- 14- Ben Hmamou, D., Salghi, R., Zarrouk, A., Zarrok, H., Hammouti, B., Al-Deyab, S.S., Bouachrine, M., Chakir, A., Zougagh, M., 2012. Alizarin red: an efficient inhibitor of C38 steel corrosion in hydrochloric acid. *Int. J. Electrochem. Sci.* 7, 5716–5733.
- 15- Wu, T., Tsai, W., 2003. Effect of KSCN and its concentration on the reactivation behavior of sensitized alloy 600 in sulfuric acid solution. *Corros. Sci.* 45, 267–280.
- 16- Abd-El-Naby B.A., Abdullatef O.A., Abd-El-Gaber A.M., Shaker M.A. and Esmail G. (2012) *Int. J. Electrochem. Sci.*: 7 pp 5864.
- 17- Zhang D.Q., Gao L.X., and Zhou G.D. (2003) *Appl. Electrochem.*: 3 pp 361.
- 18- B. A. Abd-El-Nabey, S. El-Housseiny, G. A. El-Naggar, E. A. Matter, G. Esmail , *Physical Chemistry* 2015, 5(3).
- 19- Abdel-Gaber A.M., Abd-El-Nabey B.A., Sidahmed I.M., Zayady A.M., and Saadawy M., *Mater.* (2006) *Chem. And Phys.*: 98 pp 293.
- 20- K.Aramaki, M. Hagiwara, and H. Nishihara. (1987) *Corros. Sci.*: 5 pp 487.